Stony Brook University

Synthesis, Characterization and Applications of One-Dimensional Metal Oxide Nanostructures

A Dissertation Presented

by

Alexander Santulli

to

The Graduate School

in Partial Fulfillment of the

Requirements

for the Degree of

Doctor of Philosophy

in

Chemistry

Stony Brook University

December 2011

Stony Brook University

The Graduate School

Alexander Santulli

We, the dissertation committee for the above candidate for the

Doctor of Philosophy degree, hereby recommend

acceptance of this dissertation.

Professor Stanislaus S. Wong – Dissertation Advisor
Professor, Department of Chemistry

Professor Andreas Mayr – Chairperson of Defense
Professor, Department of Chemistry

Professor Joseph W. Lauher – Third Member of Academic Committee
Professor, Department of Chemistry

Dr. Charles T. Black – Outside Member
Group Leader of Electronic Nanomaterials at the Center for Functional Nanomaterials
Brookhaven National Laboratory

This dissertation is accepted by the Graduate School

Lawrence Martin

Dean of the Graduate School

Abstract of the Dissertation

Synthesis, Characterization and Application of One-Dimensional Metal Oxide Nanomaterials

by

Alexander Santulli

Doctor of Philosophy

in

Chemistry

Stony Brook University

2011

Nanomaterials have been of keen research interest, owing to their exciting and unique properties (e.g. optical, magnetic, electronic, and mechanical). These properties allow nanomaterials to have many applications in areas of medicine, alternative energy, catalysis, and information storage. In particular, one-dimensional (1D) nanomaterials are highly advantageous, owing to the inherent anisotropic nature, which allows for effective transport and study of properties on the nanoscale. More specifically, 1D metal oxide nanomaterials are of particular interest, owing to their high thermal and chemical stability, as well as their intriguing optical, electronic, and magnetic properties. Herein, we will investigate the synthesis and characterization of vanadium oxide, lithium niobate and chromium oxide. We will explore the methodologies utilized for the synthesis of these materials, as well as the overall properties of these unique nanomaterials. Furthermore, we will explore the application of titanium dioxide nanomaterials as the electron transport layer in dye sensitized solar cells (DSSCs), with an emphasis on the effect of the nanoscale morphology on the overall device efficiency.

Dedicated to my family

Table of Contents

List of Figures

List of Tables

List of Abbreviations and Symbols

SI	International system of units
°	degrees
°C	degrees Celsius
0D	zero-dimensional
1D	one-dimensional
2D	two-dimensional
3D	three-dimensional
A	ampere
Å	angstrom
AAO	anodized aluminum oxide
AFM	antiferromagnetic
ALD	Atomic Layer Deposition
ATO	anodized titanium oxide
BET	Brunauer-Emmett-Teller
cm	centimeter
cm^{-1}	wavenumbers
CTAB	cetyltrimethyl ammonium bromide
CuSCN	Copper thiocyanine
CVD	Chemical vapor deposition
dc	direct current
DNA	Deoxyribonucleic acid
DSSC	dye sensitized solar cell
DTGS	deuterated triglycine sulfate
e	elementary charge of an electron
E_A	activation energy
EBID	e-beam induced direct metal deposition
EDAX	energy dispersive analysis of x-rays
EDS	Energy dispersive x-ray spectroscopy
eV	electron volt
exp	exponential, base *e*
FC	field cooled
FE-SEM	field emission scanning electron microscopy
FET	field effect transistor
FF	fill factor
FM	ferromagnetic
FTIR	Fourier transform infrared spectroscopy
FTO	fluorine-doped tin oxide

g	gram
GIS	gas injection system
h	hour
HAADF	high-angle annular dark field detector
$\mathbf{H}_{EB}$	exchange bias field
HRTEM	high resolution transmission electron microscopy
I	current
J	current density
J_{Max}	current density at max power point
Jsc	short circuit current density
K	Kelvin
k_B	Boltzmann constant
kOe	Kilo-Oerstead
kV	kilovolts
LUMO	lowest unoccupied molecular orbital
M	molar
m	meter
mA	milliamperes
M-I	metal insulator
min	minute
MIT	Metal-to-insulator transition
mL	milliliter
mmol	millimolar
MPMS	Magnetic Property Measurement System
mV	millivolt
N-719	di-tetrabutylammonium cis-bis(isothiocyanato) bis(2,2_- bipyridyl-4,4_-dicarboxylato) ruthenium(II)
nA	nanoamperes
nm	nanometer
NNI	National Nanotechnology Initiative
NP	nanoparticle
NPGS	nano pattern generating system
NPs	nanoparticles
NW	nanowire
NWs	nanowires
OCVD	open circuit voltage decay
Oe	Oerstead
P3HT	poly-3-hexylthiophene (P3HT)
PECVD	Plasma enhanced chemical vapor deposition
PEDOT	poly(3,4-ethylenedioxythiophene)

P_{In}	incident power
R	resistance
redox	reduction/oxidation
rpm	rotations per minute
s	seconds
SAED	selected area electron diffraction
SEM	scanning electron microscopy
SHG	Second harmonic generation
sol-gel	Solution-gelation
spiro-MeOTAD	2,2,7,7-tetrakis(N,N-di- *p*-methoxyphenylamine)-9,9-spirobifluorene
T	temperature
T_0	initial temperature
T_B	blocking temperature
TBAI	tetra-butyl ammonium iodide
TCO	transparent conducting oxide
TEM	transmission electron microscopy
TGA	thermogravometric analysis
T_N	Néel temperature
TO	transverse optical
TW	terawatts
UV	Ultraviolet
UV/Vis	ultraviolet/visible
V	voltage
VLS	Vapor Liquid Solid
V_{Max}	voltage at max power point
Voc	open circuit voltage
XRD	X-ray diffraction
ZFC	zero field cooled
η	solar cell efficiency
θp	paramagnetic curie temperature
λ	wavelength
μ_{eff}	effective paramagnetic moment
μg	microgram
μm	micrometer
ρ	resistivity
σ	conductance
τ_n	electron lifetime
Ω	Ohms

Acknowledgments

First of all, I would like to thank my advisor Dr. Stanislaus Wong, for his expert guidance, support and tutelage. His scientific intuition and expertise have been an immense inspiration to me during my PhD. research. I would also like to express my deep gratitude and thanks to my committee chair, Professor Andreas Mayr and my third member, Professor Joseph Lauher, for their insightful comments and discussions on my research. My thanks also go to my outside member, Dr. Charles Black, for taking the time to serve on my committee.

I would like to especially thank Dr. Jim Quinn for his helpful discussions and advice during my dissertation work. Susan Van Horn deserves special thanks for her assistance and help during my research. Many thanks goes to my fellow group members, Jon, Dr. Xiaohui Peng, Chris, Amanda and David, whose discussions and aid have been of immense importance to me. I would also like to deeply thank Dr. Tae-Jin Park, Dr. Jingyi Chen, Dr. Hongjun Zhou, and Dr. Fen Zhang. Their guidance during at the start of my research is greatly appreciated.

I gratefully acknowledge the support and assistance given to me by the faculty and staff from the Stony Brook University Chemistry Department, as well as the Condensed Matter Physics and Materials Science Department at Brookhaven National Laboratory. I am grateful to Professor M.C. Aronson for assistance with magnetic measurements, and Professor J.B. Parise for his assistance with X-ray diffraction measurements. I would also like to thank Dr. Charles Schmuttenmaer from Yale University for his assistance with learning to make DSSCs.

Finally, I would like to thank my immensely supportive friends and family, for their continuous love and support throughout my Ph. D. career.

List of Publications

1. **Santulli, A.C.;** Koenigsmann, C.; Tiano, A.L.; DeRosa, D.; Wong, S.S.: Correlating titania morphology and chemical composition with dye-sensitized solar cell performance, *Nanotechnology*, **2011**, *22*, 245402/1-13.
2. **Santulli, A.C.;** Feygenson, M.; Camino, F.E.; Aronson, M.C.; and Wong, S.S.: Synthesis and Characterization of One-Dimensional Cr_2O_3 Nanostructures, *Chem. Mater.*, **2011**, *23*, 1000-1008.
3. Tiano, A.L.; **Santulli, A.C.**; Koenigsmann, C.; Feygenson, M.; Aronson, M.C.; Harrington, R.; Parise, J.B.; Wong, S.S.: Toward a Reliable Synthesis of Strontium Ruthenate: Parameter Control and Property Investigation of Submicrometer- Sized Structures, *Chem. Mater.*, **2011**, *23(14)*, 3277-3288.
4. Koenigsmann, C.; **Santulli, A.C.**; Gong, Kuanping; Vukmirovic, M.B.; Zhou, W.-P.; Sutter, E.; Wong, S.S.; Adzic, R.R.: Enhanced Electrocatalytic Performance of Processed, Ultrathin, Supported, Pd-Pt Core-Shell Nanowire Catalysts for the Oxygen Reduction Reaction, *J. Am. Chem. Soc.*, **2011**, *133(25)*, 9783-9795.
5. Tiano, A.L.; Koenigsmann, C.; **Santulli, A.C.;** and Wong, S.S.: Solution Based Synthetic Strategies for One-Dimensional Metal-Containing Nanowires, *Chem. Comm.*, **2010,** 46, 8093-8130.
6. **Santulli, A.C.**; Zhou, H.; Berweger, S.; Raschke, M.B.; Sutter, E.; and Wong, S.S.: Synthesis of Single-Crystalline One-Dimensional $LiNbO_3$ Nanowires, *CrystEngComm.* **2010**, 12, 2675-2678.
7. Chen, P.; Xu, X.; Koenigsmann, C.; **Santulli, A.C.**; Wong, S.S.; and Musfeldt, J.L.: Size-Dependent Infrared Phonon Modes and Ferroelectric Phase Transition in $BiFeO_3$ Nanoparticles, *Nano Lett.*, **2010**, 10, 4526-4532.
8. Chen J.; Zhou H.; **Santulli A.C.**; Wong S.S.: Evaluating cytotoxicity and cellular uptake from the presence of variously processed TiO_2 nanostructured morphologies, *Chem. Res. Toxicol.*, **2010**, 23, 871-879.
9. **Santulli, A.C.**; Xu, W.; Parise, J.B.; Wu, L.; Aronson, M.C.; Zhang, F.; Nam, C.-Y.; Black, C.T.; Tiano, A.L.; Wong, S.S.: Synthesis and Characterization of V_2O_3 Nanorods, *PCCP*, **2009**, 11, 3718-3726.

Chapter 1. Introduction to Nanomaterials and Metal oxides

1.1 What is Nano?

In the SI system of units, the prefix 'nano' denotes a factor of 10^{-9}. In the context of nanomaterials, nanotechnology, and nanoscience, the prefix is adopted due to the length scales involved. Within these three areas, the lengths often encountered, or are of most interest, are those in the range of 1-100 nanometers (nm), which is defined as the nanoscale by the National Nanotechnology Initiative (NNI). Nanoscience is defined as the study of nanomaterials, objects possessing at least one dimension (length, width or height) between 1 and 100 nm, while nanotechnology is defined as the application of these nanomaterials. In order to contextualize the scale of the "nano" world with respect to our "macroscopic" world, Figure 1 shows some representative sizes of various objects in both.

1.2 Dimensions on the Nanoscale

Nanomaterials can come in many shapes and sizes, but are generally categorized by how many dimensions are confined to the nanoscale and are denoted as zero-dimensional (0D), one-dimensional (1D), two-dimensional (2D), or three-dimensional (3D) nanomaterials, respectively. Nanoparticles, quantum dots, or any other nanomaterials that do not possess any dimension greater than 100 nm, are categorized as a 0D nanomaterial, and do not necessarily need to be spherical in shape. In order to be classified as a 1D nanomaterial, a material must maintain two dimensions on the nanoscale. Some examples of 1D nanomaterials are nanowires, nanorods or nanotubes, all of which generally have diameters on the nanoscale, while their lengths can be up to lengths of millimeters. 2D nanomaterials, on the other hand, contain only one dimension on

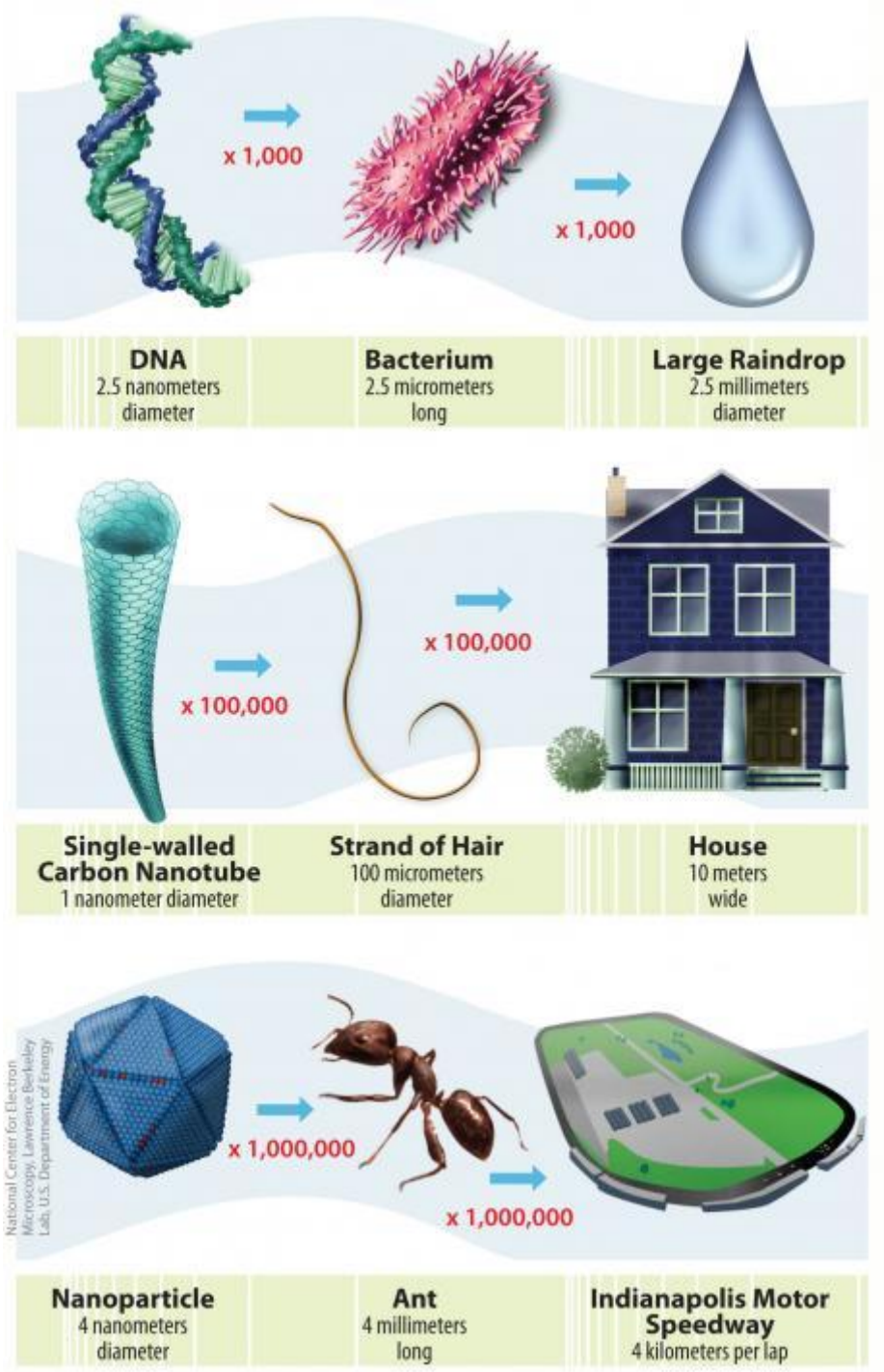

Figure 1.1: Schematic illustration of the scale of nanomaterials vs. macroscale objects. Taken from the National Nanotechnology Initiative (www.nano.gov)

the nanoscale, while the other dimensions can be on the order of centimeters. 2D nanomaterials are most often found as thin films, with thicknesses as little as a few nanometers over the entirety of a 6-inch silicon wafer. Finally, 3D nanomaterials can be thought of as nanomaterials that form larger assemblies that can exist on either the millimeter or centimeter scale. These types of 3D nanomaterials generally consist of arrays of 1D nanowires or tube, but can also consist of micrometer sized, porous, large-scale aggregates of smaller 0D nanoparticles.

1.3. 1D Nanomaterials

While nanomaterials of all dimensions offer various advantages and interesting properties, 1D nanomaterials are of particular interest for several reasons. One of the most attractive aspects of 1D nanomaterials is their inherent anisotropic morphology, which is attributable to the nanoscale confinement of the material in two dimensions.[1, 2] These types of nanomaterials combine mechanical robustness with structural flexibility, making them promising for applications as diverse as nanomechanical switches, acoustic sensors, and nanoactuators. Furthermore, 1D nanomaterials, owing to their nanoscale confinement, can manifest many intriguing properties, such as quantum confinement and ballistic transport.[3-7] It is these fascinating properties, in combination with an anisotropic morphology that allows for 1D nanomaterials to be the smallest class of materials with which one can effectively study highly unique and interesting optoelectronic transport properties.[1]

The small scale of these materials imbues them with a large surface area-to-volume ratio, often making them highly active in the areas of sensing and catalysis. However, it is again the anisotropic nature of these materials that makes them highly favorable in these areas, allowing for facile device fabrication. Furthermore, the miniscule scale of these materials allows for the

devices to maintain a small size, allowing for a greater number of devices per unit area. 1D nanomaterials have also shown promise as components in applications as diverse as field effect transistors (FET),[8] solar cells,[9] optical waveguides,[10] and lasers.[11]

1.3.1 Synthetic Strategies for 1D Nanomaterials

There is a wide variety of synthetic methods to fabricate one-dimensional nanomaterials, consisting of a desired material. These techniques and methods can be classified into three general groups. These include (i) solution-based methods, (ii) vapor-based methods, and (iii) solid-based methods. Both solution and vapor-based methods are considered to be bottom up approaches, where the nanomaterials are formed from smaller, molecular building blocks and are guided to grow along a single direction. However, solid-based methods generally refer to a top-down approach, wherein a larger material is broken down (e.g. etched) in order to form smaller nanostructures. Both solution and solid-based methods are amenable to the fabrication of soft, organic nanostructure motifs. However, the vapor-based methods are generally used for high-temperature syntheses and are less applicable for the generation of soft, organic materials.

1.3.1.1 Solution Based Synthetic Methods

There are a wide variety of solution-based methods for the synthesis of 1D nanomaterials, and these can range from ambient, room-temperature syntheses to high temperature and pressure syntheses.[2] The examples discussed herein include wet techniques, molten salt methods, sol-gel protocols, hydrothermal runs, template-directed growth, and electrospinning. While it is highly desirable to obtain these 1D nanoscale materials, there are very few materials which tend to naturally grow along a single direction without any influence from external sources. In order to ensure the formation of 1D nanomaterials, either a surfactant or a template can be employed as a

structure-directing agent. This alleviates the need for the material to crystallographically favor growth along one direction, and can offer a relatively facile method for the fabrication of 1D nanomaterials on a reasonably large scale.

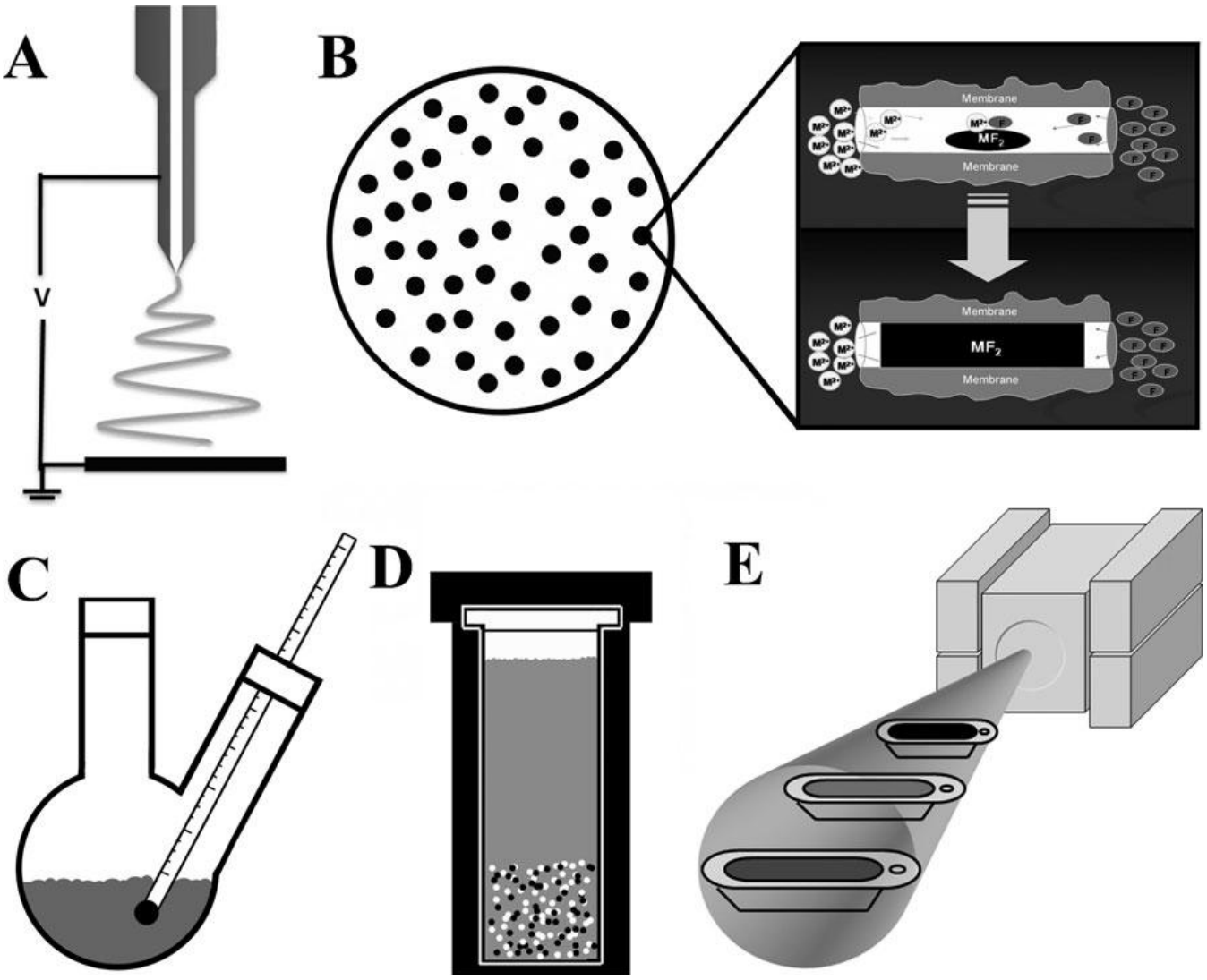

Figure 1.2: Schematic of various experimental methods for the synthesis of 1D nanostructures such as electrospinning (A), directed growth within the spatial confines of template pores (B), wet/solution-based methods (C), solvothermal/hydrothermal methods (D), and molten-salt synthesis (E). Reproduced from reference 2

1.3.1.2 Wet Chemical Techniques

As chemists, we are used to utilizing liquid solvents as a reaction medium for synthesis, so it is only natural to find synthetic schemes in which liquid solvents are the basis for the formation of 1D nanomaterials. These methods are often the simplest for the formation of 1D nanomaterials, and can utilize many types of solvents ranging from water[12, 13] and acids[14] to organic solvents such as octadecene[15] or hexane.[16] A schematic representation of this method can be found in figure 1.2C. However, as mentioned previously, it is rare to find a material, especially an inorganic material, which preferentially grows only along one direction.[1] Therefore, it is most common to find synthetic strategies that utilize either a structure directing surfactant or a hard template. In order for a surfactant to successfully direct the growth of a nanostructure, it must have a strong binding affinity to one of the materials' crystal facets.[17] This strong binding affinity drastically slows the growth of the nanomaterial along that direction, introducing an anisotropic growth direction to the material, thereby resulting in the formation of a 1D nanomaterial. While the applications of a surfactant can indeed result in a 1D nanomaterial, it is often a painstaking trial-and-error method to obtain a suitable surfactant for a desired material and size. Nonetheless, 1D nanomaterials of many semiconducting materials such as CdX (X= S, Se, Te),[18-20] as well as metals like Au,[21, 22] Ag,[23, 24] Pt,[25, 26] and Cu[27] have been fabricated, utilizing solution-based methods.

Furthermore, with careful manipulation of the reaction conditions and solvents utilized, the resulting product can form a single-crystalline nanomaterial. Single-crystalline materials consist of a contiguous, or a very nearly contiguous, crystal lattice within the nanomaterial, while by contrast, poly-crystalline nanomaterials denote a collection of smaller crystalline constituent materials which are assembled into a hierarchical motif. Single-crystalline nanomaterials are

highly desirable, owing to the fact that they evince minimal crystal grain boundaries, and often exhibit significantly fewer defects than their polycrystalline counterparts.[28] This advantage allows for effective and efficient propagation of properties through the nanomaterials with little to no resistance. However, polycrystalline materials often possess significantly higher surface roughness values than their single-crystalline counterparts, making them highly desirable in fields such as either sensing, catalysis, or batteries, where the surface area parameter is an important factor to be considered.[29]

1.3.1.3 Molten Salt Synthesis

In molten salt synthesis, traditional liquid solvents are replaced with either a salt or a salt mixture. After subsequent additions of precursors and surfactants, the mixture is then heated in a furnace to a temperature that is above the melting point of either the salt or salt mixture. A schematic representation of this method can be found in Figure 1.2E. At this point, the salt melts and becomes a molten solvent system, in which the precursors can dissolve and react with each other. This technique is quite versatile, and offers many parameters to alter and tune in order to gain a desired product.

One can imagine that the temperature at which a reaction occurs is an important parameter to control. In molten salt reactions, the reaction temperature is determined by the nature of the salt(s) utilized. Variations in the salt can be made by choosing various different salts like NaCl,[30] KCl,[31] LiCl,[32] NaOH,[33] and so on, which can result in a wide range of reaction temperatures. The temperature range of reactions can be further broadened and tuned through the use of eutectic mixtures, which are mixtures of salts that result in lower melting points than their individual components. In some cases, particularly the hydroxides, it has also been shown

that the presence of salt can aid in the formation of 1D nanostructures. The salt that is chosen also plays a critical role in determining the reaction rate, owing to the viscosity of the molten salt media. The more viscous a melt is, the slower the reaction occurs, which can hinder growth, as well as aid in the formation of a preferred morphology. However, as mentioned earlier, it is possible to add surfactants to the mix in order to aid in the formation of 1D nanomaterials, although their exact role within the reaction media is still largely unknown.

Another important aspect of the reaction medium that can be controlled in the molten salt syntheses is precursor solubility. Just as with traditional wet chemical reactions, if a precursor is not soluble in the solvent, the reaction is significantly hindered if not completely halted. Therefore, it is important to have precursors that are sufficiently soluble in the molten salt media in order for the reaction to occur and for the product to be generated. Unfortunately, owing to the high temperatures that are generally required to melt the salt(s), determining the solubility of the precursors is not trivial, and often a trial-and-error approach is taken in order to obtain appropriate precursors for the desired material.

Overall, the molten salt method is advantageous for many reasons, aside from its ability to form a desired material with a favorable morphology and composition. The products that can be obtained from the molten salt method are normally single crystalline in nature, which can prove to be highly advantageous for many applications.[2] Furthermore, the simplicity of the molten salt technique allows for it to be easily scaled up for mass production. Although this method offers many advantages, it is not without its faults. For starters, there is a requirement for high temperatures, which is not generally amenable towards the formation of organic materials. Second, there are issues with preparing nanomaterials with dimensions that possess

less than 10 nm. Finally, while surfactants can aid in the formation of a desired morphology, it is difficult to expressly control the morphology achieved.

1.3.1.4 Sol-gel Synthesis

Solution gelation chemistry, or sol-gel chemistry, has been around for quite some time, and is very effective in making a wide variety of materials. Sol-gel works by first creating a stable colloidal solution, or sol, of the desired material. A sol formed through the controlled hydrolysis of the precursor utilized. Subsequent treatment of this sol results in the formation of bridging links between individual colloidal particles. One common way that the gelation occurs is through the condensation of sol particles. The gel can then be treated in several different ways, resulting in the formation of an aerogel or xerogel, depending on experimental conditions. However, these materials are generally amorphous in nature and lack a well-defined crystalline structure.[34] The application of heat to these materials results in the crystallization of the material, although, owing to the formation and subsequent condensation of individual sol particles, the resulting product is polycrystalline in nature. While this method is versatile and allows for the creation of a wide variety of materials, it does not allow for much control over the morphology of the product. There are some experimental parameters, such as the pH and the solvent, that can be altered in order to gain some control over the resulting product.[35] However, in order to determine the morphology of the net product of a sol-gel reaction, a template can be utilized so as to dictate the anisotropic nature of the final product.[36-38] Specifically, the sol-gel methodology, in combination with a template, can allow for superior control over the morphology and chemical composition of the product. One of the most significant drawbacks for this method however is that the resultant product formed is often polycrystalline in nature.

1.3.1.5 Hydrothermal/Solvothermal Synthesis

In this method, an aqueous (hydrothermal) or other liquid (solvothermal) solvent is mixed with the desired precursors before being sealed into a Teflon lined stainless steel bomb and heated to a temperature above the boiling point of the solvent. A representation of this is shown in Figure 1.2D. At this point, the pressure in the reaction vessel becomes exceedingly high, thereby drastically increasing the solubility and reactivity of the precursors. This markedly enhanced solubility and reactivity can allow for reactions that, under normal conditions, would not be conceptually feasible to occur. This method is also highly versatile, allowing for manipulation of parameters such as temperature, time, pressure, solvent, and precursors. Moreover, this technique is also applicable to the formation of many different materials, including metals,[39] metal oxides,[40] semiconductors,[41] and even carbonaceous materials.[42] The growth conditions present within the hydrothermal/solvothermal vessel, specifically the high pressure, will also allow for the advantageous formation of single crystalline materials. Furthermore, this method maintains a relatively low reaction temperature, typically between 100 and 200°C, which renders this method relatively energy friendly. Additionally, these elevated temperatures and pressures can be achieved through the application of microwave irradiation, thereby further increasing the energy efficiency of this method by allowing for shorter reaction times in the system.[43] However, while this protocol has many advantages, it does not allow for explicit control over the morphology of the product. Hence, often a surfactant or other similar structure directing agent is necessary to initiate the formation of a 1D nanostructure.[44-47]

1.3.1.6 Template directed Synthesis

As alluded to earlier in the sol-gel section, the application of a template to a synthetic method offers superior control over the morphology of the resultant product. This is depicted in Figure 2B. Superior morphology control arises from the ability of the template to physically restrict the reaction and/or growth mechanisms to only occur within the spatial confines of the templated structure. A wide variety of materials have been utilized as templates for the formation of 1D nanomaterials, ranging from so-called hard templates such as anodized aluminum oxide (AAO), titanium oxide (ATO), track etched polycarbonate, and zeolites to so-called soft templates including DNA, polymer micelles, and even viruses.[48-53] As is common in all other synthetic methods, there are several important factors that must be considered when utilizing a template to form 1D nanostructures. First, it is important to consider the interaction between the template and the synthetic environment. For instance, it is highly undesirable to create a synthetic environment in which the template to be utilized is soluble in. In the case where this is true, the template would solubilize and would no longer be capable of spatially confining the reaction within a geometrically well-defined area. Furthermore, it is also important to consider the experimental conditions required in order to selectively remove the template, while either not dissolving or etching away the desired product.

The filling of the template pores with the desired product is critical to the success of the template method. In order to successfully infiltrate the pores of the template, there are several methods that can be utilized for precursor insertion, including dipping,[54] pressure,[55] or vacuum[56] protocols. In many cases, an additional crystallization step is required after the infiltration of the template with the desired material. This is generally accomplished through an annealing step, which exposes the loaded template to elevated temperatures, generally resulting in the formation

of a polycrystalline product. However, careful control of experimental conditions can allow for the creation of single-crystalline materials at room temperature.[57] Another disadvantage of utilizing "hard" templates is their inherently low product yield. AAO typically possesses surface porosities of 25-50%, thereby resulting in a maximum yield of 50%. "Soft" templates are not as hindered by this issue, and methods based on these materials can be effectively scaled up to bulk-like quantities.

1.3.1.7 Electrospinning

This synthetic method is quite unique in that it intrinsically creates 1D nanomaterials. A schematic representation of the electrospinning method can be found in Figure 1.2A. The principle behind electrospinning is quite simple and works by combining a sol-gel precursor with a high voltage set-up. The requirements for electrospinning are minimal, necessitating only a metal needle, a grounded collector, and a high voltage power supply. Upon application of a high voltage between the metal needle and the grounded collector, the accumulation of charge on the needle results in the formation of a cone. This then extends into a continuous jet of material. It is this formation of a continuous jet, that results in the intrinsic formation of 1D nanostructures via the electrospinning method. Collection of this material followed by subsequent treatments of the as-obtained material can result in the formation of 1D crystalline materials.

While additional components can be utilized in order to obtain more complex morphologies,[58-60] in its simplest form, only the above mentioned materials are required. One of the most advantageous aspects of this method is its ability to generate 1D nanomaterials in a continuous fashion.[58] However, control over the width of the resulting nanomaterial can be challenging because there are a number of experimental parameters that need to be adjusted in

order to vary the width of the nanostructures. Two of the more important aspects of electrospinning that need to be carefully controlled in order to reproducibly obtain nanostructures are temperature and humidity.[1, 61-63] While these two aspects may be somewhat difficult to reliably manage, there are other parameters that can be used to fundamentally determine product morphology. These include the applied voltage,[64] the conductivity of the sol,[65] sol concentration,[64, 66] the feeding rate of precursor solution,[67] the distance between the needle and the collector,[68] as well as the solvent[69] that can be used for the sol. A careful selection of precursors allows for the formation of a wide variety of crystalline materials, including metal oxides, polymers, heterostructured materials, and composites.[70-72]

1.3.2 Vapor Phase Methods

By contrast with the methods mentioned previously, vapor phase synthesis delivers a desired precursor to a substrate for growth in a gaseous form instead of in a dissolved liquid media. These types of methods are used extensively in the fabrication of inorganic materials, such as metal oxides, although carbon-based materials can also be effectively synthesized through these methods. The basic governing principle behind many vapor phase syntheses is that, first, a gaseous precursor must be formed. This can be accomplished through the application of high temperatures in order to vaporize the precursors or through the use of a precursor already in the gaseous phase. Careful manipulation and control over the saturation of the precursor in the reaction atmosphere will allow for the deposition of the desired material in a 1D motif. There are many experimental parameters that can be fine tuned in order to successfully grow the material, such as temperature, precursor, substrate temperature, and atmosphere. Vapor phase methods can be broken down into two distinctive categories, namely direct and indirect vapor phase methods. In direct vapor phase methods, the material that is

evaporated is the same as that being deposited. Hence, if the desired material were to be ZnO, then vapor phase ZnO would be used as the precursor for the growth of the material. By contrast, indirect vapor phase methods create a reactive intermediate in the vapor phase, which then reacts to form the final desired product, as was found to be the case with SiO_2.[73] Overall, vapor phase syntheses are advantageous, owing to their ability to fabricate materials possessing a high degree of purity as well as crystallinity.

1.3.3 Chemical Vapor Deposition (CVD)

This type of vapor phase synthesis utilizes volatile precursors that are either already in the gaseous phase or have been evaporated *in situ* to form gaseous materials. These precursors are then delivered to a substrate by an inert carrier gas, with a carefully controlled temperature to ensure deposition of the correct phase as well as morphology. There are many different types of CVD processes, from plasma enhanced CVD (PECVD), which utilizes a plasma field to enhance reactions and allows them to occur at lower temperatures,[74, 75] to atomic layer deposition (ALD) which is capable of deposition of a desired material one atom layer at a time.[76] While CVD offers the ability to synthesize highly crystalline materials with a tunable and controllable composition, it very rarely affords direct control over the morphology of the desired product. However, as mentioned above, careful manipulation of relevant experimental parameters can allow for the synthesis of nanowires,[77, 78] nanotubes,[79, 80] nanowhiskers[81, 82] or nanoribbons[83, 84] of a desired material. It has also been shown that ALD can be successfully combined with hard inorganic templates, such as AAO, in order to fabricate 1D nanowires or nanotubes of several different materials.[85-87]

1.3.4 Vapor Liquid Solid (VLS)

This vapor phase method relies on the combination of vapor phase precursors and a solid catalyst supported on a substrate. The VLS method introduces the ability to define and control the size of the resulting nanomaterial, by using a predefined metal or metal alloy catalyst for the growth of the nanomaterial. Therefore, by tailoring the size of the catalyst nanoparticle, one can effectively control the overall size of the nanomaterial.[88] The basic mechanism behind the VLS method that governs the growth of the 1D nanomaterial is the ability for the catalyst nanoparticle to form an alloy with the precursor material. When the catalyst material becomes supersaturated with the precursor material, precipitation is facilitated and the nanowire begins to grow. The growth direction of the nanowire, i.e. either parallel or perpendicular to the substrate, can be manipulated through control of either temperature, substrate, or catalyst material.[89, 90]

The necessity for a catalyst to be present has its advantages, such as the ability to explicitly control which areas will be conducive to nanowire formation and which are not, as well as its ability to provide control over the size of the nanowires. However, aside from these advantages, there are still several disadvantages to this method. First, the catalyst must be heated to a temperature above its melting point in order to facilitate the growth of nanowires. Careful tuning of the catalyst particle can yield a catalyst with a low melting point. However, this can often be a tedious and time-consuming endeavor. Furthermore, tuning of experimental parameters, such as substrate temperature, flow rate, and precursor material, in order to obtain a desired product or orientation, can also be somewhat tedious and time consuming. However, despite these drawbacks, the VLS method has shown promise as a reliable method for the fabrication of semiconducting materials for various applications.[91-93]

1.3.5 Applications of 1D nanomaterials

In the previous section, we discussed various viable methods for the fabrication of 1D nanomaterials, such as nanowires, nanotubes, and nanorods. The advantages and disadvantages for each of these methods must be weighed against the disadvantages, as well as the desired product. In the case that a single-crystalline product is desired synthetic methods like molten salt or hydrothermal are highly desirable as they are highly conducive to the formation of single-crystalline materials. However, if a product with predictable and controllable size is desired, than a template mediated approach may be of particular interest, owing to the ability to predictably control the size of the final material. With this in mind, we will now discuss the potential applications of these materials. As mentioned earlier, one of the most beneficial attributes of 1D nanostructures is their inherent ability to transport properties easily throughout the entirety of the nanostructure. This combined with their anisotropic, or wire-like, morphology makes them ideal for applications in devices. These nanowires can further spatially confine optical excitations and guide them along the axial length of the 1D nanostructure. This phenomenon is known as wave guiding, and is desirable for applications ranging from lasers to optical storage media.

1.3.6 Wave guiding and Optical Applications

As alluded to in previous sections, the anisotropic nature of 1D nanomaterials allows for the manifestation of interesting and exciting optical properties. By analogy with quantum dots, the small size of the nanowires can result in quantum confinement of optical excitations. This can result in the variation of the nanowires' band-gap, an observation permitting for rational tunable of optical properties. Furthermore, as mentioned before, nanowires can act as optical

waveguides, thereby allowing them to effectively act as nanoscale lasers. This type of effect has been realized in well-ordered arrays of ZnO nanowires, which, after excitation with an optical laser, emit a UV laser.[94] 1D nanomaterials are also finding applications in non-linear optics, such as with second harmonic generation (SHG). The nanowires' large aspect ratio allows for the facile fabrication of devices which can then act as effective nanoscale frequency doublers.[95-97] This concept of applications of 1D nanomaterials for non-linear optics will be further explored in our discussion concerning lithium niobate nanowires. Specifically, it has also been shown that nanowires of silicon can be fabricated with an internal *p*-*n* junction and are effective at separating photo-generated charges, rendering them applicable for solar energy conversion. It has even been shown that the small size of the nanowires can enhance the absorptivity of the nanowires, thereby further increasing the efficiency.[98]

1.3.7 Sensing and Catalysis

The small size of the 1D nanomaterials results in a large surface area-to-volume ratio, which allows for the adsorption of a large quantity of materials to the surface of the nanostructure. This is a critical aspect that is to be considered, particularly in the areas of catalysis and sensing, due to the importance of surface interactions in these processes. The facile device fabrication, combined with the enhanced surface area-to-volume ratio, makes these 1D nanomaterials ideal candidates for sensitive nanoscale sensing devices, as well as for highly active catalysts. 1D nanomaterials have been realized for the sensing of various compounds, such as various organic molecules, as well as of hydrogen, oxygen, and even NO_x materials.[99-102] These 1D nanomaterials can even be utilized for the sensing of UV light for photodetection.[103, 104] Anisotropic nanostructures have also been found to be highly advantageous as catalysts, especially for methanol oxidation and oxygen reduction reactions in direct methanol fuel

cells.[105-107] These nanomaterials can also catalyze water splitting,[108] as well as various other chemical reactions,[109-112] with high yield and extraordinary selectivity.

1.3.8 Electronics

As mentioned in previous sections thus far, the anisotropic nature of the nanowires allows for efficient transport through the nanostructure. Furthermore, devices can readily be constructed out of these types of nanomaterials, relatively easily. The small size of the nanomaterials allows for the fabrication of a large number of devices in a given area, which is very desirable in the computer industry. It has been shown that decreasing the diameter of metal nanowires can have a dramatic effect upon the conductivity of electrons. Specifically, Bi nanowires that possess a diameter below approximately 50 nm are no longer metallic conductors, but rather act more like either semiconductors or insulators. This effect can be attributed to quantum confinement within the nanowires, resulting in a migration of the valence and conduction bands away from one another which can thereby create a band-gap within the nanowires.[113] 1D nanomaterials can also have an effect on the metal-to-insulator transition (MIT) of certain materials.[114-116] These types of materials are useful for applications as sensors, smart windows, as well as memory devices.[117-119] It has been shown that the temperature of the MIT in a given material can be tuned at the nanoscale. This is due to the fact that the higher the surface area-to-volume ratio of a material, the more strained it becomes. Increased strain in a material facilitates the conversion of the material between a metal and an insulator, thereby resulting in a transition temperature lower than that of the bulk.[120] Therefore, for a given material, simply changing the size of the nanowire can effectively vary the transition temperature over a range of temperatures. This concept will be further explored in more detail in subsequent sections.

1.4 Objectives of Current Work

The discussion in the previous sections has focused primarily on the synthesis and applications of 1D nanomaterials. However, the focus of this thesis will be primarily concerned with the application of the above mentioned techniques in order to synthesize specific types of materials, namely metal oxides. Metal oxides can generally be classified into two primary categories, i.e. binary and ternary metal oxides. Binary metal oxides are materials that maintain the common formula of M_xO_y, wherein 'M' denotes a metal, such as Fe, Ti or Zn, and 'O' is oxygen. Similar to binary metal oxides, ternary metal oxides also contain a combination of metal and oxygen. However, the general formula of these materials is $A_xB_yO_3$ or $A_xB_yO_4$, wherein 'A' and 'B' denote different metals. These metal oxides can be synthesized utilizing the techniques discussed in Section 1.3.1. However, they possess several advantages over conventional elemental metals and carbonaceous materials. First, many metal oxide materials possess superb thermal stability, resisting melting to temperatures >1000°C. Furthermore, many metal oxides are also relatively chemically inert, thereby giving these materials robust structural properties.[2, 121] In addition to these advantages, metal oxide materials have also found applications in areas discussed in Section 1.3.2, rendering them highly desirable for a wide range of applications. We will also explore the effect of the nanoscale size regime upon the electronic, magnetic, and optical properties of as-synthesized metal oxide materials. The thesis is divided into chapters on the synthesis, characterization and application of various metal oxides, such as vanadium oxide, lithium niobate, chromium oxide and titanium dioxide, which we now briefly outline as follows.

1.4.1 Synthesis and characterization of V_2O_3 nanorods (Chapter 2)[122]

Oxide materials of vanadium are of particular interest, owing to their unique metal-to-insulator transitions. In this work, we utilized a hydrothermal method to produce single crystalline VO_2 nanowires in large quantities. These nanowires have been subsequently developed as a template for the formation of single crystalline V_2O_3 nanowires via a thermal reduction procedure. Through careful control and manipulation of conditions during thermal reduction, the morphology and the single crystalline nature of the precursor material can be maintained. We further investigated the effect of the nanowire morphology on the MIT of our precursor VO_2 materials via synchrotron radiation. The effect of nanoscale morphology upon the properties of V_2O_3 has also been investigated through both electronic and magnetic measurements (Figure 1.3).

1.4.2 Synthesis of single-crystalline one-dimensional $LiNbO_3$ nanowires (Chapter 3)[123]

Lithium niobate ($LiNbO_3$) is an intriguing material, owing to its favorable optical and ferroelectric properties. In our work, we have applied a molten salt technique in order to fabricate sub-micron sized $LiNbO_3$ nanowires with average widths of 300-400 nm. In this method, we again utilized a nanoscale Nb_2O_5 precursor as the template for the formation of our desired final product. This method yields large quantities of single crystalline $LiNbO_3$ structures, thereby maintaining the desired beneficial 1D morphology. We further investigated the purity and ordering within the material via Raman spectroscopy and high resolution transmission electron microscopy, which both revealed a preferential alignment of the *c*-axis along the axial length of the nanowire. These attributes afforded these nanomaterials possible applications in areas as diverse as voltage sensors, data storage, non-linear optics, and acousto-

optical modulators. A TEM and HRTEM image, with an inset containing the SAED pattern, can be found in Figure 1.4

1.4.3 Synthesis and characterization of one-dimensional Cr_2O_3 nanostructures (Chapter 4)[124]

By contrast with previous chapters where the final desired products were synthesized from existing nanostructures, we have also successfully accomplished the template-based synthesis of chromium oxide (Cr_2O_3) 1D nanostructures. Chromium sesquioxide is an important material, owing to its high thermal and oxidative stability, as well as its catalytic and sensing abilities. Chromium oxide is also an antiferromagnetic material with a bulk Néel temperature of 307 K. We were able to successfully synthesize 1D nanostructures of Cr_2O_3 by utilizing the spatial confines of a template pore in order to direct and define the formation of tubes via a sol-gel method. The resulting polycrystalline product maintained widths comparable to those of the template pores. We further characterized our nanostructures by exploring their magnetic and electronic properties on the nanoscale. A TEM image, with insets characterizing the magnetic and electronic properties, of the nanowires can be found in Figure 1.5

1.4.4 Correlating titania morphology and chemical composition with dye-sensitized solar cell performance (Chapter 5)[125]

In recent years, the growing demand for energy and the need to stem carbon emissions has collectively revitalized research into alternative energies. One of the most promising alternative energy sources is the sun, delivering approximately 120,000 terawatts (TW) of energy to the earth every hour. In recent years, a particular class of solar cells, namely dye-sensitized solar cells (DSSC), has received considerable research interest, owing to their potential as a low

cost solution to solar energy. In this work, we have investigated the use of several morphologies and chemical compositions of titania and titanate nanostructures for possible applications as electron conducting species in DSSCs. We have characterized our solar cells through current-voltage measurements under solar illumination, as well as through open circuit voltage decay curve measurements in order to determine the efficiencies and electron lifetimes within our cells. We have further characterized our nanostructured photoanodes via SEM and dye desorption experiments in order to more fully understand their ability to adsorb and utilize dye molecules for solar energy generation. A schematic diagram, along with SEM images and characteristic solar cell performance data, can be found in Figure 1.6.

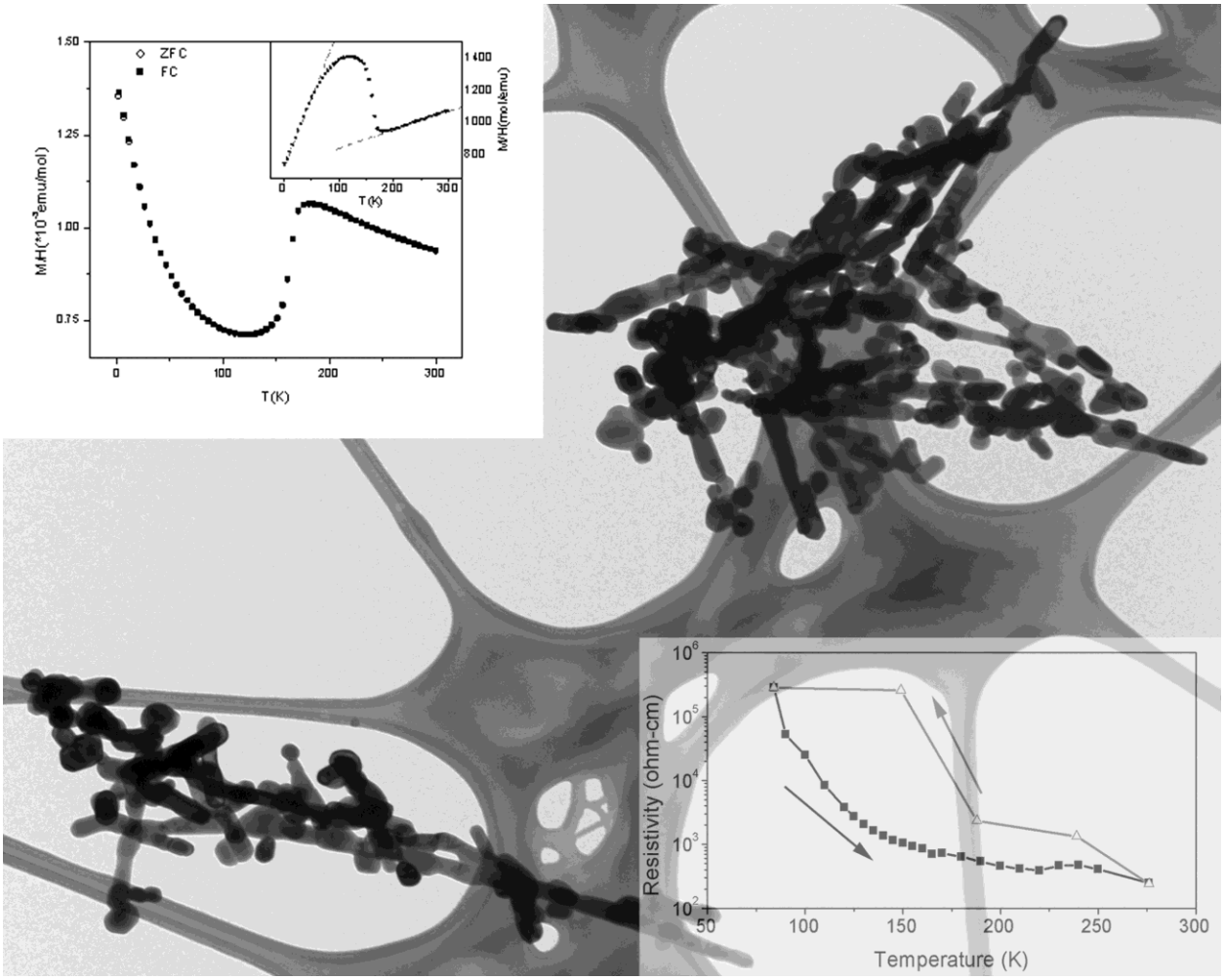

Figure 1.3. TEM image of V_2O_3 nanowires synthesized via thermal reduction of VO_2 nanowires in a hydrogen atmosphere. Inset top left: magnetization vs. temperature curve of V_2O_3 nanowires. Inset bottom right: resistivity vs. temperature of an individual nanowire device.

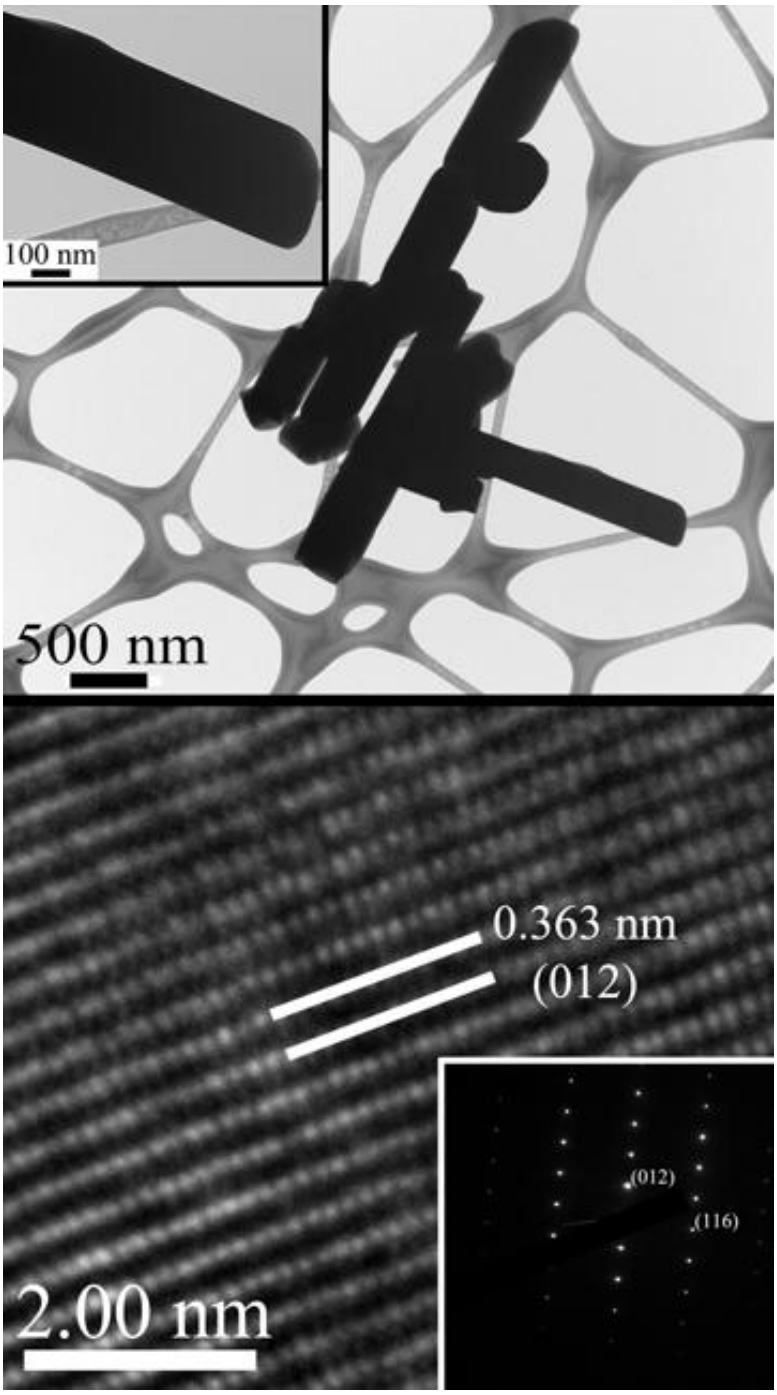

Figure 1.4. Top: TEM image of $LiNbO_3$ nanowires. Inset: Higher magnification TEM image highlighting well-defined, smooth nanowire faces. Bottom: HR-TEM image of $LiNbO_3$ nanowire giving rise to well-defined crystal planes. Inset: SAED of nanowire revealing the single crystalline nature of these nanowires.

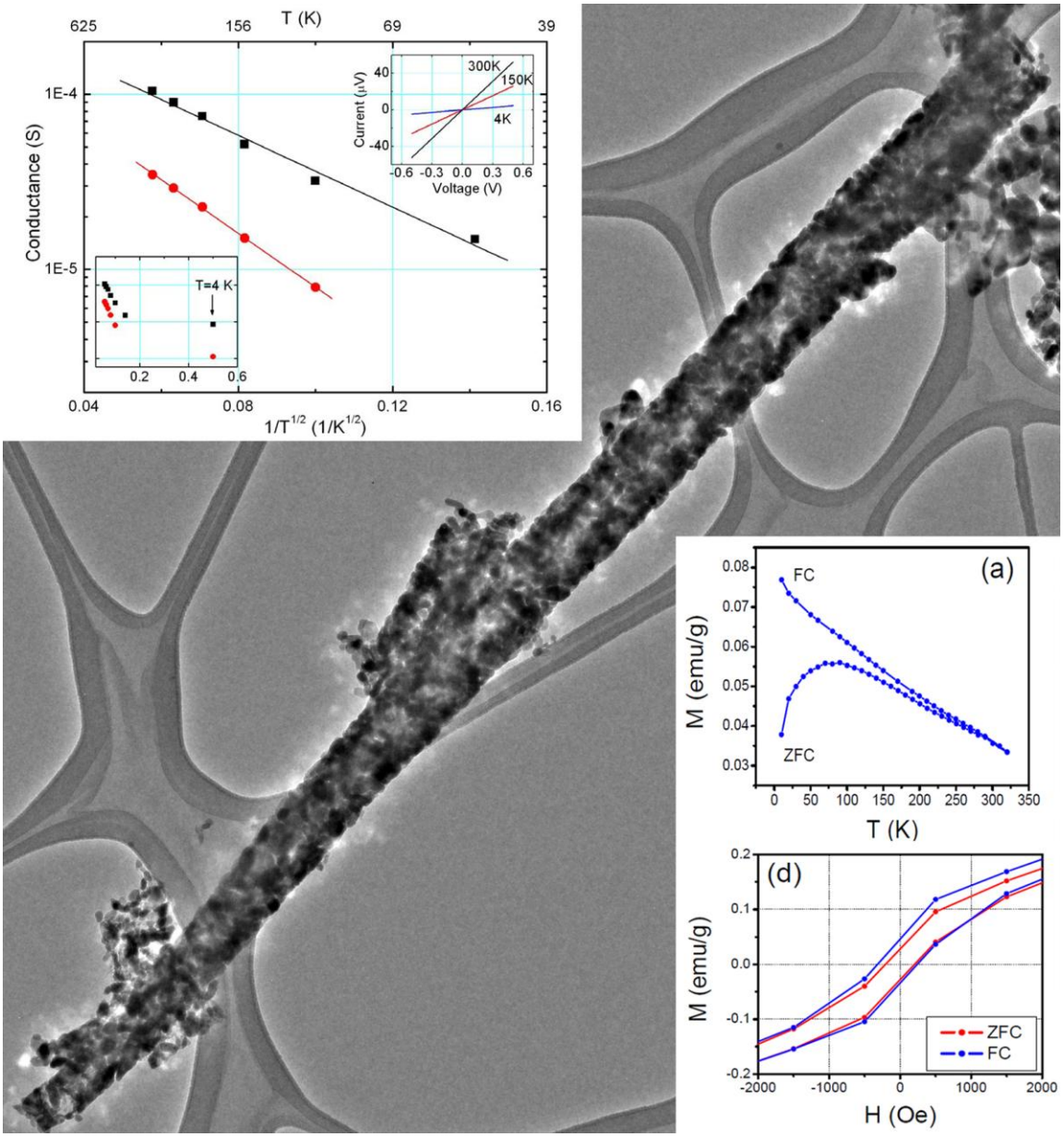

Figure 1.5. TEM image of Cr_2O_3 nanowire, revealing its polycrystalline nature. Inset top left: Conductance vs. $1/T^{1/2}$ plot. Data suggest that the conductivity mechanism of the individual nanowires proceeds via a random hopping pathway. Inset bottom right: Top reveals magnetism vs. temperature plot, showing typical antiferromagnetic behavior, while bottom highlights magnetism vs. field strength, revealing a slight exchange bias due to the presence of uncompensated surface spins.

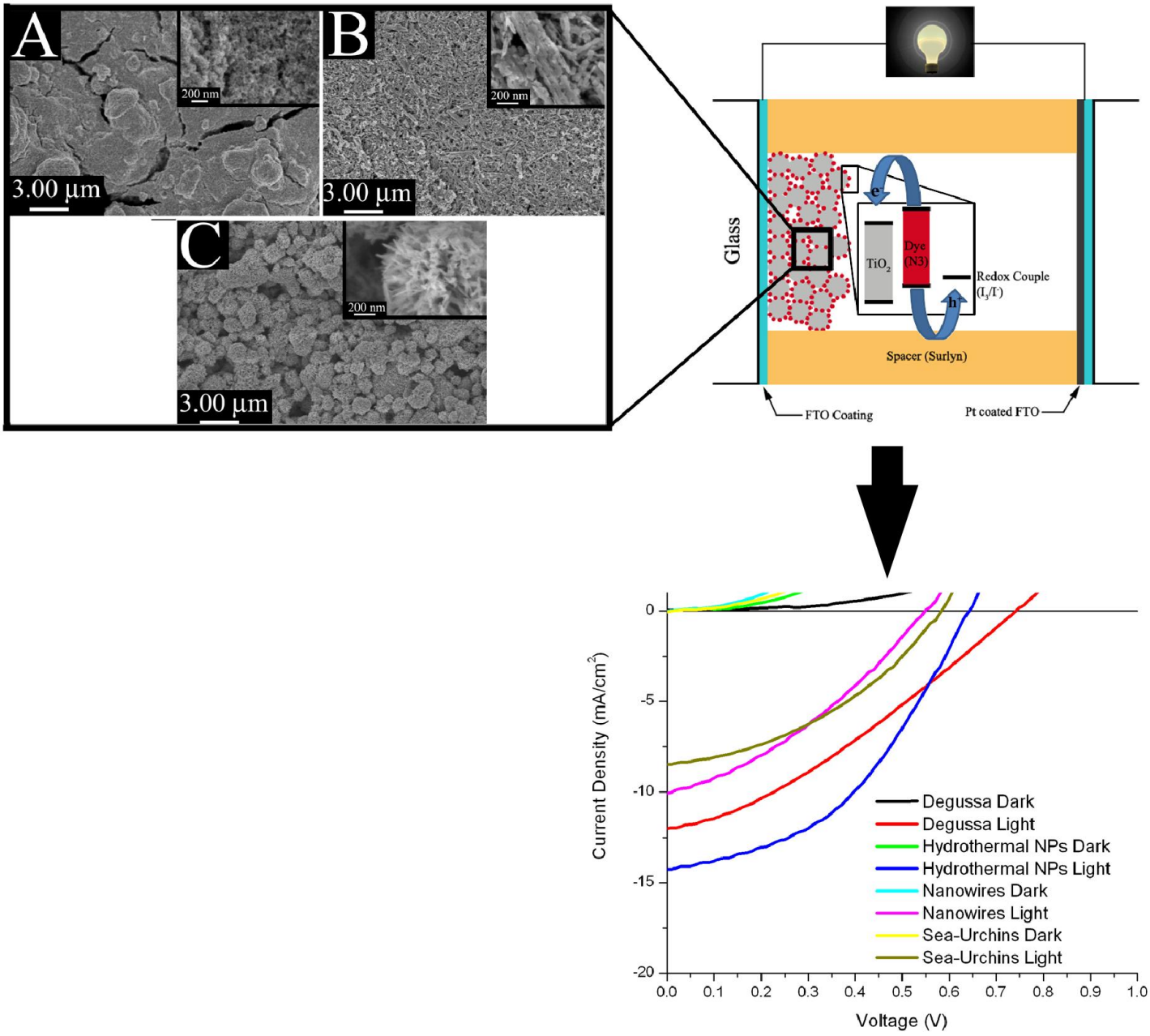

Figure 1.6. Left: SEM images of films of A) TiO_2 nanoparticles B) TiO_2 nanowires, and C) TiO_2 sea-urchins. Middle: Schematic diagram of a DSSC. Right: Current Density vs. Voltage graphs of different TiO_2 morphologies incorporated into solar cells.

1.5 References

1. Y. Xia, P. Yang, Y. Sun, Y. Wu, B. Mayers, B. Gates, Y. Yin, F. Kim and H. Yan, *Advanced Materials*, 2003, **15**, 353-389.
2. A. L. Tiano, C. Koenigsmann, A. C. Santulli and S. S. Wong, *Chemical Communications*, 2010, **46**, 8093-8130.
3. H. J. Li, W. G. Lu, J. J. Li, X. D. Bai and C. Z. Gu, *Physical Review Letters*, 2005, **95**, 086601.
4. D. Gunlycke, J. W. Mintmire and C. T. White, *The Journal of Physical Chemistry Letters*, 2010, **1**, 1082-1085.
5. L. Vayssieres, C. Sathe, S. M. Butorin, D. K. Shuh, J. Nordgren and J. Guo, *Advanced Materials*, 2005, **17**, 2320-2323.
6. J. Hu, T. W. Odom and C. M. Lieber, *Accounts of Chemical Research*, 1999, **32**, 435-445.
7. M. Bruno, M. Palummo, A. Marini, R. Del Sole, V. Olevano, A. N. Kholod and S. Ossicini, *Physical Review B*, 2005, **72**, 153310.
8. S. Jia and et al., *Nanotechnology*, 2009, **20**, 255202.
9. L.-L. Li, Y.-J. Chen, H.-P. Wu, N. S. Wang and E. W.-G. Diau, *Energy & Environmental Science*, 2011.
10. M. I. Stockman, *Physical Review Letters*, 2004, **93**, 137404.
11. D. Vanmaekelbergh and L. K. van Vugt, *Nanoscale*, 2011, **3**, 2783-2800.
12. L. Vayssieres and M. Graetzel, *Angewandte Chemie*, 2004, **116**, 3752-3756.
13. X.-F. Shen and X.-P. Yan, *Angewandte Chemie International Edition*, 2007, **46**, 7659-7663.
14. X. Zhidong and et al., *Nanotechnology*, 2005, **16**, 2647.
15. E. E. Foos, T. J. Zega, J. G. Tischler, R. M. Stroud and J. E. Boercker, *Journal of Materials Chemistry*, 2011, **21**, 2616-2623.
16. W. He and J. H. Dickerson, *Thermally driven isotropic crystallinity breaking of nanocrystals: Insight into the assembly of EuS nanoclusters and nanorods with oleate ligands*, AIP, 2011.
17. G. Wulff, *Z. Kristallogr. Mineral.*, 1901, **34**, 449-530.
18. C.-C. Chen, C.-Y. Chao and Z.-H. Lang, *Chemistry of Materials*, 2000, **12**, 1516-1518.
19. J. W. Grebinski, K. L. Hull, J. Zhang, T. H. Kosel and M. Kuno, *Chemistry of Materials*, 2004, **16**, 5260-5272.
20. M. Kuno, O. Ahmad, V. Protasenko, D. Bacinello and T. H. Kosel, *Chemistry of Materials*, 2006, **18**, 5722-5732.
21. T. K. Sau and C. J. Murphy, *Journal of the American Chemical Society*, 2004, **126**, 8648-8649.
22. K. Vasilev, T. Zhu, M. Wilms, G. Gillies, I. Lieberwirth, S. Mittler, W. Knoll and M. Kreiter, *Langmuir*, 2005, **21**, 12399-12403.
23. Y. Sun, B. Mayers, T. Herricks and Y. Xia, *Nano Letters*, 2003, **3**, 955-960.
24. Y. Sun, Y. Yin, B. T. Mayers, T. Herricks and Y. Xia, *Chemistry of Materials*, 2002, **14**, 4736-4745.
25. Y. Song, R. M. Garcia, R. M. Dorin, H. Wang, Y. Qiu, E. N. Coker, W. A. Steen, J. E. Miller and J. A. Shelnutt, *Nano Letters*, 2007, **7**, 3650-3655.
26. A. Chen and P. Holt-Hindle, *Chemical Reviews*, 2010, **110**, 3767-3804.

27. Y. Chang, M. L. Lye and H. C. Zeng, *Langmuir*, 2005, **21**, 3746-3748.
28. R. R. Piticescu, C. Monty, D. Taloi, A. Motoc and S. Axinte, *Journal of the European Ceramic Society*, 2001, **21**, 2057-2060.
29. X. P. Gao, J. L. Bao, G. L. Pan, H. Y. Zhu, P. X. Huang, F. Wu and D. Y. Song, *The Journal of Physical Chemistry B*, 2004, **108**, 5547-5551.
30. C.-Y. Xu, L. Zhen, R. Yang and Z. L. Wang, *Journal of the American Chemical Society*, 2007, **129**, 15444-15445.
31. W. Zhou, H. Liu, R. I. Boughton, G. Du, J. Lin, J. Wang and D. Liu, *Journal of Materials Chemistry*, 2010, **20**, 5993-6008.
32. Z.-Y. Jiang, T. Xu, Z.-X. Xie, Z.-W. Lin, X. Zhou, X. Xu, R.-B. Huang and L.-S. Zheng, *The Journal of Physical Chemistry B*, 2005, **109**, 23269-23273.
33. L. Liu, B. Li, D. Yu, Y. Cui, X. Zhou and W. Ding, *Chemical Communications*, 2010, **46**, 427-429.
34. L. L. Hench and J. K. West, *Chemical Reviews*, 1990, **90**, 33-72.
35. M. Niederberger, *Accounts of Chemical Research*, 2007, **40**, 793-800.
36. B. B. Lakshmi, P. K. Dorhout and C. R. Martin, *Chemistry of Materials*, 1997, **9**, 857-862.
37. N. Li and C. R. Martin, *Journal of The Electrochemical Society*, 2001, **148**, A164-A170.
38. A. Huczko, *Applied Physics A: Materials Science & Processing*, 2000, **70**, 365-376.
39. J. Wang and Y. Li, *Advanced Materials*, 2003, **15**, 445-447.
40. X. Jiaqiang, C. Yuping, C. Daoyong and S. Jianian, *Sensors and Actuators B: Chemical*, 2006, **113**, 526-531.
41. Q. Yang, K. Tang, C. Wang, Y. Qian and S. Zhang, *The Journal of Physical Chemistry B*, 2002, **106**, 9227-9230.
42. Z. Wen, Q. Wang and J. Li, *Advanced Functional Materials*, 2008, **18**, 959-964.
43. J. M. Patete, X. Peng, C. Koenigsmann, Y. Xu, B. Karn and S. S. Wong, *Green Chemistry*, 2011, **13**, 482-519.
44. G. Sun, M. Cao, Y. Wang, C. Hu, Y. Liu, L. Ren and Z. Pu, *Materials Letters*, 2006, **60**, 2777-2782.
45. L. Liu, H.-Z. Kou, W. Mo, H. Liu and Y. Wang, *The Journal of Physical Chemistry B*, 2006, **110**, 15218-15223.
46. Z. Liu, S. Li, Y. Yang, S. Peng, Z. Hu and Y. Qian, *Advanced Materials*, 2003, **15**, 1946-1948.
47. Q. Liu, H. Liu, Y. Liang, Z. Xu and G. Yin, *Materials Research Bulletin*, 2006, **41**, 697-702.
48. B. A. Hernandez, K.-S. Chang, E. R. Fisher and P. K. Dorhout, *Chemistry of Materials*, 2002, **14**, 480-482.
49. B. B. Lakshmi, C. J. Patrissi and C. R. Martin, *Chemistry of Materials*, 1997, **9**, 2544-2550.
50. Y.-J. Han, J. M. Kim and G. D. Stucky, *Chemistry of Materials*, 2000, **12**, 2068-2069.
51. M. Numata, K. Sugiyasu, T. Hasegawa and S. Shinkai, *Angewandte Chemie International Edition*, 2004, **43**, 3279-3283.
52. A. Khanal, Y. Inoue, M. Yada and K. Nakashima, *Journal of the American Chemical Society*, 2007, **129**, 1534-1535.
53. C. Bae, H. Yoo, S. Kim, K. Lee, J. Kim, M. M. Sung and H. Shin, *Chemistry of Materials*, 2008, **20**, 756-767.

54. L. Miao, S. Tanemura, S. Toh, K. Kaneko and M. Tanemura, *Journal of Crystal Growth*, 2004, **264**, 246-252.
55. H. Cao, X. Qiu, Y. Liang, M. Zhao and Q. Zhu, *Applied Physics Letters*, 2006, **88**, 241112-241112-241113.
56. T.-J. Park, Y. Mao and S. S. Wong, *Chemical Communications*, 2004, 2708-2709.
57. Z. Miao, D. Xu, J. Ouyang, G. Guo, X. Zhao and Y. Tang, *Nano Letters*, 2002, **2**, 717-720.
58. P. Katta, M. Alessandro, R. D. Ramsier and G. G. Chase, *Nano Letters*, 2004, **4**, 2215-2218.
59. Z. Liu, D. D. Sun, P. Guo and J. O. Leckie, *Nano Letters*, 2006, **7**, 1081-1085.
60. C. Wang, K.-W. Yan, Y.-D. Lin and P. C. H. Hsieh, *Macromolecules*, 2010, **43**, 6389-6397.
61. M. S. Peresin, Y. Habibi, A.-H. Vesterinen, O. J. Rojas, J. J. Pawlak and J. V. Seppälä, *Biomacromolecules*, 2010, **11**, 2471-2477.
62. S. Yurong and et al., *Nanotechnology*, 2011, **22**, 285609.
63. S. De Vrieze, T. Van Camp, A. Nelvig, B. Hagström, P. Westbroek and K. De Clerck, *Journal of Materials Science*, 2009, **44**, 1357-1362.
64. J. M. Deitzel, J. Kleinmeyer, D. Harris and N. C. Beck Tan, *Polymer*, 2001, **42**, 261-272.
65. T. Uyar and F. Besenbacher, *Polymer*, 2008, **49**, 5336-5343.
66. W. K. Son, J. H. Youk, T. S. Lee and W. H. Park, *Polymer*, 2004, **45**, 2959-2966.
67. W. Zuo, M. Zhu, W. Yang, H. Yu, Y. Chen and Y. Zhang, *Polymer Engineering & Science*, 2005, **45**, 704-709.
68. V. Beachley and X. Wen, *Materials Science and Engineering: C*, 2009, **29**, 663-668.
69. L. Wannatong, A. Sirivat and P. Supaphol, *Polymer International*, 2004, **53**, 1851-1859.
70. I.-D. Kim, A. Rothschild, B. H. Lee, D. Y. Kim, S. M. Jo and H. L. Tuller, *Nano Letters*, 2006, **6**, 2009-2013.
71. H. Chaobo and et al., *Nanotechnology*, 2006, **17**, 1558.
72. K. Sawicka and P. Gouma, *Journal of Nanoparticle Research*, 2006, **8**, 769-781.
73. C. E. Megiris and J. H. E. Glezer, *Chemical Engineering Science*, **47**, 3925-3934.
74. F. Duerinckx and J. Szlufcik, *Solar Energy Materials and Solar Cells*, 2002, **72**, 231-246.
75. W. G. Lee and S. I. Woo, *Journal of Materials Science Letters*, 2003, **22**, 1677-1678.
76. R. J. Potter, P. A. Marshall, P. R. Chalker, S. Taylor, A. C. Jones, T. C. Q. Noakes and P. Bailey, *Characterization of hafnium aluminate gate dielectrics deposited by liquid injection metalorganic chemical vapor deposition*, AIP, 2004.
77. Q.-G. Fu, H.-J. Li, X.-H. Shi, K.-Z. Li, J. Wei and Z.-B. Hu, *Materials Chemistry and Physics*, 2006, **100**, 108-111.
78. D. Wang and H. Dai, *Angewandte Chemie*, 2002, **114**, 4977-4980.
79. A. M. Cassell, J. A. Raymakers, J. Kong and H. Dai, *The Journal of Physical Chemistry B*, 1999, **103**, 6484-6492.
80. X.-P. Shen, H.-J. Liu, L. Pan, K.-M. Chen, J.-M. Hong and Z. Xu, *Chemistry Letters*, 2004, **33**, 1128-1129.
81. V. Khorenko, I. Regolin, S. Neumann, W. Prost, F.-J. Tegude and H. Wiggers, *Photoluminescence of GaAs nanowhiskers grown on Si substrate*, AIP, 2004.
82. H. T. Chen and et al., *Journal of Physics D: Applied Physics*, 2008, **41**, 025101.

83. J. Campos-Delgado, Y. A. Kim, T. Hayashi, A. Morelos-Gómez, M. Hofmann, H. Muramatsu, M. Endo, H. Terrones, R. D. Shull, M. S. Dresselhaus and M. Terrones, *Chemical Physics Letters*, 2009, **469**, 177-182.
84. Z. Zhang, J. Wang, H. Yuan, Y. Gao, D. Liu, L. Song, Y. Xiang, X. Zhao, L. Liu, S. Luo, X. Dou, S. Mou, W. Zhou and S. Xie, *The Journal of Physical Chemistry B*, 2005, **109**, 18352-18355.
85. X. P. Shen, M. Han, J. M. Hong, Z. Xue and Z. Xu, *Chemical Vapor Deposition*, 2005, **11**, 250-253.
86. G. Che, B. B. Lakshmi, C. R. Martin, E. R. Fisher and R. S. Ruoff, *Chemistry of Materials*, 1998, **10**, 260-267.
87. S. Xiao-Ping and et al., *Nanotechnology*, 2005, **16**, 2039.
88. L. Yu, B. O?Donnell, J.-L. Maurice and P. R. i. Cabarrocas, *Core-shell structure and unique faceting of Sn-catalyzed silicon nanowires*, AIP, 2010.
89. S. Paiman and et al., *Journal of Physics D: Applied Physics*, 2010, **43**, 445402.
90. E. Alarcon-Llado, S. Estrade, J. D. Prades, F. Hernandez-Ramirez, J. Arbiol, F. Peiro, J. Ibanez, L. Artus and J. R. Morante, *CrystEngComm*, 2011, **13**, 656-662.
91. H.-P. Wang, K.-Y. Lai, Y.-R. Lin, C.-A. Lin and J.-H. He, *Langmuir*, 2010, **26**, 12855-12858.
92. F. Demami, L. Ni, R. Rogel, A. C. Salaun and L. Pichon, *Procedia Engineering*, 2010, **5**, 351-354.
93. Y. Mo, J. J. Schwartz, M. H. Lynch, P. A. Ecton, A. Neogi, J. M. Perez, Y. Fujita, H. W. Seo, Q. Y. Chen, L. W. Tu and N. J. Ho, in *Nanoscale Photonics and Optoelectronics*, eds. Z. M. Wang and A. Neogi, Springer New York, 2011, pp. 131-156.
94. M. H. Huang, S. Mao, H. Feick, H. Yan, Y. Wu, H. Kind, E. Weber, R. Russo and P. Yang, *Science*, 2001, **292**, 1897-1899.
95. I. Iñiguez-de-la-Torre and et al., *Semiconductor Science and Technology*, 2010, **25**, 125013.
96. D. Cohen-Tanugi, A. Akey and N. Yao, *Nano Letters*, 2010, **10**, 852-859.
97. S. Reza, S. Marcin and A. Srinivasan, *Optical Society of America*, 2011, p. CE2_4.
98. B. Tian, X. Zheng, T. J. Kempa, Y. Fang, N. Yu, G. Yu, J. Huang and C. M. Lieber, *Nature*, 2007, **449**, 885-889.
99. N. D. Hoa, N. Van Quy and D. Kim, *Sensors and Actuators B: Chemical*, 2009, **142**, 253-259.
100. A. Kolmakov, Y. Zhang, G. Cheng and M. Moskovits, *Advanced Materials*, 2003, **15**, 997-1000.
101. C. S. Rout, S. Hari Krishna, S. R. C. Vivekchand, A. Govindaraj and C. N. R. Rao, *Chemical Physics Letters*, 2006, **418**, 586-590.
102. J. Li, Y. Lu, Q. Ye, M. Cinke, J. Han and M. Meyyappan, *Nano Letters*, 2003, **3**, 929-933.
103. H. Kind, H. Yan, B. Messer, M. Law and P. Yang, *Advanced Materials*, 2002, **14**, 158-160.
104. S. Han, W. Jin, D. Zhang, T. Tang, C. Li, X. Liu, Z. Liu, B. Lei and C. Zhou, *Chemical Physics Letters*, 2004, **389**, 176-180.
105. C. Koenigsmann, W.-p. Zhou, R. R. Adzic, E. Sutter and S. S. Wong, *Nano Letters*, 2010, **10**, 2806-2811.
106. C. Koenigsmann and S. S. Wong, *Energy & Environmental Science*, 2011, **4**, 1161-1176.

107. C. Koenigsmann, A. C. Santulli, K. Gong, M. B. Vukmirovic, W.-p. Zhou, E. Sutter, S. S. Wong and R. R. Adzic, *Journal of the American Chemical Society*, 2011, **133**, 9783-9795.
108. L. Shi, Y. Xu, S. Hark, Y. Liu, S. Wang, L.-m. Peng, K. Wong and Q. Li, *Nano Letters*, 2007, **7**, 3559-3563.
109. P. Christopher and S. Linic, *Journal of the American Chemical Society*, 2008, **130**, 11264-11265.
110. A. Fukuoka, N. Higashimoto, Y. Sakamoto, S. Inagaki, Y. Fukushima and M. Ichikawa, *Microporous and Mesoporous Materials*, 2001, **48**, 171-179.
111. W. Zhou, L. Yan, Y. Wang and Y. Zhang, *SiC nanowires: A photocatalytic nanomaterial*, AIP, 2006.
112. L. Liu, E. Pippel, R. Scholz and U. Gösele, *Nano Letters*, 2009, **9**, 4352-4358.
113. Y.-M. Lin, S. B. Cronin, J. Y. Ying, M. S. Dresselhaus and J. P. Heremans, *Transport properties of Bi nanowire arrays*, AIP, 2000.
114. B. S. Guiton, Q. Gu, A. L. Prieto, M. S. Gudiksen and H. Park, *Journal of the American Chemical Society*, 2004, **127**, 498-499.
115. P.-C. Chang and J. G. Lu, *Temperature dependent conduction and UV induced metal-to-insulator transition in ZnO nanowires*, AIP, 2008.
116. C. J. Patridge, T.-L. Wu, C. Jaye, B. Ravel, E. S. Takeuchi, D. A. Fischer, G. Sambandamurthy and S. Banerjee, *Nano Letters*, 2010, **10**, 2448-2453.
117. T. D. Manning, I. P. Parkin, M. E. Pemble, D. Sheel and D. Vernardou, *Chemistry of Materials*, 2004, **16**, 744-749.
118. E. Strelcov, Y. Lilach and A. Kolmakov, *Nano Letters*, 2009, **9**, 2322-2326.
119. C. Rossel, G. I. Meijer, D. Brémaud and D. Widmer, *Electrical current distribution across a metal?insulator?metal structure during bistable switching*, AIP, 2001.
120. Y. Sun, B. Qu, S. Jiang, C. Wu, B. Pan and Y. Xie, *Nanoscale*, 2011, **3**, 2609-2614.
121. D.-H. Kwon, K. M. Kim, J. H. Jang, J. M. Jeon, M. H. Lee, G. H. Kim, X.-S. Li, G.-S. Park, B. Lee, S. Han, M. Kim and C. S. Hwang, *Nat Nano*, 2010, **5**, 148-153.
122. A. C. Santulli, W. Xu, J. B. Parise, L. Wu, M. C. Aronson, F. Zhang, C.-Y. Nam, C. T. Black, A. L. Tiano and S. S. Wong, *Physical Chemistry Chemical Physics*, 2009, **11**, 3718-3726.
123. A. C. Santulli, H. Zhou, S. Berweger, M. B. Raschke, E. Sutter and S. S. Wong, *CrystEngComm*, 2010, **12**, 2675-2678.
124. A. C. Santulli, M. Feygenson, F. E. Camino, M. C. Aronson and S. S. Wong, *Chemistry of Materials*, 2011, **23**, 1000-1008.
125. A. C. Santulli and et al., *Nanotechnology*, 2011, **22**, 245402.
126. W. Chen, J. Peng, L. Mai, H. Yu and Y. Qi, *Chemistry Letters*, 2004, **33**, 1366-1367.
127. F. J. Morin, *Physical Review Letters*, 1959, **3**, 34.
128. N. Ballarini, A. Battisti, F. Cavani, A. Cericola, C. Cortelli, M. Ferrari, F. Trifirò and P. Arpentinier, *Applied Catalysis A: General*, 2006, **307**, 148-155.
129. E. V. Kondratenko, O. Ovsitser, J. Radnik, M. Schneider, R. Kraehnert and U. Dingerdissen, *Applied Catalysis A: General*, 2007, **319**, 98-110.
130. S. J. Yun, B.-G. Chae, J. W. Lim, J.-S. Noh and H.-T. Kim, *Electrochemical and Solid-State Letters*, 2008, **11**, H173-H175.
131. C. Tsang and A. Manthiram, *Journal of The Electrochemical Society*, 1997, **144**, 520-524.

132. J. Shi, S. Zhou, B. You and L. Wu, *Solar Energy Materials and Solar Cells*, 2007, **91**, 1856-1862.
133. B.-G. Chae, H.-T. Kim, S.-J. Yun, B.-J. Kim, Y.-W. Lee, D.-H. Youn and K.-Y. Kang, *Electrochemical and Solid-State Letters*, 2006, **9**, C12-C14.
134. G. A. Rozgonyi and W. J. Polito, *Journal of The Electrochemical Society*, 1968, **115**, 56-57.
135. L.-Q. Mai, W. Chen, Q. Xu, J.-F. Peng and Q.-Y. Zhu, *Chemical Physics Letters*, 2003, **382**, 307-312.
136. C. Tenailleau, E. Suard, J. Rodriguez-Carvajal and P. Lacorre, *Journal of Magnetism and Magnetic Materials*, 2004, **278**, 57-67.
137. D. S. Toledano, P. Metcalf and V. E. Henrich, *Surface Science*, 2001, **472**, 21-32.
138. J. B. Goodenough, *Journal of Solid State Chemistry*, 1971, **3**, 490-500.
139. A. Cavalleri, C. Toth, C. W. Siders, J. A. Squier, F. Raksi, P. Forget and J. C. Kieffer, *Physical Review Letters*, 2001, **87**, 237401.
140. Y. Muraoka and Z. Hiroi, *journal article*, 2002, **80**, 583-585.
141. R. Aliev and V. Klimov, *Physics of the Solid State*, 2004, **46**, 532-536.
142. I. Balberg and S. Trokman, *High contrast optical storage in VO_2 films*, AIP, 1975.
143. P. Liu, S.-H. Lee, H. M. Cheong, C. E. Tracy, J. R. Pitts and R. D. Smith, *Journal of The Electrochemical Society*, 2002, **149**, H76-H80.
144. G. Sudant, E. Baudrin, B. Dunn and J.-M. Tarascon, *Journal of The Electrochemical Society*, 2004, **151**, A666-A671.
145. A. Azens, G. Gustavsson, R. Karmhag and C. G. Granqvist, *Solid State Ionics*, 2003, **165**, 1-5.
146. X. Chen, X. Wang, Z. Wang, J. Wan, J. Liu and Y. Qian, *Nanotechnology*, 2004, **15**, 1685.
147. W. Chen, L. Mai, Y. Qi and Y. Dai, *Journal of Physics and Chemistry of Solids*, **67**, 896-902.
148. A. Liu, M. Ichihara, I. Honma and H. Zhou, *Electrochemistry Communications*, 2007, **9**, 1766-1771.
149. M. Niederberger, H.-J. Muhr, F. Krumeich, F. Bieri, D. Günther and R. Nesper, *Chemistry of Materials*, 2000, **12**, 1995-2000.
150. J. M. Reinoso, H.-J. Muhr, F. Krumeich, F. Bieri and R. Nesper, *Helvetica Chimica Acta*, 2000, **83**, 1724-1733.
151. H. J. Muhr, F. Krumeich, U. P. Schönholzer, F. Bieri, M. Niederberger, L. J. Gauckler and R. Nesper, *Advanced Materials*, 2000, **12**, 231-234.
152. F. Krumeich, H. J. Muhr, M. Niederberger, F. Bieri, B. Schnyder and R. Nesper, *Journal of the American Chemical Society*, 1999, **121**, 8324-8331.
153. F. Krumeich, H.-J. Muhr, M. Niederberger, F. Bieri and R. Nesper, *Zeitschrift für anorganische und allgemeine Chemie*, 2000, **626**, 2208-2216.
154. M. E. Spahr, P. Stoschitzki-Bitterli, R. Nesper, O. Haas and P. Novak, *Journal of The Electrochemical Society*, 1999, **146**, 2780-2783.
155. S. Mathur, T. Ruegamer and I. Grobelsek, *Chemical Vapor Deposition*, 2007, **13**, 42-47.
156. R. Lopez, T. E. Haynes, L. A. Boatner, L. C. Feldman and J. R. F. Haglund, *Opt. Lett.*, 2002, **27**, 1327-1329.
157. J. M. Baik, M. H. Kim, C. Larson, A. M. Wodtke and M. Moskovits, *The Journal of Physical Chemistry C*, 2008, **112**, 13328-13331.

158. B. S. Allimi, S. P. Alpay, C. K. Xie, B. O. Wells, J. I. Budnick and D. M. Pease, *Applied Physics Letters*, 2008, **92**, 202105.
159. F. Sediri and N. Gharbi, *Materials Science and Engineering: B*, 2005, **123**, 136-138.
160. D. M. Moffatt, J. P. Runt, A. Halliyal and R. E. Newnham, *Journal of Materials Science*, 1989, **24**, 609-614.
161. G. van der Lee, B. Schuller, H. Post, T. L. F. Favre and V. Ponec, *Journal of Catalysis*, 1986, **98**, 522-529.
162. C. Zheng, X. Zhang, S. He, Q. Fu and D. Lei, *Journal of Solid State Chemistry*, 2003, **170**, 221-226.
163. K. Zhang, X. Sun, G. Lou, X. Liu, H. Li and Z. Su, *Materials Letters*, 2005, **59**, 2729-2731.
164. Z. Yang, P. Cai, L. Chen, Y. Gu, L. Shi, A. Zhao and Y. Qian, *Journal of Alloys and Compounds*, 2006, **420**, 229-232.
165. N. Pinna, M. Antonietti and M. Niederberger, *Colloids and Surfaces A: Physicochemical and Engineering Aspects*, 2004, **250**, 211-213.
166. S. A. Corr, M. Grossman, J. D. Furman, B. C. Melot, A. K. Cheetham, K. R. Heier and R. Seshadri, *Chemistry of Materials*, 2008, **20**, 6396-6404.
167. G. Anderson, *Acta Chemica Scandinavica*, 1956, **10**, 623.
168. A. D. Burton and P. A. Cox, *Philisopical Magazine*, 1985, **51**, 255.
169. H. Liu, O. Vasquez, V. R. Santiago, L. Díaz and F. E. Fernandez, *Journal of Luminescence*, 2004, **108**, 233-238.
170. P. Baum, D.-S. Yang and A. H. Zewail, *Science*, 2007, **318**, 788-792.
171. M. B. Sahana, G. N. Subbanna and S. A. Shivashankar, *journal article*, 2002, **92**, 6495-6504.
172. J. C. Rakotoniaina, R. Mokrani-Tamellin, J. R. Gavarri, G. Vacquier, A. Casalot and G. Calvarin, *Journal of Solid State Chemistry*, 1993, **103**, 81-94.
173. Y. Oka, T. Yao and N. Yamamoto, *Journal of Materials Chemistry*, 1991, **1**, 815-818.
174. G. T. Chandrappa, N. Steunou, S. Cassaignon, C. Bauvais and J. Livage, *Catalysis Today*, 2003, **78**, 85-89.
175. Y. Mao and S. S. Wong, *Journal of the American Chemical Society*, 2006, **128**, 8217-8226.
176. Z. Gui, R. Fan, W. Mo, X. Chen, L. Yang, S. Zhang, Y. Hu, Z. Wang and W. Fan, *Chemistry of Materials*, 2002, **14**, 5053-5056.
177. C. Leroux, G. Nihoul and G. Van Tendeloo, *Physical Review B*, 1998, **57**, 5111.
178. D. S. Su and R. Schlögl, *Catalysis Letters*, 2002, **83**, 115-119.
179. C. V. Ramana, S. Utsunomiya, R. C. Ewing and U. Becker, *Solid State Communications*, 2006, **137**, 645-649.
180. Y. Ueda, K. Kosuge and S. Kachi, *Journal of Solid State Chemistry*, 1980, **31**, 171-188.
181. R. N. Bhowmik, R. Nagarajan and R. Ranganathan, *Physical Review B*, 2004, **69**, 054430.
182. R. N. Bhowmik and R. Ranganathan, *Solid State Communications*, 2007, **141**, 365-368.
183. J. Feinleib and W. Paul, *Physical Review*, 1967, **155**, 841.
184. C. Grygiel, A. Pautrat, W. C. Sheets, W. Prellier, B. Mercey and L. Mechin, *Journal of Physics: Condensed Matter*, 2008, **20**, 472205.

Chapter 2. Synthesis and Characterization of V_2O_3 nanorods

2.1 Introduction

As mentioned in Chapter 1, the fundamental scientific understanding of metal oxide materials has received a significant amount of research interest in recent years, owing to their many interesting and exciting applications as well as properties. Vanadium oxides are of particular interest, owing to their intriguing electronic, magnetic, optoelectronic and electrochromic properties.[126] Oxides of vanadium are of special significance due to their interesting metal-to-insulator transitions (MIT),[127] as well as their ability to catalyze the oxidation of propane to propylene.[128, 129] Furthermore, vanadium maintains several oxidation states, such as V^{3+}, V^{4+}, and V^{5+} which allows for the formation of many stable oxide phases,[130, 131] many of which possess an interesting MIT. These VO_{2+x} structures are mainly composed of edge and corner-shared distorted VO_6 octahedra, wherein the degree of edge sharing increases as the value of x increases.[131] In this work, we are specifically interested in the synthesis of VO_2 and V_2O_3, each of which exhibits a unique MIT at a temperature of 68°C[132, 133] and -100°C,[134] respectively. However these temperatures can be altered via doping with various materials like W,[132] Mo,[135, 136] and Cr.[137]

Vanadium dioxide (VO_2) is of particular interest due to the fact that its Mott M–I transition temperature, occurring at 68 °C, is the closest to room temperature of any of the undoped vanadium oxides currently known and is associated with an abrupt change in resistivity (a factor of 10^4 to 10^5). That is, at room temperature, bulk vanadium dioxide adopts a distorted $P2_1/c$ monoclinic structure with insulating properties. However, when heated above the transition temperature, it is converted into a tetragonal rutile $P4_2/mnm$ structure, possessing metallic

properties.[138] This observation renders this material as a useful candidate in possible applications ranging from robust, near-IR optical switches (reported to switch as quickly as 500 fs between the two states when excited with 50-fs laser pulses at a wavelength of 800 nm),[139] smart window coatings, heat sensors, optical modulators, field effect transistors, to optical storage media.[132, 140-145]

There are many synthetic protocols, several of which utilize solution-based methods, that have been developed to successfully synthesize 1D VO_2 nanostructures. For example, Tsang et al. have utilized a reaction in which an aqueous solution of potassium vanadate was reduced by potassium borohydride at a controlled pH of 4.[131] Another report utilized ethylene glycol to synthesize arrays of VO_2 nanorods under hydrothermal conditions.[146] Similar conditions have been employed to facilitate the formation of nanorods of VO_2 with widths of 40-60 nm and lengths of 1-2 microns using a surfactant-mediated hydrothermal synthesis at 180°C for 48 hours. Moreover, a hydrothermal synthesis can be utilized to create vanadium oxide nanotubes via an initial reactive combination of either hexadecylamine or dodecylamine along with cetyltrimethyl ammonium bromide (CTAB) for 48 h in air followed by a hydrothermal treatment at 180 °C for 1 week.[147-154]

In addition to the aforementioned solution-based synthetic strategies, there have been many reports with respect to the synthesis of VO_2 via gas phase methodologies. Nanostructures of VO_2 have been generated via CVD growth from a oxo-tri-isopropoxide precursor.[155] Furthermore, it has been found that heating VO_2 seed particles to 1000°C in an argon atmosphere results in the formation of VO_2 nanorods.[156] An analogous method which uses finely meshed VO_2 powder as the precursor has been used to successfully generate single crystalline VO_2 nanorods which can maintain a narrow size distribution.[157] Finally, well-faceted nanorods of

VO_2 on a silicon nitride substrate have been produced via a vapor transport process at 900-1000°C at low pressure in an argon atmosphere, using bulk VO_2 as the precursor.[114]

Interestingly, vanadium sesquioxide (V_2O_3) also exhibits an interesting magnetic transition that accompanies the M–I transition. That is, at room temperature, vanadium sesquioxide acts as a paramagnetic metal. However, when it is cooled below its transition temperature, it converts into an antiferromagnetic insulator. Coincident with this transition, vanadium sesquioxide undergoes a structural transformation from a rhombohedral symmetry at room temperature to a monoclinic structure below the transition temperature.[158] The interesting property changes associated with the M–I transition in vanadium sesquioxide render it as a promising candidate for applications as diverse as temperature sensors, current regulators, and components of conductive polymer composites.[159-161]

There have been many similar synthetic protocols associated with the synthesis of V_2O_3. However, the focus has centered on the synthesis of nanoparticles. Spherical nanoparticles measuring 30 nm in diameter have been fabricated by the reductive pyrolysis of ammonium oxovanadium(IV) carbonato hydroxide at 730°C in a hydrogen atmosphere.[162] Thermal decomposition of oxalate can also be utilized as a means of generating V_2O_3 nanostructures.[163] Hydrothermal reaction conditions have also shown promise for the decomposition of NH_4VO_3 into V_2O_3 nanostrucures.[164] Furthermore, the use of metal alkoxides, in combination with benzyl alcohol, has been successfully employed as a viable means of producing V_2O_3 nanoparticles with diameters between 20 and 50 nm.[165] There has also been one report of the synthesis of hollow VO_2 and V_2O_3 nanotubes via a thermal reduction process in an hydrogen–containing atmosphere of hydrothermally synthesized $V_2O_{5-\delta}$ nanoscrolls.[166]

In this work, we have been concerned with the synthesis of filled V_2O_3 nanorods via a route similar to that reported by Seshadri and co-workers.[166] Specifically, we have utilized hydrothermally derived VO_2 nanowires as a precursor material for the formation of V_2O_3 nanorods through a thermal reduction reaction. Initially we form hydrated VO_2 nanowires under hydrothermal conditions. These nanowires are subsequently dehydrated under an inert atmosphere at elevated temperatures to form VO_2(M) nanowires. It is worth reiterating that VO_2 possesses a high-temperature metallic state (VO_2(R)) above 68 °C with a tetragonal rutile structure with parameters of $a = b = 4.55$ Å and $c = 2.88$ Å, in which each vanadium ion is located at the center of an oxygen octahedron, a visual representation of this transition can be found in Figure 2.1.[167-169] The semiconducting low-temperature form, *i.e.* the ambient room-temperature motif of VO_2(M), is a monoclinic distortion of the rutile structure with $a = 5.75$ Å, $b = 4.52$ Å, and $c = 5.38$ Å, involving a pairing and off-axis displacement of alternate vanadium ions along the rutile c axis.[167, 170-172] Following dehydration, we have utilized these nanowires as a precursor for the high-yield formation of V_2O_3 nanorods in a reducing atmosphere at temperatures greater than 550°C. While it may have been logical to have used a different variation of the VO_2 intermediate in our syntheses, *i.e.* VO_2(B), the metastable nature of this latter polymorph of VO_2 has made it difficult to proceed with that particular route, owing to the oxidation of the product into the most thermodynamically stable phase, V_2O_5.[126, 173] This oxidation not only destroys the desired morphology of the product, but also inhibits the reduction to V_2O_3 during the thermal reduction.

The novelty of our work is three-fold in nature. First, we have been able to successfully synthesize filled, crystalline nanorods of V_2O_3 in a relatively large quantity (*i.e.* up to grams per run). Second, our V_2O_3 nanorods are relatively free from impurities as well as the presence of

other phases of vanadium oxide, thereby alleviating the requirement for additional purification steps. More specifically, we have not been creating mixed valence VO_x nanostructures, wherein other oxide species such as V_6O_{13}, VO_2, or V_2O_5 can potentially co-exist with our desired V_2O_3

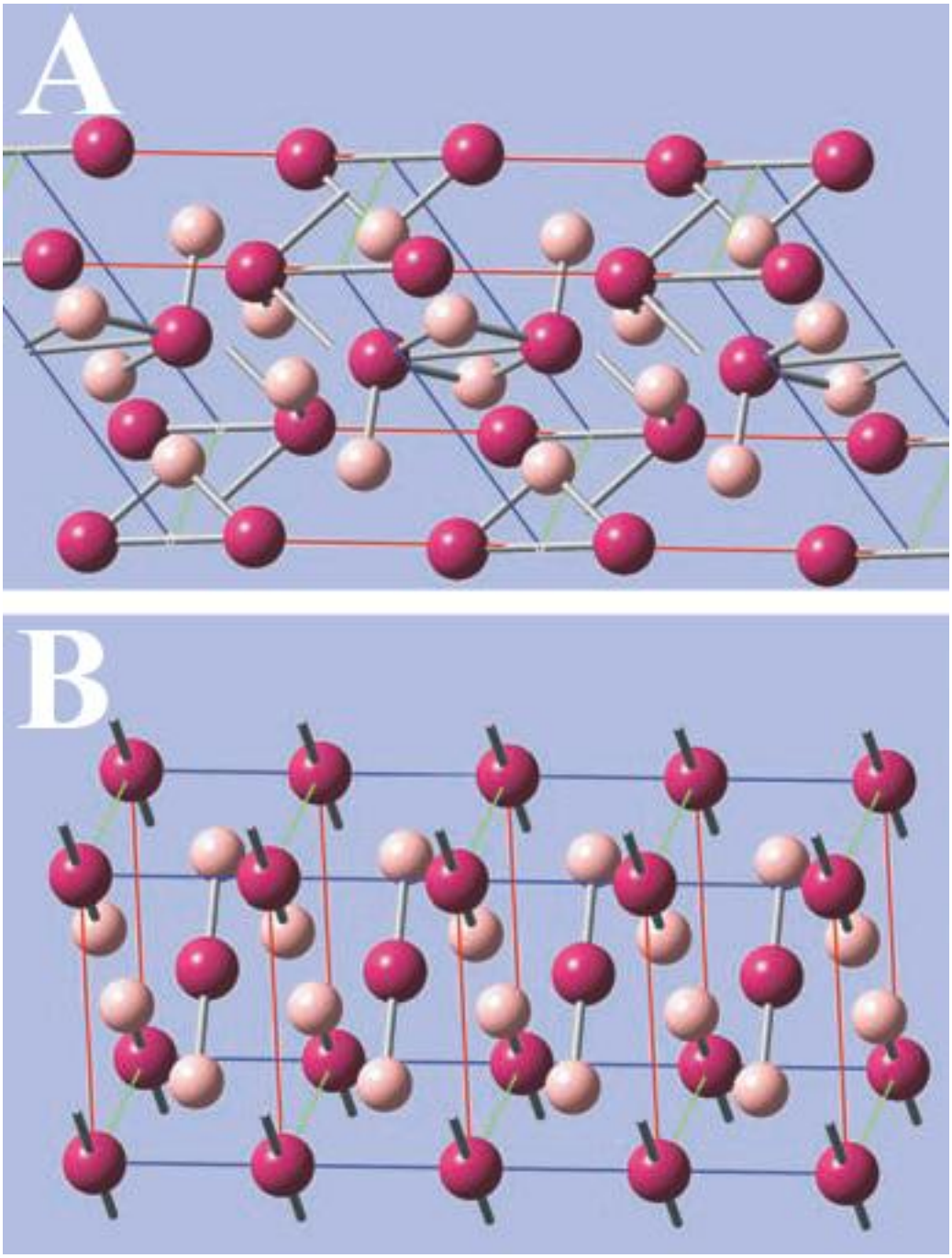

Figure 2.1: Crystal structures of A) monoclinic VO_2, and B) rutile VO_2. Adapted from reference 46.

phase.[148, 151, 174] Third, we have been able to generate these V_2O_3 nanorods by building upon nanorod motifs of VO_2 itself as an intermediate stepping stone, i.e. a necessary precursor, to this product. We have previously demonstrated[175] the feasibility of this latter idea in our laboratory in our conversion of titanate nanorods and nanotubes into anatase TiO_2 nanorods and nanoparticles, respectively, at essentially 100% yield. In that case, we showed that the size and shape of the precursor titanate structural motif strongly dictated and controlled the eventual morphology of the resulting titania products.

2.2 Synthetic Procedures

All chemicals were used as purchased, without further purification. The synthesis of hydrated VO_2 nanorods was conducted using a minor modification of a hydrothermal method previously presented by Gui *et al.*[176] We chose this particular protocol, because it avoided the high temperatures and specialized equipment associated with gas-phase techniques. Moreover, this procedure[176] could lead to the production of high-quality, single-crystalline nanorods in large quantities with reliable control over morphology without the need for sintering. Specifically, in a typical reaction, 0.2546 g of V_2O_5 (Acros Organics, 99.6+%) and 0.2412 g of KOH (Fisher Scientific) were added to a 23 mL Teflon-lined autoclave. Subsequently, 14.38 mL of H_2O was added to the autoclave and the solution was mixed thoroughly, achieving final molar concentrations of 0.10 and 0.29 M for V_2O_5 and KOH, respectively. Following this process, 50.7 μL of hydrazine (Acros Organics, 99%), selected not only for its reducing ability but also for its potential in coordinating central vanadium ions into a one-dimensional morphology,[176] was added to the tune of 0.068 M, followed by further mixing of the solution. Finally, the pH of the solution was adjusted to ~3 using HCl (EMD, ACS reagent grade) in order to prevent the formation of erroneous vanadium oxide species in solution, such as soluble oxo and hydroxo

species. The autoclave was subsequently sealed and heated at 150°C for 48 h. After heating, a blue-black product was isolated and purified by centrifugation and washing with absolute ethanol (Acros Organics, 200 proof) followed by storage in an inert atmosphere to prevent additional oxidation.

To prepare the dehydrated form of VO_2, the product of the hydrothermal reaction was heated under N_2 at 350°C for 24 h which, at elevated temperatures, likely led to the direct generation of the thermodynamically most stable VO_2(R) form, which subsequently reversibly converted to VO_2(M) at room temperature under ambient conditions. To synthesize V_2O_3, the blue–black VO_2 product in either its hydrated or dehydrated formulation was heated at 800°C at a ramp rate of 10°C min^{-1}. The black sample was subsequently removed from the oven and allowed to cool to room temperature under a reducing atmosphere so as to prevent oxidation of the product.

2.3 Materials characterization

The diameters and lengths of as-prepared nanorods were initially characterized using a field emission scanning electron microscopy instrument (FE-SEM Leo 1550), operating at an accelerating voltage of 15 kV and equipped with energy-dispersive X-ray spectroscopy (EDS) capabilities, as well as with a Hitachi S-4800 at an accelerating voltage of 1.0 kV. Samples for SEM were prepared by dispersing as-prepared nanorods in ethanol, sonicating for about 2 min, and then depositing the sample onto a silicon wafer, attached to a SEM aluminum stub.

Low magnification TEM images were taken at an accelerating voltage of 80 kV on a FEI Tecnai12 BioTwinG^2 instrument, equipped with an AMT XR-60 CCD Digital Camera System. High-resolution TEM (HRTEM) images were obtained on a JEOL 2010F instrument at accelerating voltages of 200 kV. Specimens for all of these TEM experiments were prepared by

dispersing the as-prepared product in ethanol, sonicating for 2 min to ensure adequate dispersion of the nanorods, and depositing one drop of the solution onto a 300 mesh Cu grid, coated with a lacey carbon film.

To prepare powder X-ray diffraction (XRD) samples, the resulting nanorods were rendered into slurries in ethanol, sonicated for about 1 min, and then air-dried upon deposition onto glass slides. Diffraction patterns were collected using a Scintag diffractometer, operating in the Bragg–Bretano geometry and using Cu Kα radiation (λ = 1.54 Å) from $10 \leq 2\theta \leq 80°$ at a scanning rate of 2° in 2θ per minute. Temperature-resolved synchrotron XRD data were collected at the X7B beamline at the National Synchrotron Light Source. Sample powders were loaded in a polyimide capillary with a 0.5 mm inner diameter. The X-ray beam size was adjusted using slits to match the capillary size. The temperature was controlled by an air-blower type heater with the thermocouple placed in contact with the outside of the capillary in the middle of the air stream from the heater. A 2°C/step temperature scan started from 55 °C for the heating cycle, with at least a 30 min hovering duration interval at each step. The subsequent cooling started from 69°C with the same temperature step size interval. 2-D XRD data were collected using a MAR345 imaging plate area detector with continuous 120 s exposure times. The readout time for the detector was 45 s between exposures. 2-D data were processed by the Fit2D program to obtain traditional 1-D "2θ scan" data for analysis. The wavelength used was 0.31840(2) Å.

2.4 Materials' measurements

Magnetic measurements were performed on a 11.46 mg powder sample of V_2O_3 nanowires in a Quantum Design Magnetic Property Measurement System (MPMS) with fields of up to 7 T and temperatures between 1.8 and 300 K.

Nanorod devices were fabricated by a combination of electron beam (e-beam) lithography and e-beam induced direct metal deposition (EBID) using a scanning electron microscope (SEM) (Helios, FEI) equipped with a Nano Pattern Generating System (NPGS) and an organometallic gas injection system (GIS). First, contact pads measuring 100×100 μm^2 in area and electrodes with 1 μm in width and spacing were fabricated using e-beam lithography on a Si substrate with 400-nm thick thermally grown SiO_2. In a typical run, a layer of the commercial e-beam resist, ZEP-1, was applied *via* spin-coating onto the substrate at 3000 rpm followed by 3 min of baking at 180°C. The substrate was subsequently loaded into the SEM. Contact pads and electrode patterns were then exposed by e-beam irradiation (at 30 kV accelerating voltage and 1.4 nA current), followed by development in xylenes for 2 min and rinsing in isopropyl alcohol. Finally, a 40-nm thick layer of platinum was deposited onto the substrate surface by sputter coating in a vacuum atmosphere of ~10^{-5} Torr.

V_2O_3 nanorods were then randomly transferred onto the substrate containing the fabricated contact pads by spin coating a suspension of these nanomaterials dispersed in aqueous solution at 1000 rpm. Upon localization of these V_2O_3 nanorods on the substrate using the SEM, platinum electrical contacts, maintaining a thickness of ~100 nm and a width of ~80 nm, were applied to the nanorods by direct deposition of Pt itself, derived from the decomposition of a trimethyl [(1,2,3,4,5-ETA)-1-methyl-2,4-cyclopentadien-1-yl] platinum source, that had been introduced into the vacuum chamber by a GIS, in the presence of a 30 kV e-beam with a 1.4 nA current. Current–voltage (*I*–*V*) measurements were obtained using a HFTTP4 cryogenic probe station (Lakeshore) spanning a temperature (*T*) range from 80 K to 300 K.

2.5 Results and Discussion

The results of our XRD analysis, shown in Figure 2.2, reveal that the samples prepared show no signs of crystallographic impurities, within the limits of the instrument utilized. The XRD pattern for the dehydrated nanowires (Figure 2.2A) can be indexed to a monoclinic structure, with the space group of $\boldsymbol{P}2_1/c$ (JCPDS #82-0661). From the diffraction data, we calculated the lattice parameters to be a = 5.750 ± 0.008 Å, b = 4.523 ± 0.007 Å, and c = 5.376 ± 0.018 Å. These values are in good agreement with those reported in the JCPDS database; these numbers are a = 5.752 Å, b = 4.526 Å, and c = 5.383 Å. For the sake of completeness, we also collected an XRD pattern for the hydrated nanowires as well, Figure 2.2C. The relatively poor quality of that data, however, may be partially attributable to the incompatibility between the 'hydrated' nature of the sample and the 'dry' sample acquisition process itself, as well as to the presence of impurities that were subsequently transformed to other, more desirable oxide species during later high-temperature annealing treatments.

The XRD pattern for the as-prepared V_2O_3 nanorods, shown in Figure 2.2B, reveals a rhombohedral unit cell with space group $R\bar{3}c$ (JCPDS #85-1411). From the diffraction pattern, we calculated the hexagonal unit cell parameters to be a = 4.954 ± 0.010 Å and c = 13.939 ± 0.045 Å. These values are in good agreement with those reported in the JCPDS database, namely a = 4.952 Å and c = 14.003 Å.

Visualization of the $VO_2 \bullet H_2O$ nanowires via SEM, shown in Figure 2.3A, has shown that the nanowires possess an average width of 74 ± 21 nm and lengths of up to several microns. Examination of the nanowires by HRTEM analysis, shown in Figure 2.3B, suggests the presence of well-defined lattice fringes, with a spacing of 0.485 and 0.515 nm, which are in good agreement with the values of 0.434 and 0.512 nm, derived from JCPDS database #13-0346. The

sharpness of the spots in the selected area electron diffraction (SAED) pattern, shown in Figure 2.2C, strongly suggests that the nanorods are highly crystalline. However, measured *d*-spacings from the SAED pattern and its XRD pattern (Figure 2.2C) did not match well with one another, an observation which can be reasonably attributed to sample dehydration (and corresponding lattice alteration) under electron beam irradiation, characteristic of TEM sampling conditions. Hence, we were unable to properly index that diffraction pattern.

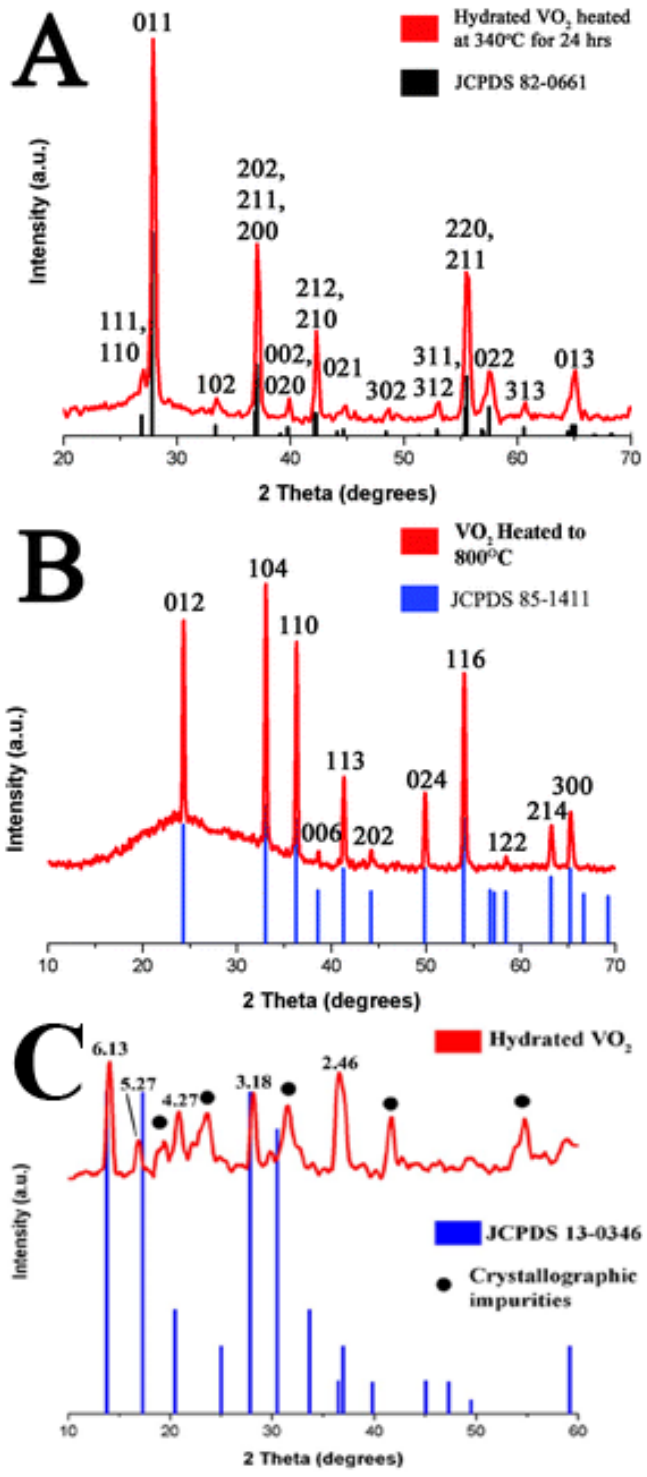

Figure 2.2: XRD patterns of A) dehydrated VO_2 nanowires, B) V_2O_3 nanorods, and C) hydrated VO_2 nanowires.

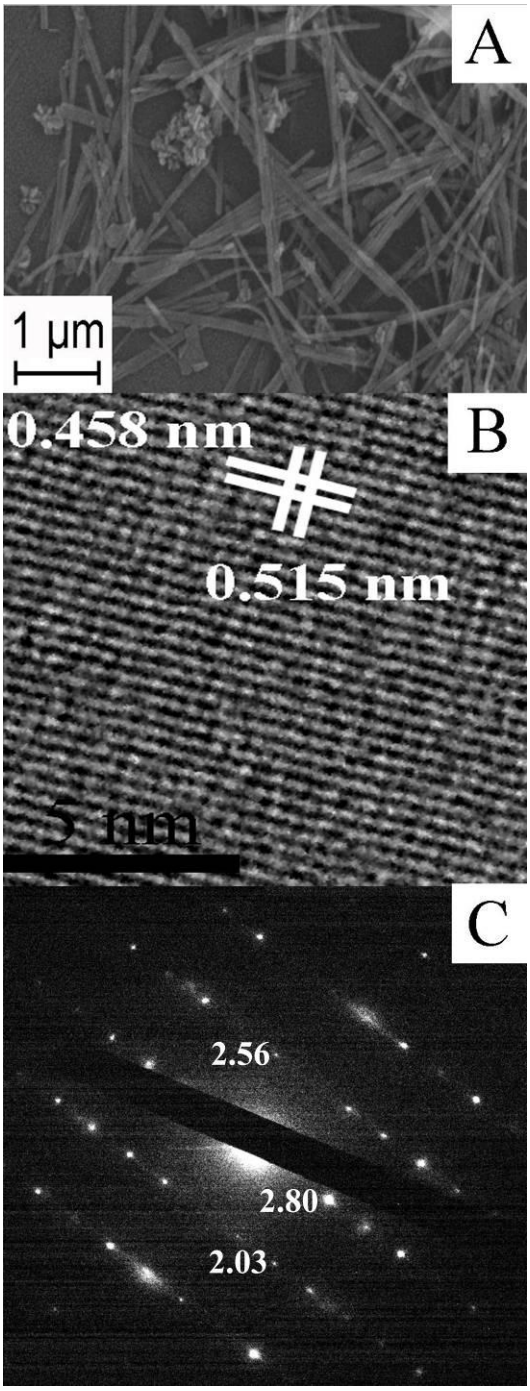

Figure 2.3: (A) SEM image of as-prepared $VO_2 \cdot H_2O$ nanorods. (B) HRTEM image of a typical, individual hydrated nanorod. (C) SAED of the nanorod probed in (B). Measured *d*-spacings in Angstroms are indicated directly to the left of indexed diffraction spots.

In order to properly investigate the MIT between the VO_2(M) and VO_2(R) phases, our as-synthesized $VO_2 \bullet H_2O$ nanowires were dehydrated by heating in an inert atmosphere for 4 hours at 350°C. The SEM investigation of these dehydrated VO_2 nanowires (Figure 2.4A) indicated that even after this processing, the material remained mostly one-dimensional, with an average width of 68 ± 12 nm, and lengths of up to several microns. As expected, there is some shrinkage of the nanomaterial due to the loss of water from the nanostructure. Furthermore, HRTEM and SAED data shown in Figure 2.4B and C revealed that the nanowires maintain their single-crystalline nature, even after the dehydration procedure. The HRTEM image (Figure 2.4B) clearly depicted lattice planes with a *d*-spacing of 0.323 nm, corresponding to the (110) lattice plane of the monoclinic VO_2 structure (*d*-spacing = 0.331 nm). In addition, the SAED pattern exhibited sharp, well-defined spots which could be indexed to the (110), (212), and (102) planes of VO_2(M), a result which is in excellent agreement with both our HRTEM and XRD data.

As shown in Figure 2.2A, upon dehydration, the nanowires are converted into pure VO_2(M), with no detectable amount of crystallographic impurities. As further characterization, we investigated the transition from VO_2(M) to VO_2(R) via temperature-dependent *in situ* synchrotron radiation measurements. The results obtained from this investigation are shown in Figure 2.5. We observed a transition in the material in the range of 63-65°C during the heating cycle, and 61-59°C during the cooling cycle. This rather small hysteresis is consistent with an expected rapid and reversible transformation,[177] as the positions and intensities of the peaks returned to their original profiles upon cooling.

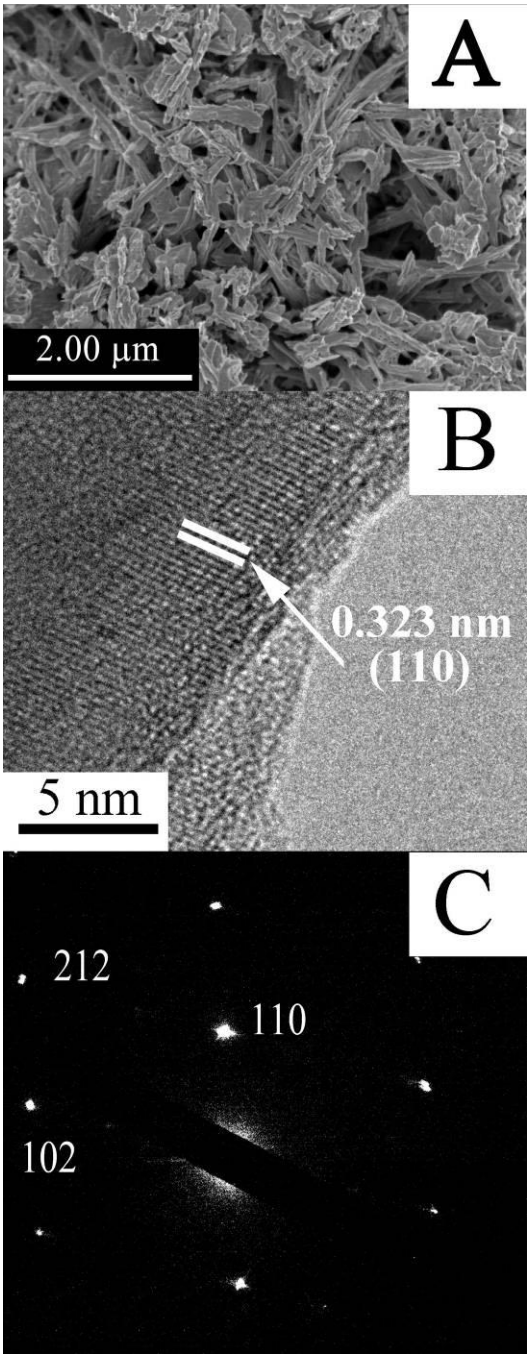

Fig. 2.4: A) SEM image of dehydrated VO_2 nanorod aggregates with individual widths of 68 ± 12 nm and lengths of up to a couple of microns. B) HRTEM image of a single VO_2 nanorod. C) SAED of the VO_2 nanorod probed in (B).

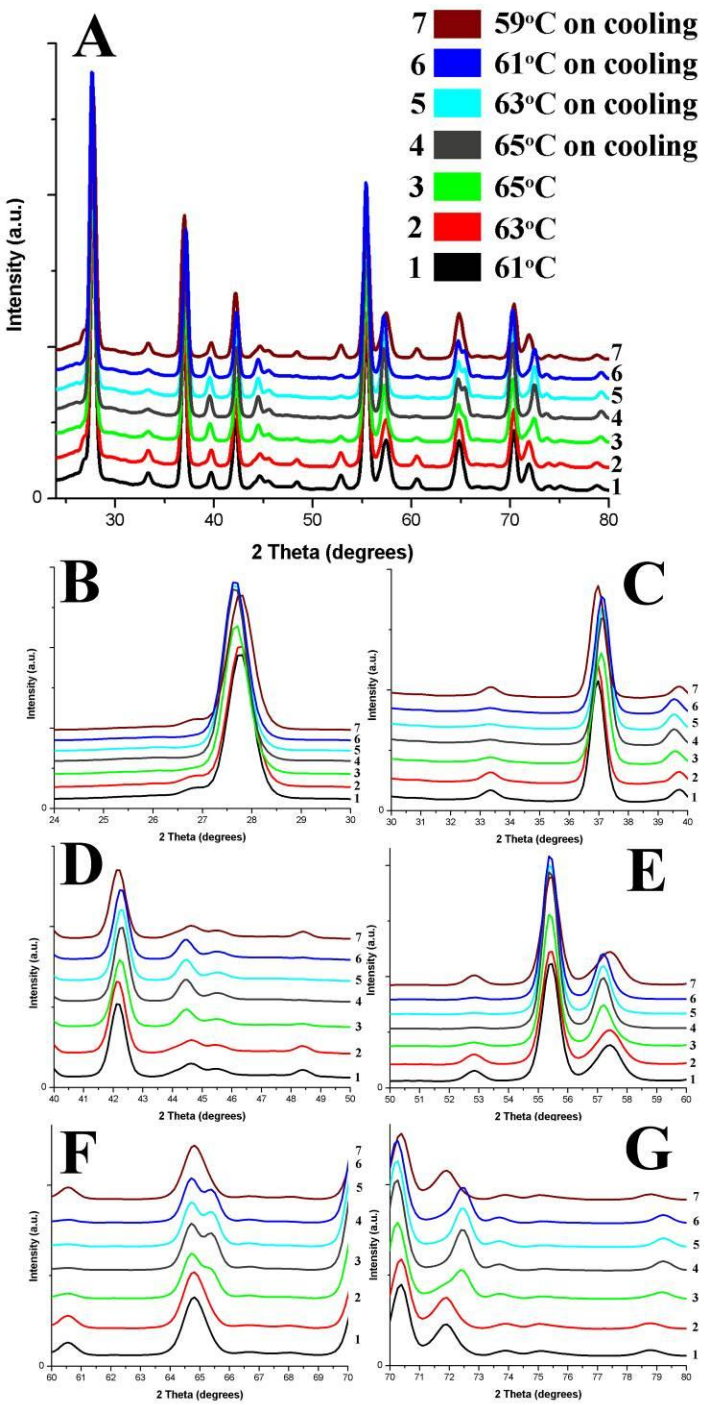

Fig. 2.5. A) Variable-temperature synchrotron diffraction data re-plotted over 24°≤ 2θ≤ 80° to simulate the familiar scale for Cu Kα radiation (λ = 1.5418 Å) commonly used on laboratory sources. The original data were collected using λ = 0.3184 Å on a synchrotron source. Indexing of peaks (monoclinic $P2_1/c$ bottom and tetragonal $P4_2/mnm$ top) for individual sections of the diffraction pattern are shown in **B)** 24°≤ 2θ≤ 30°, **C)** 30°≤ 2θ≤ 40°, **D)** 40°≤ 2θ≤ 50°, **E)** 50°≤ 2θ≤ 60°, **F)** 60°≤ 2θ≤ 70°, and **G)** 70°≤ 2θ≤ 80°, respectively. The loss of certain peaks is a diagnostic for the transition from the monoclinic to the tetragonal phase in VO_2: for example, the disappearance of monoclinic peaks (11–1,110) in (B), 30–2 in (D), (12–2, 31–1) in (E), and the 31–3 in (F).

The Mott transition is normally brought on by a change in the crystalline structure, presumably due to changes in the dimensions of the unit cell.[157] Observed peak shifts likely represent shrinkage of the unit cell, as expected with the conversion from the monoclinic to the rutile form. Upon confirmation of the validity of this transition at the nanoscale, we then set about converting our 1D nanorod sample from the starting formulation of VO_2 to the final V_2O_3 chemical structure. As previously mentioned, there have been a number of reports in the literature pertaining to the conversion of VO_2 to V_2O_3.[130, 178] Herein, we heated our sample, consisting of either $VO_2 \cdot H_2O$ or VO_2, in H_2 at temperatures ranging from 500–900°C and using reaction times up of to 5 h so as to obtain V_2O_3 nanorods. Experimentally, we found that heating of the sample to 800°C using a ramp rate of 10 °C min^{-1} followed by subsequent cooling to room temperature yielded the best results, as defined by the resulting sample purity and crystallinity as well as the prevailing nanorod morphology.

Electron microscopy images of the nanorods obtained from this optimized method are shown in Figure 2.6. While the sample consists predominantly of nanorods, the sample contained some nanoparticles, with a ratio of nanorods to nanoparticles of approximately 3: 1. The nanowires present in the sample maintained a width of 64 ± 18 nm, slightly smaller than the originating VO_2(M) nanowires, with lengths of up to a couple of microns. It is also evident from the electron microscopy images that the morphology of the nanorods transformed from relatively smooth wires to nanorods with a roughened surface texture, which may be due to the presence of V_2O_3 particulates. Analysis by HRTEM (Figure 2.6B) revealed the presence of well-defined lattice planes, with measured *d*-spacings of 0.248 and 0.268 nm, in good agreement with the (110) (d = 0.247 nm) and (104) (d = 0.271 nm) planes of V_2O_3 (JCPDS #85-1411). These experimental values are also in good agreement with data taken from powder XRD

measurements (Figure 2.2B), wherein the calculated *d*-spacings of 0.248 nm and 0.271 nm can be assigned to the (110) and (104) peaks, respectively. Furthermore, SAED data taken of the nanorods indicated the presence of sharp, well-defined spots which are suggestive of the fact that the V_2O_3 nanorods maintain the single crystalline nature of their nanowire precursors.

Previous reports have also shown that conversion of films and nanocrystals of VO_2 to V_2O_3 can be explained *via* a combination of diffusion, coalescence, and stabilization processes,[178, 179] which is consistent with what we have observed herein. Of relevance here, it was noted that the thermal reduction process involved in one of those experiments[179] involved rearrangement of oxygen polyhedra surrounding the V atoms; the reduced oxide phases essentially diffused and coalesced, leading to the formation of differently-shaped geometries. Hence, the thermally-induced (a) nucleation and growth of the V_2O_3 phase, governed to a large extent by atomic diffusion, and (b) the formation of lattice defects during the *in situ* phase transformation along microstructural defects of the parent precursor VO_2 likely yielded a highly strained intermediate defective state.[178] Diffusion is expected to occur isotropically, so that the transformed phase could initially have formed spherical particles. These particles then presumably coalesced to generate roughened, high-surface-energy nanorod-like motifs. Yet, these as-prepared V_2O_3 nanomaterials could also exist stably as spheres, since the defect density would be minimized and the presence of high surface energy surfaces would be reduced in this particular geometric configuration.

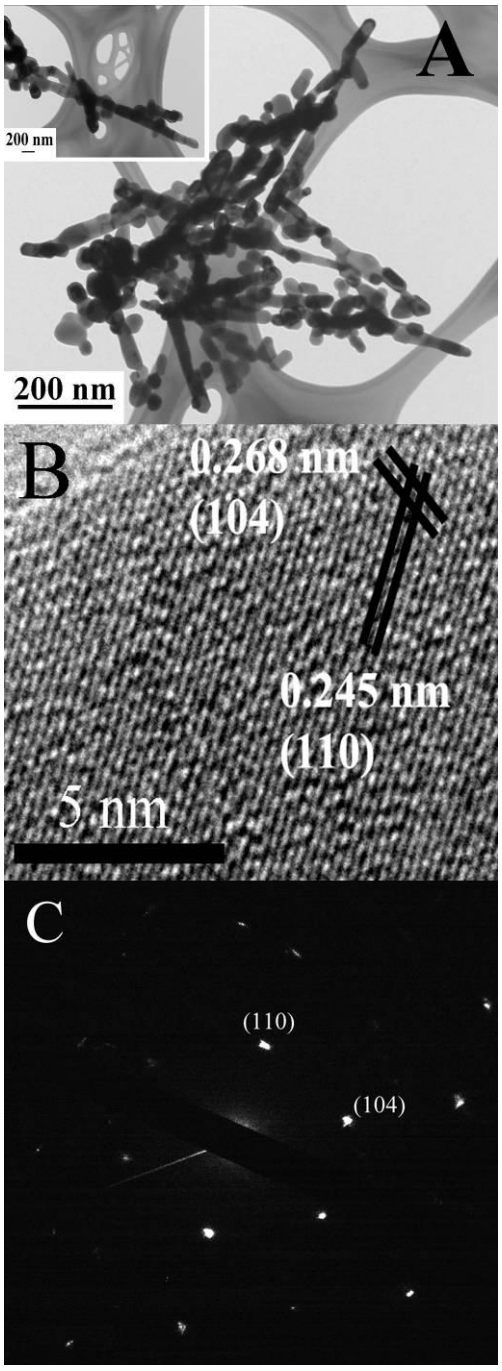

Fig. 2.6: A) TEM image of V_2O_3 nanorods. Inset shows a different region containing these metal oxide nanorods. B) HRTEM image of a representative, individual nanorod, showing lattice spacings consistent with the (104) and (110) planes of V_2O_3. C) SAED pattern of V_2O_3 nanorods, demonstrating their single crystallinity.

We indeed noted that as the reaction time and temperature were increased, fewer nanorods were produced but a preponderance of nanoparticles was clearly noted in the sample. Moreover, consistent with this growth mechanism, we also discovered that temperature was the main parameter governing this reaction. That is, our reaction medium needed to be 'hot' enough, *i.e.* heated above 800°C, in order for the conversion from VO_2 to V_2O_3 to occur. At temperatures below 800°C, the morphology of the sample retained its nanorod motif, but the product actually consisted of a heterogeneous mixture of different phases (including V_6O_{13} and V_3O_7) of vanadium oxide. Hence, our observations could be explained by *in situ* phase conversions, as evinced by diffraction analyses.

2.6 Magnetic Measurements

The temperature variation of the magnetic susceptibility M/H (H = 5.0 T) for V_2O_3 is plotted in Figure 2.7, for both ZFC (zero field cooled) as well as FC (field cooled at 5.0 T) cases. The magnetic susceptibility (M/H) was found to slowly increase from 300 K to about 200 K, with an anomalous drop in magnetic susceptibility observed at about 166 K. The magnetic susceptibility subsequently increased again at lower temperatures. We can fit the magnetic susceptibility data above 200 K using the Curie–Weiss law in Equation 1:

$$M/H = C/(T-\theta_p) \quad (1)$$

The Curie constant, C ($C = N\mu_{eff}^2/3k_B$ where N is the number of V atoms per unit cell), yields an effective paramagnetic moment per V atom, μ_{eff} = 2.64 μ_B, which is close to the Hund's rule value for V^{3+}, namely μ_{eff} = 2.8 μ_B. The calculated paramagnetic Curie temperature, θ_p, is about −634 K. The negative value here also indicates that the V moments are

antiferromagnetically coupled. Both C and θ_p parameters are in good agreement with the reported behavior for bulk V_2O_3.[180]

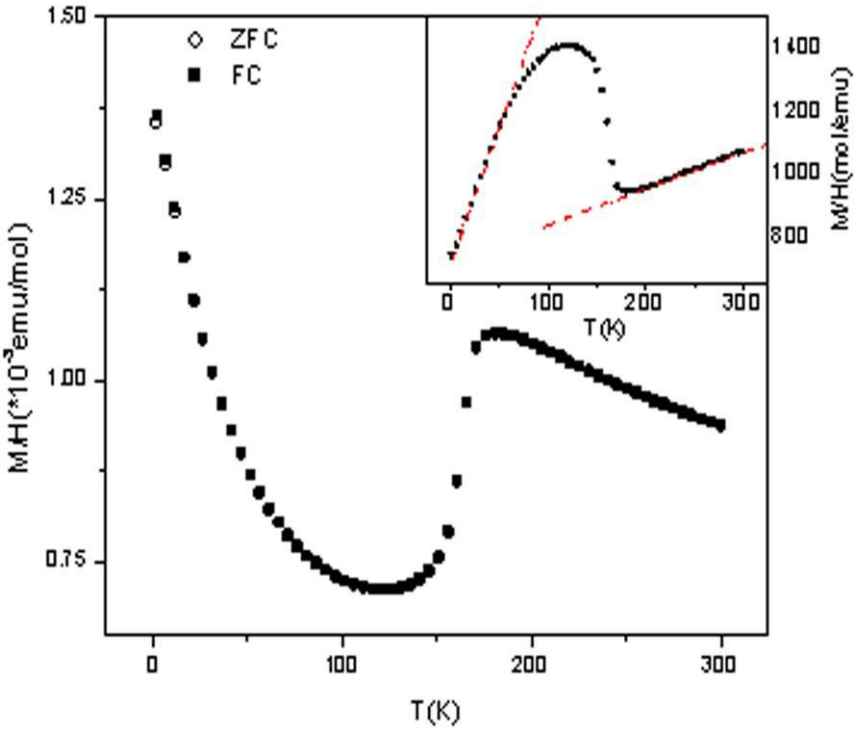

Fig. 2.7: Temperature dependence of the DC magnetization at H = 5.0 T. Both ZFC and FC curves at 5.0 T were measured, although little hysteresis was observed. Inset: H/M *vs.* T, showing that the linear regions, above 200 K and below 50 K, can be fit well with the Curie–Weiss law, wherein the slope yields the inverse of the Curie constant ($1/C$).

Figure 2.8 represents the measurement of the field dependence of the magnetization from −5.0 T to 5.0 T at different temperatures. At high temperatures, *M* is linear with the field. Both Figures 2.7 and 2.8 suggest that the V moments are spatially localized and fluctuate independently above the transition at 166 K. The anomaly observed here agrees well with that of pure bulk V_2O_3, where it corresponds to the simultaneous onset of antiferromagnetic order and the delocalization of the V *d*-electrons. Also, since the oxygen stoichiometry can significantly change the phase transition behavior,[180] the transition at 166 K may indicate that our nanorod sample is very close to the expected stoichiometric ratio of V_2O_3 without the presence of either impurities or extraneous vanadium oxide phases.

A second region of the Curie–Weiss behavior has been observed at the lowest temperatures. That is, Figure 2.8 highlights a weak nonlinearity in *M vs. H* behavior at 10 K, as expected for the paramagnetic Brillouin function. Here, the fitted Curie–Weiss law results in a significantly smaller Curie constant than the one found above 166 K (Table 1), implying that only a subset of the V atoms remains paramagnetic at low temperatures. Yet, the moment concentration is sufficiently high that this second Curie–Weiss contribution to the susceptibility cannot originate with moment-bearing impurities and hence, must be intrinsic. Previous researchers[181, 182] have suggested that the surface spins in antiferromagnetic nanoparticles are uncompensated, and may produce a paramagnetic susceptibility value below the overall Néel temperature, just as we have found with our V_2O_3 nanorods herein.

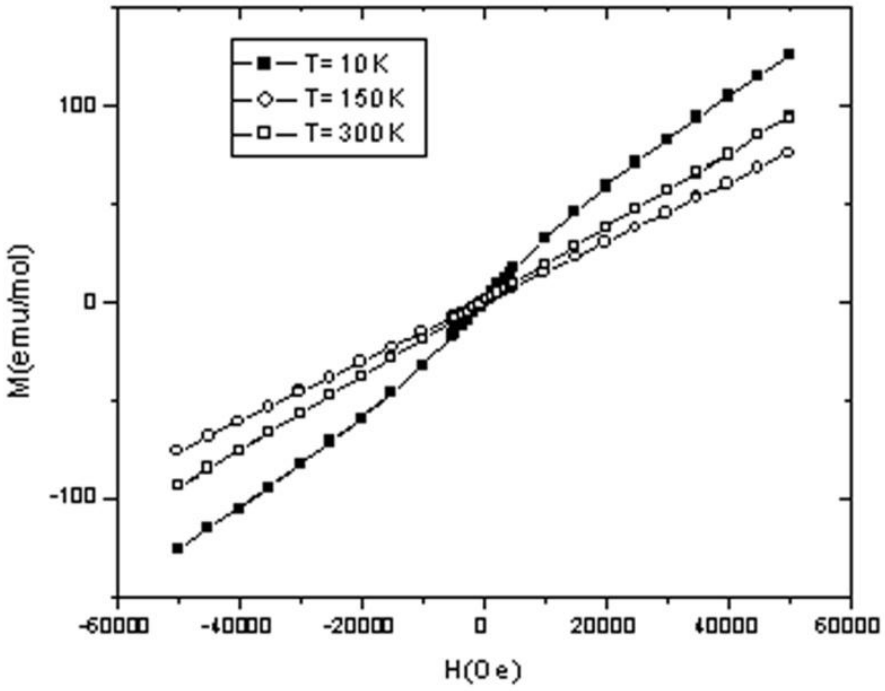

Fig. 2.8: DC magnetization measured at three different temperatures (*i.e.* 10 K, 150 K, and 300 K) with fields ranging from −50 000 Oe to 50 000 Oe.

T/K	C/emu K mol^{-1}	θ_p/K	μ_{eff}/μ_B
>200	0.874	−633.9	2.64
<50	0.115	−82.5	0.96

Table 2.1. Curie–Weiss fit parameters (M/H = C/ (T $-\theta_p$) with (C = $N\mu_{eff}^2/3k_B$) derived from M *vs.* T measurements.

We suggest that the magnetization data shown in Figures 2.7 and 2.8 represent the sum of the contributions both from the surface and the core spins. Above the 166 K transition temperature where antiferromagnetic order sets in, all V moments are paramagnetic, just as is the case with the bulk material. By contrast, below the transition temperature, the interior of the nanoparticle is antiferromagnetic, while the spins on the surface are either free or paramagnetic. When the temperature is low enough, these surface spin contributions dominate, and this situation can lead to the observed increase in susceptibility at low temperatures.

2.7 Electronic transport characterization

In order to investigate the electronic properties of our V_2O_3 nanorods, we fabricated devices on silicon substrates. We fabricated these devices in a two-step process, wherein we first deposited large lithographically defined pads. Following this step, we contacted the nanowires via EBID-defined platinum leads. An SEM image of a typical device is shown in Figure 2.9. Two-probe current-voltage (I-V) measurements taken on this device revealed a symmetric response with respect to the voltage bias at all temperatures investigated (*i.e.* three representative temperatures are shown in Figure 2.10). This result suggests that the contact properties between the EBID-platinum wire and the V_2O_3 nanorod are similar on both ends of the device.

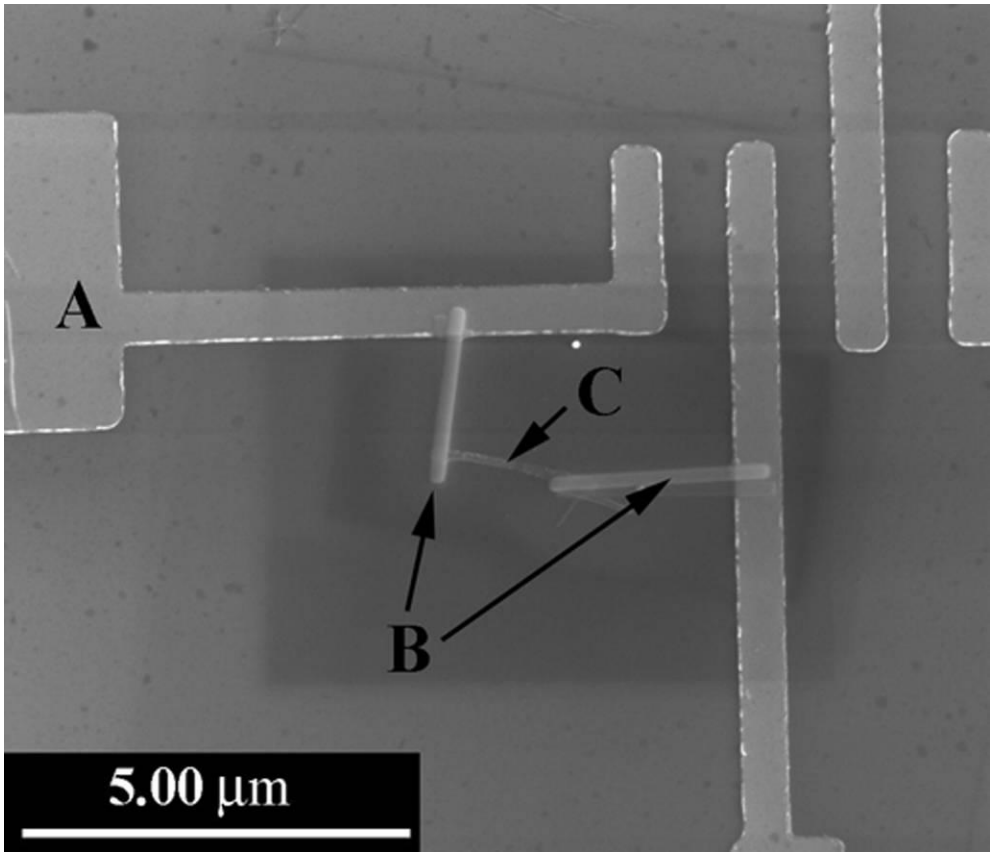

Fig. 2.9: SEM image of a V_2O_3 nanorod device used for electronic measurements. A) Electrodes deposited by a Lesker sputter coater. B) Electrodes deposited by the EBID technique. C) A representative V_2O_3 nanorod.

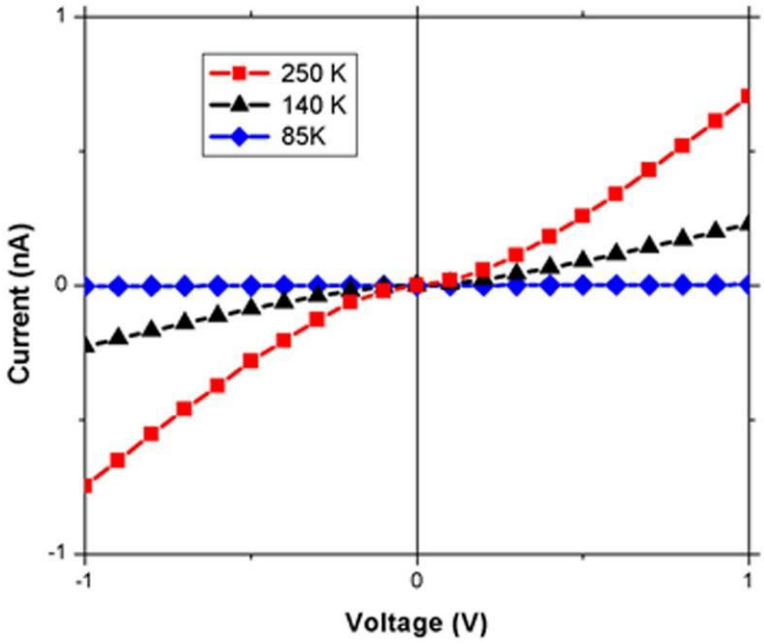

Fig. 2.10: *I–V* curves taken on a V_2O_3 nanorod at three different temperatures, associated with the warming cycle, at 250 K (red squares), 140 K (black triangles), and 85 K (blue diamonds), respectively.

The measured device current increased linearly with voltage over the bias range of 0.3 V < |*V*| < 5 V for every measured temperature (80–300 K) (Figure 2.9). We calculated the two-probe V_2O_3 nanorod resistivity (ρ) from the device's ohmic resistance ($R \equiv V/I$) according to $\rho \equiv R^*A/L$, wherein A is the cross-sectional nanorod area and L is the length of the nanorod bounded by the two Pt contacts. We assumed a circular nanorod cross-sectional area, $A = \pi r^2$, with r as the nanorod radius measured from SEM images. At a low applied voltage bias ($-0.3 < V < 0.3$ V), the *I*–*V* curve was slightly nonlinear, likely indicating the presence of a small Schottky barrier at the Pt–V_2O_3 contact (Figure 2.10).

The two-terminal V_2O_3 device resistivity (ρ) increased upon decreasing temperature from 300 to 80 K (Figure 2.11), resulting in a total resistivity change ($\Delta\rho$) of ~10^3. Despite the two-terminal nature of our measurements, separate measurements of minimal changes in the Pt lead resistance over the same temperature range (not shown) allowed us to ascribe the observed behavior to the V_2O_3 nanorod itself. Upon cooling the device, we observed an increase in the rate of nanorod resistivity change in the temperature range around 150–200 K (red open triangles), similar to the point at which we observed large changes in nanorod magnetization (Figure 2.7), and consistent with previous reports of a metal–insulator transition[183] in V_2O_3 at temperatures of around ~150 K. The total magnitude of the resistivity change has previously been used to infer information about material purity in terms of stoichiometry and crystallinity.[130] The nanorod device resistivity decreased smoothly over the entire temperature range upon warming from 80–300 K (Figure 2.11, black solid squares), such that the entire temperature cycle was noted to be hysteretic, consistent with previously reported measurements[183] of corundum-phase V_2O_3 nanotubes.[166] Moreover, previous observations of similar hysteresis in V_2O_3 film resistivities have been explained in terms of substrate-induced volume confinement effects.[184]

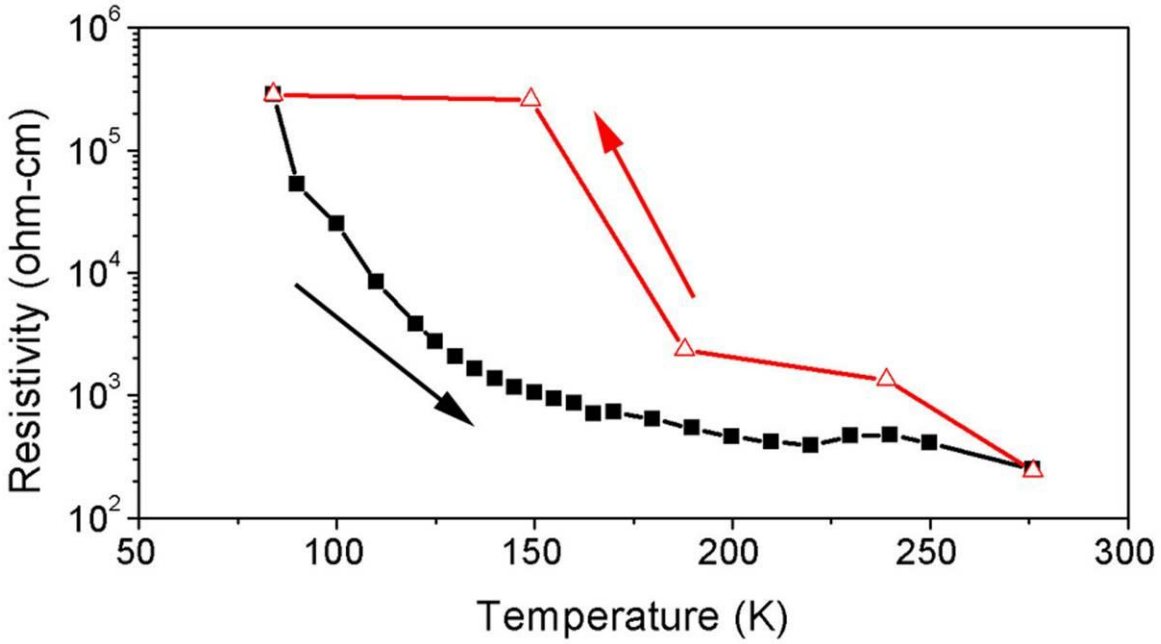

Fig. 2.11: Plot of resistivity *vs.* temperature during the cooling cycle (red, open triangles) and the warming cycle (black, solid squares) for V_2O_3 nanorods.

2.8 Conclusions

We have shown that VO_2 nanowires have been initially generated via a hydrothermal procedure and subsequently utilized as reactive precursors for the formation of V_2O_3 nanorods. Structural changes, associated with the M–I transition, from the monoclinic form to the rutile form have been investigated and confirmed using both XRD and synchrotron data, showing that the structural transition is reversible and occurs at around 63°C. When this sample was subsequently heated to 800°C in a reducing atmosphere, it was successfully converted to V_2O_3 with effective retention of its one-dimensional morphology and single crystalline nature. Furthermore, we have collected both magnetic and transport data on our samples, which are in general agreement with either bulk behavior or prior results on analogous nanoscale systems.

2.9 References

1. W. Chen, J. Peng, L. Mai, H. Yu and Y. Qi, *Chemistry Letters*, 2004, **33**, 1366-1367.
2. F. J. Morin, *Physical Review Letters*, 1959, **3**, 34.
3. N. Ballarini, A. Battisti, F. Cavani, A. Cericola, C. Cortelli, M. Ferrari, F. Trifirò and P. Arpentinier, *Applied Catalysis A: General*, 2006, **307**, 148-155.
4. E. V. Kondratenko, O. Ovsitser, J. Radnik, M. Schneider, R. Kraehnert and U. Dingerdissen, *Applied Catalysis A: General*, 2007, **319**, 98-110.
5. S. J. Yun, B.-G. Chae, J. W. Lim, J.-S. Noh and H.-T. Kim, *Electrochemical and Solid-State Letters*, 2008, **11**, H173-H175.
6. C. Tsang and A. Manthiram, *Journal of The Electrochemical Society*, 1997, **144**, 520-524.
7. J. Shi, S. Zhou, B. You and L. Wu, *Solar Energy Materials and Solar Cells*, 2007, **91**, 1856-1862.
8. B.-G. Chae, H.-T. Kim, S.-J. Yun, B.-J. Kim, Y.-W. Lee, D.-H. Youn and K.-Y. Kang, *Electrochemical and Solid-State Letters*, 2006, **9**, C12-C14.
9. G. A. Rozgonyi and W. J. Polito, *Journal of The Electrochemical Society*, 1968, **115**, 56-57.
10. L.-Q. Mai, W. Chen, Q. Xu, J.-F. Peng and Q.-Y. Zhu, *Chemical Physics Letters*, 2003, **382**, 307-312.
11. C. Tenailleau, E. Suard, J. Rodriguez-Carvajal and P. Lacorre, *Journal of Magnetism and Magnetic Materials*, 2004, **278**, 57-67.
12. D. S. Toledano, P. Metcalf and V. E. Henrich, *Surface Science*, 2001, **472**, 21-32.
13. J. B. Goodenough, *Journal of Solid State Chemistry*, 1971, **3**, 490-500.

14. A. Cavalleri, C. Toth, C. W. Siders, J. A. Squier, F. Raksi, P. Forget and J. C. Kieffer, *Physical Review Letters*, 2001, **87**, 237401.
15. Y. Muraoka and Z. Hiroi, *Applied Physics Letters*, 2002, **80**, 583-585.
16. R. Aliev and V. Klimov, *Physics of the Solid State*, 2004, **46**, 532-536.
17. I. Balberg and S. Trokman, *High contrast optical storage in VO_2 films*, AIP, 1975.
18. P. Liu, S.-H. Lee, H. M. Cheong, C. E. Tracy, J. R. Pitts and R. D. Smith, *Journal of The Electrochemical Society*, 2002, **149**, H76-H80.
19. G. Sudant, E. Baudrin, B. Dunn and J.-M. Tarascon, *Journal of The Electrochemical Society*, 2004, **151**, A666-A671.
20. A. Azens, G. Gustavsson, R. Karmhag and C. G. Granqvist, *Solid State Ionics*, 2003, **165**, 1-5.
21. X. Chen, X. Wang, Z. Wang, J. Wan, J. Liu and Y. Qian, *Nanotechnology*, 2004, **15**, 1685.
22. W. Chen, L. Mai, Y. Qi and Y. Dai, *Journal of Physics and Chemistry of Solids*, **67**, 896-902.
23. A. Liu, M. Ichihara, I. Honma and H. Zhou, *Electrochemistry Communications*, 2007, **9**, 1766-1771.
24. M. Niederberger, H.-J. Muhr, F. Krumeich, F. Bieri, D. Günther and R. Nesper, *Chemistry of Materials*, 2000, **12**, 1995-2000.
25. J. M. Reinoso, H.-J. Muhr, F. Krumeich, F. Bieri and R. Nesper, *Helvetica Chimica Acta*, 2000, **83**, 1724-1733.
26. H. J. Muhr, F. Krumeich, U. P. Schönholzer, F. Bieri, M. Niederberger, L. J. Gauckler and R. Nesper, *Advanced Materials*, 2000, **12**, 231-234.
27. F. Krumeich, H. J. Muhr, M. Niederberger, F. Bieri, B. Schnyder and R. Nesper, *Journal of the American Chemical Society*, 1999, **121**, 8324-8331.
28. F. Krumeich, H.-J. Muhr, M. Niederberger, F. Bieri and R. Nesper, *Zeitschrift für anorganische und allgemeine Chemie*, 2000, **626**, 2208-2216.
29. M. E. Spahr, P. Stoschitzki-Bitterli, R. Nesper, O. Haas and P. Novak, *Journal of The Electrochemical Society*, 1999, **146**, 2780-2783.
30. S. Mathur, T. Ruegamer and I. Grobelsek, *Chemical Vapor Deposition*, 2007, **13**, 42-47.
31. R. Lopez, T. E. Haynes, L. A. Boatner, L. C. Feldman and J. R. F. Haglund, *Opt. Lett.*, 2002, **27**, 1327-1329.
32. J. M. Baik, M. H. Kim, C. Larson, A. M. Wodtke and M. Moskovits, *The Journal of Physical Chemistry C*, 2008, **112**, 13328-13331.
33. B. S. Guiton, Q. Gu, A. L. Prieto, M. S. Gudiksen and H. Park, *Journal of the American Chemical Society*, 2004, **127**, 498-499.
34. B. S. Allimi, S. P. Alpay, C. K. Xie, B. O. Wells, J. I. Budnick and D. M. Pease, *Applied Physics Letters*, 2008, **92**, 202105.
35. F. Sediri and N. Gharbi, *Materials Science and Engineering: B*, 2005, **123**, 136-138.
36. D. M. Moffatt, J. P. Runt, A. Halliyal and R. E. Newnham, *Journal of Materials Science*, 1989, **24**, 609-614.
37. G. van der Lee, B. Schuller, H. Post, T. L. F. Favre and V. Ponec, *Journal of Catalysis*, 1986, **98**, 522-529.
38. C. Zheng, X. Zhang, S. He, Q. Fu and D. Lei, *Journal of Solid State Chemistry*, 2003, **170**, 221-226.

39. K. Zhang, X. Sun, G. Lou, X. Liu, H. Li and Z. Su, *Materials Letters*, 2005, **59**, 2729-2731.
40. Z. Yang, P. Cai, L. Chen, Y. Gu, L. Shi, A. Zhao and Y. Qian, *Journal of Alloys and Compounds*, 2006, **420**, 229-232.
41. N. Pinna, M. Antonietti and M. Niederberger, *Colloids and Surfaces A: Physicochemical and Engineering Aspects*, 2004, **250**, 211-213.
42. S. A. Corr, M. Grossman, J. D. Furman, B. C. Melot, A. K. Cheetham, K. R. Heier and R. Seshadri, *Chemistry of Materials*, 2008, **20**, 6396-6404.
43. G. Anderson, *Acta Chemica Scandinavica*, 1956, **10**, 623.
44. A. D. Burton and P. A. Cox, *Philisopical Magazine*, 1985, **51**, 255.
45. H. Liu, O. Vasquez, V. R. Santiago, L. Díaz and F. E. Fernandez, *Journal of Luminescence*, 2004, **108**, 233-238.
46. P. Baum, D.-S. Yang and A. H. Zewail, *Science*, 2007, **318**, 788-792.
47. M. B. Sahana, G. N. Subbanna and S. A. Shivashankar, *Applied Physics Letters*, 2002, **92**, 6495-6504.
48. J. C. Rakotoniaina, R. Mokrani-Tamellin, J. R. Gavarri, G. Vacquier, A. Casalot and G. Calvarin, *Journal of Solid State Chemistry*, 1993, **103**, 81-94.
49. Y. Oka, T. Yao and N. Yamamoto, *Journal of Materials Chemistry*, 1991, **1**, 815-818.
50. G. T. Chandrappa, N. Steunou, S. Cassaignon, C. Bauvais and J. Livage, *Catalysis Today*, 2003, **78**, 85-89.
51. Y. Mao and S. S. Wong, *Journal of the American Chemical Society*, 2006, **128**, 8217-8226.
52. Z. Gui, R. Fan, W. Mo, X. Chen, L. Yang, S. Zhang, Y. Hu, Z. Wang and W. Fan, *Chemistry of Materials*, 2002, **14**, 5053-5056.
53. C. Leroux, G. Nihoul and G. Van Tendeloo, *Physical Review B*, 1998, **57**, 5111.
54. D. S. Su and R. Schlögl, *Catalysis Letters*, 2002, **83**, 115-119.
55. C. V. Ramana, S. Utsunomiya, R. C. Ewing and U. Becker, *Solid State Communications*, 2006, **137**, 645-649.
56. Y. Ueda, K. Kosuge and S. Kachi, *Journal of Solid State Chemistry*, 1980, **31**, 171-188.
57. R. N. Bhowmik, R. Nagarajan and R. Ranganathan, *Physical Review B*, 2004, **69**, 054430.
58. R. N. Bhowmik and R. Ranganathan, *Solid State Communications*, 2007, **141**, 365-368.
59. J. Feinleib and W. Paul, *Physical Review*, 1967, **155**, 841.
60. C. Grygiel, A. Pautrat, W. C. Sheets, W. Prellier, B. Mercey and L. Mechin, *Journal of Physics: Condensed Matter*, 2008, **20**, 472205.

Chapter 3. Synthesis of single-crystalline one-dimensional $LiNbO_3$ nanowires

3.1 Introduction

In the previous chapter, we were able to successfully synthesize 1D nanoscale structures via a hydrothermal/thermal reduction combinatorial approach. However, as shown in Chapter 1, there are a plethora of synthetic approaches one can reasonably take in order to create 1D nanostructures. Herein, we will explore the application of a molten salt technique for the fabrication of 1D lithium niobate ($LiNbO_3$) nanowires.

Lithium niobate is an interesting material, owing to its unique non-linear optical properties, including its large piezoelectric, electro-optic and non-linear optical coefficients.[1, 2] Furthermore, $LiNbO_3$ not only possesses a small dielectric constant, but also is thermally, mechanically, and chemically stable, thereby transforming it into an excellent candidate for thin-film transducers.[3, 4] The unique combination of these properties has rendered lithium niobate as a desirable material for optical waveguides,[5] data storage media,[6] voltage sensors,[7] and acousto-optical modulators.[8]

There has been a fair amount of attention directed at the synthesis of bulk $LiNbO_3$, for large scale production. Several methods, such as the micro pull-down procedure,[9] the laser heated pedestal growth protocol,[10] and the Czochralski method,[11] have all successfully yielded bulk single crystals of $LiNbO_3$. While there has been some success in synthesizing this material at the nanoscale, there are still several challenges that remain, particularly regarding crystallinity, growth direction, and size control.

In particular, there have been several reports regarding the synthesis of 1D $LiNbO_3$ nanomaterials. Specifically, the pyrolysis of a lithium niobate precursor at 550ºC in the presence

of anodized aluminum oxide templates resulted in the formation of nanotubes measuring 180-400 nm in diameter with a thickness of a few tens of nm.[4] One significant drawback to this synthetic method is the polycrystalline nature of the product obtained. Moreover, this protocol requires the use of air-sensitive conditions in order to maintain the purity of the precursor. Another report alleviates the need for air-sensitive precursors through the use of Nb_2O_5 and LiOH as precursors for a hydrothermal reaction.[12] Treating these precursors, in the presence of various amine ligands, under hydrothermal conditions at 220ºC for 1-4 days, results in the production of smooth, monodisperse nanorods with diameters of ~800 nm and lengths of up to 3 microns. Nonetheless, while this procedure can effectively produce large quantities of $LiNbO_3$ nanorods, the individual sizes of these nanorods are still relatively large. Furthermore, nanowires with widths of ~50 nm can be generated under hydrothermal conditions at 150ºC.[13] However, the resulting nanowires tend to possess random crystallographic planes with respect to the long axis of the nanowires, which can potentially alter the optical properties of the nanowire along the long axis. There has also been a solution- phase approach towards the synthesis of 1D $LiNbO_3$ nanomaterials.[14] This protocol utilizes the directed aggregation of 7 nm nanoparticles during an aging process, resulting in the formation of rod-like structures of up to 100 nm in length. Although this method is advantageous in its low temperature approach, it tends to form polycrystalline materials, which can be less than ideal for optical applications.

Of all the prior synthetic techniques utilized, there has not been a report of a protocol which specifically uses molten salt conditions in order to synthesize $LiNbO_3$ nanowires. In this report, we have utilized molten salt conditions to successfully synthesize 1D nanostructures of lithium niobate. Furthermore, as we have noted in Chapter 2, we can take advantage of nanoscale materials possessing the desired morphology as precursors for the formation of our $LiNbO_3$

nanowires. While there have been two previous reports concerned with the production of 1D niobate nanomaterials, these methods have failed to successfully produce lithium niobate in a one-dimensional motif.[15, 16] Through this methodology, we have been able to generate large-scale, gram quantities of $LiNbO_3$ that are not only reasonably pure (*i.e.* relatively minuscule amounts of a potassium lithium niobate solid mixture as the impurity phase) and single-crystalline but also possess smooth, well-defined edges and crystal facets. One potential drawback to the technique used in this work relates to the successive high temperature steps needed for the reaction and hence, the correspondingly sizable energy requirements associated with that overall process.

3.2 Experimental

A detailed step-by-step reaction scheme, starting from bulk precursors, is shown in Scheme 1. First, this protocol involves the initial synthesis of KNb_3O_8 nanowires using a previously reported molten salt reaction.[16] Briefly, bulk Nb_2O_5 (Alfa Aesar, 99.9985%) was mixed with KCl (Mallinckrodt, 99.5-100%) in the presence of ethanol in a 1:10 molar ratio. The mixture was subsequently dried at 80ºC and then heated in a tube furnace to 800ºC for 3 hours. Upon gradual cooling to room temperature, the sample was washed several times with hot, deionized water, isolated by centrifugation, and finally oven dried at 80ºC. Second, a quantity of these as-prepared KNb_3O_8 nanowires was stirred at room temperature in 400 mL of 2M HNO_3 for 48 hours, followed by washing several times with distilled water, so as to obtain $H_3ONb_3O_8$ nanowires through an exchange reaction. Third, annealing of the $H_3ONb_3O_8$ nanowires at 550ºC for 1 hour enabled their successful conversion to Nb_2O_5 nanowires. A typical SEM image of these "precursor" nanowires is shown in Figure 3.1.

These Nb_2O_5 nanowires were ultimately used as the direct precursors for the $LiNbO_3$ synthesis reaction. The overall reaction has been previously explained for analogous $KNbO_3$ systems by using a combination of 'dissolution-precipitation' and 'template formation' mechanisms.[16] Briefly, niobium oxide nanowires were ground together with Li_2CO_3 in a 1:1 molar ratio before being mixed with an equal weight of KCl. The resulting powder was then transferred to a porcelain boat and heated to 780ºC isothermally for 10 min, prior to gradual cooling to room temperature. The ensuing product was washed several times with distilled, deionized water so as to remove any KCl, prior to dispersion in ethanol for characterization. Product yields of >90% conversion were routinely obtained, corresponding to amounts ranging from 100 mg to >1 gram, depending on the initial quantities of the precursors used.

To prepare powder X-ray diffraction (XRD) samples, samples were rendered into slurries in ethanol, sonicated for about 1 min, and then air-dried upon deposition onto glass slides. Diffraction patterns were collected using a Scintag diffractometer, operating in the Bragg configuration using Cu Ka radiation ($\lambda = 1.54$ Å) from 10 to 80° at a scanning rate of 2° per minute.

The morphology and dimensions of as-prepared samples were initially characterized using a field emission scanning electron microscopy instrument (FE-SEM Leo 1550), operating at an accelerating voltage of 15 kV and equipped with energy-dispersive X-ray spectroscopy (EDS) capabilities. Samples for scanning electron microscopy (SEM) were prepared by dispersing samples in ethanol, sonicating for about1 min, and then depositing the sample onto a silicon wafer, attached to a SEM brass stub. All of these samples were then conductively coated with gold by sputtering for 15 s in order to minimize charging effects under SEM imaging conditions.

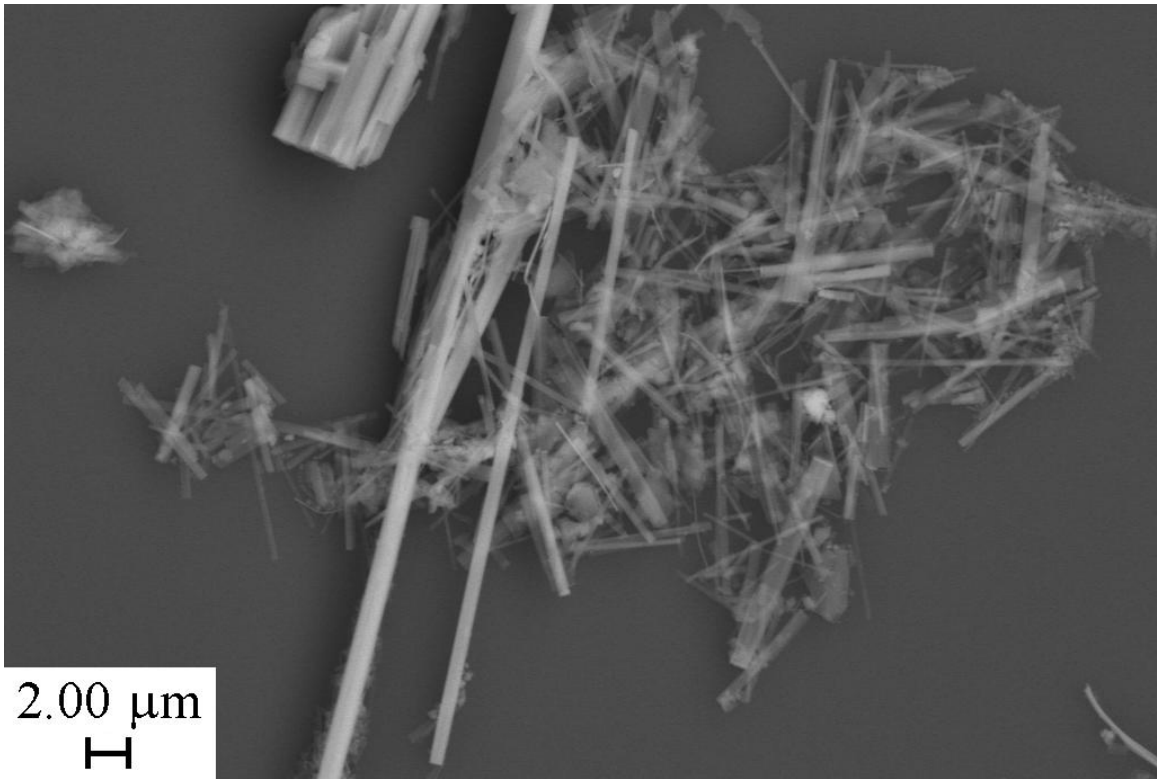

Figure 3.1. SEM image of as-prepared Nb_2O_5 nanowires.

Low magnification transmission (TEM) images were taken at an accelerating voltage of 80 kV on a FEI Tecnai12 BioTwinG2 instrument, equipped with an AMT XR-

60 CCD Digital Camera System. High-resolution TEM (HRTEM) images and selected area electron diffraction (SAED) patterns were obtained on a JEOL 2010F instrument, equipped with a Gatan high-angle annular dark field detector (HAADF) for performing incoherent HAADF or Z-contrast imaging in scanning TEM mode at accelerating voltages of 200 kV. Specimens for all of these TEM experiments were prepared by dispersing the as-prepared product in ethanol, sonicating for 2 min in order to ensure an adequate dispersion of the nanowires, and dipping one drop of the solution onto a 300 mesh Cu grid, coated with a lacey carbon film.

3.3 Results and Discussion

The X-Ray diffraction pattern of our $LiNbO_3$ nanowires obtained from the molten salt technique is shown in Figure 3.2A. It is clear from this data that the majority of the sample consists of $LiNbO_3$, with peak positions and intensities that correspond to the JCPDS database standard #85-2456, as well as to a small amount of potassium lithium niobate solid mixture impurity. $LiNbO_3$ possesses a space group of *R*3*c* (161) and a corresponding rhombohedral crystal structure. Lattice parameters calculated from the XRD pattern reveal *a* and *c* values of 5.151 Å and 13.853 Å, in excellent agreement with the literature values of $a = 5.15$ Å and $c = 13.85$ Å.

Several other salts, such as KOH, NaCl, and LiCl, have also been employed for the synthesis of $LiNbO_3$ nanowires. However, subsequent analysis by XRD (Figure 3.3) revealed that the purity of these samples was significantly less than that of KCl. Furthermore, KCl was found to be the only salt capable of producing 1D nanomaterials of $LiNbO_3$. We attribute this

observation to the favorable "solution" phase properties of the molten KCl, specifically its optimal solubility, reaction rate, and viscosity. In this particular synthesis, it was critical to control the solubility of the niobium oxide nanowire precursors in the molten salt flux. In the case where the solubility is too great, the nanowire precursors completely dissolve into the molten flux and can no longer effectively act as a template for the growth of the desired $LiNbO_3$ nanowires. Furthermore, the cation diffusion rate into the niobate structure is also crucial. If we compare the relative amounts of impurities found in the XRD patterns, we find that as the size of the cation increases, the relative amount of impurity decreases. This trend suggests that, for a given set of reaction conditions, as the cation size increases, the rate of its integration into the crystal lattice decreases.[17] It is from these results that we can conclude that two of the most influential factors governing the growth of $LiNbO_3$ nanowires are the solubility of Nb_2O_5 in the molten flux, as well as the size of the cation.

The morphology of the KCl derived material is shown in Figure 3.2B. It can be clearly seen that the sample consists of both nanowires and nanoparticles in the approximate ratio of 70 : 30, even after centrifugation at 1000 rpm, which tends to selectively remove smaller nanoparticles and nanowires. The analysis of electron microscopy images of as-obtained individual

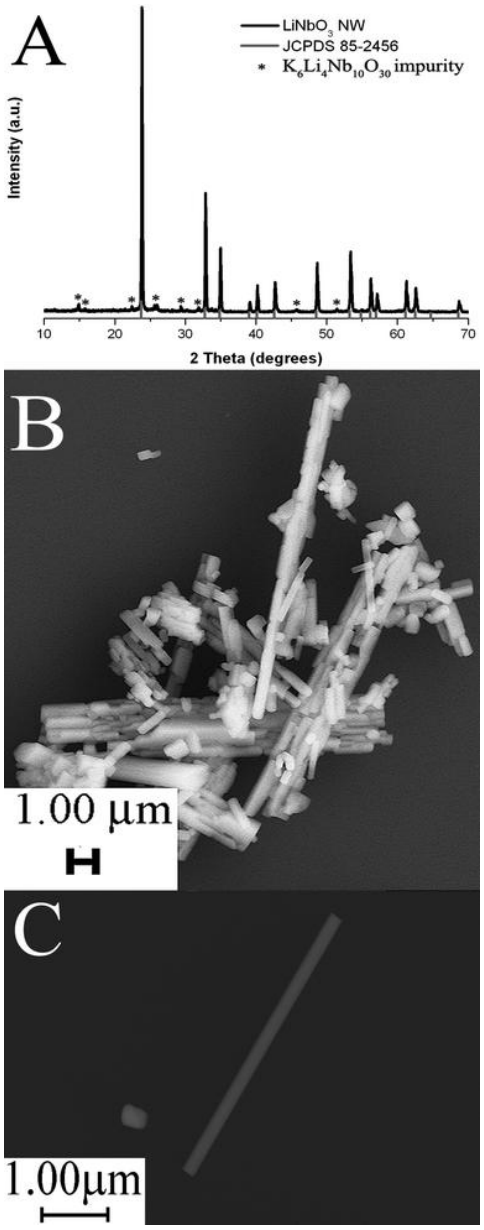

Figure 3.2: A) XRD of as-prepared $LiNbO_3$ nanowires, corresponding to the JCPDS #85-2456 database standard. B) Typical SEM image of as-prepared nanowires and nanoparticles of $LiNbO_3$. C) SEM image of an isolated $LiNbO_3$ nanowire.

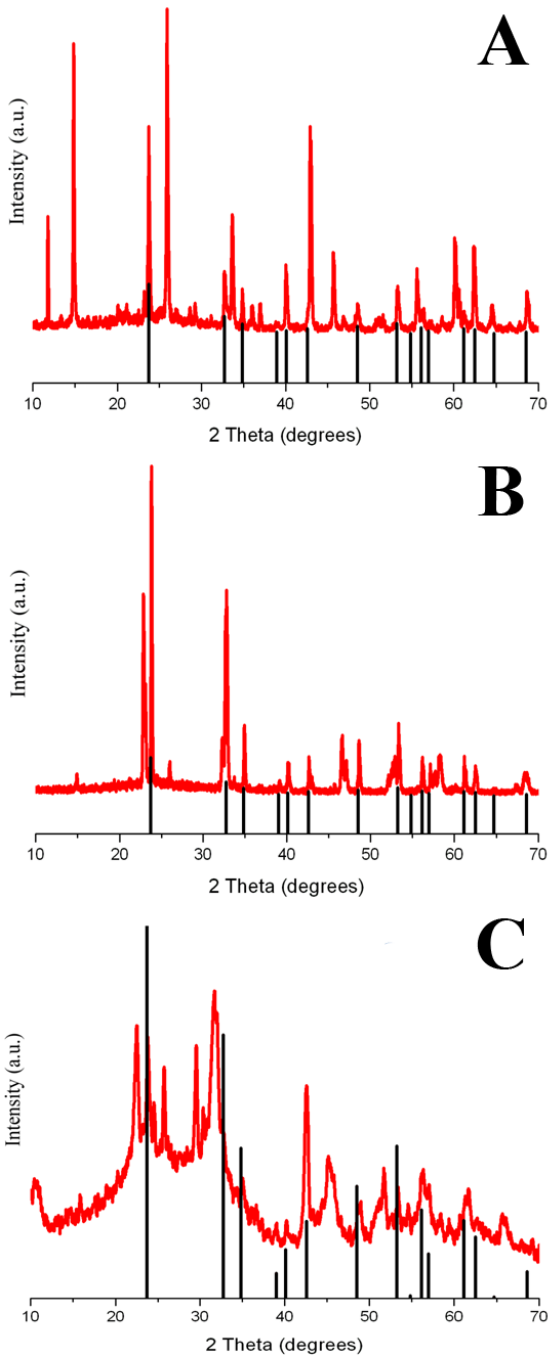

Figure 3.3: XRD of products obtained using A) LiCl, B) NaCl and C) KOH as the molten salt media. Black lines indicate the values expected for $LiNbO_3$ from JCPDS # 85-2456.

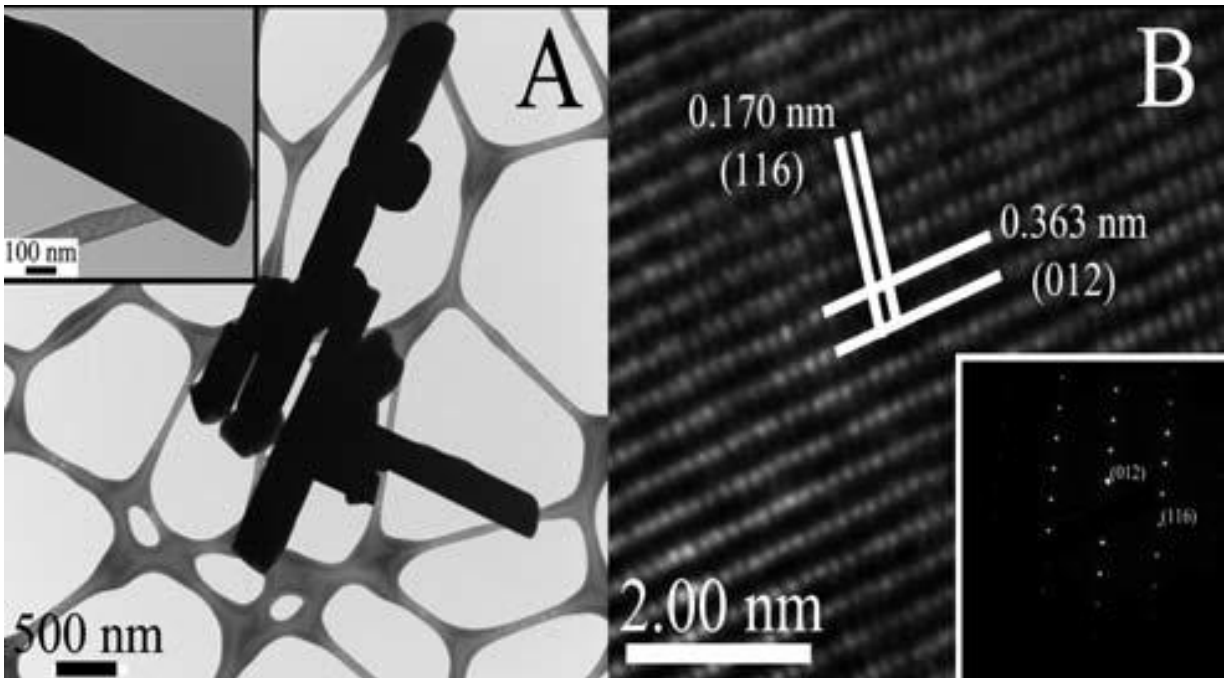

Fig. 3.4: A) TEM image of $LiNbO_3$ nanowires. Inset shows a magnified view of an individual nanowire. B) HRTEM image of highly crystalline $LiNbO_3$ nanowires, showing lattice planes corresponding to the (116) and the (012) planes, respectively, of $LiNbO_3$. Inset shows a representative SAED pattern of $LiNbO_3$ nanowires.

nanowires (Figure 3.2C) yielded an average width of 385 ± 106 nm with lengths of up to several microns. This large standard deviation is expected, due to the large variation in the size of the precursor Nb_2O_5 nanowires (Figure 3.1), measuring 374 ± 290 nm.

Further investigation of the nanowires by TEM (Figure 3.3A) revealed that these nanostructures posses smooth well-defined surfaces. The accompanying HRTEM image (Figure 3.4B) confirms the high quality and single-crystalline nature of these nanowires. The most prominent lattice plane exhibited in Figure 3.4B gives rise to a distance of 0.363 nm, which corresponds well to the (012) plane of the rhombohedral phase of $LiNbO_3$. The corresponding SAED pattern (inset of Figure 3.4B) consists of sharp diffraction spots, corroborating the single-crystalline nature of our nanowires. Furthermore, the indexing is consistent with that expected for rhombohedral $LiNbO_3$. It is important to note here that the results from this data are consistent with the idea of growth along the *c*-axis.

In order to more fully characterize our nanowires, we utilized a home-built confocal micro-Raman scattering setup. Through direct probing of the frequency of characteristic phonon modes, Raman scattering is sensitive to impurities, stoichiometry, and strain. Furthermore, the capability to probe material symmetry allows not only for material identification but also for determination of the crystallographic phase, where minute yet symmetry-breaking lattice displacements can affect the Raman selection rules. The Raman spectrum of a single nanowire in the spectral range of 100 to 900 wavenumbers is shown in Figure 3.5. As the Raman scattering cross-section of $LiNbO_3$ is very large, high signal-to-noise ratios are noted. Apart from silicon peaks corresponding to the supporting substrate, as indicated in Figure 3.5, a summary of the main $LiNbO_3$ phonon modes and their assignments can be found in Table 3.1, a representation of atomic motion associated with the A_1 Raman modes can be found in Figure 3.6. Peaks observed

at 151, 237, 365, and 578 cm^{-1} correspond to the strongest characteristic *E* transverse optical (TO) phonon modes of $LiNbO_3$, consistent with a hexagonal ferroelectric phase.[18-20] The strongest fundamental A_1 TO mode, which was expected at 630 cm^{-1}, shifted to a lower wavenumber of 621 cm^{-1} for our nanowires, an observation which may be due to a mixing of A_1 TO and *E* TO modes. However, that result is consistent with phonon propagation at an angle of 65° relative to the surface normal.[21] Similarly the peak observed at 870 cm^{-1}, which is expected at 883 cm^{-1}, can be assigned to the quasi TO mode.

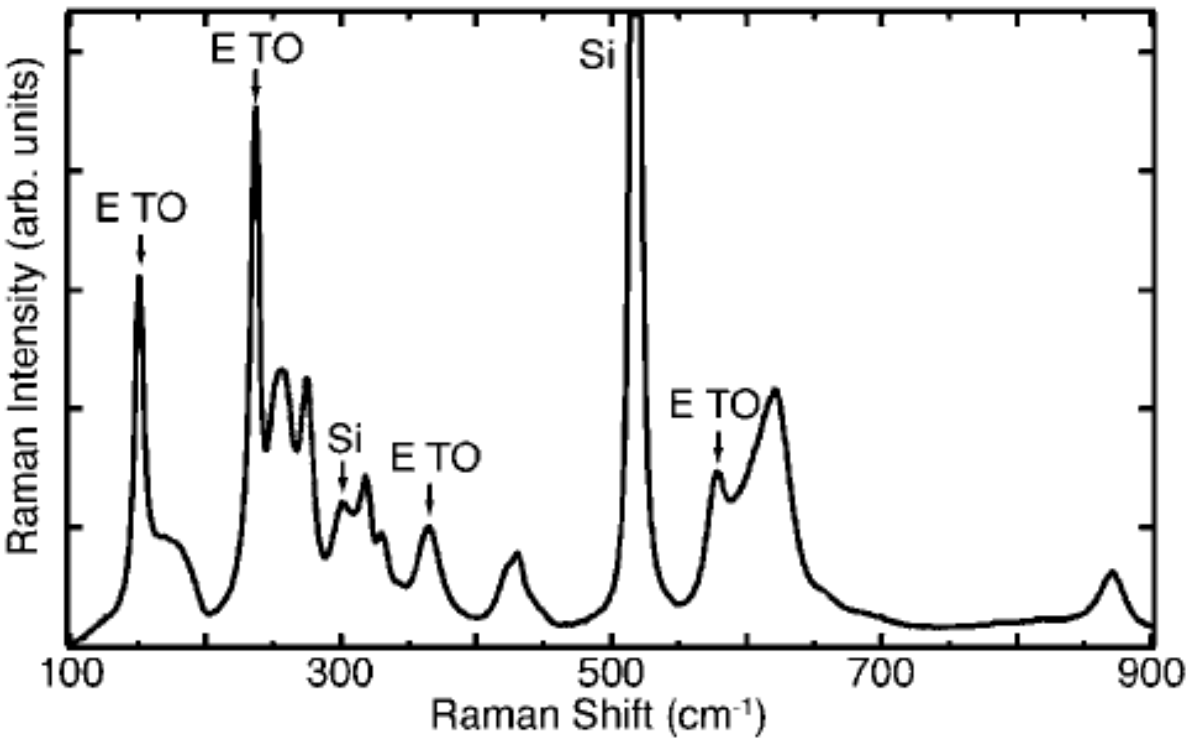

Fig. 3.5: Raman spectrum of an individual $LiNbO_3$ nanowire. It is essentially spectrally identical to that of bulk and of single crystal analogues.

Table 1	
Peak Position (cm^{-1})	**Peak Assignments**
151	*E* TO
237	*E* TO
256	*E* TO / quasi TO
275	quasi TO
318	*E* TO
331	*E* TO
365	*E* TO
423	*E* LO
430	*E* TO
578	*E* TO
621	A_1 TO / *E* TO
870	quasi LO

Table 3.1: Peak positions and identification of peaks in a LiNbO3 nanowire Raman spectrum.

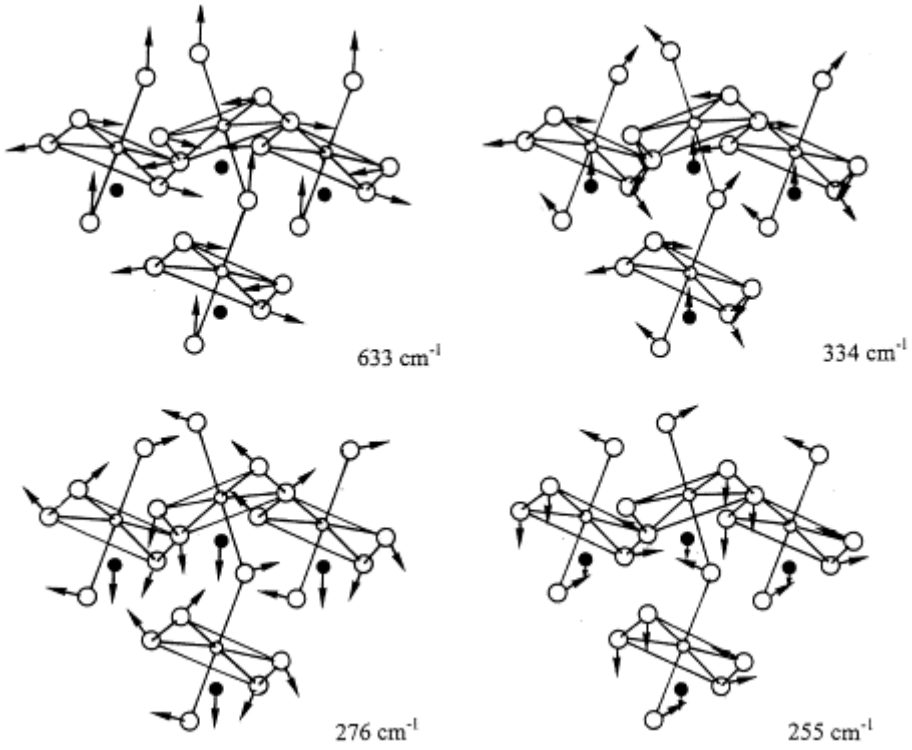

Figure 3.6: Cartesian displacements of atoms in A_1 normal modes of $LiNbO_3$. (O oxygen atoms; ○: niobium atoms; •: lithium atoms). Reproduced from reference 18.

3.4 Conclusions

We have been able to adapt an existing molten salt method[16] to produce, for the first time, single-crystalline nanowires of $LiNbO_3$ on a large scale with minimal detectable levels of impurities. Furthermore, these nanowires possess smooth, well defined crystal surfaces with a preferential growth direction along the *c*-axis. Finally, Raman investigation of these nanowires has confirmed the high quality and purity of these materials, and has revealed the presence of phonon propagation at an angle of 65° with respect to the nanowire surface.

3.5 References

1. A. Polman, *Erbium implanted thin film photonic materials*, AIP, 1997.
2. F. Abdi, M. Aillerie, P. Bourson, M. D. Fontana and K. Polgar, *Electro-optic properties in pure LiNbO3 crystals from the congruent to the stoichiometric composition*, AIP, 1998.
3. N. F. Foster, *The Deposition and Piezoelectric Characteristics of Sputtered Lithium Niobate Films*, AIP, 1969.
4. L. Zhao, M. Steinhart, M. Yosef, S. K. Lee and S. Schlecht, *Sensors and Actuators B: Chemical*, 2005, **109**, 86-90.
5. A. Ruso, M. Aillerie, N. Fressengeas and M. Ferriol, *Applied Physics B: Lasers and Optics*, 2009, **95**, 573-578.
6. C. Nölleke, J. Imbrock and C. Denz, *Applied Physics B: Lasers and Optics*, 2009, **95**, 391-397.
7. Y.-S. Yim and S.-Y. Shin, *Optics Communications*, 1998, **152**, 225-228.
8. N. Courjal, M.-P. Bernal, G. Ulliac, J. Dahdah, S. Benchabane and J.-M. Merolla, *Journal of the European Optical Society Rapid Publications*, 2009, **4**, 09018.
9. D.-H. Yoon, I. Yonenaga, T. Fukuda and N. Ohnishi, *Journal of Crystal Growth*, 1994, **142**, 339-343.
10. Y. S. Luh, M. M. Fejer, R. L. Byer and R. S. Feigelson, *Journal of Crystal Growth*, 1987, **85**, 264-269.
11. K. Polgár, Á. Péter, L. Kovács, G. Corradi and Z. Szaller, *Journal of Crystal Growth*, 1997, **177**, 211-216.
12. M. Liu and D. Xue, *The Journal of Physical Chemistry C*, 2008, **112**, 6346-6351.
13. R. Grange, J.-W. Choi, C.-L. Hsieh, Y. Pu, A. Magrez, R. Smajda, L. Forró and D. Psaltis, *Lithium niobate nanowires synthesis, optical properties, and manipulation*, AIP, 2009.
14. B. D. Wood, V. Mocanu and B. D. Gates, *Advanced Materials*, 2008, **20**, 4552-4556.
15. C.-Y. Xu, L. Zhen, R. Yang and Z. L. Wang, *Journal of the American Chemical Society*, 2007, **129**, 15444-15445.

16. L. Li, J. Deng, J. Chen, X. Sun, R. Yu, G. Liu and X. Xing, *Chemistry of Materials*, 2009, **21**, 1207-1213.
17. R. E. Schaak and T. E. Mallouk, *Chemistry of Materials*, 2002, **14**, 1455-1471.
18. Y. Repelin, E. Husson, F. Bennani and C. Proust, *Journal of Physics and Chemistry of Solids*, 1999, **60**, 819-825.
19. A. S. Barker and R. Loudon, *Physical Review*, 1967, **158**, 433.
20. R. F. Schaufele and M. J. Weber, *Physical Review*, 1966, **152**, 705.
21. S. Berweger and M. B. Raschke, *Journal of Raman Spectroscopy*, 2009, **40**, 1413-1419.

Chapter 4. Synthesis and Characterization of One-Dimensional Cr_2O_3 nanostructures

4.1 Introduction

In Chapters 1 and 2, we explored the use of template-free synthetic techniques for the formation of single-crystalline 1D nanomaterials. While these methods have many favorable aspects, which were discussed in detail in prior chapters, they lack the ability to explicitly and predictably control the dimensions of the nanomaterial. Herein, we explore the use of a template mediated sol-gel technique for the formation of 1D Cr_2O_3 nanowires.

Chromium sesquioxide (Cr_2O_3) is of particular interest, owing to its high melting point and oxidative resistance.[1, 2] Due to these highly advantageous properties, this material has found use in a wide variety of applications, such as coatings[3, 4] for wear resistance and thermal protection,[5] as well as for solar energy collectors, liquid crystal displays, and catalysts (*i.e.* associated with hydrogenation and dehydrogenation of selected olefins, methanol synthesis, and SO_2 reduction).[6-12] Furthermore, particles with dimensions less than 50 nm have been utilized as colorants.[5] In addition, Cr_2O_3 is a wide band gap, *p*-type semiconductor (especially at low temperatures), with a band gap of ~ 3.4 eV, revealing potential applications in optical devices. Of further interest in terms of its material properties are the high electrical conductivity with reasonable levels of electron transfer, associated with chromium oxide, thereby rendering this material as a promising candidate for electronic devices.[13] In addition to these interesting optical and electronic properties, bulk Cr_2O_3 is an antiferromagnetic material with a Néel temperature of 307 K.[14-16] However, in nanoscale Cr_2O_3, the observed magnetic properties are primarily driven by the presence of uncompensated surface spins.[17] Because it is also sensitive to hydrogen adsorption,[18] chromium sesquioxide has also been used as a component of gas sensors for

ethanol and ammonia vapor, operating through the detection of minute electrical changes that can be probed by means of ac impedance spectroscopy and work function measurements.[19, 20]

With this wide variety of applications in mind, the need for nanoscale Cr_2O_3 is 2-fold. First, the high surface-area-to volume ratio afforded by nanoscale materials is highly desirable for the many applications aforementioned,[7] and commercial bulk Cr_2O_3 is difficult to sinter. Second, magnetic solids possessing nanoscale dimensions have been known to exhibit anomalous magnetic behavior, relative to their bulk forms.[21] There have been quite a few distinctive methods established towards the synthesis of Cr_2O_3 nanoparticles and aerogels, including but not limited to hydrothermal processing,[22, 23] the use of supercritical fluids,[7, 24] precipitation-gelation reaction,[2, 4, 25] solid thermal decomposition reactions,[26] mechanochemical processing,[5] hydrazine reduction reactions coupled with thermal treatment, [27] precursor calcination and annealing,[14, 15] laser-induced deposition from solution,[28] laser-induced pyrolysis,[29] room-temperature sonochemical reduction,[30] forced hydrolysis from chromium precursors,[1, 6] as well as microwave plasma processing.[17]

It is noteworthy that in stark contrast to the vast amount of literature pertaining to the synthesis of nanoparticles and aerogels, there have been only a few reports regarding the synthesis of anisotropic, 1D Cr_2O_3. For instance, Cr_2O_3 nanobelts have been synthesized via a chemical vapor deposition, in which ethanol was flowed over chromium metal at 800°C.[31] Although this methodology successfully produced single-crystalline nanobelts of Cr_2O_3, the method required the use of high temperatures in a controlled gaseous atmosphere (whose precise role in the formation mechanism for these nanostructures was not fully understood), and, moreover, yielded a relatively polydisperse product, with nanobelt widths ranging from tens of nanometers to hundreds of nanometers. Furthermore, similar high temperature treatments were

required for the synthesis of Cr_2O_3 nanorods and nanowires, in which $Cr(OH)_3$ nanoparticles are sintered at temperatures of 1027 K in order to form nanorods and nanowires with diameters of 50 nm and lengths of several hundreds of nanometers.[32] In addition, nanotubes measuring 80 nm in diameter and lengths of 550 nm have been synthesized through a solvothermal reduction route at 180°C in the presence of acetyl acetone and ethylene glycol.[33]

A few groups have latched onto the idea of utilizing different types of templates as a successful medium for the formation of 1D chromium oxide. For example, mesoporous silica has been used to successfully and spatially confine hydrated precursors of Cr_2O_3 which, upon calcination at 550-650°C, results in the formation of single crystalline nanowire bundles.[34, 35] An analogous calcination process at 550°C using multiwalled carbon nanotubes as a template via a supercritical fluid-mediated route has also been demonstrated to produce chromium oxide nanotubes.[36] A third approach reports the formation of Cr_2O_3 nanowires through the impregnation of an alumina template with a $Cr(OH)_3$ sol, initially created using hydrazine, by application of 1.3 atmospheres of pressure for 4-5 hours. Subsequently, these nanowires were crystallized by annealing at 600°C for 5 hours under an inert atmosphere.[13]

Aside from the fact that our synthesis does not rely on the use of either a microemulsion or an autoclave, the method we have reported herein for the synthesis of high-aspect-ratio Cr_2O_3 nanowires is distinguishable from all of these previous experiments mentioned, in several ways. First, we do not require the use of either specialized or inert gases during our annealing procedure, which can actually be run under air. Second, our procedure does not require any high-temperature annealing treatment in order to specifically isolate the product from within the template. In fact, our polycarbonate template is actually burned off as a normal byproduct of our

synthesis steps. Third, while our specific synthesis method necessitates the application of pressure, its duration is much more rapid (30-45 min) as compared with previous reports, and overall, our reaction times are noticeably faster than those of previous groups. Fourth, while our procedure is based upon a sol-gel methodology, we have tried to simplify the process as much as possible. For example, we do not use either hydrazine, supercritical fluids, or any particularly hazardous conditions in order to facilitate the reaction progression. We have demonstrated the catalytic behavior of our nanostructures for the particular destruction of $KClO_4$.

Moreover, we have also investigated the magnetic properties of our Cr_2O_3 nanowires. We find that, in as-prepared 1D Cr_2O_3 nanostructures, the magnetic properties are strongly modified as compared with those of the bulk, due to the emergence of a net magnetic moment induced by uncompensated surface spins, as has been previously reported for Cr_2O_3 nanoparticles.[14, 15, 37, 38] Furthermore, previous reports have indicated the presence of an exchange bias effect in Cr_2O_3 nanoparticles, as a result of the exchange coupling between the surface spins and core; we have sought an analogous effect for our samples herein.[15, 38]

4.2 Experimental Methods

All chemicals were used as received without additional purification. Our methodology is based upon an adaptation of a sol-gel procedure that has been previously reported[25] for a generic synthesis of metal oxide aerogels using inorganic salt precursors. Specifically, to the resulting aqueous, translucent, dark green solution of chromium chloride hexahydrate (Strem Chemicals) was added an aliquot of propylene oxide (Acros Organic, 99.5%) in a molar ratio of ~1: 3.5 with thorough stirring. The purpose of the propylene oxide in the solution is to act as a gelation

promoter.[25] Upon thorough mixing, droplets of the sol precursor solution were forced into the hollow pores of 6 μm thick porous Whatman polycarbonate track-etched membranes (containing 200 nm pore sizes) by systematic and continuous application of pressure through the mediation of a 25 mL syringe, until the template pore channels appeared to be fully saturated with solution, upon visual inspection. After cleaning, by wiping the surface of the template with a dry Kim wipe to dryness, the polycarbonate template was subsequently placed into a porcelain crucible (i.e., a glazed porcelain boat) and heated in air to 600°C for 1 h at a ramp rate of 5°C/min followed by natural cooling to room temperature. In additional experiments, we also used templates with nominal pore sizes of 100, 50, and 15 nm, respectively. Of significance, we should note that it has been previously shown for polycarbonate templates with pore sizes less than 100 nm that (i) the pore size is often not consistent throughout the full length of the template and (ii), hence, as-obtained nanowire diameters can be larger than expected by factors of as much as 2-4.[39, 40]

4.3 Characterization Methods

To prepare powder X-ray diffraction (XRD) samples, the resulting chromate nanorods were rendered into slurries in ethanol, sonicated for about 1 min, and then air-dried upon deposition onto glass slides. Diffraction patterns were collected using a Scintag diffractometer, operating in the Bragg- Bretano configuration using Cu Kα radiation (λ=1.54 Å) from 20 to 70 at a scanning rate of 2° per minute.

Mid-infrared spectra were obtained on a Nexus 670 (ThermoNicolet) equipped with a Smart Orbit accessory, a KBr beam splitter, and a deuterated triglycine sulfate (DTGS) KBr detector. As-prepared solid powder samples were placed onto a diamond crystal where data were taken with a reproducible pressure. A background correction was performed using the diamond

crystal in the spectral range studied. UV-visible spectra were collected at high resolution on a Beckmann Coulter model DU 640 spectrometer using quartz cells with a 10 mm path length. Spectra were obtained for as-prepared samples, which were sonicated in distilled water so as to yield homogeneous dispersions. UV-visible absorption spectra were recorded using distilled water as a blank. We have also obtained analogous spectral data in ethanol, dimethylformamide (DMF), and cyclohexane with a series of nanowire concentrations ranging from <1 μg/mL to 0.5 mg/mL. Raman data were taken using a WiTec alpha 300 microscope using an excitation wavelength of 532 nm with a power of ~0.5 mW to avoid strong laser heating. Spectra were acquired with an integration time of 10 s with a total of 30 scans. Scattered light was analyzed using a 600 mm^{-1} spectrometer grating with a spectral resolution of ~3 cm^{-1}.

The diameters and lengths of as-prepared 200 nm diameter nanorods were initially characterized using a field emission scanning electron microscopy instrument (FE-SEM Leo 1550), operating at an accelerating voltage of 20 kV and equipped with energy-dispersive X-ray spectroscopy (EDS) capabilities. The corresponding diameters and lengths of as-prepared 100, 50, and 15 nm diameter nanorods were analyzed using a Hitachi S4800, operating at an accelerating voltage of 5 kV. Samples for SEM were prepared by dispersing as-prepared chromate nanorods in ethanol, sonicating for about 2 min, and then depositing several drops of the sample solution onto a silicon wafer, attached to a SEM aluminum stub.

High-resolution transmission electron microscopy (HRTEM) images and selected area electron diffraction (SAED) patterns were obtained on a JEOL 2010F instrument at accelerating voltages of 200 kV. Specimens for all of these TEM experiments were prepared by dispersing the as-prepared product in ethanol, sonicating for 2 min to ensure an adequate dispersion of the

nanowires, and dripping one drop of the solution onto a 300 mesh Cu grid, coated with a lacey carbon film.

To perform electrical characterization, Pt contacts were defined by ion beam assisted deposition using the Ga ions of a dual beam SEM/focused ion beam (FIB) system. This fabrication method was chosen because our nanowires showed poor adhesion to substrates (600 nm SiO_2/n^+ Si) during the electrode metal lift-off stage of conventional e-beam lithography. Current-voltage (C-V) curves at different temperatures were measured for two nanowires (named A and B here) using a cryogenic probe station that spanned the 4 to 300 K temperature range. C-V curves were Ohmic from 300 K down to 4 K, as can be seen from the upper inset of Figure 4.5. Only curves at 4 K were considered to be slightly non-Ohmic.

In order to study the magnetic properties of Cr_2O_3 nanowires, we measured both the temperature and field dependence of direct current (dc) magnetization at a range from 10 to 320 K and in magnetic fields as large as 50 kOe, using a Quantum Design Magnetic Property Measurement System (MPMS-XL7) instrument. In a typical experiment, 3 mg of nanowires were contained in gelatin capsules and fastened in plastic straws for immersion into the magnetometer. No subtraction of the diamagnetic signal associated with the sample container was made for the magnetization data.

As part of our study of Cr_2O_3 reactivity, thermogravimetric analysis (TGA) was performed in a dry air environment using a TA Instruments Q500 TGA model. Experiments were carried out from room temperature to 700°C at a heating rate of 5°C/ min. Samples of 3 to 4 mg were placed in a platinum pan for individual runs.

4.4 Synthesis and Structural Characterization Results

In order to probe the crystallinity and purity of our as-prepared chromium oxide nanowires, an initial characterization was performed utilizing powder X-ray diffraction (XRD). As can be seen from the data presented in Figure 4.1A (red curve), all of the diffraction peaks observed from the as-prepared samples can be readily ascribed to a rhombohedral-phase crystal structure with lattice constants of a = 4.922 Å and c = 13.62 Å, which is in good agreement with those reported for pure bulk Cr_2O_3 (Figure 4.1A, blue curve), which possess corresponding lattice constants of a = 4.958 Å and c = 13.58 Å (JCPDS #85-0869). There were no peaks readily apparent that could be ascribed to an impurity phase, such as either a hydrated or nonstoichiometric chromium oxide species, although it is important to note here that the broad peak present from 2θ values of 20 to 40° is associated with the amorphous glass slide used to support the sample. We attribute this observation mainly to the complete high-temperature conversion and crystallization of the precursor gel into chromium oxide. Furthermore, the fact that the template utilized to create these nanostructures is composed of polycarbonate implied that it could be completely burned off and removed *in situ* during the required heating procedure to 600°C. Because of this relatively high-temperature sintering process, the presence of any carbonaceous material should have been very minimal to none. Furthermore, apart from XRD, additional SEM ant TEM characterizations revealed no evidence of the presence of any discernible amount of carbonaceous material that could be unambiguously ascribed to the template. Therefore, isolation of our product did not necessitate either any additional separation or purification steps, unlike for other previously reported methods.[13]

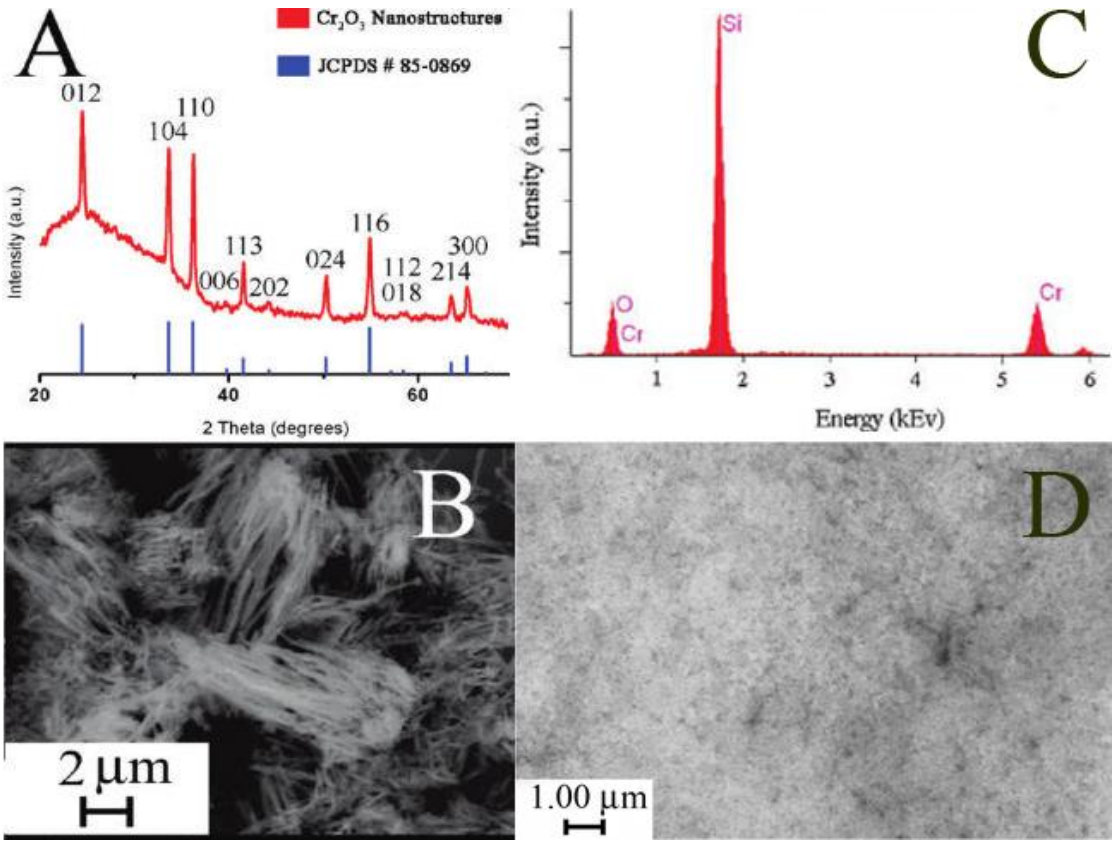

Figure 4.1: A) Powder XRD of Cr_2O_3 nanowires. B) Representative low-magnification SEM image of Cr_2O_3 nanowires. C) EDS of sample shown in (B). D) SEM of sample obtained by cleaning of the template with a dampened Kimwipe, resulting primarily in the formation of nanoparticles.

In order to optically visualize our nanostructures, we utilized FE-SEM to conclusively determine the final morphology of our nanostructures. It is clearly evident from the SEM image shown in Figure 4.1B that the as-obtained sample consists primarily of 1D wire-like nanostructures with a small amount of nanoparticles (<10%) present in the sample. That is, on average, there was a minimum of 90% nanowires present in the sample. Additional experiments, Figure 4.1D, reveal that both the nature and extent of the cleaning of the external template surface, prior to its

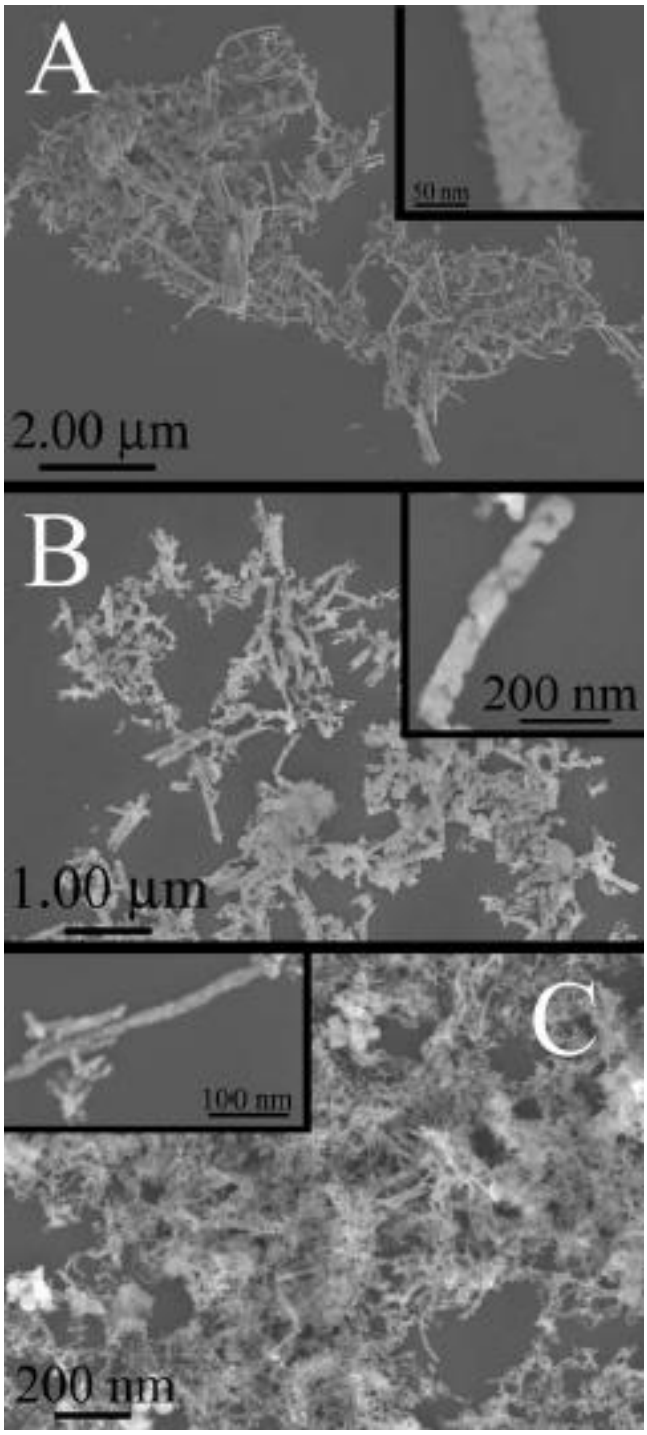

Figure 4.2: SEM image of as-prepared nanowires fabricated using a polycarbonate template with (A) 100 nm pore sizes, (B) 50 nm pore sizes, and (c) 15 nm pore sizes, respectively. Insets show magnified views of individual nanowires, revealing their constituent fine substructure. heating, were directly correlated with the amount of nanoparticles present in the final sample.

Closer examination of the nanowires revealed diameters of 179 ± 29 nm, consistent with the width of the 200 nm template pores, and lengths of up to several microns. Furthermore, by changing the pore sizes to 100, 50, and 15 nm, the sizes of the nanowires could be altered to 143 ± 21, 87 ± 12, and 31 ± 5 nm, respectively (Figure 4.2). However, we were not able to isolate a sufficient amount of nanowires from these samples to effectively characterize them. It is important to note here that all of these 1D nanostructures are structurally robust, as they can withstand 30 min of sonication without evident disintegration and loss of morphology. As can be seen from the EDS spectrum shown in Figure 4.1C, the only elements present in the sample are chromium and oxygen (e.g. the large silicon peak present is attributed to the silicon substrate used to support the sample), further highlighting the purity of our nanowire sample. We note herein that subsequent magnetic and optoelectronic measurements were performed on the nanowires obtained and isolated from the 200 nm pore size templates, because these were easiest to fabricate as morphologically and crystallographically pure, crystalline 1D motifs in relatively large quantities.

Transmission electron microscopy images shown in Figure 4.3A and B clearly reinforce the view that not only are the nanowires straight, but also possess a relatively roughened and irregular surface, as if they were composed of a constituent nanoparticulate substructure. Indeed, the individual nanowires are cylindrical in nature and appear to be composed of smaller, constituent nanoparticles, sintered and aggregated together so as to form a discrete polycrystalline 1D superstructure. This observation, coupled with the nontrivial selected area electron diffraction pattern (SAED), shown as the inset of Figure 4.3A, further supports the idea of the overall polycrystalline nature of our nanowires. Even further proof of this assertion is

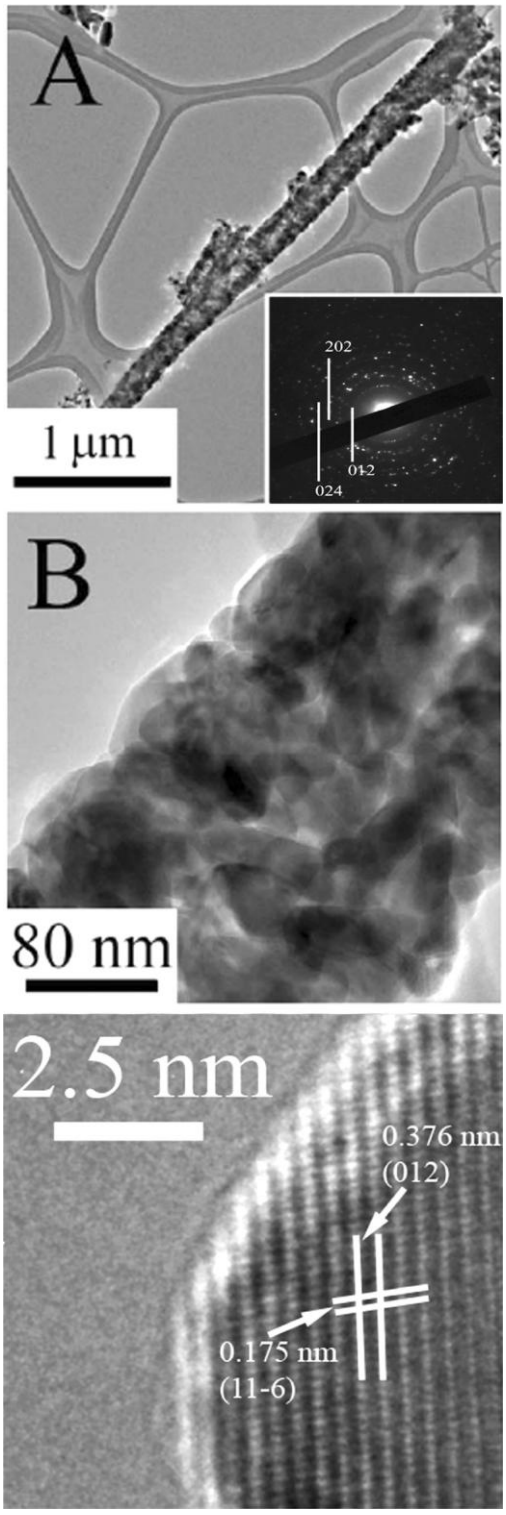

Figure 4.3: A) Low-magnification TEM of a single Cr_2O_3 nanowire. Inset: selected area electron diffraction pattern of this nanowire. B) Higher magnification TEM image of nanowire presented in (A). C) HRTEM image of an individual, crystalline constituent nanoparticle within the nanowire shown in A). Lattice planes shown correspond to the (11-6) and (012) planes of Cr_2O_3.

provided upon investigation of the nanowires at higher magnifications (Figure 4.3C) wherein the lattice planes of the individual, constituent single-crystalline nanoparticles can be clearly discerned. The most prominent lattice planes present have been indexed to the 012 plane and the 11-6 planes of the rhombohedral phase of chromium oxide (JCPDS # 85-0869), consistent with our XRD results. In fact, the measured lattice distance for the 012 plane, in particular, was determined to be 0.374 ± 0.05 nm, which is only a 2% difference from the expected JCPDS value of 0.364 nm. Based upon the aforementioned results, it is clear that the nanowires are likely composed of single-crystalline nanoparticles, with dimensions of 36 ± 17 nm, that can be sintered together in order to create a hierarchical 1D nanostructure. Our group has previously observed a very similar structural motif for hydrothermally derived TiO_2 nanowires.[41]

4.5 Opto-Electronic Properties

Subsequent spectroscopic analysis of our as-prepared nanowires further supported the notion that our nanowires are crystalline Cr_2O_3. Bands present in the infrared (IR) spectrum of our nanomaterials, shown in Figure 4.4A, correspond reasonably well with those previously reported in the literature for bulk Cr_2O_3. For instance, the peaks in the region from 850 to 1100 cm^{-1} can be readily identified as various combination lattice modes. Specifically, peaks at 1092, 948, and 882 cm^{-1} can be ascribed to the $E_2' + A_2'$, $E_2' + E_3'$, and 2 E_2' modes, respectively;[42] another group has assigned the band centered at 1092 cm^{-1} to a stretching vibration of the Cr=O bond.[43] Additional peaks present at lower wavenumbers, more specifically at 609, 512 and 441 cm^{-1}, respectively, have been associated with the stretching vibrations of Cr-O bonds of crystalline α-Cr_2O_3, in agreement with previous data,[1, 7, 43, 44] and have been attributed to fundamental infrared-active vibrations, corresponding to the E_4, E_3, and E_2 modes respectively.[42]

Further investigation of the optical properties of the nanowires was conducted via UV-visible spectroscopy (Figure 4.4B). In order to collect the spectrum, the nanowires were dispersed into water, prior to data acquisition. While the spectrum presented in Figure 4.4B is clearly dominated by a broad feature, there are noticeable shoulder peaks located at 378, 472, and 591 nm, respectively. These values correspond reasonably well with those reported in prior literature for chromium oxide species.[26, 45-47] The peak centered around 378 nm has been previously associated with either Cr^{4+} ions[47] or with the O-Cr^{6+} charge transfer transition of chromate species with tetrahedrally coordinated Cr^{6+} ions,[45] suggesting the potential presence of these ions within the Cr_2O_3 nanostructures we have synthesized. The two remaining peaks centered around 472 and 591 nm have been assigned to the intrinsic $^4A_{2g} \rightarrow {}^4T_{1g}$ and the $^4A_{2g} \rightarrow {}^4T_{2g}$ transitions of Cr^{3+} ions, maintaining a six-coordinate geometry and octahedral symmetry, respectively.[26] Further spectral data obtained by dispersing the nanostructures in ethanol, DMF, and cyclohexane, respectively, at various nanowire concentrations, were similarly broadened, an observation which has been previously ascribed to (i) light scattering due to the relatively large size of the nanowires, (ii) the relatively low inherent solubility of the product, and (iii) solvent dipole effects.[48] Furthermore, it is important to note here that the UV-visible spectra were obtained utilizing physical suspensions of nanowires, as opposed to true, optically transparent solutions of completely solubilized nanowires.

Raman investigation of the nanowires, shown in Figure 4.4C, reveals several distinctive peaks for our chromium oxide nanowires. More specifically, peaks present at 315, 355, 556 and 612 cm^{-1} are consistent with both our bulk data (Figure 4.4D) as well as with values reported in the literature.[49] In fact, the most intense peak centered around 556 cm^{-1} has been attributed to a

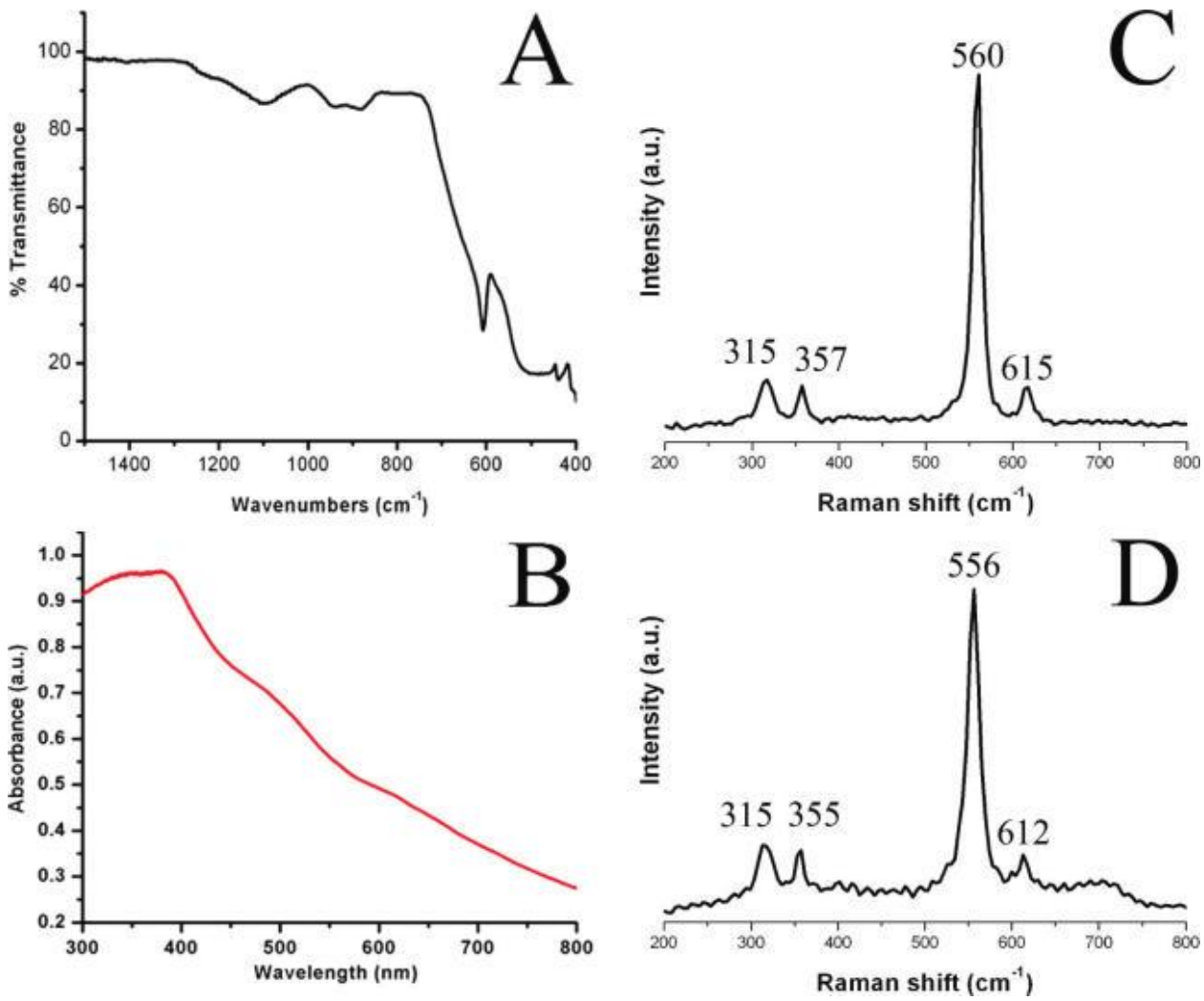

Figure 4.4: A) Infrared data and B) corresponding UV-visible spectrum of Cr_2O_3 nanowires. Raman spectrum of C) bulk Cr_2O_3 and of D) Cr_2O_3 nanowires.

vibrational mode of A_{1g} symmetry, whereas all remaining, noticeable peaks can be attributed to E_g symmetry.[49, 50]

In order to explore the electronic properties of our nanomaterials, we measured the current vs. voltage (I-V) characteristics of our nanowires at various temperatures in the range of 4 to 300 K. Figure 4.5 plots the conductance vs. temperature between ~50 and 300 K. A thermal activation conductance of the form, $\sigma \propto \exp(-E_A/k_BT)$, wherein E_A is the activation energy and k_B is the Boltzmann constant, does not fit well with the data acquired from nanowire A (black squares). Instead, the data for both nanowires fit well with the general hopping form, i.e. $\sigma \propto \exp(T_0/T)^n$. As a reference, data have been plotted using $n = ½$, which is the expected exponent for variable-range hopping in 1D materials.[51] However, due to the limited variation of the conductance in this temperature range, there is a large uncertainty in the value of the exponent. Furthermore, additional detailed measurements are required in order to more clearly identify the kind of hopping conduction mechanism present within these nanowires.

The lower inset of Figure 4.5 shows that upon cooling to 4 K, the conductance in the nanowires no longer fits with the data from higher temperatures, indicating the presence of two distinctive modes of electron conduction, i.e. one for above ~50 K and one for below. This temperature-dependent conductivity behavior down to approximately 50 K has been previously ascribed to the presence of a hopping mechanism for electrons between the Cr^{3+} and Cr^{2+} oxidation states, perhaps attributable to the formation of ferromagnetic spinel Cr_3O_4 impurities.[52] While this explanation may be valid for our system, another option we will delve into more deeply in later sections to account for the observed data is the possibility of uncompensated surface spins. Nevertheless, previous studies on both thin film and bulk chromium oxide systems have yielded similar results, though the inflection point in the transition temperature was closer

to ~200 K as opposed to 50 K found here in our study.[52, 53] It may also be noteworthy that no magnetoresistance was observed at 4 K in these nanowires for fields of up to 1 T in magnitude.

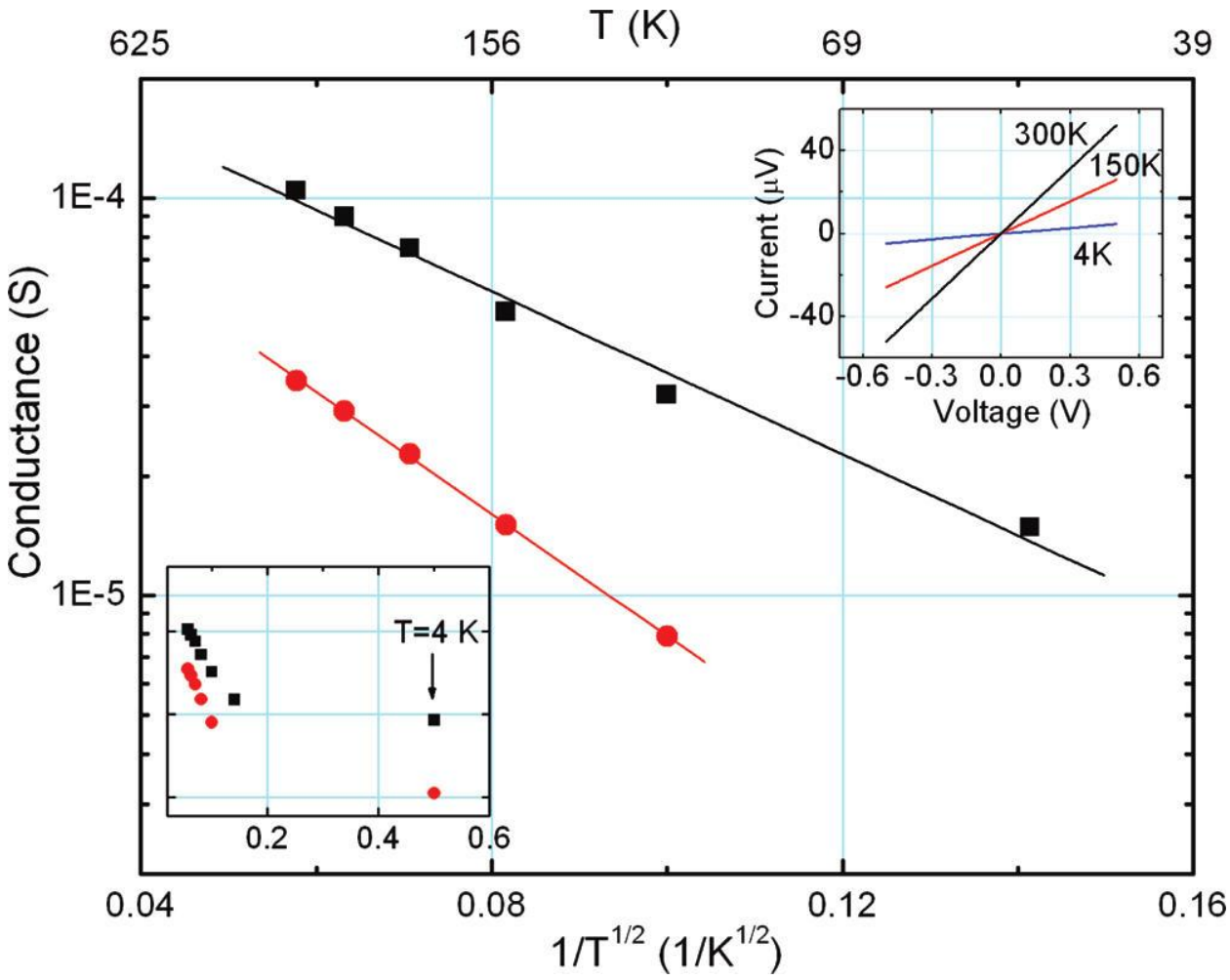

Figure 4.5: Temperature dependence of the conductance from ~50 to 300 K for two nanowires: A (black squares) and B (red dots). Solid lines are fits to the form of $\sigma \propto \exp(T_0/T)^{1/2}$. Top inset: Current-voltage curves measured at three temperatures for nanowire A (nanowire B showed similar results). Bottom inset: Same as main graph but including points measured at 4 K. The graph shows the onset of a distinctive transport mechanism for temperatures below 50 K.

4.6 Magnetic Measurements

The results of magnetization measurements are summarized in Figure 4.6. The zero-field cooled (ZFC) and field cooled (FC) magnetizations measured at an applied magnetic field of 500 Oe coincide at high temperatures (Figure 4.6A) but separate below the blocking temperature of about 290 K. While antiferromagnetic order has been first observed in bulk Cr_2O_3 at its Néel temperature of 308 K, there is no sign of either a peak or slope change in the magnetization that would identify T_N in our Cr_2O_3 nanowires. This is not unexpected, since there is only a ~10% reduction of T_N to 270 K in spherical 7.8 nm nanoparticles,[54] where finite size effects may play a much more profound role than, for instance, in our 179 nm nanowires. The TEM images of our nanowires indicates the presence of substructure, but the large magnitude of the blocking temperature, T_B, which is normally linearly proportional to the nanoparticle volume, indicates that the length scale controlling the magnetic behavior is much larger in our samples than in either 15 nm nanoparticles (T_B = 160 K)[38] or 7.8 nm nanoparticles (T_B = 28 K).[54]

The field-dependent magnetization measured at 10, 150, and 320 K is consistent with the presence of a composite magnetic structure within the nanowires, consisting of (i) unsaturated moments which lead to the linear, paramagnetic contribution to the magnetization (Figure 4.6B) and (ii) saturated moments, which can yield a closed ferromagnetic loop with a nonzero coercive field below the blocking temperature (Figure 4.6C). Such magnetic behavior can be explained by the presence of uncompensated spins at the surfaces of Cr_2O_3 nanowires, as has been previously reported for Cr_2O_3 nanoparticles.[14, 15, 37, 38] In nanostructures, the uncompensated surface spins possess a lower coordination number. Therefore, a net magnetic moment can be induced on the surfaces of either nominally nonmagnetic nanowires or antiferromagnetic nanoparticles.[55-57]

To further probe the effect of the surface spins, we have tested for the possibility of an exchange bias effect in Cr_2O_3 nanowires.[58, 59] Conventionally, the exchange bias effect can be observed in composite nanostructures simultaneously possessing both ferromagnetic (FM) and antiferromagnetic (AFM) components with a common interface, such as in ferromagnetic-core/antiferromagnetic-shell nanoparticles.[59, 60] In these nanostructures, the exchange interactions between the FM and AFM components can lead to a shift of the hysteresis loop along the field axis, once the system has been field cooled. The absolute value of the loop shift is known as the exchange bias field, $\mathbf{H}_{EB}$.

Such a nonzero exchange bias field can also be observed in single phase nanostructures, including in Cr_2O_3 nanoparticles.[15, 38] In the case of antiferromagnetic nanoparticles, the exchange bias field would be a result of the exchange interactions between uncompensated surface spins, which play the role of the FM domain, and the AFM core interior of the nanoparticle. As such, we measured the hysteresis loop of Cr_2O_3 nanowires at 10 K, after cooling down from 350 K in an applied field of 50 kOe, and compared our data with zero-field data (Figure 4.6D). An apparent shift of the FC hysteresis loop is clearly observed with H_{EB} = 60 Oe. This value is much smaller than those reported for Cr_2O_3 nanoparticles.[38, 54] It is possible that there is an element of disorder in the interface between the antiferromagnetic core and the uncompensated surface moments. Alternatively, the thickness of the surface layer is very small, and the exchange coupling to the antiferromagnetic core may simply be too large to allow for the independent reorientation of the shell that lies at the heart of the exchange bias effect. Finally, we cannot rule out the possibility that we are not observing an exchange bias effect at all but rather

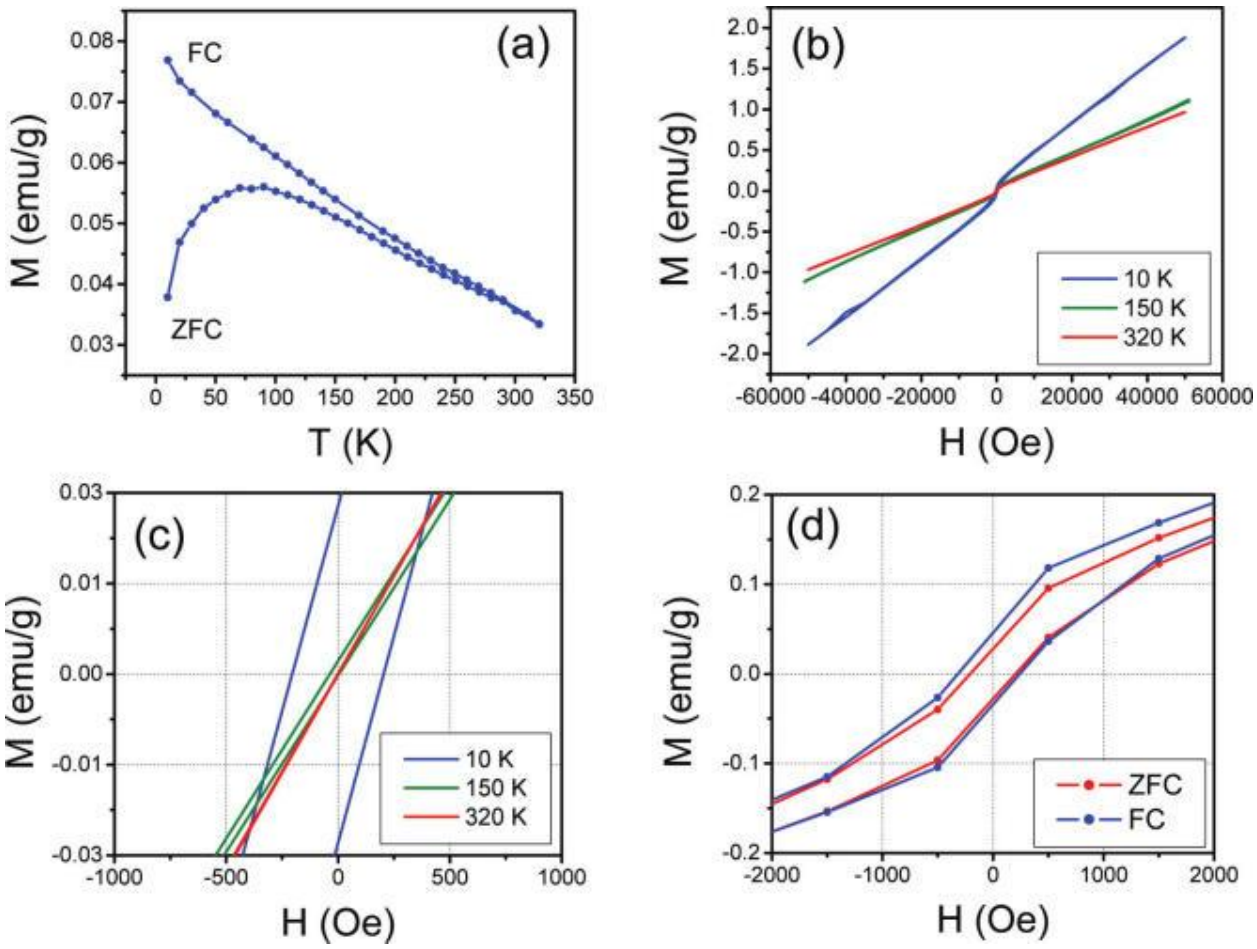

Figure 4.6: A) Temperature dependence of FC and ZFC magnetizations at an applied field of 500 Oe; B) the magnetic field dependence of magnetization at 10, 150, and 320 K; C) identical to (B) but obtained at low magnetic fields; D) magnetic field dependencies of ZFC and FC magnetizations taken at 10 K. The FC magnetization was obtained by cooling the sample from 350 to 10 K at an applied magnetic field of 50 kOe.

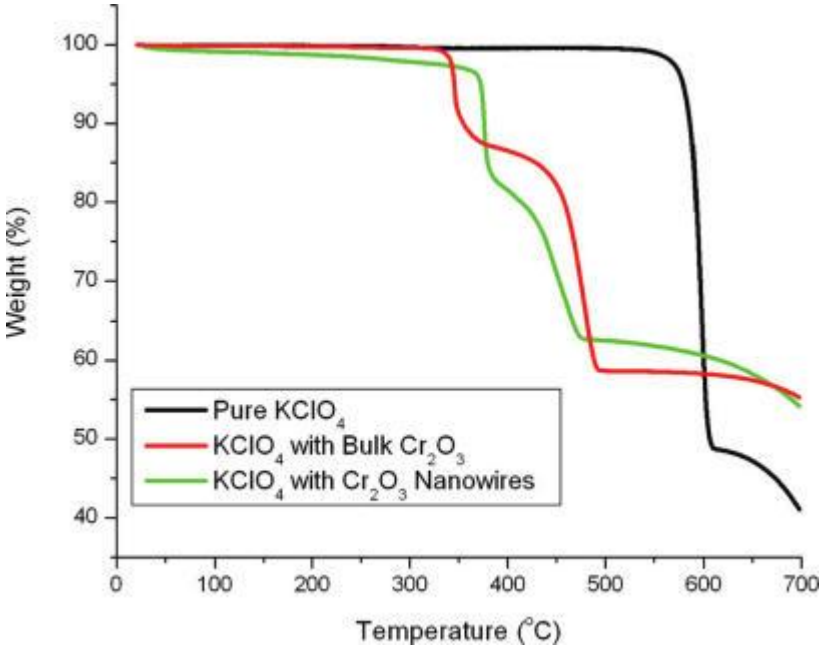

Figure 4.7: Thermal decomposition of pure $KClO_4$ (black), $KClO_4$ in the presence of bulk Cr_2O_3 (red), and $KClO_4$ in the presence of Cr_2O_3 nanowires (green).

the formation of an antiferromagnetic substructure in an antiferromagnetic particle, as has been observed in other systems such as NiO.[57, 61] We conclude that the magnetism of these Cr_2O_3 nanowires has all the complexity and subtlety expected of a nanoparticle system. The overall promise of this system for combined electronic and magnetic functionality renders it pressing to carry out thorough parametric studies with the goal of determining the fundamental limits of these behaviors.

4.7 Effect of Cr_2O_3 on the Thermal Decomposition of $KClO_4$

We have explored the use of our Cr_2O_3 nanowires as a catalyst for the degradation of $KClO_4$ into KCl and oxygen at elevated temperatures. It has been shown previously that chromium oxide can effectively lower the decomposition temperature of $KClO_4$, by favoring certain novel mechanistic pathways, such as the enhanced removal of oxygen from $KClO_4$, owing to its *p-n* nature, as well as, its high electronegativity.[62] As such, Figure 4.7 shows individual TGA plots of the decomposition of pure $KClO_4$, as well as of $KClO_4$ mixed with bulk Cr_2O_3 and with our Cr_2O_3 nanowires. We have found that both our nanowires and the bulk chromium oxide induce decomposition at lower temperatures, as compared with pure $KClO_4$ alone. Furthermore, the shoulder present in the data corresponding to both the bulk and nanowire systems can be attributed to the formation of $K_2Cr_2O_7$, whereas the small hump present near the tail of the TGA plot can be ascribed to the production of KCl salt.[62]

4.8 Conclusions

In this work, we have successfully synthesized 1D Cr_2O_3 nanowires via a template mediated sol-gel technique. The resulting nanowires are crystallographically pure and consist of smaller constituent nanoparticles that appear to be fused together so as to form a hierarchical 1D motif. The key point is that this high-yield, low-waste synthetic method is a distinctive

improvement over previous synthetic efforts in that (i) we do not require the use of either specialized or inert gases; (ii) we do not necessitate any particular high-temperature annealing treatment; (iii) our reaction times are reasonably rapid (<1 hour); and (iv) our precursors do not involve hydrazine, supercritical fluids, or any particularly hazardous reaction conditions.

We have explored both the magnetic and electronic properties of these nanowires. From the former, we can conclude that uncompensated surface spins coupled by the exchange interactions to the interior of the nanowires play a dominant role in the magnetic properties of the Cr_2O_3 nanostructures. From the latter, it was evident that the nanostructures evinced temperature-dependent conductivity trends, analogous to what has been observed for bulk and thin film analogues. Moreover, we have shown that the addition of our chromium oxide nanowires to a model compound, $KClO_4$, effectively induced its decomposition at a much lower temperature, as compared with its pure, un-catalyzed form.

4.9 References

1. M. Ocaña, *Journal of the European Ceramic Society*, 2001, **21**, 931-939.
2. D.-W. Kim, S.-I. Shin, J.-D. Lee and S.-G. Oh, *Materials Letters*, 2004, **58**, 1894-1898.
3. B. Bhushan, G. S. A. M. Theunissen and X. Li, *Thin Solid Films*, 1997, **311**, 67-80.
4. M. Chatterjee, B. Siladitya and D. Ganguli, *Materials Letters*, 1995, **25**, 261-263.
5. T. Tsuzuki and P. G. McCormick, *Acta Materialia*, 2000, **48**, 2795-2801.
6. S. Music, M. Maljkovic, S. Popovic and R. Trojko, *Croatica Chemica Acta*, 1999, **72**, 789.
7. L. Znaidi and C. Pommier, *European Journal of Solid State and Inorganic Chemistry*, **35**, 405-417.
8. W. A. Lazier and J. V. Vaughen, *Journal of the American Chemical Society*, 1932, **54**, 3080-3095.
9. B. M. Weckhuysen and R. A. Schoonheydt, *Catalysis Today*, 1999, **51**, 223-232.
10. B. Grzybowska, J. Sloczynski, R. Grabowski, L. Keromnes, K. Wcislo and T. Bobinska, *Applied Catalysis A: General*, 2001, **209**, 279-289.
11. H. Thakuria, B. M. Borah and G. Das, *Journal of Molecular Catalysis A: Chemical*, 2007, **274**, 1-10.
12. C. M. Pradier, F. Rodrigues, P. Marcus, M. V. Landau, M. L. Kaliya, A. Gutman and M. Herskowitz, *Applied Catalysis B: Environmental*, 2000, **27**, 73-85.
13. H. Cao, X. Qiu, Y. Liang, M. Zhao and Q. Zhu, *Sol-gel synthesis and photoluminescence of p-journal article semiconductor Cr2O3 nanowires*, AIP, 2006.

14. M. Banobre-Lopez, C. Vazquez-Vazquez, J. Rivas and M. A. Lopez-Qunitela, *Nanotechnology*, 2003, **14**, 318.
15. W. S. Zhang, E. Brück, Z. D. Zhang, O. Tegus, W. F. Li, P. Z. Si, D. Y. Geng and K. H. J. Buschow, *Physica B: Condensed Matter*, 2005, **358**, 332-338.
16. S. Foner, *Physical Review*, 1963, **130**, 183.
17. D. Vollath, D. V. Szabó and J. O. Willis, *Materials Letters*, 1996, **29**, 271-279.
18. R. L. Burwell and H. S. Taylor, *Journal of the American Chemical Society*, 1936, **58**, 697-705.
19. S. Pokhrel, C. E. Simion, V. Quemener, N. Bârsan and U. Weimar, *Sensors and Actuators B: Chemical*, 2008, **133**, 78-83.
20. X. Liang, T. Zhong, H. Guan, F. Liu, G. Lu and B. Quan, *Sensors and Actuators B: Chemical*, 2009, **136**, 479-483.
21. U. Balachandran, R. W. Siegel, Y. X. Liao and T. R. Askew, *Nanostructured Materials*, **5**, 505-512.
22. Z. Pei, H. Xu and Y. Zhang, *Journal of Alloys and Compounds*, 2009, **468**, L5-L8.
23. Z. Pei and Y. Zhang, *Materials Letters*, 2008, **62**, 504-506.
24. M. Abecassis-Wolfovich, H. Rotter, M. V. Landau, E. Korin, A. I. Erenburg, D. Mogilyansky and E. Gartstein, *Journal of Non-Crystalline Solids*, 2003, **318**, 95-111.
25. A. E. Gash, T. M. Tillotson, J. H. Satcher Jr, L. W. Hrubesh and R. L. Simpson, *Journal of Non-Crystalline Solids*, 2001, **285**, 22-28.
26. Li, Z. F. Yan, G. Q. Lu and Z. H. Zhu, *The Journal of Physical Chemistry B*, 2005, **110**, 178-183.
27. Z. Gui, R. Fan, W. Mo, X. Chen, L. Yang and Y. Hu, *Materials Research Bulletin*, 2003, **38**, 169-176.
28. Z. C. Zhong, R. H. Cheng, J. Bosley, P. A. Dowben and D. J. Sellmyer, *Applied Surface Science*, 2001, **181**, 196-200.
29. G. Peters, K. Jerg and B. Schramm, *Materials Chemistry and Physics*, 1998, **55**, 197-201.
30. N. A. Dhas, Y. Koltypin and A. Gedanken, *Chemistry of Materials*, 1997, **9**, 3159-3163.
31. W.-Q. Han, L. Wu, A. Stein, Y. Zhu, J. Misewich and J. Warren, *Angewandte Chemie International Edition*, 2006, **45**, 6554-6558.
32. J. Wang, J. Sun and X. Bian, *Modelling, Measurement & Control, C: Energetics, Chemistry & Chemical Engineering, Earth, Resources, Environment, Biomedical Problems*, 2004, **65**, 47.
33. Z. Yu-Feng, L. Zheng-Song and C. Qian-Wang, *Chininese Journal of Inorganic Chemistry*, 2004, **20**, 971.
34. B. Tian, X. Liu, H. Yang, S. Xie, C. Yu, B. Tu and D. Zhao, *Advanced Materials*, 2003, **15**, 1370-1374.
35. C. Dickinson, W. Zhou, R. P. Hodgkins, Shi, Zhao and He, *Chemistry of Materials*, 2006, **18**, 3088-3095.
36. A. Guimin and et al., *Nanotechnology*, 2008, **19**, 035504.
37. C. Vázquez-Vázquez, M. Bañobre-López, M. A. López-Quintela, L. E. Hueso and J. J. Rivas, *Journal of Magnetism and Magnetic Materials*, 2004, **272-276**, 1547-1548.
38. S. A. S. A. Makhlouf, *Journal of Magnetism and Magnetic Materials*, 2004, **272-276**, 1530-1532.

39. C. Schönenberger, B. M. I. van der Zande, L. G. J. Fokkink, M. Henny, C. Schmid, M. Krüger, A. Bachtold, R. Huber, H. Birk and U. Staufer, *The Journal of Physical Chemistry B*, 1997, **101**, 5497-5505.
40. M. Tian, J. Wang, J. Kurtz, T. E. Mallouk and M. H. W. Chan, *Nano Letters*, 2003, **3**, 919-923.
41. Y. Mao, M. Kanungo, T. Hemraj-Benny and S. S. Wong, *The Journal of Physical Chemistry B*, 2005, **110**, 702-710.
42. P. Ratnasamy and A. J. Leonard, *The Journal of Physical Chemistry*, 1972, **76**, 1838-1843.
43. G. An, Y. Zhang, Z. Liu, Z. Miao, B. Han, S. Miao and J. Li, *Nanotechnology*, 2008, **19**, 035504/035501.
44. N. T. McDevitt and W. L. Baun, *Spectrochimica Acta*, 1964, **20**, 799-808.
45. H. Li, Y. Yue, C. Miao, Z. Xie, W. Hua and Z. Gao, *Chinese Journal of Catalysis*, 2006, **27**, 4-6.
46. B. M. Weckhuysen, I. E. Wachs and R. A. Schoonheydt, *Chemical Reviews*, 1996, **96**, 3327-3350.
47. L. D. Zhang, C. M. Mo, W. L. Cai and G. Chen, *Nanostructured Materials*, 1997, **9**, 563-566.
48. H. H. Willard, L. L. Merritt and J. A. Dean, *Instrumental methods of analysis*, D. Van Nostrand Company, Inc., 1965.
49. C. Lin, P. Shen and S. Chen, *Applied Physics B: Lasers and Optics*, 2010, **98**, 443-450.
50. J. Mougin, T. Le Bihan and G. Lucazeau, *Journal of Physics and Chemistry of Solids*, 2001, **62**, 553-563.
51. N. F. Mott and E. A. Davis, *Electronic Process in Non-Crystalline Materials*, 1979.
52. P. Borisov, A. Hochstrat, V. V. Shvartsman, W. Kleemann, T. Eimüller and A. F. RodrÍguez, *Ferroelectrics*, 2008, **370**, 147-152.
53. C.-S. Cheng, H. Gomi and H. Sakata, *physica status solidi (a)*, 1996, **155**, 417-425.
54. D. Tobia, E. L. Winkler, R. D. Zysler, M. Granada and H. E. Troiani, *Journal of Alloys and Compounds*, 2010, **495**, 520-523.
55. M. P. Morales and et al., *Journal of Physics: Condensed Matter*, 1997, **9**, 5461.
56. X. Teng, M. Feygenson, Q. Wang, J. He, W. Du, A. I. Frenkel, W. Han and M. Aronson, *Nano Letters*, 2009, **9**, 3177-3184.
57. M. Feygenson, A. Kou, L. E. Kreno, A. L. Tiano, J. M. Patete, F. Zhang, M. S. Kim, V. Solovyov, S. S. Wong and M. C. Aronson, *Physical Review B*, 2010, **81**, 014420.
58. J. Nogués and I. K. Schuller, *Journal of Magnetism and Magnetic Materials*, 1999, **192**, 203-232.
59. J. Nogués, J. Sort, V. Langlais, V. Skumryev, S. Suriñach, J. S. Muñoz and M. D. Baró, *Physics Reports*, 2005, **422**, 65-117.
60. S. E. Inderhees, J. A. Borchers, K. S. Green, M. S. Kim, K. Sun, G. L. Strycker and M. C. Aronson, *Physical Review Letters*, 2008, **101**, 117202.
61. R. H. Kodama, S. A. Makhlouf and A. E. Berkowitz, *Physical Review Letters*, 1997, **79**, 1393.
62. A. A. Said, E. A. Hassan and K. M. Abd El-Salaam, *Surface Technology*, 1983, **20**, 131-137.

Chapter 5. Correlating Titania Morphology and Chemical Composition with Dye-Sensitized Solar Cell Performance.

5.1 Introduction

All preceding chapters have been more focused on the synthesis of novel nanoscale materials, and the exploration of their nanoscale properties. By contrast with these previous chapters, we will now explore the application of various morphologies of TiO_2 nanostructures in dye sensitized solar cells (DSSCs). Herein, we will focus on the device applications of the solar cells, as opposed to the synthesis of a particular nanomaterial.

With the growing demand for energy, as well as the necessity to stem an increase in CO_2 emissions, the need to develop clean, renewable sources of energy is becoming more and more crucial. Of all renewable energy sources, solar energy in particular holds the possibility of addressing this energy concern, as it can provide an average of ~120 000 TW of power a day to the Earth's surface. However, despite this promising fact, the relatively high production cost of conventional solar cells has resulted in a severe limitation to their widespread commercialization.[1] The fabrication of DSSCs is of particular interest, owing to their potential to be an inexpensive alternative to traditional Si-based solar cells.[2] However, these types of solar cells maintain efficiencies of only 11-13%, which are considerably lower than what is considered to be acceptable for most conventional cells.[3] It is, therefore, imperative that additional research be conducted in order to more fully understand basic design issues of DSSCs and to subsequently rationally enhance their performance.

DSSCs generally consist of four components, working together in a delicate balance so as to produce a functional system. These four components include: (i) the sensitizing dye, (ii) the

electrolyte or hole-conductor, (iii) the counter electrode, and (iv) the porous semiconducting film. Each of these individual components has received significant research attention in recent years, resulting in a better and more fundamental understanding of how DSSCs function at a basic level. The basic principle behind DSSCs is the same as that for all other solar cells, i.e. solar irradiation is utilized to excite a material and, after separation of the excited state into electrons and holes, electrons are put to work in an external circuit. However, the execution of this fundamental process is slightly different in DSSCs, as compared with Si and organic solar cells. Specifically, a dye attached to an electron conducting metal oxide (e.g. TiO_2, ZnO, Nb_2O_5) is excited via solar illumination. Subsequently, electron transfer occurs from the lowest un-occupied molecular orbital (LUMO) of the dye to the conduction band of the metal oxide material. The electron then proceeds through the metal oxide material, via a random walk path, until it reaches the transparent conducting oxide (TCO) layer. At the TCO/metal oxide interface, the charge is then transferred to the TCO layer, where it subsequently proceeds through an external circuit to do work. This charge then re-enters the solar cell at the counter electrode, where it recombines with the holes that have diffused through a liquid electrolyte to the counter electrode. This process is visualized via a schematic drawing, shown in Figure 5.1.

First, the selection of dye has been rationally explored with the hope of increasing the overall utilization of the solar spectrum and, in turn, the efficiency of the solar cell. There have been several promising dyes developed over the years. These contain metal centers of ruthenium,[4, 5] osmium,[6, 7] iron,[8] and zinc.[9, 10] However, transition metal-free dyes, such as tetrathiafulvalene, 3-{5-[*N*,*N*-bis(9,9-dimethylfluorene-2-yl)phenyl]-thiophene-2-yl}-2-cyano-

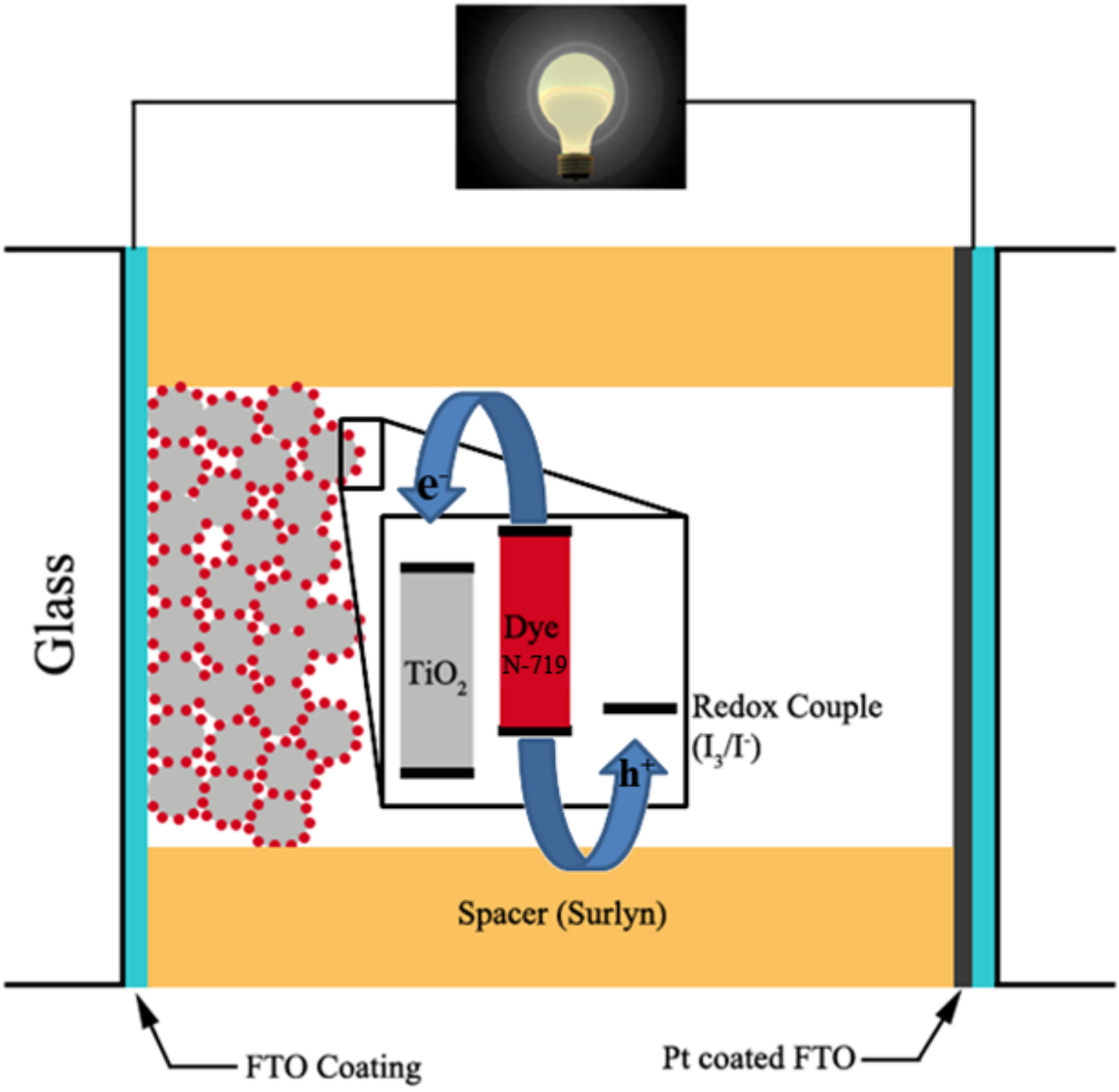

Figure 5.1: Schematic representation of a DSSC.

acrylic acid, and coumarin derivatives have also been of keen research interest in recent years.[11-13] A recent review by Hagfeldt et al.[14] has extensively analyzed the advantages and disadvantages of many different dyes for applications in DSSCs. In addition, complementary work by Ding et al.[15] further highlights the application of plasmon enhanced absorption as a means of increasing light absorption as well as light scattering within the solar cell.

Second, recent research into the application of either different electrolytes or hole conductors has resulted in the development of many interesting materials. Indeed, optimizing the electrolyte has involved efforts aimed at reducing the light absorbed by the electrolyte, through the application of colorless electrolytes, as well as utilizing redox couples with different potentials, such as Ni or Co-based molecules, for better matching with a wider variety of dyes.[16-19] Specifically, much research has focused on the utilization of either gelled electrolytes, utilizing amino acid derivatives as gelation agents, or solid hole conductors such as polysiloxane in order to create a semi-solid material.[20, 21] Nevertheless, the efficiencies of these solar cells become limited by the lower decreased diffusion rates of the redox couples within the semi-solid material, thereby resulting in an overall lower efficiency as compared with traditional liquid electrolytes. In order to effectively alleviate the diffusion limitation in these types of solar cells, the use of several types of solid hole-conducting materials has been reported, including organic polymers, such as poly(3,4-ethylenedioxythiophene) (PEDOT),[22] poly-3-hexylthiophene (P3HT),[23] and 2,2,7,7-tetrakis(N,N-di- *p*-methoxyphenylamine)-9,9-spirobifluorene (spiro-MeOTAD),[24] as well as spiro-MeOTAD-like materials.[25] In addition to these polymeric materials, several studies have also revealed the possibility of several promising inorganic *p*-type materials, such as CuI,[26] CuSCN,[2, 27] and NiO.[28]

The third component of DSSCs, which has received slightly less attention in recent years, is the counter electrode. Conventionally, the use of an iodide/ tri-iodide redox couple has limited the range of applicable materials for the counter electrode to either Pt or carbon, since both of these materials exhibit a catalytic propensity towards the iodide/tri-iodide reaction.[29-32] However, recent research has shown that both PEDOT[33] and CoS[34] have been successfully utilized as the counter electrode material in conjunction with the iodide/tri-iodide electrolyte.

The fourth component of DSSCs, and the area which we intend to further optimize, is the semiconducting layer. There has been rigorous research interest aimed at optimizing the structure of the semiconducting layer, in an attempt to increase the efficiency of the solar cells, such as through altering the morphology of the semiconducting material[35-41] or by modifying the nature of the metal oxide itself.[42-44] It has been shown in previous work that the conduction of electrons in the nanoparticulate metal oxide layer proceeds via a random walk process.[45] In light of this fact, there has been recent research interest in utilizing metal oxide nanostructures possessing 1D nanoscale morphology for their potential ability to increase the nature of electron conduction through the metal oxide film. In particular, the anisotropic nature of 1D materials introduces a degree of directionality into the film, which would effectively decrease the number of undesirable intergrain boundaries and, not surprisingly, allow for a more direct pathway for photogenerated electrons to reach the conductive glass electrode.

For example, zinc oxide nanowires have displayed a ten-fold enhancement in electron mobility of 1 $cm^2 V^{-1} s^{-1}$, when compared with corresponding nanoparticulate analogs (0.01 $cm^2 V^{-1} s^{-1}$) as a result of their anisotropic nature, which allows for the creation of spatial channels for the electrons to traverse.[46] Despite this tangible improvement in conductivity, the use of solely 1D materials can result in a reduction of overall surface area by comparison with 0D structures,

which can therefore lead to lower dye loading and, consequently, less absorbed light as well as a correspondingly lower photocurrent.[36, 38, 39, 47, 48] Therefore, while these applications of 1D materials are clearly beneficial to electron conduction, the loss of absorbed light generally outweighs any potential advantages gained from increased charge collection, ultimately resulting in a lower solar cell efficiency. In order to combine the idea of directionality associated with the 1D nanoscale materials with the favorable high surface area of 0D nanoparticulate films, two approaches have been investigated in the literature.

In the first approach, nanoparticles and nanowires have been mixed together within the same paste, thereby combining the advantages of the high surface area of nanoparticles with that of the inherent anisotropic directionality of the 1D materials.[39, 49-51] In a second approach, anodized TiO_2 nanotube arrays have been utilized in the fabrication of conventional DSSCs, which have incorporated traditional dyes with an iodine/tri-iodide electrolyte. The rational use of these arrays combines the inherent advantages of a 1D morphology with those of a well-ordered periodic structure.[36, 47, 48, 52-60] While these methods have displayed promising results, there has not been any systematic exploration of the effect of semiconductor morphology including 0D, 1D, and 3D nanostructured motifs upon the corresponding device efficiency.

Thus, the focus herein involves the systematic modification of the porous semiconducting layer so as to include highly crystalline nanostructures possessing a wide range of structures and sizes in order to rationally explore the effect of the semiconductor morphology on the corresponding device parameters. More specifically, it is through reproducible manipulation of the morphology of the semiconducting layer with which we intend to observe its specific effect upon electron transport capabilities as well as dye adsorption properties. Several groups have

attempted a similar strategy to mitigate the loss of accessible surface area through the utilization of different structural morphologies,[39, 49-51] such as hierarchical structures.[61-63]

As shown above, the idea of tailoring the morphology of TiO_2 is not novel in and of itself. However, we explore the purposeful application of titania materials unique to our lab. Specifically, in this report, we demonstrate the applicability of three different morphologies of TiO_2, including nanoparticles, nanowires, and 3D sea-urchin-like motifs, that have been previously synthesized by our group.[64] Through the application of these morphologies, we intend to incorporate the advantageous electron transport characteristics of one-dimensional nanostructures into the film, without any detrimental loss in surface area.[65] We have systematically investigated the effect of our morphologies on four key solar cell parameters, namely open circuit voltage (V_{OC}), short circuit current density (J_{SC}), fill factor (FF), and efficiency (η). These parameters are defined as follows.

V_{OC} corresponds to the voltage at which the solar cell produces no current, and is determined from the *x*-intercept of the current density vs. voltage (J-V) curves of the solar cells. The J_{SC} for a solar cell is the current drawn out of a cell when no voltage is applied, and is determined from the *y*-intercept of the J-V curves of the solar cells. The FF of a solar cell is an ideality factor which determines the ratio between the point at which maximum power is produced (e.g. V_{Max} = Voltage at maximum power point, J_{Max} = Current density at the maximum power point) by the solar cell and the corresponding J_{SC} and V_{OC} values. This FF value is calculated from Equation 1. Finally, the η of the solar cell is computed by means of Equation 2, where P_{In} denotes the power incident upon the solar cell which is generally 100 mA/cm^2, and determines the amount of power generated by the solar cell, by comparison with the amount of power actually supplied to the solar cell.

$$FF = (V_{Max})(J_{Max})/(V_{OC})(J_{SC}) \quad (1)$$

$$\eta = (J_{SC})(V_{OC})(FF)/(P_{In}) \quad (2)$$

Furthermore, we have compared these values with the corresponding data associated with three commercially available materials, including Degussa P25, Aldrich (<25 nm) nanoparticles, as well as Nanostructured and Amorphous Materials (5 nm) nanoparticles.

We also have utilized the technique of open circuit voltage decay (OCVD) in order to probe the electron lifetimes within our cells. These various analytical measurements have been utilized in order to more precisely track the trend associated with a systematic alteration of the TiO_2 morphology. Importantly, we should state that we most certainly could have altered parameters such as the nature of the electrolyte, the composition of the dye, the semiconducting layer thickness, as well as the use of a titanium chloride ($TiCl_4$) treatment in order to more fully optimize our solar cell performance, and thereby obtain higher measured efficiencies. However, that was not our objective. In fact, in this Chapter, we deliberately chose to more carefully isolate the precise effect of morphology in order to draw forth direct and reasonably unambiguous comparisons amongst the various TiO_2 structural motifs probed under otherwise identical experimental conditions.

5.2 Solar Cell Preparation

Various morphologies of TiO_2 have been synthesized, as previously reported in our group.[64, 66, 67] Pastes of these materials have also been prepared, as described in prior work.[67] Briefly, pastes were fabricated by grinding the desired powder in the presence of dilute acetic acid (pH = 2– 3) using a mortar and pestle. To further assist in nanostructure dispersion and coating of the fluorine-doped tin oxide (FTO) glass (Pilkington TEC7), several drops of the

surfactant Triton X-100 (EM Industries) were added to the paste and carefully mixed in, by grinding. These pastes were subsequently stored in sealed vials under ambient conditions, until needed. Prior to use, these pastes were sonicated for several minutes so as to ensure complete dispersion of the nanoparticles in the paste. The active area of the solar cell was fabricated by masking a portion of the FTO (Pilkington TEC 7 glass) with a piece of tape (Scotch® Brand Gloss Finish MultiTask Tape), modified by a 0.25" diameter (0.317 cm^2) hole. The desired paste was then applied using the doctor blade technique and allowed to dry for several minutes under ambient conditions, prior to removal of the tape. After tape removal, the film was sintered at 400°C for 30 min. This application process was repeated, as necessary, in order to obtain the desired film thickness, which was generally ~10 μm. The films were then sensitized by immersion into a 0.3 mM solution of di-tetrabutylammonium cis-bis(isothiocyanato) bis(2,2_-bipyridyl-4,4_-dicarboxylato) ruthenium(II) (N719, Solaronix) in a mixture, containing acetonitrile and tert-butanol in a 1:1 volume ratio.

To ensure complete adsorption, the films were immersed in solution while still warm (~80°C), and were left, as such, for a minimum of 24 h. It should be noted here that immersion for times longer than 24 h did not result in any significant increase in dye adsorption. Upon removal of the film from the dye solution, it was thoroughly washed with water and ethanol, and subsequently dried in air. The cell was then sealed using a 25 μm thick hot melt spacer (Solaronix Meltonix 1170-25) using a pre-drilled piece of FTO, coated with Pt, as previously reported.[67] The cell was then heated on a hot plate with pressure applied to order to fully seal the cell. The electrolyte we used consisted of 0.6 M tetra-butyl ammonium iodide (TBAI, Aldrich), 0.04 M iodine (99.999%, Fisher Scientific), 0.025 M lithium iodide (LiI, 99.9% Aldrich), 0.05 M guanidinium thiocyanate (>99%, Aldrich), and 0.28 M tert-butyl pyridine (96%, Aldrich) in a

85: 15 vol: vol % solution of acetonitrile (extra dry, EMD) and valeronitrile (99.5%, Aldrich). The electrolyte was then introduced into the cell through the pre-drilled hole in the counter electrode through vacuum backfilling. Finally, the hole was sealed using a piece of hot melt spacer and a piece of aluminum foil.

5.3 Solar Cell and Morphological Characterization

Open circuit voltage decay (OCVD) measurements were performed on the solar cells by illuminating them under steady state conditions with AM 1.5 light. Subsequently, the light was turned off and the voltage decay was monitored as a function of time. Electron lifetimes were determined using a derivative of the decay transient measurement.[68] Powder X-ray diffraction measurements (XRD) were conducted using a Scintag diffractometer in the Bragg–Brentano configuration with Cu Kα (λ = 1.54 Å) irradiation from $20° \leq 2\theta \leq 70°$ at a scanning rate of 2° in 2θ min^{-1}. Powder diffraction samples were prepared by rendering the dried powders into slurries in ethanol after sonication for several minutes. The slurries were then air dried onto glass slides.

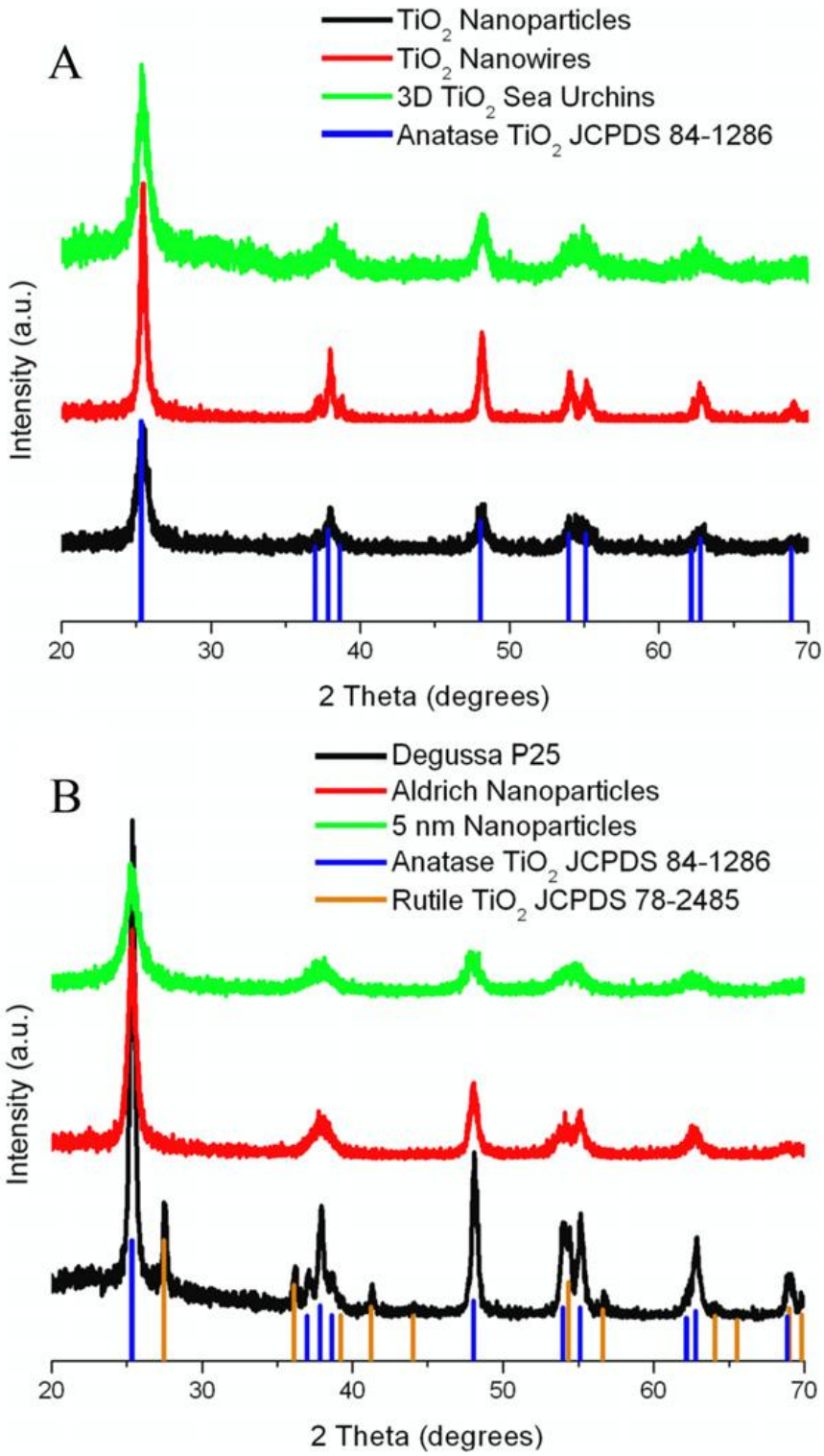

Figure 5.2: (A) Powder XRD pattern of hydrothermally derived TiO_2 samples, with the corresponding JCPDS standard. (B) Powder XRD pattern of commercial TiO_2 materials with the corresponding JCPDS standards.

The structural morphology of our samples was characterized initially with low magnification transmission (TEM) images taken at an accelerating voltage of 80 kV on a FEI Tecnai12 BioTwinG2 instrument, equipped with an AMT XR-60 CCD digital camera system. Specimens for all of these TEM experiments were prepared by diluting the sample with ethanol, sonicating for 2 min in order to ensure adequate dispersion of the nanostructures, and evaporating one drop of the solution onto a 300 mesh Cu grid, coated with a lacey carbon film. Scanning electron microscopy (SEM) images were obtained utilizing a field emission scanning electron microscope (Hitachi S-4800), operating at an accelerating voltage of 15 kV. SEM samples were prepared by dispersing in ethanol and sonicating for several minutes, followed by drop-casting onto a silicon wafer. Profilometry was conducted using a Technor Instruments Alpha-Step 300 device, which is a computerized, high-sensitivity stylus-based surface profiler.

5.4 Powder XRD Analysis

Previous studies have shown that the crystallographic phase of TiO_2 used, e.g. either anatase, rutile or brookite, can have a significant impact upon the resulting device's performance.[69] It is with this idea in mind that we investigated our nanomaterials using powder X-ray diffraction (XRD) analysis, in order to confirm the nature of the crystalline phase(s) of TiO_2 present. Previous work has demonstrated that the application of rutile TiO_2 as the active area in a DSSC can result in lower cell performance, due to an increased resistance within the cell, as compared with use of the anatase phase.[70] It is therefore important to elucidate the crystallographic phase of the materials we have probed in our study. As can be seen in Figure 5.2A, nanomaterials synthesized via our hydrothermal method show peaks corresponding to only

the uniquely advantageous anatase phase, with no detectable amount of a rutile phase present within the samples.

Furthermore, the XRD patterns, Figure 5.2B, of the two commercial nanoparticles, purchased from Sigma Aldrich and Nanostructured and Amorphous Materials (e.g. 5 nm nanoparticles), again revealed the presence of only the anatase phase of TiO_2. Of the materials discussed herein, only the Degussa P25 nanoparticles contained sizable quantities of the undesirable rutile TiO_2 phase. Whereas the presence of the rutile phase within the Degussa P25 nanoparticles is problematic from the point of view of solar cell performance, it has been previously reported that this commercial material possess a nominal ratio of anatase to rutile phases of 70: 30, which is in excellent agreement with our XRD study.

5.5 TEM Characterization

In order to fully understand the morphology of the materials utilized in the cells, further structural investigation of the nanoparticulate materials using TEM (e.g. Figure 5.3) as well as with SEM for the larger 1D and 3D sea-urchin-like structures was performed in order to analyze their sizes. The results obtained from these experiments are reported in Table 5.1. In the case of the nanoparticle systems, the TEM analysis revealed that the hydrothermally prepared nanoparticles maintained a size of 12 ± 3 nm, which is comparable with that of commercial Aldrich nanoparticles (11 ± 2 nm). By contrast, nanoparticles purchased from Nanostructured and Amorphous Materials (henceforth referred to as 5 nm NPs) maintained an average diameter of 6 ± 1 nm, which is in good agreement with the company's reported value of 5 nm.

Hydrothermally derived nanowires maintained larger average sizes, with diameters of 85 ± 55 nm and lengths of up to several microns. Moreover, they possessed a textured appearance along the longitudinal axis of the nanowire, as expected.[64] While this observation implies a

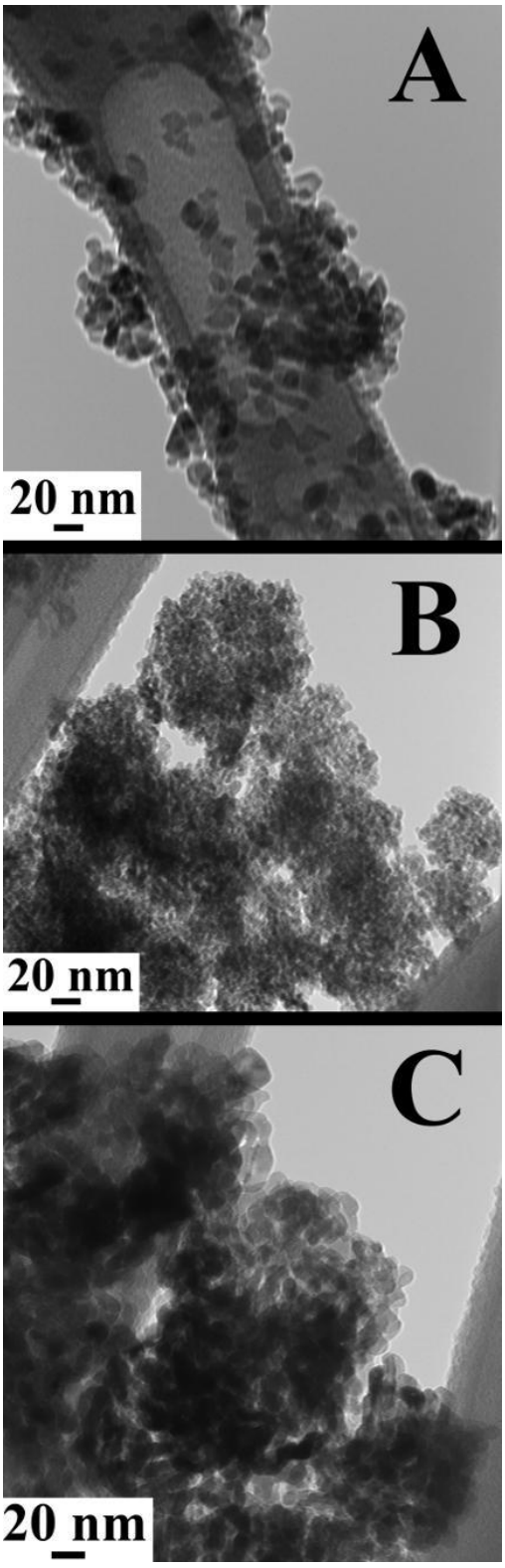

Figure 5.3: Representative TEM images of (A) hydrothermally-derived nanoparticles, (B) commercial Nanostructured & Amorphous Materials (5 nm) nanoparticles, and (C) commercial <25 nm Aldrich nanoparticles.

	Average particle size (nm)	BET surface area ($m^2\ g^{-1}$)	Dye loading ($\times 10^{-8}$ mmol of dye cm^{-2})	J_{sc} (mA cm^{-2})	V_{oc} (V)	FF	η (%)
Degussa P25 nanoparticles	25 ± 10	63	5.83	12.88 ± 1.73	0.711 ± 0.042	0.318 ± 0.042	2.94 ± 0.68
(<25 nm) Aldrich nanoparticles	11 ± 2	130	9.49	9.8 ± 3.64	0.715 ± 0.031	0.362 ± 0.089	2.57 ± 1.33
Commercially available 5 nm nanoparticles	6 ± 1	260	11.5	11.41 ± 2.47	0.703 ± 0.015	0.487 ± 0.018	3.92 ± 0.95
Hydrothermally derived nanoparticles	12 ± 3	73	15.9	14.01 ± 1.77	0.668 ± 0.017	0.406 ± 0.067	3.75 ± 0.43
Hydrothermally derived nanowires	85 ± 55	68	6.40	10.37 ± 0.32	0.527 ± 0.097	0.349 ± 0.047	1.95 ± 0.65
3D TiO_2 sea-urchin-like structures	1130 ± 293 (16 ± 3)[a]	83	6.86	8.27 ± 0.43	0.605 ± 0.053	0.39 ± 0.021	1.97 ± 0.39

[a] These values denote the sizes of the smaller, individual nanowires that constitute the larger 3D sea-urchin-like structures.

Table 5.1: Summary of key structural and solar cell parameters obtained for pastes derived from both commercial and hydrothermal sources. The error bars listed for the various parameters of the solar cells constructed were calculated after measuring a minimum of four devices for each type of TiO_2 tested.

polycrystalline nature to the product, previous HRTEM analysis has revealed that these structures are actually single crystalline in nature. Finally, as-synthesized 3D TiO_2 sea-urchins possessed an average, overall size of 1130 ± 293 nm, although these materials were actually comprised of a hierarchical structure consisting of an aggregation of smaller, discrete single-crystalline nanowires with an average, individual width of 16 ± 3 nm.

Following the TEM analysis, the samples were rendered into slurries and applied to FTO substrates via doctor blading techniques. Specifically, Scotch tape was utilized as a spacer to produce films with a thickness of approximately 10 μm, as confirmed by profilometry, in order to maintain consistency amongst the various pastes. Analysis of the 5 nm and <25 nm Aldrich nanoparticle samples, prior to this film preparation, has revealed that aggregates were present in these materials, as received. Furthermore, we have found that, despite thorough mechanical grinding and sonication with a sonic dismembrator, these aggregates do not appear to physically disintegrate to any appreciable degree, as shown in Figure 5.3. Moreover, it is apparent that the aggregates evidently present in the <25 nm Aldrich and 5 nm particulate films are likely formed during the manufacturing process of the material, as they do not appear to readily respond to extensive physical processing, such as either sonication or mechanical grinding. By stark contrast with these commercial materials, TEM investigation of the hydrothermally derived nanoparticles has revealed that these nanoparticles remain largely dispersed.

5.6 SEM Characterization

In order to observe the quality of the films, consisting of the various TiO_2 materials, we utilized SEM to visualize the as-deposited materials (Figure 5.4). Investigation of the film comprised of P25 nanoparticles revealed a relatively flat, uniform film composed of the

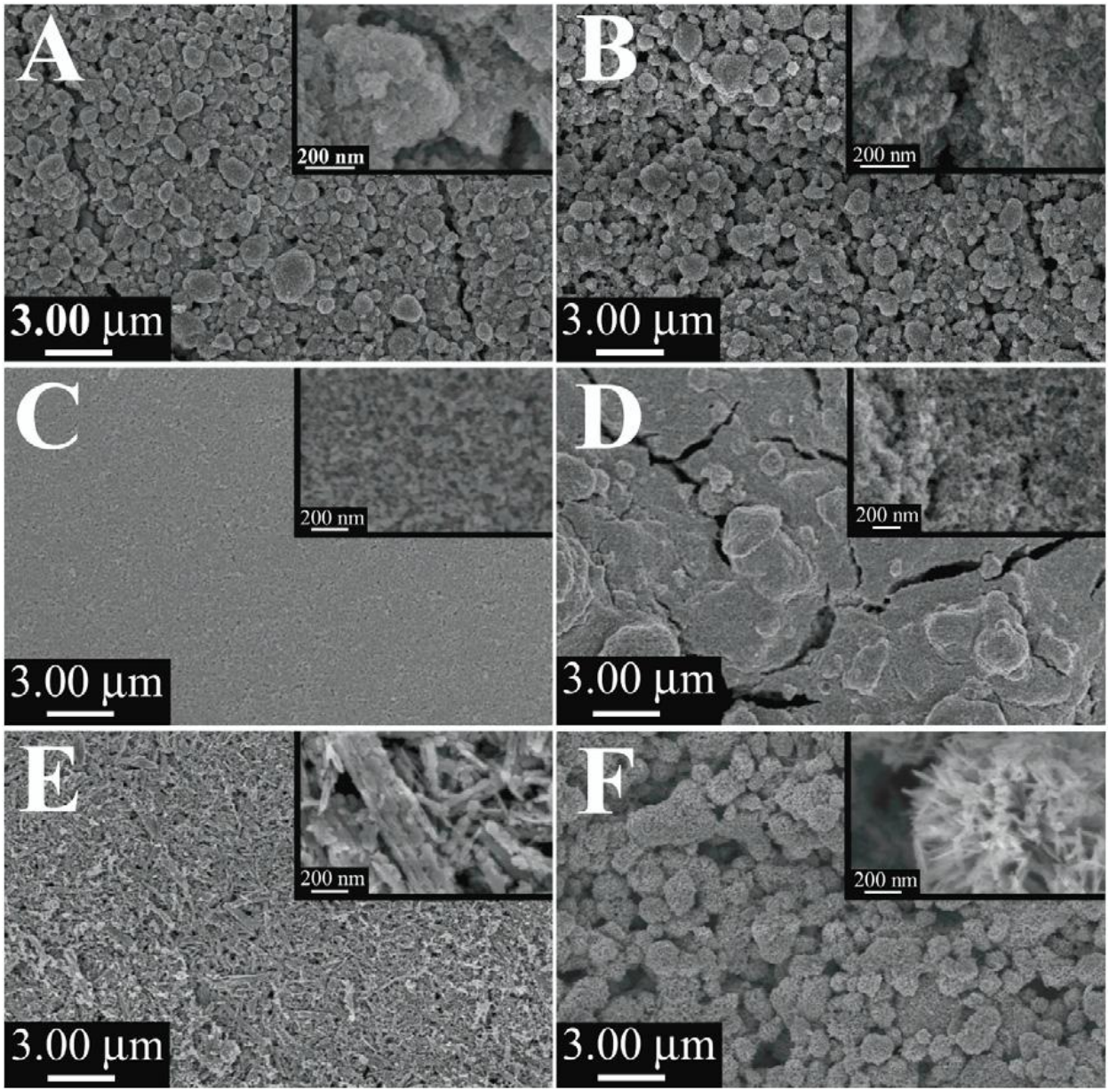

Figure 5.4: SEM images of TiO_2 films used in various as-prepared solar cells. Cells are based on (A) <25 nm Aldrich nanoparticles, (B) Nanostructured and Amorphous Materials (5 nm) nanoparticles, (C) Degussa P25 nanoparticles, (D) hydrothermally-derived nanoparticles, (E) hydrothermally-derived nanowires, and (F) hydrothermally produced sea-urchin-like motifs, respectively. Insets represent higher-magnification images of the localized areas of these films.

aforementioned 25 ± 10 nm nanoparticles (Figure 5.4C), an observation in excellent agreement with previous reports.[67] Closer investigation (Figure 5.4C, inset) revealed that the film maintained a porous nature, which is crucial for both the adsorption of dye molecules onto the surface as well as penetration of the electrolyte into the film.

However, visualization of the other three nanoparticulate films revealed a strikingly different structural appearance and morphology as compared with the P25 film. Specifically, the 5 nm (Figure 5.4A) and <25 nm Aldrich (5.3B) NP films exhibited a high degree of nanoparticle aggregation, resulting in the formation of large sphere-like agglomerations of nanoparticles. In fact, the aggregates varied in size for the <25 nm Aldrich and the 5 nm NP films, with measurements of 852 ± 384 nm and 889 ± 204 nm, respectively. By contrast, while our hydrothermally derived nanoparticles (Figure 5.3D) do exhibit some degree of aggregation, these assemblies are less defined structurally, and, as will be discussed further below, are likely formed during the actual drying process of the paste. Representative TEM images of the hydrothermally derived nanoparticles (Figure 5.3) reveal that, unlike the commercial nanoparticle samples, single nanocrystals are readily apparent, confirming that these particles are not physically aggregated prior to their application onto the FTO glass, as is the case with the commercial samples. Moreover, the high degree of aggregation within the film can also be attributed to the high concentration, ~30 wt%, of nanoparticles within the paste. Similar phenomena have also been observed in a recent report by Park et al.,[59] wherein the roughness of the active area could be controlled through manipulation of the TiO_2 concentration within the paste. This is an interesting observation, for it further confirms that simple physical manipulation of the application paste can lead to reliable control over aggregate formation and morphology within the resulting nanoparticle film.

Several recent reports[37, 59, 63, 71-73] have shown that a hierarchical ordering of nanoparticles within the active area film can result in an advantageous increase in solar cell performance. In particular, the presence of aggregates can increase light scattering[37, 71] as well as enhance electron conduction through the TiO_2 film.[63, 72, 73] However, in these previous reports, the formation of these aggregates required special treatment protocols, such as either hydrothermal or sol-gel reactions. Interestingly, we noted the presence of similar aggregate-like structures in our nanoparticulate films, which could be produced without any extraneous synthetic processing required and, in fact, are present within commercially purchased materials. Hence, these results implied that hierarchical, high surface area texturing of the semiconductor film can be achieved without significant post synthesis manipulation steps.

A cursory inspection of films comprising 1D nanowires and 3D sea-urchin-like assemblies revealed film morphologies that were clearly distinctive from those associated with nanoparticulate films (Figure 5.4E and 5.4F). Specifically, for films consisting of 1D nanowires, a uniform, flat coating was observed. Moreover, we did not observe any significant aggregation, as reported for the nanoparticle films, though we did not expect this to be detrimental to solar cell performance, due to the advantages associated with using nanowire structural motifs. In particular, due to their inherent anisotropic nature, the nanowire materials tend to show intrinsically increased electron conduction behavior.[74] Furthermore, the relatively large diameter (85 ± 55 nm) of the nanowires has allowed them to more effectively scatter light as compared with isolated, dispersed nanoparticles.[71]

Electron micrographs of films prepared using sea-urchin-like TiO_2 microstructures also demonstrate the formation of uniform, flat films consisting of our desired material. It is important to note that even after mechanical grinding, sonication and multiple heating steps, our

3D TiO_2 sea-urchin-like structures still manage to conserve their morphology. However, it is apparent from the SEM image, Figure 5.4F, that the film morphology consisting of the 3D TiO_2 sea-urchin-like motifs contains a significant number of large voids. Indeed, while the sea-urchin-like morphology results in a large surface area, an observation which will be further discussed below, the presence of these macroporous voids can effectively lower the active surface area of the *film* and, therefore, the degree of dye loading.[37] Furthermore, the presence of these large voids indicates a less densely packed film, subsequently decreasing the number of electron pathways through the film and, hence, increasing the length of the electron path to the electrode.[72] Hence, the sea-urchin-like nanostructures do not necessarily form a highly favorable semiconducting film surface, despite their uniquely advantageous high surface area and single crystalline hierarchical structure.

5.7 BET analysis

In order to more fully understand the surface properties of our nanomaterials, we utilized BET data in order to determine the surface area of each powdered material. This is a critical aspect of the material, as the surface area directly impacts the amount of dye that can be adsorbed. These results are summarized in Table 5.1. The observed trends are in excellent agreement with those expected for both size and morphology. First, not surprisingly, as the particle size decreases from 25 to 5 nm, the surface area of the material increases from 63 to 260 m^2g^{-1}. Second, the structural change from the use of hydrothermally prepared nanoparticles to that of the hydrothermally synthesized nanowires slightly decreases the measured surface area from 74 to 68 m^2g^{-1}. This decrease in surface area is expected, since one-dimensional nanostructures maintain lower absolute surface areas as compared with nanoparticles. However,

despite the large size and wire-like morphology, the surface itself remains similar to that of the nanoparticles.[75] In fact, the relative closeness in surface area between these two morphologies can be readily ascribed to the roughened texture of the nanowires, an observation which is highlighted in the SEM images. Furthermore, BET analysis of sea-urchin-like TiO_2 nanostructures yielded a surface area of 83 m^2g^{-1}, which is significantly higher than that found for both hydrothermally derived nanoparticles and nanowires. Hence, these results confirm the advantageous morphology-dependent properties of sea-urchin-like motifs, in that these structures couple the unique advantages of (i) the anisotropy and directionality associated with their constituent nanowires with (ii) the high surface area that is intrinsic to nanoparticulate films.

5.8 Dye Adsorption Analysis

Further investigation into the morphology of our as prepared films was conducted via dye desorption analysis in order to determine the effective surface area present within the various films for dye adsorption. Herein, the films were sensitized with N719, after which the dye was desorbed from the TiO_2 surface through immersion in a known volume of 0.1 M KOH. Analysis by UV-visible spectroscopy allowed us to determine the concentration of dye present in solution, and subsequently the amount of dye present on the film. This technique permitted us to better identify the amount of surface area accessible within the films available for dye adsorption. These results are also reported in Table 1.

Based upon the BET analysis, we anticipated the trend of efficiency of dye adsorption to follow the pattern of commercial 5 nm NPs > (<25 nm) Aldrich NPs > 3D sea-urchin-like assemblies > hydrothermally produced NPs > 1D hydrothermally derived nanowires > Degussa P25 NPs. However, the desorption results clearly showed that the amount of dye within each

film does not necessarily correlate with the surface area data. In fact, the observed trend is significantly different.

In fact, we found a pattern of decreasing dye adsorption, following the trend of hydrothermally produced NPs > commercial 5 nm NPs > (<25 nm) Aldrich NPs > 3D Sea-urchin-like assemblies > 1D hydrothermally derived nanowires > Degussa P25 NPs. This behavior revealed that although the commercial 5 nm and <25 nm Aldrich nanoparticulate materials maintained relatively high surface areas prior to their incorporation into a working device, the entirety of their surface area was not accessible for dye adsorption in the cell, thereby leading to the observed presence of lower current. This low surface area could arise during the sintering process, necessary for film formation, whereupon the grain sizes and degree of necking between the particles increased. Similar surface area effects have been observed in previous reports,[73, 76, 77] all of which could be attributed to the loss of mesoporosity within the material during sintering. Not surprisingly, BET analysis, performed on the Aldrich <25 nm and 5 nm TiO_2 nanoparticles isolated after being rendered into films and subsequently sintered, revealed significant decreases in the accessible surface area of these respective materials. Specifically, the measured BET surface areas were found to decrease to 51 m^2g^{-1} and 54 m^2g^{-1} for the Aldrich and 5 nm nanoparticles, respectively, incorporated into films. Hence, as a general comment, the use of nanomaterials in DSSCs can result in unforeseen changes in their physical and packing properties, thereby invalidating a simple, direct 1:1 correlation between morphology and device performance.

Investigation of the dye loadings for the 3D sea-urchin-like assemblies revealed lower values than expected, presumably due to a relatively inefficient packing within the films. As evinced by the SEM images (Figure 5.4F), there are large voids present within the 3D sea-urchin

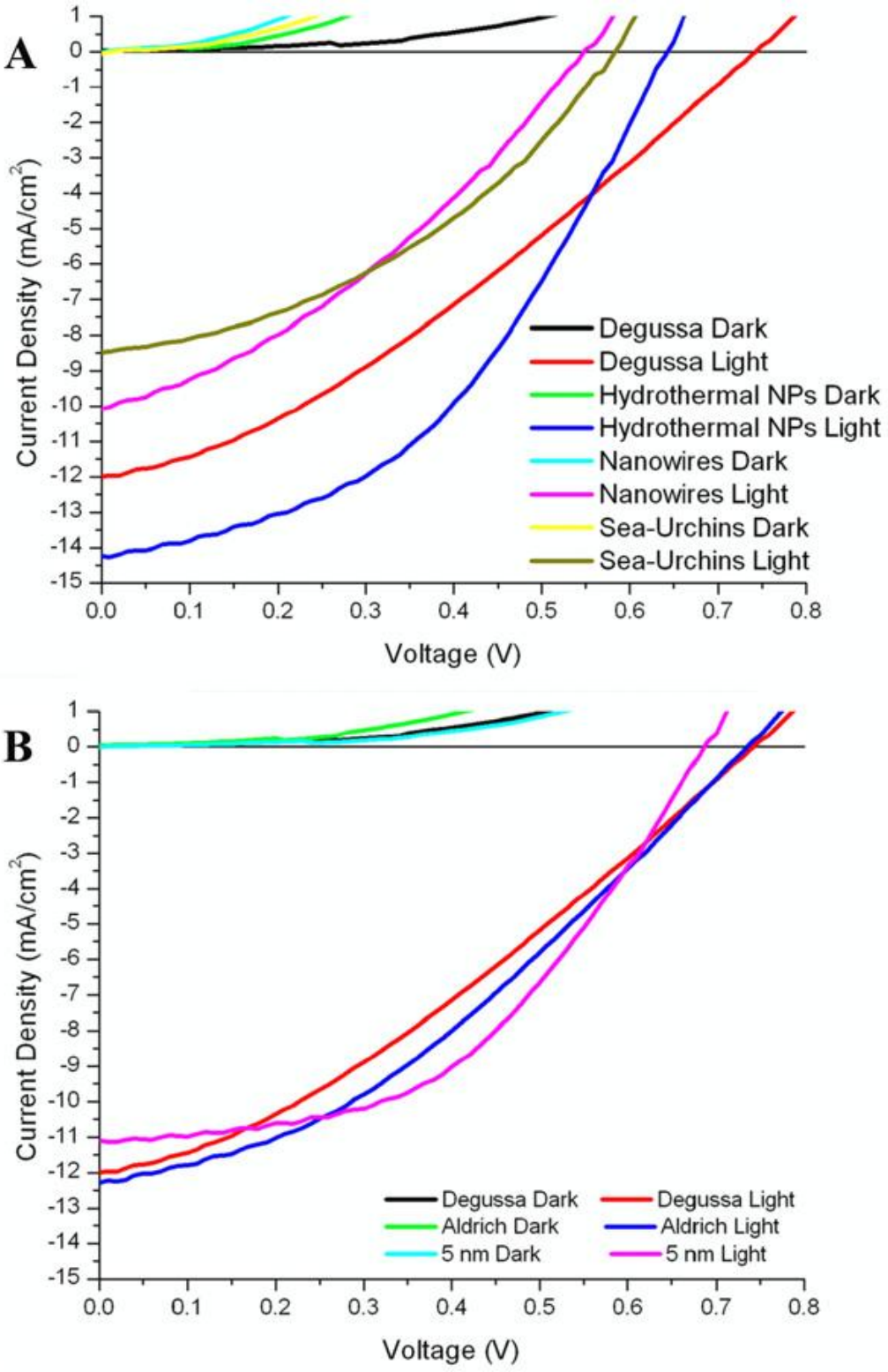

Figure 5.5: (A) Typical *J –V* curves of hydrothermally derived TiO_2 materials. (B) Typical *J –V* curves of the corresponding commercially derived TiO_2 materials.

films, thereby leading to a decrease in available, accessible surface area for dye loading. Therefore, even though the 3D sea-urchin-like motifs presented some of the highest available surface areas, their poor organization and packing within our as-generated semiconducting films most likely led to a lower observed dye loading. Finally, the lower dye loadings observed within the 1D nanowires films are consistent with the correspondingly lower BET surface areas of these materials, which translated into a decreased area accessible for dye adsorption.

5. 9 Solar Cell Performance

Following these characterization experiments, the films were utilized in the formation of solar cells, as detailed in Section 5.2. To test their efficiencies, these solar cells were analyzed under illumination with an AM 1.5 light source. Current density versus voltage (J-V) curves for our hydrothermally derived and commercial TiO_2 pastes are depicted in Figures 5.5A and 5.5B, respectively. The average values, determined by the analysis of no less than four solar cells, for the J_{SC}, V_{OC}, FF, and η are listed in Table 1.

It is particularly interesting that the values obtained for the nanoparticle cells reveal that the J_{SC} values do not necessarily trend with the amount of adsorbed dye. Not surprisingly, the hydrothermally prepared nanoparticles maintain the highest degree of dye adsorption and, correspondingly, the highest J_{SC} value of 14.01 mA cm^{-2}. In stark contrast, the Degussa P25 nanoparticles maintained the lowest dye adsorption level but possessed the second highest value for J_{SC}, namely 12.88 mA cm^{-2}. This number, by comparison with the amount of dye adsorbed, is significantly higher than that found for all other commercial materials. We attribute this observation to the more dispersed nature of the P25 film as well as to the homogeneous distribution of the constituent particles, thereby allowing a greater degree of light penetration

into these cells. However, the presence of aggregation in the Aldrich and 5 nm samples is expected to increase light scattering, which, though nominally beneficial for the purposes of increasing the path length within the solar cell, can also be detrimental in terms of fostering deleterious light scattering effects as well as decreasing the overall levels of light penetration into the cell.[37, 71]

Not surprisingly, the V_{OC} values for the nanoparticles are close to each other, with magnitudes of 0.711 ± 0.042, 0.688 ± 0.017, 0.715 ± 0.031, and 0.703 ± 0.015 V for the commercial Degussa P25, hydrothermally prepared nanoparticles, <25 nm Aldrich nanoparticles, and 5 nm nanoparticles, respectively. The slightly lower value noted for the V_{OC} of the hydrothermal nanoparticles can be readily explained by two distinctive parameters. First, a lower Fermi level within the nanoparticles, caused by an increased trap density,[72] can lower the energy difference between the nanoparticles and the redox couple, thereby limiting the voltage of the solar cell. Second, an increased recombination within the cell can also effectively lower the V_{OC} of the cells through a significant decrease in charge, capable of reaching the external circuit.[78] OCVD data presented below will provide further insight into the origin of this voltage loss in the hydrothermally derived nanoparticle cells.

The fill factors of the nanoparticles films vary widely between the different materials used. The values obtained for the various films are as follows: 0.318 ± 0.042, 0.406 ± 0.067, 0.362 ± 0.089, and 0.487 ± 0.018 for the commercial Degussa P25, hydrothermally prepared, <25 nm Aldrich, and commercial 5 nm nanoparticles, respectively. While these parameters are less than ideal,[67] this observation can be readily ascribed to the use of an electrolyte containing both LiI and TBAI. Higher fill factors and thus comparably greater efficiencies could have been obtained by optimizing the content of the electrolyte, for instance.[6] Further effects of the

recombination rate on the fill factor will be explored during our OCVD analysis. Furthermore, analysis of the linear region, at more positive voltages, of the current-voltage curves reveals a higher series resistance in the cells that possess a lower FF, namely those containing <25 nm Aldrich and Degussa P25 nanoparticles, which are on the order of 100 Ω.

By contrast with this value, the commercial 5 nm and the hydrothermally derived nanoparticles show a relatively lower series resistance, e.g. on the order of 40 Ω. This is indicative of the observation that films composed of the hydrothermally derived nanoparticles and 5 nm nanoparticles possess a higher conductivity as compared with their <25 nm Aldrich and Degussa P25 nanoparticle counterparts. The decreased resistance presented by the hydrothermally derived and 5 nm nanoparticulate films likely arises from the crystallinity of the material, as well as from increased necking and connectivity between the particles. All of these are factors which likely facilitate electron movement from particle to particle within the films. As a second point, as stated earlier, the nature of the aggregation of the nanoparticles within the film, as observed via SEM analysis, can enhance the conduction of charge carriers through improved particle connectivity and increased electron lifetimes, a point which shall be further discussed in later sections.

Ultimately, the combination of these factors (J_{SC}, V_{OC}, and FF) results in average solar cell efficiencies of 2.94 ± 0.68, 3.75 ± 0.43, 2.57 ± 1.33, and 3.92 ± 0.95 % for the Degussa P25, hydrothermally derived, <25 nm Aldrich, and 5 nm nanoparticles, respectively. From these efficiency results, it is clear that the major cause for variation in the solar cell efficiencies resides in the innate differences in the V_{OC} and J_{SC} values. Specifically, the cells produced from the hydrothermal nanoparticles exhibit the highest J_{SC} values, yet their V_{OC} is 43 mV lower as compared with the other commercial TiO_2 nanoparticles. It is this loss of voltage, for reasons

discussed, that can result in an overall lower solar cell efficiency. However, for the <25 nm Aldrich and 5 nm nanoparticulate cells, the greatest limiting factor of the efficiency is associated with the J_{SC} value, as a direct result of not only the lower dye loading within these cells, resulting from a loss of surface area during sintering, but also through absorptive losses due to scattering within the cell, as was thoroughly discussed above. It is these real losses in the optical absorption that ultimately limit the overall observed efficiencies associated with the solar cells fabricated utilizing <25 nm Aldrich and 5 nm nanoparticles.

In addition to investigating the nature of the commercial nanoparticle systems, we have also rationally explored the device performance of hydrothermally prepared nanostructures as a function of morphology, specifically that of 1D nanowires and 3D sea-urchins. Investigation of the *J-V* curves for the 1D nanowires and the 3D sea-urchins reveals results that are notably lower as compared with those for the nanoparticles themselves. In particular, the J_{SC} values for these two materials are 10.37 ± 0.32 and 8.27 ± 0.43 $mA \cdot cm^{-2}$ for the 1D nanowire and 3D sea-urchin solar cells, respectively. While these values are lower than those reported for the hydrothermally derived nanoparticle film, films consisting of 1D nanowires and 3D sea-urchin-like, while presenting similar dye loading values, maintain different current density values. We believe that the overall enhanced J_{SC} values, as compared with commercial samples, arises from a more favorable film geometry, which allows for greater light penetration within the cell, although this is somewhat tempered by the presence of enhanced scattering within the solar cell, emanating from the nanowires themselves.

The fill factors of these two hierarchical materials are also comparatively lower than those found for the hydrothermally derived nanoparticles, indicating a less than ideal film. We propose two different but plausible explanations for the lower fill factors associated with 1D

nanowires and 3D sea-urchin-like structures. In the case of 1D nanowires, we believe that the lower observed FF is caused by less efficient electron transport through the nanowire film, thereby resulting in increased recombination, and, therefore, a decreased FF. This inefficient electron transport can be ascribed to both the random orientation of the nanowires within the film as well as the granular nature of that film. Both of these factors limit the positive benefits of the nanowires' anisotropic nature. Furthermore, increased trap state density may also be a contributing factor to the lower fill factor. For the 3D sea-urchin-like structures, we hypothesize that their suppressed FF arises from a wholly different reason, namely the substantial macroporosity of the films, as described earlier. This very real possibility can lead to longer electron path lengths within the cell, thereby resulting in increased recombination and, subsequently, a lower FF.[72] Furthermore, the increased porosity can decrease the number of connections between adjacent sea-urchin-like structures, thereby leading to less efficient charge transfer through the film to the back contact. The resulting efficiency values of 1.95 and 1.97%, measured for the 1D nanowires and 3D sea-urchin-like structures, respectively, likely reflect the inherently lower J_{SC}, V_{OC}, and FF values measured for these materials.

5.10 OCVD analysis

In order to more fully comprehend the nature of electron conduction and recombination within our cells, we collected a number of OCVD measurements. Electron lifetimes obtained for the different cells are presented in Figure 5.6. It is important to note here that these lifetimes are also a measure of the relative rates of recombination within the cell, and are determined by treating a voltage decay curve with equation 1.[68]

$$\tau_n = -(k_B T/e)(dV_{OC}/dT)^{-1} \qquad [1]$$

where τ_n is the electron lifetime, k_B is the Boltzmann constant, T is the temperature, *e* is the elementary charge, and dV_{OC}/dT is the derivative of the voltage decay curve. It is apparent from the OCVD transients that the cell fabricated using our in-house hydrothermally derived

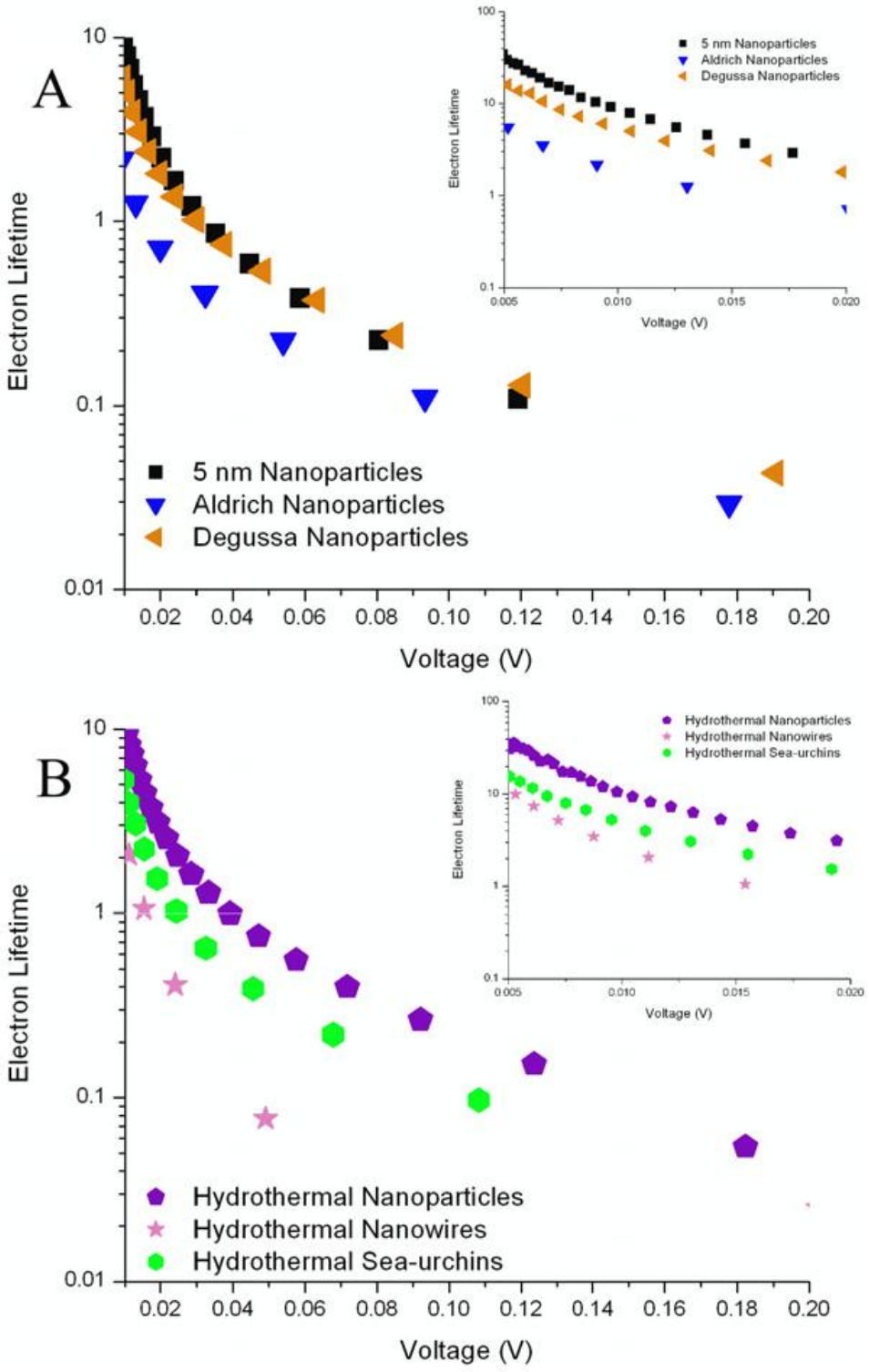

Figure 5.6: Electron lifetimes (in seconds) associated with (A) commercial nanoparticles as well as of (B) hydrothermally derived nanomaterials, as determined from the open circuit voltage decay curves of various TiO_2 nanomaterials used to fabricate solar cells. Insets denote regions of the voltage decay curves at low open circuit voltages.

nanoparticles outperformed all of the commercial samples at both higher and lower V_{OC}, thereby highlighting the superior transport characteristics of charge carriers through both individual grains and grain boundaries. Previous reports have also shown that electron lifetimes increase with increasing particle size due to a decrease in the number of grain boundaries.[79] However, in the broader sense, it is evident from these data that the hydrothermally derived nanoparticles gave rise to the longest electron lifetimes on average, owing to the high degree of crystallinity of this sample.[64] These results are further support for the increased conduction of the films, as shown above in the analysis of the fill factors of the solar cells.

Because it is a rather sophisticated technique, OCVD can be used to probe the nature of the contributions of recombination and conduction pathways. Specifically, at high V_{OC} values, OCVD yields insight into the conduction of charge carriers through the particle interconnects, as this region represents an area of high carrier flux. By contrast, at lower V_{OC} values, insight can be provided into the nature of the conduction of carriers through individual particle grains.[45, 72] In this context, the performance of the cells prepared from the commercial samples can be independently probed with respect to those derived from hydrothermally processed nanoparticles. Specifically, the electron lifetime of the hydrothermal nanoparticles becomes comparable to that of the Degussa P25 nanoparticles at high open circuit voltages. This is not an unexpected result, considering the high degree of continuity and the lack of macroscopic cracks in these films, which can thereby enhance the interparticle connectivity. By contrast, the 5 nm NPs display substantially suppressed lifetimes at high V_{OC}, which is also not surprising, given the inhomogeneity of the 5 nm NP film in combination with the poor interconnectivity of the micron-sized aggregates.[45, 72] Furthermore, it has been shown that the introduction of small

nanoparticles increases electron recombination due to an increase in the number of grain boundaries present within the cell.[80]

By contrast with the observed trend at high V_{OC}, comparison of the OCVD transient under low OCVD conditions reveals that the 5 nm nanoparticles maintain superior lifetimes as compared with their commercial Degussa P25 NP counterparts. In this region, the nature of the decay of the 5 nm NPs approaches that of the hydrothermally produced nanoparticles, thereby implying that these nanostructures suppress recombination of charge carriers present within the individual crystalline grains. This is understandable given the hierarchical nature of these nanostructures, wherein the 5 nm NPs form highly interconnected nanoporous aggregates, which can prevent recombination of charge carriers with the electrolyte. Not unexpectedly, amongst the nanoparticle motifs, the <25 nm Aldrich NPs display the lowest lifetimes for both the high and low V_{OC} regions, an observation which is consistent with the low DSSC efficiency results noted amongst the 0D systems. By means of comparison, representative values of electron lifetimes for the various materials studied at higher voltages are 157 ms at 123 mV, 114 at 119 mV, 129 ms at 120 mV, 100 ms at 109 mV, 110 ms at 93 mV, and 77.9 ms at 49 mV for the hydrothermally derived nanoparticles, 5 nm nanoparticles, Degussa P25 nanoparticles, 3D sea-urchin-like assemblies, <25 nm Aldrich nanoparticles, and 1D hydrothermally produced nanowires, respectively. By contrast, at lower open circuit voltages, the corresponding values are as follows: 10.63 s at 10 mV, 9.37 s at 10 mV, 6.00 s at 9 mV, 5.28 s at 10 mV, 3.46 s at 9 mV, and 2.17 s at 9 mV for the hydrothermally derived nanoparticles, 5 nm nanoparticles, Degussa P25 nanoparticles, 3D sea-urchin-like assemblies, 1D hydrothermally produced nanowires, and < 25 nm Aldrich nanoparticles, respectively.

A similar analysis can be applied to the anisotropic 1D nanostructured systems, wherein the recombination pathways can be probed as a function of morphology. The 3D sea-urchin-like nanostructures display analogous behavior to that of the 5 nm NPs, wherein a significant bottle necking effect emerges as a result of the less than optimal packing of these hierarchical structures as well as the poor interconnection between the nanostructures. In fact, the lower lifetime values observed at both high and low V_{OC} for the 3D sea-urchin-like motifs as compared with the hydrothermally processed and 5 nm NPs are reasonable, given the very poor interconnection and interdigitation amongst not only individual, discrete nanowires but also adjacent individual sea-urchin-like structures.[72] Specifically, narrow interconnections between sea-urchin-like structures are highlighted in Figure 5.7, wherein only a small bridging unit between adjacent urchins is visible. These data also support the fact that the lower V_{OC} values observed for the sea-urchins are likely a result of the dynamic interplay between the porosity of the film and the hindered electron conduction through the film.

These two factors allow for the observed increased recombination rate within these cells, thereby leading to lower overall efficiencies. Finally, the 1D nanowires exhibit the lowest electron lifetimes under high V_{OC} conditions, owing to their highly granulated nature, shown in Figure 5.3E. This observation, in conjunction with the V_{OC} values obtained from the *J-V* curves, would suggest that the nanowires contain a significant amount of surface trap states. We should note that the poor crystallinity of the commercial Aldrich nanoparticles is suggested by their poor lifetimes, measured at low V_{OC}. In this region, the hydrothermally derived nanowires exhibit a slightly higher measured lifetime. Nonetheless, the inadequate interconnectivity amongst the 1D nanowires is particularly evident at higher V_{OC}; in fact, the electron lifetimes measured for these

1D motifs under these conditions are perceptibly lower than that observed for any of the other nanomaterials we have tested in this study.

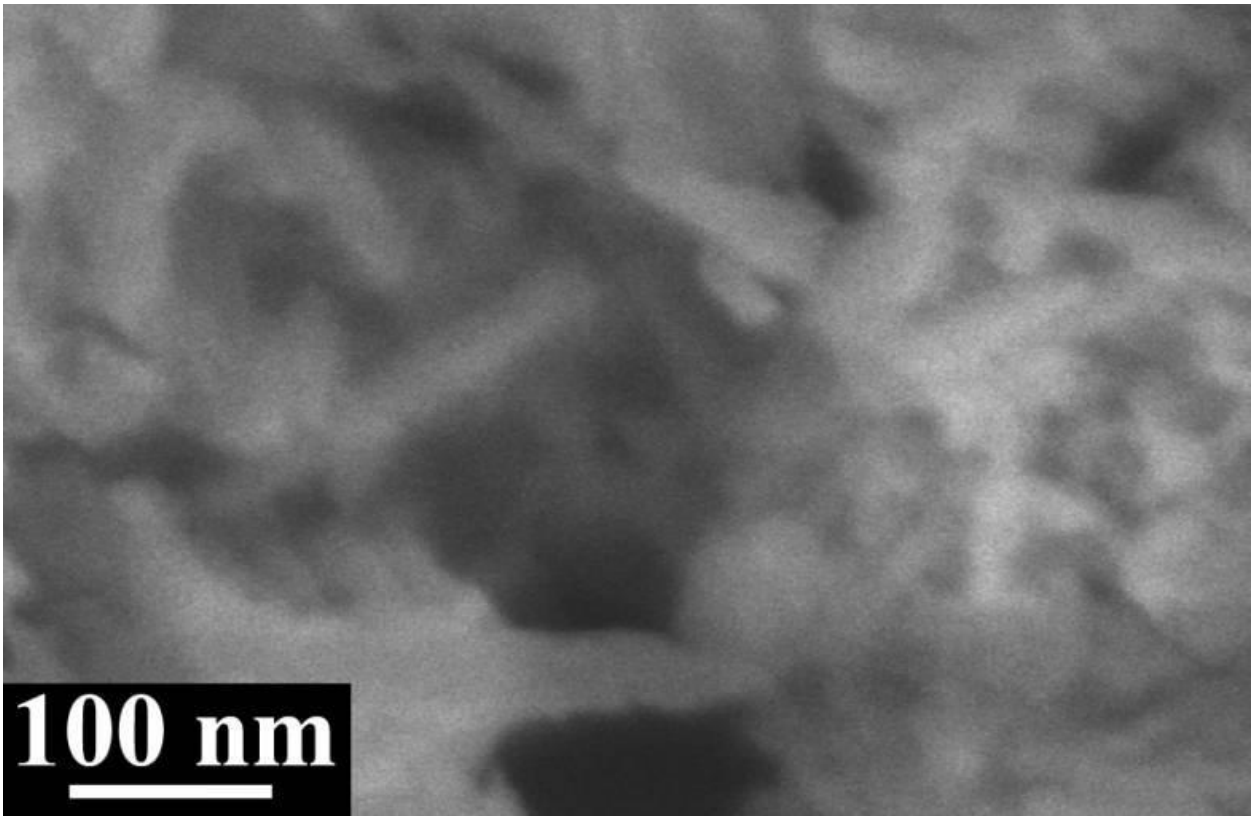

Figure 5.7: SEM image of narrow nanowire interconnects connecting individual 3D TiO_2 sea-urchin-like structures.

5.11 Morphology Mixtures

Taking into consideration the types of analysis of solar cells prepared from pure TiO_2 morphologies, we have mixed samples consisting of individual morphologies together. The mixtures of hydrothermally prepared materials explored herein are comprised of 10% nanoparticles/90% sea-urchins (0D/3D), 10% nanowires/90% sea-urchins (1D/3D), 10% nanowires/90% nanoparticles (1D/0D), and finally, 10% nanowires/10% nanoparticle/80% sea-urchins (1D/0D/3D). Results obtained from this series of solar cells are located in Table 5.2, along with the corresponding dye loadings for each cell. From these data, we have observed that the J_{SC} and dye loadings for the cells trend differently from one another. Specifically, the cell with the highest dye loading does not produce the largest J_{SC}. In fact, Degussa P25 solar cells yield the highest J_{SC} of 12.88 mA cm^{-2}, but exhibit the lowest dye loading measured of $5.83 \cdot 10^{-8}$ mmol cm^{-2}, as compared with cells fabricated using mixtures of hydrothermally derived morphologies. By comparison, the cell comprised of 1D/0D nanomaterials exhibits the second highest measured J_{SC}, 8.68 mA cm^{-2}, but maintains the highest dye absorption of 17.7 mmol cm^{-2} with respect to all of the systems we have tested.

This trend further emphasizes the inefficient degree of light penetration into the cells comprised of hydrothermally derived materials, which can be ascribed to the increased degree of light scattering within these cells.[37, 71] However, while the combination of these different morphologies into a single paste did not effectively resolve the issue of light absorption within the cells, analysis of the various fill factors of these different cells reveals the potentially

Sample	Dye loading ($\times 10^{-8}$ mmol cm^{-2})	J_{sc} (mA cm^{-2})	V_{oc} (V)	FF	η (%)
Degussa P25	5.83	12.88	0.71	0.318	2.94
0D/3D	12.3	7.36	0.69	0.553	2.79
1D/0D	17.7	8.68	0.69	0.524	3.12
1D/3D	8.76	6.91	0.72	0.474	2.39
1D/0D/3D	7.61	7.72	0.72	0.466	2.59

Table 5.2: Summary of solar cell parameters for DSSCs, prepared using mixtures of hydrothermally derived nanomaterials, produced in our laboratory.

positive, synergistic effect of combining different, complementary morphologies and structural motifs.

In particular, the trend found for the fill factors of the mixture cells can be noted as follows: 0D/3D > 1D/0D > 1D/3D > 1D/0D/3D > Degussa P25. This trend reveals, for instance, that the incorporation of a small percentage (e.g. 10%) of 0D nanoparticles into the 3D material can effectively increase the connectivity between individual 3D sea-urchin-like motifs. This increase in connectivity presumably reduces the degree of recombination within the cell, thereby increasing the FF. Moreover, this potential for increased connectivity is further highlighted in the V_{OC} values for cells containing mixtures of nanostructures. Specifically, unlike cells fabricated using only one hydrothermally derived morphology, the measured V_{OC} values for solar cells composed of either mixtures of our structural motifs or Degussa P25 are similar to one another in magnitude, thereby further highlighting the importance of reliable channels for electron transport and conduction between individual nanostructures.

The structural composition of the films was investigated through SEM analysis shown in Figure 5.8. These images reveal the advantages of utilizing mixtures of complementary, hydrothermally-derived nanomaterials. This is most apparent in the SEM of the 0D/3D films (Figure 5.8A), wherein it is clearly noted that the empty void space present in the film containing a mixture of nanostructures is noticeably less than that associated with the pure 3D sea-urchin-like films (Figure 5.3F). Furthermore, these structurally beneficial effects are also evident within the 1D/0D film (Figure 5.8B). The data reveal a much more uniform crack-free film, as compared with the film composed of only hydrothermally derived nanoparticles (Figure 5.3D). The SEM images of the 1D/3D, shown in Figure 5.8C, and the 1D/0D/3D films, shown in Figure 5.8D, reveal some beneficial filling of the very porous 3D TiO_2 structure. However, as the dye

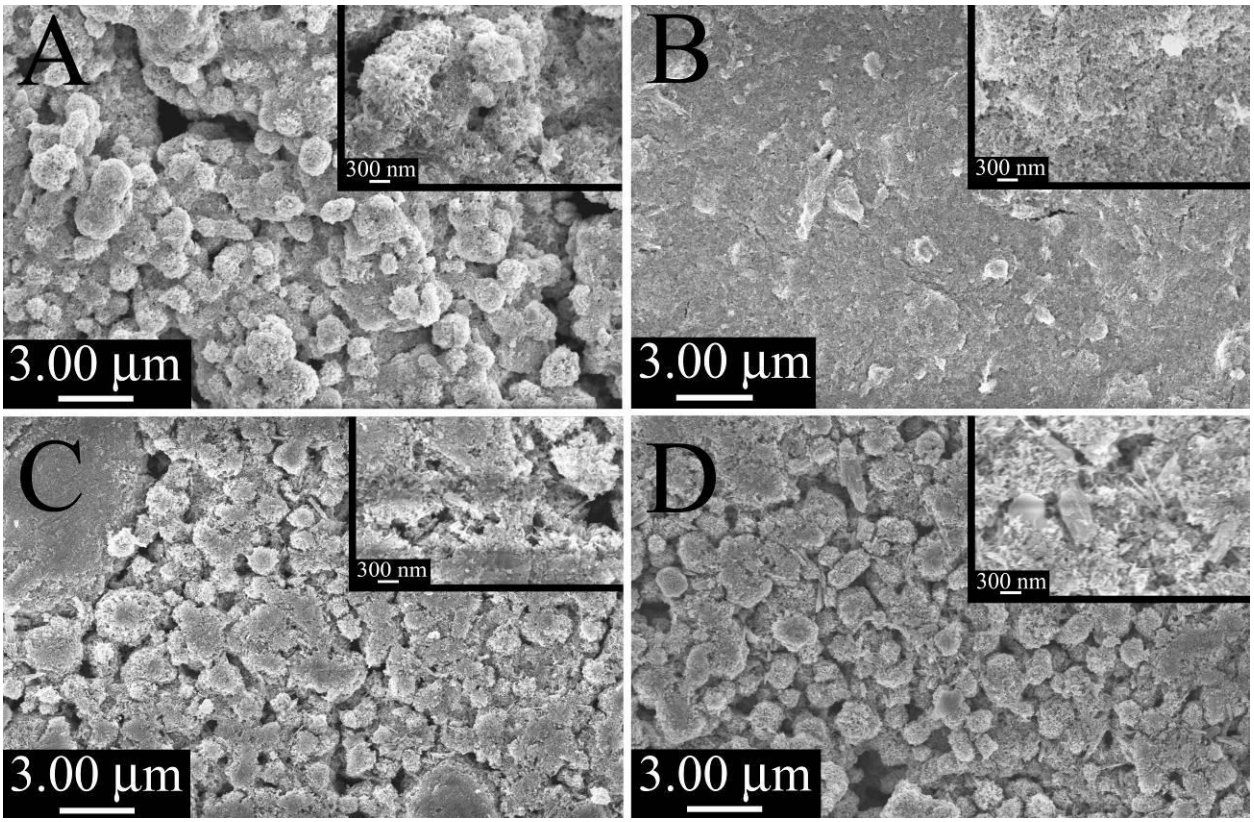

Figure 5.8: (A) SEM image of a film of a mixture of 0D / 3D nanostructures. (B) SEM image of a film of a mixture of 0D / 1D nanostructures. (C) SEM image of a film of a mixture of 0D / 1D / 3D nanostructures. (D) SEM image of a film of a mixture of 1D / 3D nanostructures.

desorption shows, the filling is not as great as in the 0D/3D film. Furthermore, the lower FF for these cells reveals the detrimental effects of incorporating poorly performing hydrothermally derived nanowires into these films.

In terms of overall efficiency, only the 1D/0D mixture evinced a higher efficiency (3.12 %) as compared with conventional Degussa P25 cells (2.94 %). While the remaining mixed morphology cells did not obviously outperform Degussa P25 cells, they were noticeably better than cells consisting solely of pure nanoscale morphologies. These results are highlighted further in Table 5.2. The lower observed efficiencies can be ascribed to decreased J_{SC} values within the cells, which were likely suppressed for reasons associated with poor light absorption and penetration as well as unwanted light scattering, all of which are determinant factors which have been outlined and detailed above.

5.12 Comparison with a Series of Chemically Distinctive Metal Oxides

We utilized several compositionally distinctive titanates (e.g. $BaTiO_3$, $SrTiO_3$, $CaTiO_3$, $Ba_{0.5}Ca_{0.5}TiO_3$, $Ba_{0.5}Sr_{0.5}TiO_3$, and $Ca_{0.5}Sr_{0.5}TiO_3$) fabricated in our laboratory as the semiconducting component within our dye-sensitized solar cell. Previously, these materials have been utilized either as pure materials or as coatings for TiO_2 for the fabrication of DSSCs.[81, 82] In the latter case, TiO_2 nanoparticles were specifically coated with layers of barium and calcium titanate. Whereas the use of these materials as thin coatings for TiO_2 resulted in an increase in solar cell performance, as the coating thickness increased, the solar cell performance decreased in a parallel fashion. A summary of all relevant solar cell parameters is shown in Table 5.3. We note that, in the application of these materials, the inefficiency of the as-produced solar cells can

be ascribed to the poor adhesion of the dye onto the titanate materials, thereby effectively preventing charge injection from the dye into the conduction band of the semiconductor. Furthermore, the particle sizes utilized in the films were all greater than 100 nm, which could have lowered the effective, accessible surface area of the film as compared with films comprised of significantly smaller nanoparticles. Finally, it was noted that adhesion between the titanates and the FTO was relatively poor, resulting in flaking of material off the electrode surface as well as inefficient charge conduction from the film to the external circuit. We therefore concluded that the use of these titanate materials in the context of current DSSC motifs is not as feasible as might have been envisioned, based upon their favorable morphology and crystallinity.

Titanates	Short circuit current density (mA cm^{-2})	Open circuit voltage (mV)	Fill factor	Efficiency (%)	Particle size (nm)
Calcium	0.13	0.27	0.32	0.011	170 ± 69
Strontium	0.079	0.39	0.30	0.0091	153 ± 56
Barium	0.13	0.36	0.29	0.013	374 ± 138
Calcium–strontium	0.11	0.07	0.20	0.0015	186 ± 63
Strontium–barium	0.077	0.41	0.28	0.0088	179 ± 66

Table 5.3: Summary of essential solar cell parameters for DSSCs prepared using compositionally distinctive titanate nanoparticles.

5.13 Conclusions

In conclusion, we have shown that altering the structural morphology of the TiO_2 used in the fabrication of a DSSC can dramatically affect its performance. Specifically, the TiO_2 morphology directly affects the constituent film morphology as well as the nature of the electron conduction through the film to the back contact. Furthermore, we highlight the importance of organization of the nanomaterials within the device film. Our results suggest that the use of nanoparticles synthesized using our in-house hydrothermal protocol result in the highest dye loadings, the highest current densities, as well as the longest electron lifetimes, thereby leading to devices performing as well as or better than as-produced, commercial materials. We find that even though the commercial (<25 nm) Aldrich and 5 nm nanoparticles give rise to the largest surface area, the formation of aggregates within these materials can result in a loss of active surface area during the subsequent annealing steps required for solar cell fabrication. This loss in surface area can detrimentally affect dye adsorption and ultimately lower the efficiency in these cells. However, our hydrothermally produced nanoparticles remain well dispersed in the films, allowing for a high degree of dye adsorption onto the surfaces of the TiO_2, a situation which can thereby increase the light harvesting potential and subsequent current produced by the resulting cell.

Through the use of OCVD, SEM, and dye desorption experiments, we find that the major limiting factor for 1D nanowires and 3D sea-urchins consists of the surface morphology of the film structure created during the sintering steps. That structure can determine the degree of efficiency of electron transport through the films. Overall, the results of our OCVD analysis again reveal the superior nature of our hydrothermally produced nanoparticles, as films of these materials maintain increased electron lifetimes within these cells. The increased electron

conduction, combined with the large, dye-accessible surface area of hydrothermally derived nanoparticles, likely accounts for the highest efficiency values we have measured. Furthermore, we have explored the idea of utilizing mixtures of different morphologies in order to increase the degree of electron diffusion within the films and, thereby, correspondingly enhance electron lifetimes and cell efficiencies. Our data show that solar cells composed of a film containing a mixture of hydrothermally derived nanostructures possess slightly higher electron lifetimes and currents as well as increased efficiencies as compared with our control materials, including hydrothermally produced nanoparticles alone. We further demonstrate that the disadvantages of utilizing solely 1D nanowires and 3D sea-urchin-like motifs can be somewhat mitigated through the rational combination of these different morphologies into a single paste. Most notably, the incorporation of a small amount of 0D nanoparticles into a 3D sea-urchin-like paste results in a more efficient solar cell, as compared with the use of only high surface area sea-urchin- like motifs. In fact, this observation can be attributed to the increased connectivity between individual nanostructures, thereby leading to better electron transport throughout the resulting film. We have also conducted an investigation into the application of various compositionally distinctive titanate nanomaterials as the primary semiconducting material motif within DSSCs, thereby revealing several shortcomings, such as poor dye adsorption and poor film adhesion within these materials. All of these problems resulted in inferior DSSC performance. Nonetheless, overall, it is through these diverse sets of experiments that we have gained important insights into the various processes and parameters within the solar cell that must be carefully manipulated and optimized in order to properly maximize efficiency.

Titania tested	Advantages	Disadvantages
Degussa	Uniform film morphology	Mixture of anatase and rutile phases, low fill factor, suppressed electron lifetimes
>25 nm Aldrich nanoparticles	Pure anatase crystallinity, high open circuit voltage	Low dye adsorption, aggregates cause loss of surface area
5 nm nanoparticles	Pure anatase crystallinity, high open circuit voltage and fill factor	Aggregates cause loss of surface area
Hydrothermally derived nanoparticles	Pure anatase crystallinity, high surface area, enhanced electron lifetime	Aggregation during drying, lower open circuit voltage
Hydrothermally derived nanowires	Anisotropic morphology, pure anatase crystallinity	Very low open circuit voltage, low electron lifetime
Hydrothermally derived 3D sea-urchins	Very high surface area, incorporation of one-dimensional constituent motifs	Poor film morphology leading to loss of surface area, low open circuit voltage, and low dye adsorption

Table 5.4. Summary of advantages and disadvantages of the use of various titania motif structures in DSSC architectures.

In Table 5.4, we highlight the advantages and disadvantage associated with each material investigated within this paper. In summary, we find that the most effective material for DSSCs should combine a high surface area for dye loading, while simultaneously maintaining high electron mobility. Furthermore, it is important to understand and control the film morphology of the materials utilized in order to fully maximize effective use of the surface area of the material. The film morphology also has a significant impact upon electron mobility, and can either enhance or suppress electron lifetimes within the material of interest, depending on the degree of connectivity amongst the various individual constituent nanostructures within the cell. Furthermore, the organization of a titania structural motif into films is a critical factor in determining the degree of effective light penetration into the cell, as well as the depth to which light can efficiently generate electron–hole pairs within the cell. Finally, as we have previously implied, the optimization of the film thickness, dye composition, electrolyte choice, as well as the application of a $TiCl_4$ treatment will inevitably lead to a more efficiently operating solar cell.

5.14 References

1. A. Luque and A. Marti, *Electronics Letters*, 2008, **44**, 943-945.
2. B. O'Regan and D. T. Schwartz, *Journal of Applied Physics*, 1996, **80**, 4749-4754.
3. Y. Chiba, A. Islam, Y. Watanabe, R. Komiya, N. Koide and L. Han, *Japanese Journal of Applied Physics*, 2006, **45**, L638-L640.
4. M. Wang, S.-J. Moon, D. Zhou, F. Le Formal, N.-L. Cevey-Ha, R. Humphry-Baker, C. Grätzel, P. Wang, S. M. Zakeeruddin and M. Grätzel, *Advanced Functional Materials*, 2010, **20**, 1821-1826.
5. K.-M. Lee, S.-J. Wu, C.-Y. Chen, C.-G. Wu, M. Ikegami, K. Miyoshi, T. Miyasaka and K.-C. Ho, *Journal of Materials Chemistry*, 2009, **19**, 5009-5015.
6. A. C. Onicha and F. N. Castellano, *The Journal of Physical Chemistry C*, 2010, **114**, 6831-6840.
7. G. Sauvé, M. E. Cass, S. J. Doig, I. Lauermann, K. Pomykal and N. S. Lewis, *The Journal of Physical Chemistry B*, 2000, **104**, 3488-3491.

8. G. Zanotti, N. Angelini, S. Notarantonio, A. M. Paoletti, G. Pennesi, G. Rossi, A. Lembo, D. Colonna, A. Di Carlo, A. Reale, T. M. Brown and G. Calogero, *International Journal of Photoenergy*, 2010, **2010**.
9. P. Y. Reddy, L. Giribabu, C. Lyness, H. J. Snaith, C. Vijaykumar, M. Chandrasekharam, M. Lakshmikantam, J.-H. Yum, K. Kalyanasundaram, M. Grätzel and M. K. Nazeeruddin, *Angewandte Chemie International Edition*, 2007, **46**, 373-376.
10. L. Giribabu, C. Vijay Kumar, V. Gopal Reddy, P. Yella Reddy, C. Srinivasa Rao, S.-R. Jang, J.-H. Yum, M. K. Nazeeruddin and M. Grätzel, *Solar Energy Materials and Solar Cells*, 2007, **91**, 1611-1617.
11. S. Wenger, P.-A. Bouit, Q. Chen, J. l. Teuscher, D. D. Censo, R. Humphry-Baker, J.-E. Moser, J. L. Delgado, N. Martín, S. M. Zakeeruddin and M. Grätzel, *Journal of the American Chemical Society*, 2010, **132**, 5164-5169.
12. S. Kim, J. K. Lee, S. O. Kang, J. Ko, J. H. Yum, S. Fantacci, F. De Angelis, D. Di Censo, M. K. Nazeeruddin and M. Grätzel, *Journal of the American Chemical Society*, 2006, **128**, 16701-16707.
13. Z.-S. Wang, Y. Cui, Y. Dan-oh, C. Kasada, A. Shinpo and K. Hara, *The Journal of Physical Chemistry C*, 2007, **111**, 7224-7230.
14. A. Hagfeldt, G. Boschloo, L. Sun, L. Kloo and H. Pettersson, *Chemical Reviews*, 2010, **110**, 6595-6663.
15. I. K. Ding, J. Zhu, W. Cai, S.-J. Moon, N. Cai, P. Wang, S. M. Zakeeruddin, M. Grätzel, M. L. Brongersma, Y. Cui and M. D. McGehee, *Advanced Energy Materials*, 2011, **1**, 52-57.
16. M. J. Scott, J. J. Nelson, S. Caramori, C. A. Bignozzi and C. M. Elliott, *Inorganic Chemistry*, 2007, **46**, 10071-10078.
17. T. C. Li, A. M. Spokoyny, C. She, O. K. Farha, C. A. Mirkin, T. J. Marks and J. T. Hupp, *Journal of the American Chemical Society*, 2010, **132**, 4580-4582.
18. S. Nakade, Y. Makimoto, W. Kubo, T. Kitamura, Y. Wada and S. Yanagida, *The Journal of Physical Chemistry B*, 2005, **109**, 3488-3493.
19. B. M. Klahr and T. W. Hamann, *The Journal of Physical Chemistry C*, 2009, **113**, 14040-14045.
20. W. Kubo, K. Murakoshi, T. Kitamura, Y. Wada, K. Hanabusa, H. Shirai and S. Yanagida, *Chemistry Letters*, 1998, **27**, 1241-1242.
21. Y. Ren, Z. Zhang, E. Gao, S. Fang and S. Cai, *Journal of Applied Electrochemistry*, 2001, **31**, 445-447.
22. Y. Saito, T. Kitamura, Y. Wada and S. Yanagida, *Synthetic Metals*, 2002, **131**, 185-187.
23. P. Ravirajan, A. M. Peiró, M. K. Nazeeruddin, M. Graetzel, D. D. C. Bradley, J. R. Durrant and J. Nelson, *The Journal of Physical Chemistry B*, 2006, **110**, 7635-7639.
24. U. Bach, D. Lupo, P. Comte, J. E. Moser, F. Weissortel, J. Salbeck, H. Spreitzer and M. Gratzel, *Nature*, 1998, **395**, 583-585.
25. U. Bach, K. De Cloedt, H. Spreitzer and M. Grätzel, *Advanced Materials*, 2000, **12**, 1060-1063.
26. K. Tennakone, G. R. R. A. Kumara, A. R. Kumarasinghe, K. G. U. Wijayantha and P. M. Sirimanne, *Semiconductor Science and Technology*, 1995, **10**, 1689.
27. G. R. R. A. Kumara, A. Konno, G. K. R. Senadeera, P. V. V. Jayaweera, D. B. R. A. De Silva and K. Tennakone, *Solar Energy Materials and Solar Cells*, 2001, **69**, 195-199.

28. J. Bandara and H. Weerasinghe, *Solar Energy Materials and Solar Cells*, 2005, **85**, 385-390.
29. N. Papageorgiou, W. F. Maier and M. Gratzel, *Journal of The Electrochemical Society*, 1997, **144**, 876-884.
30. H. Pettersson, T. Gruszecki, R. Bernhard, L. Häggman, M. Gorlov, G. Boschloo, T. Edvinsson, L. Kloo and A. Hagfeldt, *Progress in Photovoltaics: Research and Applications*, 2007, **15**, 113-121.
31. A. Kay and M. Grätzel, *Solar Energy Materials and Solar Cells*, 1996, **44**, 99-117.
32. A. Hauch and A. Georg, *Electrochimica Acta*, 2001, **46**, 3457-3466.
33. L. Bay, K. West, B. Winther-Jensen and T. Jacobsen, *Solar Energy Materials and Solar Cells*, 2006, **90**, 341-351.
34. M. Wang, A. M. Anghel, B. t. Marsan, N.-L. Cevey Ha, N. Pootrakulchote, S. M. Zakeeruddin and M. Grätzel, *Journal of the American Chemical Society*, 2009, **131**, 15976-15977.
35. J. Yu, J. Fan and K. Lv, *Nanoscale*, 2010, **2**, 2144-2149.
36. Y. Alivov and Z. Y. Fan, *Applied Physics Letters*, 2009, **95**, 063504.
37. D. Chen, F. Huang, Y.-B. Cheng and R. A. Caruso, *Advanced Materials*, 2009, **21**, 2206-2210.
38. X. Feng, K. Shankar, O. K. Varghese, M. Paulose, T. J. Latempa and C. A. Grimes, *Nano Letters*, 2008, **8**, 3781-3786.
39. H. Hafez, Z. Lan and Q. Li, *Nanotechnology, Science and Applications*, 2010, **3**, 45-51.
40. S. R. Gajjela, K. Ananthanarayanan, C. Yap, M. Gratzel and P. Balaya, *Energy & Environmental Science*, 2010, **3**, 838-845.
41. I. C. Baek, M. Vithal, J. A. Chang, J.-H. Yum, M. K. Nazeeruddin, M. Grätzel, Y.-C. Chung and S. I. Seok, *Electrochemistry Communications*, 2009, **11**, 909-912.
42. J. Han, F. Fan, C. Xu, S. Lin, M. Wei, X. Duan and Z. L. Wang, *Nanotechnology*, 2010, **21**, 405203.
43. L. Zhang, Y. Shi, S. Peng, J. Liang, Z. Tao and J. Chen, *Journal of Photochemistry and Photobiology A: Chemistry*, 2008, **197**, 260-265.
44. R. Jose, V. Thavasi and S. Ramakrishna, *Journal of the American Ceramic Society*, 2009, **92**, 289-301.
45. M. J. Cass, F. L. Qiu, A. B. Walker, A. C. Fisher and L. M. Peter, *The Journal of Physical Chemistry B*, 2002, **107**, 113-119.
46. K. Yu and J. Chen, *Nanoscale Research Letters*, 2008, **4**, 1-10.
47. D. Kuang, J. r. m. Brillet, P. Chen, M. Takata, S. Uchida, H. Miura, K. Sumioka, S. M. Zakeeruddin and M. Grätzel, *ACS Nano*, 2008, **2**, 1113-1116.
48. B.-X. Lei, J.-Y. Liao, R. Zhang, J. Want, C.-Y. Su and D.-B. Kuang, *Journal of Physical Chemistry C*, 2010, **114**, 15228-15233.
49. B. Tan and Y. Wu, *The Journal of Physical Chemistry B*, 2006, **110**, 15932-15938.
50. K. Asagoe, S. Ngamsinlapasathian, Y. Suzuki and S. Yoshikawa, *Central European Journal of Chemistry*, 2007, **5**, 605-619.
51. Y. Qiu, W. Chen and S. Yang, *Angewandte Chemie International Edition*, 2010, **49**, 3675-3679.
52. C. Yip, C. Mak, A. Djurišić, Y. Hsu and W. Chan, *Applied Physics A: Materials Science & Processing*, 2008, **92**, 589-593.

53. G. K. Mor, K. Shankar, M. Paulose, O. K. Varghese and C. A. Grimes, *Nano Letters*, 2005, **6**, 215-218.
54. K. Zhu, N. R. Neale, A. Miedaner and A. J. Frank, *Nano Letters*, 2006, **7**, 69-74.
55. C.-J. Lin, W.-Y. Yu and S.-H. Chien, *Journal of Materials Chemistry*, 2010, **20**, 1073-1077.
56. Z. B. Xie, S. Adams, D. J. Blackwood and J. Wang, *Nanotechnology*, 2008, **19**, 405701.
57. P. Chen, J. Brillet, H. Bala, P. Wang, S. M. Zakeeruddin and M. Gratzel, *Journal of Materials Chemistry*, 2009, **19**, 5325-5328.
58. P. Roy, D. Kim, K. Lee, E. Spiecker and P. Schmuki, *Nanoscale*, 2010, **2**, 45-59.
59. J. T. Park, D. K. Roh, R. Patel, E. Kim, D. Y. Ryu and J. H. Kim, *Journal of Materials Chemistry*, 2010, **20**, 8521-8530.
60. H. Wang, C. T. Yip, K. Y. Cheung, A. B. Djurisic, M. H. Xie, Y. H. Leung and W. K. Chan, *Applied Physics Letters*, 2006, **89**, 2221502.
61. J.-K. Oh, J.-K. Lee, H.-S. Kim, S.-B. Han and K.-W. Park, *Chemistry of Materials*, 2009, **22**, 1114-1118.
62. F. Sauvage, F. Di Fonzo, A. Li Bassi, C. S. Casari, V. Russo, G. Divitini, C. Ducati, C. E. Bottani, P. Comte and M. Graetzel, *Nano Letters*, 2010, **10**, 2562-2567.
63. W. Shao, F. Gu, C. Li and M. Lu, *Inorganic Chemistry*, 2010, **49**, 5453-5459.
64. Y. Mao and S. S. Wong, *Journal of the American Chemical Society*, 2006, **128**, 8217-8226.
65. E. Ghadiri, N. Taghavinia, S. M. Zakeeruddin, M. Grätzel and J.-E. Moser, *Nano Letters*, 2010, **10**, 1632-1638.
66. Y. Mao, M. Kanungo, T. Hemraj-Benny and S. S. Wong, *The Journal of Physical Chemistry B*, 2005, **110**, 702-710.
67. S. Ito, T. N. Murakami, P. Comte, P. Liska, C. Grätzel, M. K. Nazeeruddin and M. Grätzel, *Thin Solid Films*, 2008, **516**, 4613-4619.
68. A. Zaban, M. Greenshtein and J. Bisquert, *ChemPhysChem*, 2003, **4**, 859-864.
69. M. Koelsch, S. Cassaignon, C. Ta Thanh Minh, J. F. Guillemoles and J. P. Jolivet, *Thin Solid Films*, 2004, **451-452**, 86-92.
70. N. G. Park, J. van de Lagemaat and A. J. Frank, *The Journal of Physical Chemistry B*, 2000, **104**, 8989-8994.
71. F. Huang, D. Chen, X. L. Zhang, R. A. Caruso and Y.-B. Cheng, *Advanced Functional Materials*, 2010, **20**, 1301-1305.
72. F. d. r. Sauvage, D. Chen, P. Comte, F. Huang, L.-P. Heiniger, Y.-B. Cheng, R. A. Caruso and M. Graetzel, *ACS Nano*, 2010, **4**, 4420-4425.
73. Y. Zhang, Z. Xie and J. Wang, *ACS Applied Materials & Interfaces*, 2009, **1**, 2789-2795.
74. P. S. Archana, R. Jose, C. Vijila and S. Ramakrishna, *The Journal of Physical Chemistry C*, 2009, **113**, 21538-21542.
75. J. Jiu, S. Isoda, F. Wang and M. Adachi, *The Journal of Physical Chemistry B*, 2006, **110**, 2087-2092.
76. K. Hou, B. Tian, F. Li, Z. Bian, D. Zhao and C. Huang, *Journal of Materials Chemistry*, 2005, **15**, 2414-2420.
77. Y.-Q. Wang, S.-G. Chen, X.-H. Tang, O. Palchik, A. Zaban, Y. Koltypin and A. Gedanken, *Journal of Materials Chemistry*, 2001, **11**, 521-526.
78. W. Meili, C. Huang, Y. Cao, Q. Yu, Z. Deng, Y. Liu, Z. Huang, J. Huang, Q. Huang, W. Guo and J. Liang, *Journal of Physics D: Applied Physics*, 2009, **42**, 155104.

79. S. Nakade, Y. Saito, W. Kubo, T. Kitamura, Y. Wada and S. Yanagida, *The Journal of Physical Chemistry B*, 2003, **107**, 8607-8611.
80. Y. Alivov and Z. Fan, *Journal of Materials Science*, 2010, **45**, 2902-2906.
81. S. Burnside, J.-E. Moser, K. Brooks, M. Grätzel and D. Cahen, *The Journal of Physical Chemistry B*, 1999, **103**, 9328-9332.
82. S. Yang, H. Kou, H. Wang, K. Cheng and J. Wang, *Electrochimica Acta*, 2009, **55**, 305-310.

Chapter 6. Conclusions

Working at the nanoscale represents an interesting and exciting area for research, owing to the distinctive ability of materials to alter their properties simply by changing their size. However, it is critical to be able to rationally design and effectively control the size and shape of nanomaterials. This is of particular importance for 1D nanomaterials, where the ability to spatially confine a material to grow at the nanoscale level is of utmost importance. Additionally, 1D nanomaterials are of interest, due to the fact that they are the smallest unit which can effectively transport properties through a material. While many materials are of interest for study at the nanoscale, the analysis of nanoscale metal oxides is of particular interest, owing to their stability and robustness. In this work, not only were the properties of several 1D nanoscale metal oxides studied but also the methods which were utilized for their formation were also probed. From a synthetic approach, this work has shown that many different methods can be utilized for the synthesis of 1D nanoscale metal oxide materials, often times requiring the application of multiple steps. It has also been shown that the application of nanoscale materials as a template, or as a building block, for a desired material is a highly advantageous synthetic route for 1D nanoscale metal oxide materials. Furthermore, correlations between morphology and device performance were investigated, allowing us to probe the properties of our nanoscale materials under device-like operations. This gives us insight into essential device design characteristics, as well as information on how our materials behave during operation.

In Chapter 2, a combination of synthetic techniques was successfully utilized to synthesize nanowires of V_2O_3. This method first involved generation of single-crystalline nanowires of VO_2 via a hydrothermal protocol. A subsequent high temperature annealing in a reducing atmosphere resulted in the complete transformation of the VO_2 nanowires into V_2O_3

nanowires. This method not only maintained the 1D nanoscale morphology, for the most part, but also ensured that the beneficial single-crystalline nature present within the starting material was retained. The investigation of the electronic and magnetic properties of the V_2O_3 nanowires revealed that although the material maintained dimensions on the nanoscale, the properties of the bulk were still conserved. More specifically, the material exhibited a MIT at ~150 K, consistent with reports for bulk V_2O_3. This is an interesting observation, for it allows one to take advantage of bulk properties, while maintaining a nanoscale device size. This particular property of our nanoscale material can be quite useful as a nanoscale temperature sensor, thus allowing for an accurate measure, and control, of temperature on the nanoscale while still maintaining the accuracy and magnitude of a larger, macro scale device.

In Chapter 3, the synthesis of $LiNbO_3$ nanowires was completed via a molten salt synthesis technique. Similar to the method utilized in Chapter 2, 1D nanoscale Nb_2O_5 was utilized as both the precursor and the template for the formation of $LiNbO_3$ nanowires. It was found that careful control of experimental reaction parameters, such as salt, temperature, and time allowed for the desired 1D morphology of the precursor to be mostly maintained. In addition to this beneficial nanowire morphology, the $LiNbO_3$ material is single-crystalline in nature, thereby rendering it highly desirable for optical applications, such as optical waveguides and optical storage. Data analysis of the nanowires by HRTEM was consistent with a preferential alignment of the *c*-axis along the axial direction of the nanowires, again highlighting the exciting possibilities for optical applications. The probing of individual nanowires via Raman spectroscopy revealed the high quality of the nanowires as well as a propagation of optical properties nearly along the axis of the nanowires. This is highly desirable for device

applications, where it is crucial to transport properties along the axis of the nanowires with minimal disruption from crystal defects or crystal misalignments.

In Chapter 4, exploration of a template-inspired sol-gel reaction was undertaken for the synthesis of Cr_2O_3 nanowires. This method proved to be facile and quite versatile, allowing for the creation of various sizes of nanowires, strictly based upon the physical pore size of the template channels utilized in the synthesis. Furthermore, the application of polycarbonate templates resulted in the complete removal and isolation of the nanowires during the subsequent high temperature crystallization and annealing step. Thus, it is not essential to either further purify or isolate the nanowires from the template utilized for the synthesis. Electron microscopy investigations (TEM and HRTEM) have revealed that the nanowires consisted of individual, single-crystalline nanoparticles physically adjoined to form a hierarchical 1D nanowire architecture. Subsequent analysis of the magnetic properties of the nanowire sample was consistent with a small exchange bias, owing to the small size of the constituent nanoparticles. This is a particularly interesting result, as it shows that the properties of a larger structure, in this case the 200 nm nanowire, are governed by the constituent component crystallites contained within, therefore, combining the ease of working with slightly larger structures with the advantageous properties of the smaller nanometer scale. These nanowires also showed activity towards the degradation of $KClO_4$, a model for pollutants, thereby rendering our Cr_2O_3 nanowires as a potential remediation catalyst. Furthermore, the chromium oxide nanowires possessed interesting electronic properties, making them desirable in devices such as gas sensors for various, potentially harmful, gases like hydrogen or ammonia..

Finally, in Chapter 5, the focus shifted from the synthesis of nanoscale materials to applications of nanomaterials in useful devices. The application of various morphologies of TiO_2

was investigated for use in dye sensitized solar cell architectures. It was noted that, although a nanostructure may appear to have an extremely beneficial morphology, it is crucial to observe its applicability in an efficient device structure. More specifically, although our 3D sea-urchin-like materials exhibited a high functional surface area, when applied to a solar cell, it was found that the material packed inefficiently, thereby resulting in a loss of dye adsorption as well as a decrease in the number of possible electron pathways throughout the cell. However, another important factor observed was that some poor materials' properties can be mitigated by utilizing a combination of different morphologies. More specifically, when a small amount of nanoparticles was added to the 3D sea-urchin-like material, an increase of nearly 1% was observed in the solar cell efficiency. This enhancement was attributed to the increased dye adsorption, as well as to increased bridging possibilities between the individual 3D motifs. The use of various other titanates was also investigated for uses in solar cells. It was found that these materials were far from ideal, thereby revealing low dye adsorption, low adhesion to the FTO, and overall low observed efficiencies.

It is through this compilation of work that it has been shown that various techniques can be utilized in order to effectively create 1D nanomaterials. Indeed, the crystallinity, phase, and substructure of the material can be altered through the application of different synthetic techniques. It has also been shown that the fabrication of working devices is imperative towards the full characterization of a material, for it is only in a working device that advances in materials' synthesis and generation can be fully exploited.

Bibiliography

1. Y. Xia, P. Yang, Y. Sun, Y. Wu, B. Mayers, B. Gates, Y. Yin, F. Kim and H. Yan, *Advanced Materials*, 2003, **15**, 353-389.
2. A. L. Tiano, C. Koenigsmann, A. C. Santulli and S. S. Wong, *Chemical Communications*, 2010, **46**, 8093-8130.
3. H. J. Li, W. G. Lu, J. J. Li, X. D. Bai and C. Z. Gu, *Physical Review Letters*, 2005, **95**, 086601.
4. D. Gunlycke, J. W. Mintmire and C. T. White, *The Journal of Physical Chemistry Letters*, 2010, **1**, 1082-1085.
5. L. Vayssieres, C. Sathe, S. M. Butorin, D. K. Shuh, J. Nordgren and J. Guo, *Advanced Materials*, 2005, **17**, 2320-2323.
6. J. Hu, T. W. Odom and C. M. Lieber, *Accounts of Chemical Research*, 1999, **32**, 435-445.
7. M. Bruno, M. Palummo, A. Marini, R. Del Sole, V. Olevano, A. N. Kholod and S. Ossicini, *Physical Review B*, 2005, **72**, 153310.
8. S. Jia and et al., *Nanotechnology*, 2009, **20**, 255202.
9. L.-L. Li, Y.-J. Chen, H.-P. Wu, N. S. Wang and E. W.-G. Diau, *Energy & Environmental Science*, 2011.
10. M. I. Stockman, *Physical Review Letters*, 2004, **93**, 137404.
11. D. Vanmaekelbergh and L. K. van Vugt, *Nanoscale*, 2011, **3**, 2783-2800.
12. L. Vayssieres and M. Graetzel, *Angewandte Chemie*, 2004, **116**, 3752-3756.
13. X.-F. Shen and X.-P. Yan, *Angewandte Chemie International Edition*, 2007, **46**, 7659-7663.
14. X. Zhidong and et al., *Nanotechnology*, 2005, **16**, 2647.
15. E. E. Foos, T. J. Zega, J. G. Tischler, R. M. Stroud and J. E. Boercker, *Journal of Materials Chemistry*, 2011, **21**, 2616-2623.
16. W. He and J. H. Dickerson, *Thermally driven isotropic crystallinity breaking of nanocrystals: Insight into the assembly of EuS nanoclusters and nanorods with oleate ligands*, AIP, 2011.
17. G. Wulff, *Z. Kristallogr. Mineral.*, 1901, **34**, 449-530.
18. C.-C. Chen, C.-Y. Chao and Z.-H. Lang, *Chemistry of Materials*, 2000, **12**, 1516-1518.
19. J. W. Grebinski, K. L. Hull, J. Zhang, T. H. Kosel and M. Kuno, *Chemistry of Materials*, 2004, **16**, 5260-5272.
20. M. Kuno, O. Ahmad, V. Protasenko, D. Bacinello and T. H. Kosel, *Chemistry of Materials*, 2006, **18**, 5722-5732.
21. T. K. Sau and C. J. Murphy, *Journal of the American Chemical Society*, 2004, **126**, 8648-8649.
22. K. Vasilev, T. Zhu, M. Wilms, G. Gillies, I. Lieberwirth, S. Mittler, W. Knoll and M. Kreiter, *Langmuir*, 2005, **21**, 12399-12403.
23. Y. Sun, B. Mayers, T. Herricks and Y. Xia, *Nano Letters*, 2003, **3**, 955-960.
24. Y. Sun, Y. Yin, B. T. Mayers, T. Herricks and Y. Xia, *Chemistry of Materials*, 2002, **14**, 4736-4745.
25. Y. Song, R. M. Garcia, R. M. Dorin, H. Wang, Y. Qiu, E. N. Coker, W. A. Steen, J. E. Miller and J. A. Shelnutt, *Nano Letters*, 2007, **7**, 3650-3655.
26. A. Chen and P. Holt-Hindle, *Chemical Reviews*, 2010, **110**, 3767-3804.

27. Y. Chang, M. L. Lye and H. C. Zeng, *Langmuir*, 2005, **21**, 3746-3748.
28. R. R. Piticescu, C. Monty, D. Taloi, A. Motoc and S. Axinte, *Journal of the European Ceramic Society*, 2001, **21**, 2057-2060.
29. X. P. Gao, J. L. Bao, G. L. Pan, H. Y. Zhu, P. X. Huang, F. Wu and D. Y. Song, *The Journal of Physical Chemistry B*, 2004, **108**, 5547-5551.
30. C.-Y. Xu, L. Zhen, R. Yang and Z. L. Wang, *Journal of the American Chemical Society*, 2007, **129**, 15444-15445.
31. W. Zhou, H. Liu, R. I. Boughton, G. Du, J. Lin, J. Wang and D. Liu, *Journal of Materials Chemistry*, 2010, **20**, 5993-6008.
32. Z.-Y. Jiang, T. Xu, Z.-X. Xie, Z.-W. Lin, X. Zhou, X. Xu, R.-B. Huang and L.-S. Zheng, *The Journal of Physical Chemistry B*, 2005, **109**, 23269-23273.
33. L. Liu, B. Li, D. Yu, Y. Cui, X. Zhou and W. Ding, *Chemical Communications*, 2010, **46**, 427-429.
34. L. L. Hench and J. K. West, *Chemical Reviews*, 1990, **90**, 33-72.
35. M. Niederberger, *Accounts of Chemical Research*, 2007, **40**, 793-800.
36. B. B. Lakshmi, P. K. Dorhout and C. R. Martin, *Chemistry of Materials*, 1997, **9**, 857-862.
37. N. Li and C. R. Martin, *Journal of The Electrochemical Society*, 2001, **148**, A164-A170.
38. A. Huczko, *Applied Physics A: Materials Science & Processing*, 2000, **70**, 365-376.
39. J. Wang and Y. Li, *Advanced Materials*, 2003, **15**, 445-447.
40. X. Jiaqiang, C. Yuping, C. Daoyong and S. Jianian, *Sensors and Actuators B: Chemical*, 2006, **113**, 526-531.
41. Q. Yang, K. Tang, C. Wang, Y. Qian and S. Zhang, *The Journal of Physical Chemistry B*, 2002, **106**, 9227-9230.
42. Z. Wen, Q. Wang and J. Li, *Advanced Functional Materials*, 2008, **18**, 959-964.
43. J. M. Patete, X. Peng, C. Koenigsmann, Y. Xu, B. Karn and S. S. Wong, *Green Chemistry*, 2011, **13**, 482-519.
44. G. Sun, M. Cao, Y. Wang, C. Hu, Y. Liu, L. Ren and Z. Pu, *Materials Letters*, 2006, **60**, 2777-2782.
45. L. Liu, H.-Z. Kou, W. Mo, H. Liu and Y. Wang, *The Journal of Physical Chemistry B*, 2006, **110**, 15218-15223.
46. Z. Liu, S. Li, Y. Yang, S. Peng, Z. Hu and Y. Qian, *Advanced Materials*, 2003, **15**, 1946-1948.
47. Q. Liu, H. Liu, Y. Liang, Z. Xu and G. Yin, *Materials Research Bulletin*, 2006, **41**, 697-702.
48. B. A. Hernandez, K.-S. Chang, E. R. Fisher and P. K. Dorhout, *Chemistry of Materials*, 2002, **14**, 480-482.
49. B. B. Lakshmi, C. J. Patrissi and C. R. Martin, *Chemistry of Materials*, 1997, **9**, 2544-2550.
50. Y.-J. Han, J. M. Kim and G. D. Stucky, *Chemistry of Materials*, 2000, **12**, 2068-2069.
51. M. Numata, K. Sugiyasu, T. Hasegawa and S. Shinkai, *Angewandte Chemie International Edition*, 2004, **43**, 3279-3283.
52. A. Khanal, Y. Inoue, M. Yada and K. Nakashima, *Journal of the American Chemical Society*, 2007, **129**, 1534-1535.
53. C. Bae, H. Yoo, S. Kim, K. Lee, J. Kim, M. M. Sung and H. Shin, *Chemistry of Materials*, 2008, **20**, 756-767.

54. L. Miao, S. Tanemura, S. Toh, K. Kaneko and M. Tanemura, *Journal of Crystal Growth*, 2004, **264**, 246-252.
55. H. Cao, X. Qiu, Y. Liang, M. Zhao and Q. Zhu, *Applied Physics Letters*, 2006, **88**, 241112-241112-241113.
56. T.-J. Park, Y. Mao and S. S. Wong, *Chemical Communications*, 2004, 2708-2709.
57. Z. Miao, D. Xu, J. Ouyang, G. Guo, X. Zhao and Y. Tang, *Nano Letters*, 2002, **2**, 717-720.
58. P. Katta, M. Alessandro, R. D. Ramsier and G. G. Chase, *Nano Letters*, 2004, **4**, 2215-2218.
59. Z. Liu, D. D. Sun, P. Guo and J. O. Leckie, *Nano Letters*, 2006, **7**, 1081-1085.
60. C. Wang, K.-W. Yan, Y.-D. Lin and P. C. H. Hsieh, *Macromolecules*, 2010, **43**, 6389-6397.
61. M. S. Peresin, Y. Habibi, A.-H. Vesterinen, O. J. Rojas, J. J. Pawlak and J. V. Seppälä, *Biomacromolecules*, 2010, **11**, 2471-2477.
62. S. Yurong and et al., *Nanotechnology*, 2011, **22**, 285609.
63. S. De Vrieze, T. Van Camp, A. Nelvig, B. Hagström, P. Westbroek and K. De Clerck, *Journal of Materials Science*, 2009, **44**, 1357-1362.
64. J. M. Deitzel, J. Kleinmeyer, D. Harris and N. C. Beck Tan, *Polymer*, 2001, **42**, 261-272.
65. T. Uyar and F. Besenbacher, *Polymer*, 2008, **49**, 5336-5343.
66. W. K. Son, J. H. Youk, T. S. Lee and W. H. Park, *Polymer*, 2004, **45**, 2959-2966.
67. W. Zuo, M. Zhu, W. Yang, H. Yu, Y. Chen and Y. Zhang, *Polymer Engineering & Science*, 2005, **45**, 704-709.
68. V. Beachley and X. Wen, *Materials Science and Engineering: C*, 2009, **29**, 663-668.
69. L. Wannatong, A. Sirivat and P. Supaphol, *Polymer International*, 2004, **53**, 1851-1859.
70. I.-D. Kim, A. Rothschild, B. H. Lee, D. Y. Kim, S. M. Jo and H. L. Tuller, *Nano Letters*, 2006, **6**, 2009-2013.
71. H. Chaobo and et al., *Nanotechnology*, 2006, **17**, 1558.
72. K. Sawicka and P. Gouma, *Journal of Nanoparticle Research*, 2006, **8**, 769-781.
73. C. E. Megiris and J. H. E. Glezer, *Chemical Engineering Science*, **47**, 3925-3934.
74. F. Duerinckx and J. Szlufcik, *Solar Energy Materials and Solar Cells*, 2002, **72**, 231-246.
75. W. G. Lee and S. I. Woo, *Journal of Materials Science Letters*, 2003, **22**, 1677-1678.
76. R. J. Potter, P. A. Marshall, P. R. Chalker, S. Taylor, A. C. Jones, T. C. Q. Noakes and P. Bailey, *Characterization of hafnium aluminate gate dielectrics deposited by liquid injection metalorganic chemical vapor deposition*, AIP, 2004.
77. Q.-G. Fu, H.-J. Li, X.-H. Shi, K.-Z. Li, J. Wei and Z.-B. Hu, *Materials Chemistry and Physics*, 2006, **100**, 108-111.
78. D. Wang and H. Dai, *Angewandte Chemie*, 2002, **114**, 4977-4980.
79. A. M. Cassell, J. A. Raymakers, J. Kong and H. Dai, *The Journal of Physical Chemistry B*, 1999, **103**, 6484-6492.
80. X.-P. Shen, H.-J. Liu, L. Pan, K.-M. Chen, J.-M. Hong and Z. Xu, *Chemistry Letters*, 2004, **33**, 1128-1129.
81. V. Khorenko, I. Regolin, S. Neumann, W. Prost, F.-J. Tegude and H. Wiggers, *Photoluminescence of GaAs nanowhiskers grown on Si substrate*, AIP, 2004.
82. H. T. Chen and et al., *Journal of Physics D: Applied Physics*, 2008, **41**, 025101.

83. J. Campos-Delgado, Y. A. Kim, T. Hayashi, A. Morelos-Gómez, M. Hofmann, H. Muramatsu, M. Endo, H. Terrones, R. D. Shull, M. S. Dresselhaus and M. Terrones, *Chemical Physics Letters*, 2009, **469**, 177-182.
84. Z. Zhang, J. Wang, H. Yuan, Y. Gao, D. Liu, L. Song, Y. Xiang, X. Zhao, L. Liu, S. Luo, X. Dou, S. Mou, W. Zhou and S. Xie, *The Journal of Physical Chemistry B*, 2005, **109**, 18352-18355.
85. X. P. Shen, M. Han, J. M. Hong, Z. Xue and Z. Xu, *Chemical Vapor Deposition*, 2005, **11**, 250-253.
86. G. Che, B. B. Lakshmi, C. R. Martin, E. R. Fisher and R. S. Ruoff, *Chemistry of Materials*, 1998, **10**, 260-267.
87. S. Xiao-Ping and et al., *Nanotechnology*, 2005, **16**, 2039.
88. L. Yu, B. O?Donnell, J.-L. Maurice and P. R. i. Cabarrocas, *Core-shell structure and unique faceting of Sn-catalyzed silicon nanowires*, AIP, 2010.
89. S. Paiman and et al., *Journal of Physics D: Applied Physics*, 2010, **43**, 445402.
90. E. Alarcon-Llado, S. Estrade, J. D. Prades, F. Hernandez-Ramirez, J. Arbiol, F. Peiro, J. Ibanez, L. Artus and J. R. Morante, *CrystEngComm*, 2011, **13**, 656-662.
91. H.-P. Wang, K.-Y. Lai, Y.-R. Lin, C.-A. Lin and J.-H. He, *Langmuir*, 2010, **26**, 12855-12858.
92. F. Demami, L. Ni, R. Rogel, A. C. Salaun and L. Pichon, *Procedia Engineering*, 2010, **5**, 351-354.
93. Y. Mo, J. J. Schwartz, M. H. Lynch, P. A. Ecton, A. Neogi, J. M. Perez, Y. Fujita, H. W. Seo, Q. Y. Chen, L. W. Tu and N. J. Ho, in *Nanoscale Photonics and Optoelectronics*, eds. Z. M. Wang and A. Neogi, Springer New York, 2011, pp. 131-156.
94. M. H. Huang, S. Mao, H. Feick, H. Yan, Y. Wu, H. Kind, E. Weber, R. Russo and P. Yang, *Science*, 2001, **292**, 1897-1899.
95. I. Iñiguez-de-la-Torre and et al., *Semiconductor Science and Technology*, 2010, **25**, 125013.
96. D. Cohen-Tanugi, A. Akey and N. Yao, *Nano Letters*, 2010, **10**, 852-859.
97. S. Reza, S. Marcin and A. Srinivasan, *Optical Society of America*, 2011, p. CE2_4.
98. B. Tian, X. Zheng, T. J. Kempa, Y. Fang, N. Yu, G. Yu, J. Huang and C. M. Lieber, *Nature*, 2007, **449**, 885-889.
99. N. D. Hoa, N. Van Quy and D. Kim, *Sensors and Actuators B: Chemical*, 2009, **142**, 253-259.
100. A. Kolmakov, Y. Zhang, G. Cheng and M. Moskovits, *Advanced Materials*, 2003, **15**, 997-1000.
101. C. S. Rout, S. Hari Krishna, S. R. C. Vivekchand, A. Govindaraj and C. N. R. Rao, *Chemical Physics Letters*, 2006, **418**, 586-590.
102. J. Li, Y. Lu, Q. Ye, M. Cinke, J. Han and M. Meyyappan, *Nano Letters*, 2003, **3**, 929-933.
103. H. Kind, H. Yan, B. Messer, M. Law and P. Yang, *Advanced Materials*, 2002, **14**, 158-160.
104. S. Han, W. Jin, D. Zhang, T. Tang, C. Li, X. Liu, Z. Liu, B. Lei and C. Zhou, *Chemical Physics Letters*, 2004, **389**, 176-180.
105. C. Koenigsmann, W.-p. Zhou, R. R. Adzic, E. Sutter and S. S. Wong, *Nano Letters*, 2010, **10**, 2806-2811.
106. C. Koenigsmann and S. S. Wong, *Energy & Environmental Science*, 2011, **4**, 1161-1176.

107. C. Koenigsmann, A. C. Santulli, K. Gong, M. B. Vukmirovic, W.-p. Zhou, E. Sutter, S. S. Wong and R. R. Adzic, *Journal of the American Chemical Society*, 2011, **133**, 9783-9795.
108. L. Shi, Y. Xu, S. Hark, Y. Liu, S. Wang, L.-m. Peng, K. Wong and Q. Li, *Nano Letters*, 2007, **7**, 3559-3563.
109. P. Christopher and S. Linic, *Journal of the American Chemical Society*, 2008, **130**, 11264-11265.
110. A. Fukuoka, N. Higashimoto, Y. Sakamoto, S. Inagaki, Y. Fukushima and M. Ichikawa, *Microporous and Mesoporous Materials*, 2001, **48**, 171-179.
111. W. Zhou, L. Yan, Y. Wang and Y. Zhang, *SiC nanowires: A photocatalytic nanomaterial*, AIP, 2006.
112. L. Liu, E. Pippel, R. Scholz and U. Gösele, *Nano Letters*, 2009, **9**, 4352-4358.
113. Y.-M. Lin, S. B. Cronin, J. Y. Ying, M. S. Dresselhaus and J. P. Heremans, *Transport properties of Bi nanowire arrays*, AIP, 2000.
114. B. S. Guiton, Q. Gu, A. L. Prieto, M. S. Gudiksen and H. Park, *Journal of the American Chemical Society*, 2004, **127**, 498-499.
115. P.-C. Chang and J. G. Lu, *Temperature dependent conduction and UV induced metal-to-insulator transition in ZnO nanowires*, AIP, 2008.
116. C. J. Patridge, T.-L. Wu, C. Jaye, B. Ravel, E. S. Takeuchi, D. A. Fischer, G. Sambandamurthy and S. Banerjee, *Nano Letters*, 2010, **10**, 2448-2453.
117. T. D. Manning, I. P. Parkin, M. E. Pemble, D. Sheel and D. Vernardou, *Chemistry of Materials*, 2004, **16**, 744-749.
118. E. Strelcov, Y. Lilach and A. Kolmakov, *Nano Letters*, 2009, **9**, 2322-2326.
119. C. Rossel, G. I. Meijer, D. Brémaud and D. Widmer, *Electrical current distribution across a metal?insulator?metal structure during bistable switching*, AIP, 2001.
120. Y. Sun, B. Qu, S. Jiang, C. Wu, B. Pan and Y. Xie, *Nanoscale*, 2011, **3**, 2609-2614.
121. D.-H. Kwon, K. M. Kim, J. H. Jang, J. M. Jeon, M. H. Lee, G. H. Kim, X.-S. Li, G.-S. Park, B. Lee, S. Han, M. Kim and C. S. Hwang, *Nat Nano*, 2010, **5**, 148-153.
122. A. C. Santulli, W. Xu, J. B. Parise, L. Wu, M. C. Aronson, F. Zhang, C.-Y. Nam, C. T. Black, A. L. Tiano and S. S. Wong, *Physical Chemistry Chemical Physics*, 2009, **11**, 3718-3726.
123. A. C. Santulli, H. Zhou, S. Berweger, M. B. Raschke, E. Sutter and S. S. Wong, *CrystEngComm*, 2010, **12**, 2675-2678.
124. A. C. Santulli, M. Feygenson, F. E. Camino, M. C. Aronson and S. S. Wong, *Chemistry of Materials*, 2011, **23**, 1000-1008.
125. A. C. Santulli and et al., *Nanotechnology*, 2011, **22**, 245402.
126. W. Chen, J. Peng, L. Mai, H. Yu and Y. Qi, *Chemistry Letters*, 2004, **33**, 1366-1367.
127. F. J. Morin, *Physical Review Letters*, 1959, **3**, 34.
128. N. Ballarini, A. Battisti, F. Cavani, A. Cericola, C. Cortelli, M. Ferrari, F. Trifirò and P. Arpentinier, *Applied Catalysis A: General*, 2006, **307**, 148-155.
129. E. V. Kondratenko, O. Ovsitser, J. Radnik, M. Schneider, R. Kraehnert and U. Dingerdissen, *Applied Catalysis A: General*, 2007, **319**, 98-110.
130. S. J. Yun, B.-G. Chae, J. W. Lim, J.-S. Noh and H.-T. Kim, *Electrochemical and Solid-State Letters*, 2008, **11**, H173-H175.
131. C. Tsang and A. Manthiram, *Journal of The Electrochemical Society*, 1997, **144**, 520-524.

132. J. Shi, S. Zhou, B. You and L. Wu, *Solar Energy Materials and Solar Cells*, 2007, **91**, 1856-1862.
133. B.-G. Chae, H.-T. Kim, S.-J. Yun, B.-J. Kim, Y.-W. Lee, D.-H. Youn and K.-Y. Kang, *Electrochemical and Solid-State Letters*, 2006, **9**, C12-C14.
134. G. A. Rozgonyi and W. J. Polito, *Journal of The Electrochemical Society*, 1968, **115**, 56-57.
135. L.-Q. Mai, W. Chen, Q. Xu, J.-F. Peng and Q.-Y. Zhu, *Chemical Physics Letters*, 2003, **382**, 307-312.
136. C. Tenailleau, E. Suard, J. Rodriguez-Carvajal and P. Lacorre, *Journal of Magnetism and Magnetic Materials*, 2004, **278**, 57-67.
137. D. S. Toledano, P. Metcalf and V. E. Henrich, *Surface Science*, 2001, **472**, 21-32.
138. J. B. Goodenough, *Journal of Solid State Chemistry*, 1971, **3**, 490-500.
139. A. Cavalleri, C. Toth, C. W. Siders, J. A. Squier, F. Raksi, P. Forget and J. C. Kieffer, *Physical Review Letters*, 2001, **87**, 237401.
140. Y. Muraoka and Z. Hiroi, *journal article*, 2002, **80**, 583-585.
141. R. Aliev and V. Klimov, *Physics of the Solid State*, 2004, **46**, 532-536.
142. I. Balberg and S. Trokman, *High contrast optical storage in VO_2 films*, AIP, 1975.
143. P. Liu, S.-H. Lee, H. M. Cheong, C. E. Tracy, J. R. Pitts and R. D. Smith, *Journal of The Electrochemical Society*, 2002, **149**, H76-H80.
144. G. Sudant, E. Baudrin, B. Dunn and J.-M. Tarascon, *Journal of The Electrochemical Society*, 2004, **151**, A666-A671.
145. A. Azens, G. Gustavsson, R. Karmhag and C. G. Granqvist, *Solid State Ionics*, 2003, **165**, 1-5.
146. X. Chen, X. Wang, Z. Wang, J. Wan, J. Liu and Y. Qian, *Nanotechnology*, 2004, **15**, 1685.
147. W. Chen, L. Mai, Y. Qi and Y. Dai, *Journal of Physics and Chemistry of Solids*, **67**, 896-902.
148. A. Liu, M. Ichihara, I. Honma and H. Zhou, *Electrochemistry Communications*, 2007, **9**, 1766-1771.
149. M. Niederberger, H.-J. Muhr, F. Krumeich, F. Bieri, D. Günther and R. Nesper, *Chemistry of Materials*, 2000, **12**, 1995-2000.
150. J. M. Reinoso, H.-J. Muhr, F. Krumeich, F. Bieri and R. Nesper, *Helvetica Chimica Acta*, 2000, **83**, 1724-1733.
151. H. J. Muhr, F. Krumeich, U. P. Schönholzer, F. Bieri, M. Niederberger, L. J. Gauckler and R. Nesper, *Advanced Materials*, 2000, **12**, 231-234.
152. F. Krumeich, H. J. Muhr, M. Niederberger, F. Bieri, B. Schnyder and R. Nesper, *Journal of the American Chemical Society*, 1999, **121**, 8324-8331.
153. F. Krumeich, H.-J. Muhr, M. Niederberger, F. Bieri and R. Nesper, *Zeitschrift für anorganische und allgemeine Chemie*, 2000, **626**, 2208-2216.
154. M. E. Spahr, P. Stoschitzki-Bitterli, R. Nesper, O. Haas and P. Novak, *Journal of The Electrochemical Society*, 1999, **146**, 2780-2783.
155. S. Mathur, T. Ruegamer and I. Grobelsek, *Chemical Vapor Deposition*, 2007, **13**, 42-47.
156. R. Lopez, T. E. Haynes, L. A. Boatner, L. C. Feldman and J. R. F. Haglund, *Opt. Lett.*, 2002, **27**, 1327-1329.
157. J. M. Baik, M. H. Kim, C. Larson, A. M. Wodtke and M. Moskovits, *The Journal of Physical Chemistry C*, 2008, **112**, 13328-13331.

158. B. S. Allimi, S. P. Alpay, C. K. Xie, B. O. Wells, J. I. Budnick and D. M. Pease, *Applied Physics Letters*, 2008, **92**, 202105.
159. F. Sediri and N. Gharbi, *Materials Science and Engineering: B*, 2005, **123**, 136-138.
160. D. M. Moffatt, J. P. Runt, A. Halliyal and R. E. Newnham, *Journal of Materials Science*, 1989, **24**, 609-614.
161. G. van der Lee, B. Schuller, H. Post, T. L. F. Favre and V. Ponec, *Journal of Catalysis*, 1986, **98**, 522-529.
162. C. Zheng, X. Zhang, S. He, Q. Fu and D. Lei, *Journal of Solid State Chemistry*, 2003, **170**, 221-226.
163. K. Zhang, X. Sun, G. Lou, X. Liu, H. Li and Z. Su, *Materials Letters*, 2005, **59**, 2729-2731.
164. Z. Yang, P. Cai, L. Chen, Y. Gu, L. Shi, A. Zhao and Y. Qian, *Journal of Alloys and Compounds*, 2006, **420**, 229-232.
165. N. Pinna, M. Antonietti and M. Niederberger, *Colloids and Surfaces A: Physicochemical and Engineering Aspects*, 2004, **250**, 211-213.
166. S. A. Corr, M. Grossman, J. D. Furman, B. C. Melot, A. K. Cheetham, K. R. Heier and R. Seshadri, *Chemistry of Materials*, 2008, **20**, 6396-6404.
167. G. Anderson, *Acta Chemica Scandinavica*, 1956, **10**, 623.
168. A. D. Burton and P. A. Cox, *Philisopical Magazine*, 1985, **51**, 255.
169. H. Liu, O. Vasquez, V. R. Santiago, L. Díaz and F. E. Fernandez, *Journal of Luminescence*, 2004, **108**, 233-238.
170. P. Baum, D.-S. Yang and A. H. Zewail, *Science*, 2007, **318**, 788-792.
171. M. B. Sahana, G. N. Subbanna and S. A. Shivashankar, *journal article*, 2002, **92**, 6495-6504.
172. J. C. Rakotoniaina, R. Mokrani-Tamellin, J. R. Gavarri, G. Vacquier, A. Casalot and G. Calvarin, *Journal of Solid State Chemistry*, 1993, **103**, 81-94.
173. Y. Oka, T. Yao and N. Yamamoto, *Journal of Materials Chemistry*, 1991, **1**, 815-818.
174. G. T. Chandrappa, N. Steunou, S. Cassaignon, C. Bauvais and J. Livage, *Catalysis Today*, 2003, **78**, 85-89.
175. Y. Mao and S. S. Wong, *Journal of the American Chemical Society*, 2006, **128**, 8217-8226.
176. Z. Gui, R. Fan, W. Mo, X. Chen, L. Yang, S. Zhang, Y. Hu, Z. Wang and W. Fan, *Chemistry of Materials*, 2002, **14**, 5053-5056.
177. C. Leroux, G. Nihoul and G. Van Tendeloo, *Physical Review B*, 1998, **57**, 5111.
178. D. S. Su and R. Schlögl, *Catalysis Letters*, 2002, **83**, 115-119.
179. C. V. Ramana, S. Utsunomiya, R. C. Ewing and U. Becker, *Solid State Communications*, 2006, **137**, 645-649.
180. Y. Ueda, K. Kosuge and S. Kachi, *Journal of Solid State Chemistry*, 1980, **31**, 171-188.
181. R. N. Bhowmik, R. Nagarajan and R. Ranganathan, *Physical Review B*, 2004, **69**, 054430.
182. R. N. Bhowmik and R. Ranganathan, *Solid State Communications*, 2007, **141**, 365-368.
183. J. Feinleib and W. Paul, *Physical Review*, 1967, **155**, 841.
184. C. Grygiel, A. Pautrat, W. C. Sheets, W. Prellier, B. Mercey and L. Mechin, *Journal of Physics: Condensed Matter*, 2008, **20**, 472205.
185. W. Chen, J. Peng, L. Mai, H. Yu and Y. Qi, *Chemistry Letters*, 2004, **33**, 1366-1367.
186. F. J. Morin, *Physical Review Letters*, 1959, **3**, 34.

187. N. Ballarini, A. Battisti, F. Cavani, A. Cericola, C. Cortelli, M. Ferrari, F. Trifirò and P. Arpentinier, *Applied Catalysis A: General*, 2006, **307**, 148-155.
188. E. V. Kondratenko, O. Ovsitser, J. Radnik, M. Schneider, R. Kraehnert and U. Dingerdissen, *Applied Catalysis A: General*, 2007, **319**, 98-110.
189. S. J. Yun, B.-G. Chae, J. W. Lim, J.-S. Noh and H.-T. Kim, *Electrochemical and Solid-State Letters*, 2008, **11**, H173-H175.
190. C. Tsang and A. Manthiram, *Journal of The Electrochemical Society*, 1997, **144**, 520-524.
191. J. Shi, S. Zhou, B. You and L. Wu, *Solar Energy Materials and Solar Cells*, 2007, **91**, 1856-1862.
192. B.-G. Chae, H.-T. Kim, S.-J. Yun, B.-J. Kim, Y.-W. Lee, D.-H. Youn and K.-Y. Kang, *Electrochemical and Solid-State Letters*, 2006, **9**, C12-C14.
193. G. A. Rozgonyi and W. J. Polito, *Journal of The Electrochemical Society*, 1968, **115**, 56-57.
194. L.-Q. Mai, W. Chen, Q. Xu, J.-F. Peng and Q.-Y. Zhu, *Chemical Physics Letters*, 2003, **382**, 307-312.
195. C. Tenailleau, E. Suard, J. Rodriguez-Carvajal and P. Lacorre, *Journal of Magnetism and Magnetic Materials*, 2004, **278**, 57-67.
196. D. S. Toledano, P. Metcalf and V. E. Henrich, *Surface Science*, 2001, **472**, 21-32.
197. J. B. Goodenough, *Journal of Solid State Chemistry*, 1971, **3**, 490-500.
198. A. Cavalleri, C. Toth, C. W. Siders, J. A. Squier, F. Raksi, P. Forget and J. C. Kieffer, *Physical Review Letters*, 2001, **87**, 237401.
199. Y. Muraoka and Z. Hiroi, *Applied Physics Letters*, 2002, **80**, 583-585.
200. R. Aliev and V. Klimov, *Physics of the Solid State*, 2004, **46**, 532-536.
201. I. Balberg and S. Trokman, *High contrast optical storage in VO_2 films*, AIP, 1975.
202. P. Liu, S.-H. Lee, H. M. Cheong, C. E. Tracy, J. R. Pitts and R. D. Smith, *Journal of The Electrochemical Society*, 2002, **149**, H76-H80.
203. G. Sudant, E. Baudrin, B. Dunn and J.-M. Tarascon, *Journal of The Electrochemical Society*, 2004, **151**, A666-A671.
204. A. Azens, G. Gustavsson, R. Karmhag and C. G. Granqvist, *Solid State Ionics*, 2003, **165**, 1-5.
205. X. Chen, X. Wang, Z. Wang, J. Wan, J. Liu and Y. Qian, *Nanotechnology*, 2004, **15**, 1685.
206. W. Chen, L. Mai, Y. Qi and Y. Dai, *Journal of Physics and Chemistry of Solids*, **67**, 896-902.
207. A. Liu, M. Ichihara, I. Honma and H. Zhou, *Electrochemistry Communications*, 2007, **9**, 1766-1771.
208. M. Niederberger, H.-J. Muhr, F. Krumeich, F. Bieri, D. Günther and R. Nesper, *Chemistry of Materials*, 2000, **12**, 1995-2000.
209. J. M. Reinoso, H.-J. Muhr, F. Krumeich, F. Bieri and R. Nesper, *Helvetica Chimica Acta*, 2000, **83**, 1724-1733.
210. H. J. Muhr, F. Krumeich, U. P. Schönholzer, F. Bieri, M. Niederberger, L. J. Gauckler and R. Nesper, *Advanced Materials*, 2000, **12**, 231-234.
211. F. Krumeich, H. J. Muhr, M. Niederberger, F. Bieri, B. Schnyder and R. Nesper, *Journal of the American Chemical Society*, 1999, **121**, 8324-8331.

212. F. Krumeich, H.-J. Muhr, M. Niederberger, F. Bieri and R. Nesper, *Zeitschrift für anorganische und allgemeine Chemie*, 2000, **626**, 2208-2216.
213. M. E. Spahr, P. Stoschitzki-Bitterli, R. Nesper, O. Haas and P. Novak, *Journal of The Electrochemical Society*, 1999, **146**, 2780-2783.
214. S. Mathur, T. Ruegamer and I. Grobelsek, *Chemical Vapor Deposition*, 2007, **13**, 42-47.
215. R. Lopez, T. E. Haynes, L. A. Boatner, L. C. Feldman and J. R. F. Haglund, *Opt. Lett.*, 2002, **27**, 1327-1329.
216. J. M. Baik, M. H. Kim, C. Larson, A. M. Wodtke and M. Moskovits, *The Journal of Physical Chemistry C*, 2008, **112**, 13328-13331.
217. B. S. Guiton, Q. Gu, A. L. Prieto, M. S. Gudiksen and H. Park, *Journal of the American Chemical Society*, 2004, **127**, 498-499.
218. B. S. Allimi, S. P. Alpay, C. K. Xie, B. O. Wells, J. I. Budnick and D. M. Pease, *Applied Physics Letters*, 2008, **92**, 202105.
219. F. Sediri and N. Gharbi, *Materials Science and Engineering: B*, 2005, **123**, 136-138.
220. D. M. Moffatt, J. P. Runt, A. Halliyal and R. E. Newnham, *Journal of Materials Science*, 1989, **24**, 609-614.
221. G. van der Lee, B. Schuller, H. Post, T. L. F. Favre and V. Ponec, *Journal of Catalysis*, 1986, **98**, 522-529.
222. C. Zheng, X. Zhang, S. He, Q. Fu and D. Lei, *Journal of Solid State Chemistry*, 2003, **170**, 221-226.
223. K. Zhang, X. Sun, G. Lou, X. Liu, H. Li and Z. Su, *Materials Letters*, 2005, **59**, 2729-2731.
224. Z. Yang, P. Cai, L. Chen, Y. Gu, L. Shi, A. Zhao and Y. Qian, *Journal of Alloys and Compounds*, 2006, **420**, 229-232.
225. N. Pinna, M. Antonietti and M. Niederberger, *Colloids and Surfaces A: Physicochemical and Engineering Aspects*, 2004, **250**, 211-213.
226. S. A. Corr, M. Grossman, J. D. Furman, B. C. Melot, A. K. Cheetham, K. R. Heier and R. Seshadri, *Chemistry of Materials*, 2008, **20**, 6396-6404.
227. G. Anderson, *Acta Chemica Scandinavica*, 1956, **10**, 623.
228. A. D. Burton and P. A. Cox, *Philisopical Magazine*, 1985, **51**, 255.
229. H. Liu, O. Vasquez, V. R. Santiago, L. Díaz and F. E. Fernandez, *Journal of Luminescence*, 2004, **108**, 233-238.
230. P. Baum, D.-S. Yang and A. H. Zewail, *Science*, 2007, **318**, 788-792.
231. M. B. Sahana, G. N. Subbanna and S. A. Shivashankar, *Applied Physics Letters*, 2002, **92**, 6495-6504.
232. J. C. Rakotoniaina, R. Mokrani-Tamellin, J. R. Gavarri, G. Vacquier, A. Casalot and G. Calvarin, *Journal of Solid State Chemistry*, 1993, **103**, 81-94.
233. Y. Oka, T. Yao and N. Yamamoto, *Journal of Materials Chemistry*, 1991, **1**, 815-818.
234. G. T. Chandrappa, N. Steunou, S. Cassaignon, C. Bauvais and J. Livage, *Catalysis Today*, 2003, **78**, 85-89.
235. Y. Mao and S. S. Wong, *Journal of the American Chemical Society*, 2006, **128**, 8217-8226.
236. Z. Gui, R. Fan, W. Mo, X. Chen, L. Yang, S. Zhang, Y. Hu, Z. Wang and W. Fan, *Chemistry of Materials*, 2002, **14**, 5053-5056.
237. C. Leroux, G. Nihoul and G. Van Tendeloo, *Physical Review B*, 1998, **57**, 5111.
238. D. S. Su and R. Schlögl, *Catalysis Letters*, 2002, **83**, 115-119.

239. C. V. Ramana, S. Utsunomiya, R. C. Ewing and U. Becker, *Solid State Communications*, 2006, **137**, 645-649.
240. Y. Ueda, K. Kosuge and S. Kachi, *Journal of Solid State Chemistry*, 1980, **31**, 171-188.
241. R. N. Bhowmik, R. Nagarajan and R. Ranganathan, *Physical Review B*, 2004, **69**, 054430.
242. R. N. Bhowmik and R. Ranganathan, *Solid State Communications*, 2007, **141**, 365-368.
243. J. Feinleib and W. Paul, *Physical Review*, 1967, **155**, 841.
244. C. Grygiel, A. Pautrat, W. C. Sheets, W. Prellier, B. Mercey and L. Mechin, *Journal of Physics: Condensed Matter*, 2008, **20**, 472205.
245. A. Polman, *Erbium implanted thin film photonic materials*, AIP, 1997.
246. F. Abdi, M. Aillerie, P. Bourson, M. D. Fontana and K. Polgar, *Electro-optic properties in pure LiNbO3 crystals from the congruent to the stoichiometric composition*, AIP, 1998.
247. N. F. Foster, *The Deposition and Piezoelectric Characteristics of Sputtered Lithium Niobate Films*, AIP, 1969.
248. L. Zhao, M. Steinhart, M. Yosef, S. K. Lee and S. Schlecht, *Sensors and Actuators B: Chemical*, 2005, **109**, 86-90.
249. A. Ruso, M. Aillerie, N. Fressengeas and M. Ferriol, *Applied Physics B: Lasers and Optics*, 2009, **95**, 573-578.
250. C. Nölleke, J. Imbrock and C. Denz, *Applied Physics B: Lasers and Optics*, 2009, **95**, 391-397.
251. Y.-S. Yim and S.-Y. Shin, *Optics Communications*, 1998, **152**, 225-228.
252. N. Courjal, M.-P. Bernal, G. Ulliac, J. Dahdah, S. Benchabane and J.-M. Merolla, *Journal of the European Optical Society Rapid Publications*, 2009, **4**, 09018.
253. D.-H. Yoon, I. Yonenaga, T. Fukuda and N. Ohnishi, *Journal of Crystal Growth*, 1994, **142**, 339-343.
254. Y. S. Luh, M. M. Fejer, R. L. Byer and R. S. Feigelson, *Journal of Crystal Growth*, 1987, **85**, 264-269.
255. K. Polgár, Á. Péter, L. Kovács, G. Corradi and Z. Szaller, *Journal of Crystal Growth*, 1997, **177**, 211-216.
256. M. Liu and D. Xue, *The Journal of Physical Chemistry C*, 2008, **112**, 6346-6351.
257. R. Grange, J.-W. Choi, C.-L. Hsieh, Y. Pu, A. Magrez, R. Smajda, L. Forró and D. Psaltis, *Lithium niobate nanowires synthesis, optical properties, and manipulation*, AIP, 2009.
258. B. D. Wood, V. Mocanu and B. D. Gates, *Advanced Materials*, 2008, **20**, 4552-4556.
259. C.-Y. Xu, L. Zhen, R. Yang and Z. L. Wang, *Journal of the American Chemical Society*, 2007, **129**, 15444-15445.
260. L. Li, J. Deng, J. Chen, X. Sun, R. Yu, G. Liu and X. Xing, *Chemistry of Materials*, 2009, **21**, 1207-1213.
261. R. E. Schaak and T. E. Mallouk, *Chemistry of Materials*, 2002, **14**, 1455-1471.
262. Y. Repelin, E. Husson, F. Bennani and C. Proust, *Journal of Physics and Chemistry of Solids*, 1999, **60**, 819-825.
263. A. S. Barker and R. Loudon, *Physical Review*, 1967, **158**, 433.
264. R. F. Schaufele and M. J. Weber, *Physical Review*, 1966, **152**, 705.
265. S. Berweger and M. B. Raschke, *Journal of Raman Spectroscopy*, 2009, **40**, 1413-1419.

266. M. Ocaña, *Journal of the European Ceramic Society*, 2001, **21**, 931-939.
267. D.-W. Kim, S.-I. Shin, J.-D. Lee and S.-G. Oh, *Materials Letters*, 2004, **58**, 1894-1898.
268. B. Bhushan, G. S. A. M. Theunissen and X. Li, *Thin Solid Films*, 1997, **311**, 67-80.
269. M. Chatterjee, B. Siladitya and D. Ganguli, *Materials Letters*, 1995, **25**, 261-263.
270. T. Tsuzuki and P. G. McCormick, *Acta Materialia*, 2000, **48**, 2795-2801.
271. S. Music, M. Maljkovic, S. Popovic and R. Trojko, *Croatica Chemica Acta*, 1999, **72**, 789.
272. L. Znaidi and C. Pommier, *European Journal of Solid State and Inorganic Chemistry*, **35**, 405-417.
273. W. A. Lazier and J. V. Vaughen, *Journal of the American Chemical Society*, 1932, **54**, 3080-3095.
274. B. M. Weckhuysen and R. A. Schoonheydt, *Catalysis Today*, 1999, **51**, 223-232.
275. B. Grzybowska, J. Sloczynski, R. Grabowski, L. Keromnes, K. Wcislo and T. Bobinska, *Applied Catalysis A: General*, 2001, **209**, 279-289.
276. H. Thakuria, B. M. Borah and G. Das, *Journal of Molecular Catalysis A: Chemical*, 2007, **274**, 1-10.
277. C. M. Pradier, F. Rodrigues, P. Marcus, M. V. Landau, M. L. Kaliya, A. Gutman and M. Herskowitz, *Applied Catalysis B: Environmental*, 2000, **27**, 73-85.
278. H. Cao, X. Qiu, Y. Liang, M. Zhao and Q. Zhu, *Sol-gel synthesis and photoluminescence of p-journal article semiconductor Cr2O3 nanowires*, AIP, 2006.
279. M. Banobre-Lopez, C. Vazquez-Vazquez, J. Rivas and M. A. Lopez-Qunitela, *Nanotechnology*, 2003, **14**, 318.
280. W. S. Zhang, E. Brück, Z. D. Zhang, O. Tegus, W. F. Li, P. Z. Si, D. Y. Geng and K. H. J. Buschow, *Physica B: Condensed Matter*, 2005, **358**, 332-338.
281. S. Foner, *Physical Review*, 1963, **130**, 183.
282. D. Vollath, D. V. Szabó and J. O. Willis, *Materials Letters*, 1996, **29**, 271-279.
283. R. L. Burwell and H. S. Taylor, *Journal of the American Chemical Society*, 1936, **58**, 697-705.
284. S. Pokhrel, C. E. Simion, V. Quemener, N. Bârsan and U. Weimar, *Sensors and Actuators B: Chemical*, 2008, **133**, 78-83.
285. X. Liang, T. Zhong, H. Guan, F. Liu, G. Lu and B. Quan, *Sensors and Actuators B: Chemical*, 2009, **136**, 479-483.
286. U. Balachandran, R. W. Siegel, Y. X. Liao and T. R. Askew, *Nanostructured Materials*, **5**, 505-512.
287. Z. Pei, H. Xu and Y. Zhang, *Journal of Alloys and Compounds*, 2009, **468**, L5-L8.
288. Z. Pei and Y. Zhang, *Materials Letters*, 2008, **62**, 504-506.
289. M. Abecassis-Wolfovich, H. Rotter, M. V. Landau, E. Korin, A. I. Erenburg, D. Mogilyansky and E. Gartstein, *Journal of Non-Crystalline Solids*, 2003, **318**, 95-111.
290. A. E. Gash, T. M. Tillotson, J. H. Satcher Jr, L. W. Hrubesh and R. L. Simpson, *Journal of Non-Crystalline Solids*, 2001, **285**, 22-28.
291. Li, Z. F. Yan, G. Q. Lu and Z. H. Zhu, *The Journal of Physical Chemistry B*, 2005, **110**, 178-183.
292. Z. Gui, R. Fan, W. Mo, X. Chen, L. Yang and Y. Hu, *Materials Research Bulletin*, 2003, **38**, 169-176.
293. Z. C. Zhong, R. H. Cheng, J. Bosley, P. A. Dowben and D. J. Sellmyer, *Applied Surface Science*, 2001, **181**, 196-200.

294. G. Peters, K. Jerg and B. Schramm, *Materials Chemistry and Physics*, 1998, **55**, 197-201.
295. N. A. Dhas, Y. Koltypin and A. Gedanken, *Chemistry of Materials*, 1997, **9**, 3159-3163.
296. W.-Q. Han, L. Wu, A. Stein, Y. Zhu, J. Misewich and J. Warren, *Angewandte Chemie International Edition*, 2006, **45**, 6554-6558.
297. J. Wang, J. Sun and X. Bian, *Modelling, Measurement & Control, C: Energetics, Chemistry & Chemical Engineering, Earth, Resources, Environment, Biomedical Problems*, 2004, **65**, 47.
298. Z. Yu-Feng, L. Zheng-Song and C. Qian-Wang, *Chininese Journal of Inorganic Chemistry*, 2004, **20**, 971.
299. B. Tian, X. Liu, H. Yang, S. Xie, C. Yu, B. Tu and D. Zhao, *Advanced Materials*, 2003, **15**, 1370-1374.
300. C. Dickinson, W. Zhou, R. P. Hodgkins, Shi, Zhao and He, *Chemistry of Materials*, 2006, **18**, 3088-3095.
301. A. Guimin and et al., *Nanotechnology*, 2008, **19**, 035504.
302. C. Vázquez-Vázquez, M. Bañobre-López, M. A. López-Quintela, L. E. Hueso and J. J. Rivas, *Journal of Magnetism and Magnetic Materials*, 2004, **272-276**, 1547-1548.
303. S. A. S. A. Makhlouf, *Journal of Magnetism and Magnetic Materials*, 2004, **272-276**, 1530-1532.
304. C. Schönenberger, B. M. I. van der Zande, L. G. J. Fokkink, M. Henny, C. Schmid, M. Krüger, A. Bachtold, R. Huber, H. Birk and U. Staufer, *The Journal of Physical Chemistry B*, 1997, **101**, 5497-5505.
305. M. Tian, J. Wang, J. Kurtz, T. E. Mallouk and M. H. W. Chan, *Nano Letters*, 2003, **3**, 919-923.
306. Y. Mao, M. Kanungo, T. Hemraj-Benny and S. S. Wong, *The Journal of Physical Chemistry B*, 2005, **110**, 702-710.
307. P. Ratnasamy and A. J. Leonard, *The Journal of Physical Chemistry*, 1972, **76**, 1838-1843.
308. G. An, Y. Zhang, Z. Liu, Z. Miao, B. Han, S. Miao and J. Li, *Nanotechnology*, 2008, **19**, 035504/035501.
309. N. T. McDevitt and W. L. Baun, *Spectrochimica Acta*, 1964, **20**, 799-808.
310. H. Li, Y. Yue, C. Miao, Z. Xie, W. Hua and Z. Gao, *Chinese Journal of Catalysis*, 2006, **27**, 4-6.
311. B. M. Weckhuysen, I. E. Wachs and R. A. Schoonheydt, *Chemical Reviews*, 1996, **96**, 3327-3350.
312. L. D. Zhang, C. M. Mo, W. L. Cai and G. Chen, *Nanostructured Materials*, 1997, **9**, 563-566.
313. H. H. Willard, L. L. Merritt and J. A. Dean, *Instrumental methods of analysis*, D. Van Nostrand Company, Inc., 1965.
314. C. Lin, P. Shen and S. Chen, *Applied Physics B: Lasers and Optics*, 2010, **98**, 443-450.
315. J. Mougin, T. Le Bihan and G. Lucazeau, *Journal of Physics and Chemistry of Solids*, 2001, **62**, 553-563.
316. N. F. Mott and E. A. Davis, *Electronic Process in Non-Crystalline Materials*, 1979.
317. P. Borisov, A. Hochstrat, V. V. Shvartsman, W. Kleemann, T. Eimüller and A. F. RodrÍguez, *Ferroelectrics*, 2008, **370**, 147-152.
318. C.-S. Cheng, H. Gomi and H. Sakata, *physica status solidi (a)*, 1996, **155**, 417-425.

319. D. Tobia, E. L. Winkler, R. D. Zysler, M. Granada and H. E. Troiani, *Journal of Alloys and Compounds*, 2010, **495**, 520-523.
320. M. P. Morales and et al., *Journal of Physics: Condensed Matter*, 1997, **9**, 5461.
321. X. Teng, M. Feygenson, Q. Wang, J. He, W. Du, A. I. Frenkel, W. Han and M. Aronson, *Nano Letters*, 2009, **9**, 3177-3184.
322. M. Feygenson, A. Kou, L. E. Kreno, A. L. Tiano, J. M. Patete, F. Zhang, M. S. Kim, V. Solovyov, S. S. Wong and M. C. Aronson, *Physical Review B*, 2010, **81**, 014420.
323. J. Nogués and I. K. Schuller, *Journal of Magnetism and Magnetic Materials*, 1999, **192**, 203-232.
324. J. Nogués, J. Sort, V. Langlais, V. Skumryev, S. Suriñach, J. S. Muñoz and M. D. Baró, *Physics Reports*, 2005, **422**, 65-117.
325. S. E. Inderhees, J. A. Borchers, K. S. Green, M. S. Kim, K. Sun, G. L. Strycker and M. C. Aronson, *Physical Review Letters*, 2008, **101**, 117202.
326. R. H. Kodama, S. A. Makhlouf and A. E. Berkowitz, *Physical Review Letters*, 1997, **79**, 1393.
327. A. A. Said, E. A. Hassan and K. M. Abd El-Salaam, *Surface Technology*, 1983, **20**, 131-137.
328. A. Luque and A. Marti, *Electronics Letters*, 2008, **44**, 943-945.
329. B. O'Regan and D. T. Schwartz, *Journal of Applied Physics*, 1996, **80**, 4749-4754.
330. Y. Chiba, A. Islam, Y. Watanabe, R. Komiya, N. Koide and L. Han, *Japanese Journal of Applied Physics*, 2006, **45**, L638-L640.
331. M. Wang, S.-J. Moon, D. Zhou, F. Le Formal, N.-L. Cevey-Ha, R. Humphry-Baker, C. Grätzel, P. Wang, S. M. Zakeeruddin and M. Grätzel, *Advanced Functional Materials*, 2010, **20**, 1821-1826.
332. K.-M. Lee, S.-J. Wu, C.-Y. Chen, C.-G. Wu, M. Ikegami, K. Miyoshi, T. Miyasaka and K.-C. Ho, *Journal of Materials Chemistry*, 2009, **19**, 5009-5015.
333. A. C. Onicha and F. N. Castellano, *The Journal of Physical Chemistry C*, 2010, **114**, 6831-6840.
334. G. Sauvé, M. E. Cass, S. J. Doig, I. Lauermann, K. Pomykal and N. S. Lewis, *The Journal of Physical Chemistry B*, 2000, **104**, 3488-3491.
335. G. Zanotti, N. Angelini, S. Notarantonio, A. M. Paoletti, G. Pennesi, G. Rossi, A. Lembo, D. Colonna, A. Di Carlo, A. Reale, T. M. Brown and G. Calogero, *International Journal of Photoenergy*, 2010, **2010**.
336. P. Y. Reddy, L. Giribabu, C. Lyness, H. J. Snaith, C. Vijaykumar, M. Chandrasekharam, M. Lakshmikantam, J.-H. Yum, K. Kalyanasundaram, M. Grätzel and M. K. Nazeeruddin, *Angewandte Chemie International Edition*, 2007, **46**, 373-376.
337. L. Giribabu, C. Vijay Kumar, V. Gopal Reddy, P. Yella Reddy, C. Srinivasa Rao, S.-R. Jang, J.-H. Yum, M. K. Nazeeruddin and M. Grätzel, *Solar Energy Materials and Solar Cells*, 2007, **91**, 1611-1617.
338. S. Wenger, P.-A. Bouit, Q. Chen, J. l. Teuscher, D. D. Censo, R. Humphry-Baker, J.-E. Moser, J. L. Delgado, N. Martín, S. M. Zakeeruddin and M. Grätzel, *Journal of the American Chemical Society*, 2010, **132**, 5164-5169.
339. S. Kim, J. K. Lee, S. O. Kang, J. Ko, J. H. Yum, S. Fantacci, F. De Angelis, D. Di Censo, M. K. Nazeeruddin and M. Grätzel, *Journal of the American Chemical Society*, 2006, **128**, 16701-16707.

340. Z.-S. Wang, Y. Cui, Y. Dan-oh, C. Kasada, A. Shinpo and K. Hara, *The Journal of Physical Chemistry C*, 2007, **111**, 7224-7230.
341. A. Hagfeldt, G. Boschloo, L. Sun, L. Kloo and H. Pettersson, *Chemical Reviews*, 2010, **110**, 6595-6663.
342. I. K. Ding, J. Zhu, W. Cai, S.-J. Moon, N. Cai, P. Wang, S. M. Zakeeruddin, M. Grätzel, M. L. Brongersma, Y. Cui and M. D. McGehee, *Advanced Energy Materials*, 2011, **1**, 52-57.
343. M. J. Scott, J. J. Nelson, S. Caramori, C. A. Bignozzi and C. M. Elliott, *Inorganic Chemistry*, 2007, **46**, 10071-10078.
344. T. C. Li, A. M. Spokoyny, C. She, O. K. Farha, C. A. Mirkin, T. J. Marks and J. T. Hupp, *Journal of the American Chemical Society*, 2010, **132**, 4580-4582.
345. S. Nakade, Y. Makimoto, W. Kubo, T. Kitamura, Y. Wada and S. Yanagida, *The Journal of Physical Chemistry B*, 2005, **109**, 3488-3493.
346. B. M. Klahr and T. W. Hamann, *The Journal of Physical Chemistry C*, 2009, **113**, 14040-14045.
347. W. Kubo, K. Murakoshi, T. Kitamura, Y. Wada, K. Hanabusa, H. Shirai and S. Yanagida, *Chemistry Letters*, 1998, **27**, 1241-1242.
348. Y. Ren, Z. Zhang, E. Gao, S. Fang and S. Cai, *Journal of Applied Electrochemistry*, 2001, **31**, 445-447.
349. Y. Saito, T. Kitamura, Y. Wada and S. Yanagida, *Synthetic Metals*, 2002, **131**, 185-187.
350. P. Ravirajan, A. M. Peiró, M. K. Nazeeruddin, M. Graetzel, D. D. C. Bradley, J. R. Durrant and J. Nelson, *The Journal of Physical Chemistry B*, 2006, **110**, 7635-7639.
351. U. Bach, D. Lupo, P. Comte, J. E. Moser, F. Weissortel, J. Salbeck, H. Spreitzer and M. Gratzel, *Nature*, 1998, **395**, 583-585.
352. U. Bach, K. De Cloedt, H. Spreitzer and M. Grätzel, *Advanced Materials*, 2000, **12**, 1060-1063.
353. K. Tennakone, G. R. R. A. Kumara, A. R. Kumarasinghe, K. G. U. Wijayantha and P. M. Sirimanne, *Semiconductor Science and Technology*, 1995, **10**, 1689.
354. G. R. R. A. Kumara, A. Konno, G. K. R. Senadeera, P. V. V. Jayaweera, D. B. R. A. De Silva and K. Tennakone, *Solar Energy Materials and Solar Cells*, 2001, **69**, 195-199.
355. J. Bandara and H. Weerasinghe, *Solar Energy Materials and Solar Cells*, 2005, **85**, 385-390.
356. N. Papageorgiou, W. F. Maier and M. Gratzel, *Journal of The Electrochemical Society*, 1997, **144**, 876-884.
357. H. Pettersson, T. Gruszecki, R. Bernhard, L. Häggman, M. Gorlov, G. Boschloo, T. Edvinsson, L. Kloo and A. Hagfeldt, *Progress in Photovoltaics: Research and Applications*, 2007, **15**, 113-121.
358. A. Kay and M. Grätzel, *Solar Energy Materials and Solar Cells*, 1996, **44**, 99-117.
359. A. Hauch and A. Georg, *Electrochimica Acta*, 2001, **46**, 3457-3466.
360. L. Bay, K. West, B. Winther-Jensen and T. Jacobsen, *Solar Energy Materials and Solar Cells*, 2006, **90**, 341-351.
361. M. Wang, A. M. Anghel, B. t. Marsan, N.-L. Cevey Ha, N. Pootrakulchote, S. M. Zakeeruddin and M. Grätzel, *Journal of the American Chemical Society*, 2009, **131**, 15976-15977.
362. J. Yu, J. Fan and K. Lv, *Nanoscale*, 2010, **2**, 2144-2149.
363. Y. Alivov and Z. Y. Fan, *Applied Physics Letters*, 2009, **95**, 063504.

364. D. Chen, F. Huang, Y.-B. Cheng and R. A. Caruso, *Advanced Materials*, 2009, **21**, 2206-2210.
365. X. Feng, K. Shankar, O. K. Varghese, M. Paulose, T. J. Latempa and C. A. Grimes, *Nano Letters*, 2008, **8**, 3781-3786.
366. H. Hafez, Z. Lan and Q. Li, *Nanotechnology, Science and Applications*, 2010, **3**, 45-51.
367. S. R. Gajjela, K. Ananthanarayanan, C. Yap, M. Gratzel and P. Balaya, *Energy & Environmental Science*, 2010, **3**, 838-845.
368. I. C. Baek, M. Vithal, J. A. Chang, J.-H. Yum, M. K. Nazeeruddin, M. Grätzel, Y.-C. Chung and S. I. Seok, *Electrochemistry Communications*, 2009, **11**, 909-912.
369. J. Han, F. Fan, C. Xu, S. Lin, M. Wei, X. Duan and Z. L. Wang, *Nanotechnology*, 2010, **21**, 405203.
370. L. Zhang, Y. Shi, S. Peng, J. Liang, Z. Tao and J. Chen, *Journal of Photochemistry and Photobiology A: Chemistry*, 2008, **197**, 260-265.
371. R. Jose, V. Thavasi and S. Ramakrishna, *Journal of the American Ceramic Society*, 2009, **92**, 289-301.
372. M. J. Cass, F. L. Qiu, A. B. Walker, A. C. Fisher and L. M. Peter, *The Journal of Physical Chemistry B*, 2002, **107**, 113-119.
373. K. Yu and J. Chen, *Nanoscale Research Letters*, 2008, **4**, 1-10.
374. D. Kuang, J. r. m. Brillet, P. Chen, M. Takata, S. Uchida, H. Miura, K. Sumioka, S. M. Zakeeruddin and M. Grätzel, *ACS Nano*, 2008, **2**, 1113-1116.
375. B.-X. Lei, J.-Y. Liao, R. Zhang, J. Want, C.-Y. Su and D.-B. Kuang, *Journal of Physical Chemistry C*, 2010, **114**, 15228-15233.
376. B. Tan and Y. Wu, *The Journal of Physical Chemistry B*, 2006, **110**, 15932-15938.
377. K. Asagoe, S. Ngamsinlapasathian, Y. Suzuki and S. Yoshikawa, *Central European Journal of Chemistry*, 2007, **5**, 605-619.
378. Y. Qiu, W. Chen and S. Yang, *Angewandte Chemie International Edition*, 2010, **49**, 3675-3679.
379. C. Yip, C. Mak, A. Djurišić, Y. Hsu and W. Chan, *Applied Physics A: Materials Science & Processing*, 2008, **92**, 589-593.
380. G. K. Mor, K. Shankar, M. Paulose, O. K. Varghese and C. A. Grimes, *Nano Letters*, 2005, **6**, 215-218.
381. K. Zhu, N. R. Neale, A. Miedaner and A. J. Frank, *Nano Letters*, 2006, **7**, 69-74.
382. C.-J. Lin, W.-Y. Yu and S.-H. Chien, *Journal of Materials Chemistry*, 2010, **20**, 1073-1077.
383. Z. B. Xie, S. Adams, D. J. Blackwood and J. Wang, *Nanotechnology*, 2008, **19**, 405701.
384. P. Chen, J. Brillet, H. Bala, P. Wang, S. M. Zakeeruddin and M. Gratzel, *Journal of Materials Chemistry*, 2009, **19**, 5325-5328.
385. P. Roy, D. Kim, K. Lee, E. Spiecker and P. Schmuki, *Nanoscale*, 2010, **2**, 45-59.
386. J. T. Park, D. K. Roh, R. Patel, E. Kim, D. Y. Ryu and J. H. Kim, *Journal of Materials Chemistry*, 2010, **20**, 8521-8530.
387. H. Wang, C. T. Yip, K. Y. Cheung, A. B. Djurisic, M. H. Xie, Y. H. Leung and W. K. Chan, *Applied Physics Letters*, 2006, **89**, 2221502.
388. J.-K. Oh, J.-K. Lee, H.-S. Kim, S.-B. Han and K.-W. Park, *Chemistry of Materials*, 2009, **22**, 1114-1118.
389. F. Sauvage, F. Di Fonzo, A. Li Bassi, C. S. Casari, V. Russo, G. Divitini, C. Ducati, C. E. Bottani, P. Comte and M. Graetzel, *Nano Letters*, 2010, **10**, 2562-2567.

390. W. Shao, F. Gu, C. Li and M. Lu, *Inorganic Chemistry*, 2010, **49**, 5453-5459.
391. Y. Mao and S. S. Wong, *Journal of the American Chemical Society*, 2006, **128**, 8217-8226.
392. E. Ghadiri, N. Taghavinia, S. M. Zakeeruddin, M. Grätzel and J.-E. Moser, *Nano Letters*, 2010, **10**, 1632-1638.
393. Y. Mao, M. Kanungo, T. Hemraj-Benny and S. S. Wong, *The Journal of Physical Chemistry B*, 2005, **110**, 702-710.
394. S. Ito, T. N. Murakami, P. Comte, P. Liska, C. Grätzel, M. K. Nazeeruddin and M. Grätzel, *Thin Solid Films*, 2008, **516**, 4613-4619.
395. A. Zaban, M. Greenshtein and J. Bisquert, *ChemPhysChem*, 2003, **4**, 859-864.
396. M. Koelsch, S. Cassaignon, C. Ta Thanh Minh, J. F. Guillemoles and J. P. Jolivet, *Thin Solid Films*, 2004, **451-452**, 86-92.
397. N. G. Park, J. van de Lagemaat and A. J. Frank, *The Journal of Physical Chemistry B*, 2000, **104**, 8989-8994.
398. F. Huang, D. Chen, X. L. Zhang, R. A. Caruso and Y.-B. Cheng, *Advanced Functional Materials*, 2010, **20**, 1301-1305.
399. F. d. r. Sauvage, D. Chen, P. Comte, F. Huang, L.-P. Heiniger, Y.-B. Cheng, R. A. Caruso and M. Graetzel, *ACS Nano*, 2010, **4**, 4420-4425.
400. Y. Zhang, Z. Xie and J. Wang, *ACS Applied Materials & Interfaces*, 2009, **1**, 2789-2795.
401. P. S. Archana, R. Jose, C. Vijila and S. Ramakrishna, *The Journal of Physical Chemistry C*, 2009, **113**, 21538-21542.
402. J. Jiu, S. Isoda, F. Wang and M. Adachi, *The Journal of Physical Chemistry B*, 2006, **110**, 2087-2092.
403. K. Hou, B. Tian, F. Li, Z. Bian, D. Zhao and C. Huang, *Journal of Materials Chemistry*, 2005, **15**, 2414-2420.
404. Y.-Q. Wang, S.-G. Chen, X.-H. Tang, O. Palchik, A. Zaban, Y. Koltypin and A. Gedanken, *Journal of Materials Chemistry*, 2001, **11**, 521-526.
405. W. Meili, C. Huang, Y. Cao, Q. Yu, Z. Deng, Y. Liu, Z. Huang, J. Huang, Q. Huang, W. Guo and J. Liang, *Journal of Physics D: Applied Physics*, 2009, **42**, 155104.
406. S. Nakade, Y. Saito, W. Kubo, T. Kitamura, Y. Wada and S. Yanagida, *The Journal of Physical Chemistry B*, 2003, **107**, 8607-8611.
407. Y. Alivov and Z. Fan, *Journal of Materials Science*, 2010, **45**, 2902-2906.
408. S. Burnside, J.-E. Moser, K. Brooks, M. Grätzel and D. Cahen, *The Journal of Physical Chemistry B*, 1999, **103**, 9328-9332.
409. S. Yang, H. Kou, H. Wang, K. Cheng and J. Wang, *Electrochimica Acta*, 2009, **55**, 305-310.